METHODS OF CORRELATING TEXTURE AND MAGNETIC PROPERTIES IN ELECTRICAL STEELS

by

Marius Stefan Birsan

A Thesis Submitted to the Faculty of Graduate Studies
and Research in Partial Fulfilment of the Requirements
for the degree of Doctor of Philosophy

Department of Mining and Metallurgical Engineering
McGill University
Montreal, Canada

August 1995

ABSTRACT

Electrical steels are soft magnetic materials used for magnetic cores in electrical machines. The magnetic properties of electrical steels may be significantly improved by a texture in such a way that magnetically preferred crystal directions are oriented parallel to those directions in the material in which they are needed. Therefore, for technological applications, macroscopic anisotropy of magnetic properties in these materials is desirable. The correlation between texture and the magnetic properties of electrical steels is the focus of this study.

The principal aspects of texture analysis theory are discussed briefly. Texture is described with the aid of the orientation distribution function (ODF). The theoretical aspects of the magnetization process in soft magnetic materials are presented, and the different models developed for correlating texture and magnetic properties of electrical steels are reviewed.

Texture measurements are performed using X-ray and neutron diffraction. Several other methods have been used to determine properties such as the magnetic anisotropy energy, domain wall spacing, permeability and power losses. Barkhausen noise measurements are used to demonstrate the correlation between the power losses obtained from the standard Epstein test and the

microscopic processes contributing to the total magnetization.

New models linking magnetic properties to texture and microstructure of materials have been proposed. The theoretical values of magnetic properties such as the reversible magnetization rotation, permeability, power loss, and the magnetic Barkhausen noise power obtained from these models, have been compared to the experimental data. It is shown that the developed models correctly describe the corresponding properties, and that these models contribute to a better description of magnetization mechanisms in ferromagnetic polycrystalline materials.

Neutron diffraction and neutron depolarization measurements are shown to be helpful in examining the influence of texture on the anisotropy of magnetic properties in materials. The possibility of neutron diffraction measurement of magnetic texture is reported.

Other aspects of the present study concern the application of some of the above mentioned magnetic methods in monitoring the quality of electrical steels. From this viewpoint, new non-destructive methods based on the Barkhausen noise measurements, and on the measurement of the magnetization rotation using a modified torquemeter, have been developed and tested. The latter method could be easily implemented on-line.

RÉSUMÉ

Les aciers électriques font partie des matériaux magnétiques mous et sont utilisés dans les noyaux magnétiques des machines électriques. Les propriétés magnétiques des aciers électriques peuvent être significativement améliorées par une texture de façon à ce que les directions préférées de magnétisation du cristal sont parallèlement orientées avec les directions de magnétisation imposées. Donc, pour tels matériaux, l'anisotropie macroscopique des propriétés magnétiques est désirable pour les applications technologiques. La corrélation entre la texture et les propriétés magnétiques des aciers électriques représente le but de cet étude.

Les principaux aspects de la théorie de l'analyse de la texture sont brièvement présentés. La texture est décrite par la fonction de la distribution des orientations (ODF). Sont aussi présentés les aspects théoriques des processus d'aimantation des matériaux mous, ainsi que les différents modèles développés pour faire la corrélation entre la texture et les propriétés électriques et magnétiques.

Les mesures de texture sont effectuées à l'aide des rayons X

et la diffraction des neutrons. D'autres méthodes ont été utilisées pour déterminer des propriétés comme l'énergie anisotrope magnétique, l'espace entre les parois des domaines, la perméabilité et les pertes de puissance. Les mesures de bruit Barkhausen sont utilisées pour démontrer la corrélation entre les pertes de puissance obtenues à la suite du test Epstein et les processus microscopiques qui contribuent à l'aimantation totale.

Des nouveaux modèles reliant les propriétés magnétiques et la texture ainsi que la microstructure des matériaux ont été proposés. Les valeurs théoriques des propriétés magnétiques comme la rotation magnétique réversible, la perméabilité, les pertes de puissance et la puissance des bruits magnétique Barkhausen obtenues a l'aide de ces modèles ont été comparées avec les données des expériences. On a démontré que les modèles développés décrivent correctement les propriétés correspondantes et que ces modèles contribuent à une meilleure description des mécanismes d'aimantation dans les matériaux ferromagnétiques poly-cristallines.

La diffraction des neutrons et les mesures concernant la dépolarisation des neutrons ont été présentés pour aider à l'analyse de l'influence de la texture sur l'anisotropie des propriétés magnétiques dans les matériaux. On a aussi exposé la possibilité de mesurer la texture magnétique à l'aide de la diffraction des neutrons.

D'autres aspects du présent travail implique l'utilisation de quelques méthodes présentées antérieurement pour l'inspection de la qualité des aciers électriques. De ce point de vue, de nouvelles méthodes non-distructives basées sur les mesures du bruit Barkhausen et sur les mesures de la rotation magnétique en utilisant un appareil modifié pour le couple magnétique ont été développées et testées. La dernière méthode pourra être facilement implanter "on-line".

ACKNOWLEDGEMENTS

I am grateful for the support and guidance of my supervisor, Professor J.A.Szpunar. He has a high degree of insight and enthusiasm for physical metallurgy. The extent to which I have been influenced by his attitudes regarding science, administration and relationships, is significant. He introduced me to the exciting field of materials science, and constantly encouraged me during the progress of this study.

I would like to thank Dr. T.W.Krause from Queen's University, Kingston, who supported the Barkhausen noise part of this academic project, in the perspective of an industrial application.

I am indebted to Drs. J.Root and Z.Tun from Atomic Energy of Canada Lim. (AECL) who granted access to the research facilities in the Chalk River Nuclear Laboratory. I learned a vast amount from their professional experience, and applied that knowledge to successfully completing this thesis.

I recognize the technical support of S. Poplawsky, who carried out most of the experimental X-ray analysis with extreme care.

To all these people, I say "thank you".

Also, I want to thank NSERC for the scholarship.

TABLE OF CONTENTS

ABSTRACT 1
RESUME 3
ACKNOWLEDGEMENTS 5
TABLE OF CONTENTS 6
LIST OF SYMBOLS 8
LIST OF FIGURES 12

1. INTRODUCTION 15

2. TEXTURE AND MAGNETIC PROPERTIES OF ELECTRICAL STEELS 21

   2.1. The texture of materials 22
   2.2. Magnetic domain structure 34
   2.3. Dynamic properties of magnetization 43
   2.4. Anisotropy of magnetic properties 47

3. EVALUATION OF THE QUALITY OF ELECTRICAL STEELS 53

   3.1. Description of materials 53
   3.2. Epstein method for macromagnetic property determination 55
   3.3. Macromagnetic characterization of the materials used for investigation 57

4. EXPERIMENTAL METHODS AND RESULTS OF TEXTURE ANALYSIS 64

   4.1. Texture measurements using X-ray diffraction 65
   4.2. Texture measurements using neutron diffraction 70
   4.3. Texture analysis 83

5. METHODS OF CORRELATING TEXTURE AND MAGNETIC ANISOTROPY ENERGY 100

- 5.1. Construction of a torque magnetometer 101
- 5.2. Results of magnetic torque measurements 114
- 5.3. Correlating texture and magnetocrystalline energy 120
- 5.4. The influence of texture on the reversible magnetization rotation 125

6. NON-DESTRUCTIVE METHODS OF CORRELATING TEXTURE, MICROSTRUCTURE AND POWER LOSSES 145

- 6.1. Correlation between texture, domain spacing and power losses in grain oriented materials 147
- 6.2. NDE method of correlating texture, microstructure and power losses 157

7. NEUTRON SCATTERING METHODS FOR MAGNETIC TEXTURE DETERMINATION 177

- 7.1. Magnetic texture 178
- 7.2. Method of measuring magnetic texture using non-polarized neutron diffraction 178
- 7.3. Method to analyze the magnetic texture using polarized neutron diffraction 195
- 7.4. Analysis of neutron depolarization in a grain oriented material 204

8. MODEL-BASED METHODS OF CORRELATING TEXTURE AND MAGNETIC PROPERTIES 215

- 8.1. Anisotropy of permeability in textured soft magnetic materials 216
- 8.2. Anisotropy of power losses in textured soft magnetic materials 224
- 8.3. New interpretation of the excess loss 230
- 8.4. Correlation between texture and rotational loss in non-oriented electrical steels 241
- 8.5. Comparison between different proposed models 243

9. SUMMARY AND CONCLUSIONS 249

STATEMENT OF ORIGINALITY AND CONTRIBUTION TO KNOWLEDGE 255

REFERENCES 258

FREQUENTLY USED SYMBOLS AND ABBREVIATIONS:

a_1, a_2, a_3	Directional angles
a_n, b_n	Fourier coefficients
A	Surface area
b	Coherent scattering amplitude of atomic nuclei
B	Magnetic induction
B_{10}	Induction @ 10 Oe
C	Coefficient representing the contribution of the magnetic anisotropy to the rotation process
C_l^{mn}	Series expansion coefficients
d, <d>	Domain wall spacing
$D(\chi,\eta)$	Magnetic signal
e_{ij}	Lattice strains
e_l^{mn}	Coefficients of physical property series expansion
E	Entropy

E_a	Magnetocrystalline energy
E_λ	Magnetoelastic energy
E_{ex}	Exchange energy
E_w	Domain wall energy
E_D	Magnetostatic energy
E_H	Energy due to the presence of the field
f_m	Magnetizing frequency
f_0	Density of pinning centres per unit critical field
$f(g)$	Orientation distribution function (ODF)
$F(\omega)$	Barkhausen noise power spectrum
F_d	Driving force (magnetic)
F_r	Retarding force
F_4, F_6	Fourth and sixth order texture parameters
g	Grain orientation in sample reference frame
$g^2 = 1/(2\xi^2)$	
G^w	Dumping coefficient of a single domain wall
$\mathbf{h}$	Crystal direction
(hkl), $\{hkl\}$	Miller indices of latice plane and symmetrically equivalent set
H	Magnetic field
I	Magnetization
I_0	Incident intensity of radiation
J	Exchange integral
$k_l^m(\mathbf{h})$	Surface spherical harmonics
K_A, x, y, z	Sample coordinate system, axes
K_B, X, Y, Z	Crystal coordinate system, axes
K_1, K_2	Cubic anisotropy constants
L	Length of the crystallite
$2L$	Domain wall spacing
$L(\eta)$	Magnetic torque
$\mathbf{m}$	Magnetic moment
MBN	Magnetic Barkhausen noise
$M(\chi,\eta)$	Magnetic texture
n	Number of active magnetic objects

$\mathbf{n}$	Normal vector
N	Number of domain walls
N_d	Demagnetizing factor
N_{11}, N_{22}, N_{33}	Demagnetizing factors along the principal axes of an ellipsoid
ND	Normal direction
ODF	Orientation distribution function, $f(g)$
p	Magnetic scattering amplitude of atoms
P	Power losses
$\mathbf{P}$	Polarization vector
P_{MBN}	Magnetic Barkhausen noise power
$P(\varepsilon_1)$	Radiation reflecting power
$P_{(hkl)}(\mathbf{y})$	Pole figure (hkl)
$P_l^m(\chi)$	Normalized associated Legendre functions
$\mathbf{q}$	Interaction vector ($q = \sin\psi$)
Q	Average scattering cross section per unit volume
RD	Rolling direction
s	Average dimension of the grain
S	Lamination cross section area
$\mathbf{S}$	Atomic spin vector
[uvw], <uvw>	Zone axis symbol of lattice direction and symmetrically equivalent set
V_0	Characteristic field
t	Time, thickness
T	Thickness of the grain, of the sample
TD	Transverse direction
$T_l^{mn}(g)$	Generalized spherical harmonics
$\mathbf{y} = (\chi, \eta)$	Direction in the sample reference frame
$W(\Delta)$	Angular distribution of mosaic blocks
W_r	Rotational hysteresis
$\alpha_1, \alpha_2, \alpha_3$	Directional cosines
$\alpha_2, \alpha_4, \alpha_6$	Magnitudes of the misalignment with respect to the easy direction or phases of the

	corresponding harmonics
γ	Angle between the magnetic moment and the direction of the field
δ	Effective field parameter
ε	Elongation
ε_1	Divergence of the incident beam
Δ	Magnitude of the angular deviation
$\mathbf{\Delta k}$	Scattering vector
$\varphi_1, \phi, \varphi_2$	Euler angles
$\varphi_4(\mathbf{h}), \varphi_6(\mathbf{h})$	Cubic symmetrical functions
ϕ	Magnetic flux
λ	Radiation wavelength
λ	Polarization vector
λ_n	Undetermined multipliers
ψ	Angle between the magnetic moment and the scattering vector
ξ	Standard deviation of Gaussian distribution
μ	Permeability
μ_{rev}	Reversible permeability
μ_0	Absorption factor, permeability of vacuum
ν	Volume of magnetic domain
(χ, η)	Spherical polar coordinates
Ω_0	Half-maximum width of the Gaussian representation of ODF
σ	Electrical conductivity
$\sigma(\varepsilon_1)$	Diffracting cross section per unit of volume and intensity

LIST OF FIGURES:

Fig.2.1. The orientation of a crystallite in a polycrystalline material
Fig.2.2. Important lines in the Euler space

Fig.3.1. Diagram of the Epstein tester

Fig.4.1. Principle of texture measurement
Fig.4.2. Principle axes of texture goniometer
Fig.4.3. Diffracted intensity versus sample thickness (original structure)
Fig.4.4. Diffracted intensity versus sample thickness (altered structure)
Fig.4.5. ODF Phi2=0° sections of grain oriented samples of different quality
Fig.4.6. (a to d) In plane alignment of the <001> direction
Fig.4.7. (a to d) Out of plane alignment of the <001> direction
Fig.4.8. (a to d) ODFs of non-oriented samples
Fig.4.9. Skeleton lines for non-oriented samples
Fig.4.10. (a to c) μ, α and γ fibres of non-oriented samples

Fig.5.1. Torquemeter head (torque transducer)
Fig.5.2. Electronic diagram of the torquemagnetometer
Fig.5.3. Calibration method
Fig.5.4. Calibration curve
Fig.5.5. (a to c) Torque curves (experimental and corrected) for samples OR-1A, OR-1B and OR-1C
Fig.5.6. Torque curves (experimental) for non-oriented samples
Fig.5.7. (a to d) Comparison between experimental and calculated

coefficients of the torque curves (grain oriented samples)
Fig.5.8. Comparison between experimental and calculated coefficients of the torque curves (non-oriented samples)
Fig.5.9. C^2 coefficient as a function of angle from rolling direction
Fig.5.10. Magnetocrystalline energy for sample OR-1B
Fig.5.11. Magnetocrystalline plus shape anisotropy energy for sample OR-1B
Fig.5.12. Theoretical (full line) and experimental torques at 22.5° and 45° for sample OR-1B
Fig.5.13. Theoretical (full line) and experimental torques at 22.5° and 45° for sample OR-1C
Fig.5.14. The influence of the demagnetizing field on torque curve for sample OR-1B
Fig.5.15. The influence of the demagnetizing field on torque curve for sample OR-1C
Fig.5.16. Experimental setup for texture quality inspection
Fig.5.17. Torque signal [mV] recorded from two grain oriented samples of different texture quality

Fig.6.1. (a to e) Magnetic domains in grain oriented samples
Fig.6.2. Proposed domain structure for band domain in sample OR-1A
Fig.6.3. (a to b) Grain size - domain spacing correlation in 9 mil grain oriented samples
Fig.6.4. (a to b) Grain size - domain spacing correlation in 7 mil grain oriented samples
Fig.6.5. Magnetic Barkhausen noise (MBN) instrument
Fig.6.6. MBN power versus sweep field in grain oriented samples
Fig.6.7. MBN power versus angle from rolling direction in grain oriented samples
Fig.6.8. Dependence of MBN power on $<\cos\gamma>$
Fig.6.9. MBN power versus sweep field in non-oriented samples

Fig.6.10. MBN power versus angle from rolling direction in non-oriented samples

Fig.7.1. Relationship between various vectors involved in neutron diffraction

Fig.7.2. Experimental setup for non-polarized neutron diffraction in a magnetic field

Fig.7.3. Magnetic scattering in the test sample

Fig.7.4. (110) pole figure of the investigated sample

Fig.7.5. Magnetic scattering at 150 mA magnetizing current

Fig.7.6.a. Computer generated magnetic texture

Fig.7.6.b. Calculated magnetic scattering

Fig.7.6.c. Restored magnetic texture

Fig.7.7. Calculated magnetic texture at 150 mA magnetizing current

Fig.7.8. (200) pole figure of the investigated sample

Fig.7.9. Experimental setup for polarized neutron diffraction

Fig.7.10.a. Non-spin flip (110) pole figures

Fig.7.10.b. UU - DD pole figure (magnetic signal)

Fig.7.11. (110) pole figure of grain oriented sample

Fig.7.12. Experimental setup for magnetic measurements using neutron depolarization

Fig.7.13. Depolarization in the sample magnetized at constant magnetization

Fig.7.14. Depolarization in the sample magnetized at constant applied field

Fig.8.1. (a to c) Permeability (experimental and calculated) versus angle from rolling direction for three grain oriented samples

Fig.8.2. (a to c) Power loss and $E_4(\eta)$ versus angle from rolling direction

Fig.8.3. Model of magnetic domain structure

Fig.8.4. Rotational loss versus $V(\langle 111 \rangle \parallel \mathrm{ND})$ %

Fig.8.5. Power losses versus $F_4(\eta)$ in grain oriented samples

Fig.8.6. Power losses versus $\langle \sin\gamma \rangle$ in grain oriented samples

Fig.8.7. (a to b) Power losses versus MBN power

CHAPTER 1.

INTRODUCTION

Most of the magnetic materials with industrial applicability are ferromagnetic. They can be broadly classified into two categories: hard and soft. The first are used as magnetic field generators, the second as magnetic field conductors.

The magnetic properties of soft magnetic materials are strongly anisotropic, i.e. they depend on the crystal direction in which they are being considered. Magnetic anisotropies may have crystallographic origins, but they may also be derived from the crystallite shape and/or from internal stresses; these parameters determine the microscopic magnetic anisotropy of the specimen.

The soft magnetic materials are usually polycrystalline, and they may or may not have a preferred orientation (texture) of their grains. In general, the magnetic properties of polycrystalline materials depend on the properties of the individual crystallites and on the structural parameters of polycrystal, such as the sizes, shapes, arrangements and crystallographic orientation of the constitutive crystallites, and also on internal stresses, precipitates, dislocation density, etc.

In this study, we will use the word "texture" to describe the orientation distribution function (ODF) of the crystallites, regardless of their sizes, shapes and arrangements. Even if there are other structural parameters which influence the magnetic properties of a polycrystalline material, these properties are often closely related to the crystallographic texture.

Soft magnetic materials are used for a variety of diverse applications, the most important of which are magnetic cores for electrical and electronic devices. For this reason, these materials are also called "electrical" (or magnetic) steels.

Magnetic cores for electrical machines (transformers, motors and generators) require soft magnetic materials with a suitable combination of properties. Among them, core loss and permeability are of fundamental interest. The core loss is the electric power dissipated as heat when the core is subject to an alternating magnetic field. The permeability characterizes the ability of a material to achieve a high flux density at a small magnetic field intensity. In general, low core loss and high permeability are desirable in soft magnetic materials. Core loss and permeability are structure sensitive and they have been improved by controlling metallurgical variables such as texture, grain size, impurities, residual stress, degree of crystallographic order, etc.

The development of preferred orientations has profound effects on the magnetic properties of soft magnetic materials. The cores for power and distribution transformers are manufactured, such that the rolling direction in the sheet is parallel to the direction of magnetization. The texture which provides the required magnetic properties, i.e. low core loss and high permeability in the magnetization direction, is {hkl} <001> because this texture makes the magnetically preferred crystal directions parallel to the field. Such a texture has been achieved in grain oriented silicon steel, where the {110}<001>, or Goss texture, has been developed.

In rotating machines cores (motors and generators), the angle between the magnetic field and the rolling direction is variable. The optimum texture for materials used in making such machinery is a fibre texture, in which all grains have a <100> direction normal to the sheet plane, because the sheet would be isotropic in its own plane. The so-called non-oriented electrical steels are soft magnetic materials which, ideally, have isotropic magnetic properties in the sheet plane. In these materials, low core loss and high permeability in the magnetization direction are also required, and these properties could be improved through the development of a suitable texture.

The above examples illustrate the importance of the orientation distribution of crystallites in soft magnetic materials, where the application requires an anisotropy of magnetic properties. In recent years, much progress has been made in the determination of textures, and in their interpretation and control. The orientation distribution function (ODF) provides a more complete description of texture than pole figures. On the one hand, this approach has permitted detailed theories of texture development to be tested in a highly rigorous manner. On the other hand, however, the ODF has contributed much to understanding the quantitative relationships between the texture and the properties of materials. From this approach, the correlation between texture and the resulting anisotropy of the magnetic properties is the focus of this study.

Properties, such as the magnetocrystalline energy and the magnetostriction of a polycrystalline ferromagnetic material in an external magnetic field sufficient to saturate the material, are given as a function of the direction of magnetization. In these cases, the influence of texture on properties is calculated by averaging the crystallite properties over the orientation distribution function. For other properties, such as the power loss and permeability, where the magnetic field strength is lower than the saturation field, the theory of averaging the crystallite property over the texture function is much more complex. It is well known that there is a direct relationship between texture and the power loss and permeability, but this correlation was, until recently, only semi-empirically established. At present, there is not enough evidence to demonstrate that such a correlation remains valid for a variety of textures existing in the same material, or if it can be applied to very sharp textures like the ones observed in grain oriented steels.

The purpose of this study is to develop new methods of correlating texture and magnetic properties in soft magnetic materials. Property calculations cannot be self-consistently determined without full quantitative models of the magnetization changes in the polycrystalline materials. Such models are proposed in this study, and their validity is tested by comparing the theoretical results with the experimental data. For a better understanding of the correlation existing between texture, microstructure and magnetic properties, it has been necessary to develop new experimental techniques. Of particular importance among them is the application of neutron diffraction and neutron depolarization to magnetic texture determination.

Comprehending the correlation between the texture and magnetic properties allows us, on the one hand, to predict various magnetic properties of polycrystalline soft magnetic materials from texture and, on the other hand, to produce these materials to the required specifications.

The presentation of the studies undertaken in this thesis is divided into the following chapters:

Chapter 2: A brief summary of the relevant texture - magnetic anisotropy problem is given. The theoretical aspects of the magnetization process in soft magnetic materials, and the existing models which describe the texture related anisotropy of magnetic properties in these materials are reviewed.

Chapter 3: The commercial grain oriented and non-oriented electrical steels which were used in this work have been characterized from the macromagnetic point of view. The specimens are classified as a function of their power losses, which were obtained from the standard Epstein test.

Chapter 4: The experimental results of the quantitative texture analysis are presented and discussed.

Chapter 5: The correlation between texture and magnetic anisotropy energy is presented. The formalism for predicting the magnetic torque obtained at saturation in polycrystalline ferromagnetic materials is reviewed, and then we discuss the influence of texture on the magnetization process from saturation to remanence. The values obtained from the developed mathematical models are compared to the experimental data. The correlation between texture and magnetic anisotropy energy is investigated using a torque magnetometer. The technical details of an automated torquemeter, designed and built as a part of this project, are also presented.

Chapter 6: Non-destructive methods of correlating texture, microstructure and power losses are described. The magnetic Barkhausen noise is related to the total power losses through a model containing parameters characterizing the material texture and microstructure.

Chapter 7: New methods are developed for determining magnetic texture using neutrons.

Chapter 8: The influence of texture on the anisotropy of power loss and permeability is calculated by averaging these properties over the orientation distribution function. A new interpretation of the power loss mechanism in electrical steels is also presented, and a comparison between the theoretical predictions and the experimental values is made to evaluate the proposed models.

Finally, the general conclusions of this study are drawn.

HISTORY OF ELECTRICAL STEELS

The grain oriented silicon steel was invented by Norman Goss in 1934. This led to a revolutionary reduction in core loss, largely through the development of preferred orientation by secondary recrystallization. The Goss process developed a sharp cube-on-edge texture, (110)[001], in 3% Si steel where the easy direction of magnetization lies roughly in the sheet plane and is almost parallel to the rolling direction.

Since that time, escalating energy costs have forced researchers to place more emphasis on high efficiency transformer cores. A substantial amount of fundamental research was performed on the nature of losses, leading to the development of, not only better materials, but mathematical models which describe the behaviour of power loss in transformer sheets. These models have been used to lower core losses. There are several directions to improve losses, which were often deduced from the mathematical models:

> (1) increasing the electrical resistivity by increasing the silicon content; (2) decreasing the thickness (or gage) of the material; and (3) decreasing the domain spacing by domain refining.

Directly connected to these improvements is good texture, clean steel, small grain size, applying tensile stress in rolling direction, etc.

From a historical point of view, much of the improvement in 60Hz losses at 1.5 T, from 3.0 W/Kg in 1934 to 1.01 W/Kg in 1980, is the result of improvements in texture on the same thickness of final product, i.e. standard products of 0.28 - 0.35 mm. In 1981, the introduction of the first thin gage 0.22 mm (9 mil) conventional grain oriented silicon steel offered immediate loss improvements, simply from being thinner than the standard product.

A second important class of soft magnetic materials includes the so-called "non-oriented electrical steels" which are mainly used in the construction of electric motors and generators. This steel was developed by R. Hadfield in 1900 through the introduction of silicon into iron. The beneficial effects of silicon on magnetic properties made the Si-Fe alloy the preferred core material.

The silicon content of non-oriented steels ranges from 0.40% to 4.5%, and they usually have manganese or phosphorus additions to raise the resistivity. Although these steels are non-oriented, they develop a weak texture, and applications in rotating machinery would clearly benefit from textures which maximize the <100> component in the sheet plane.

CHAPTER 2.

Review
TEXTURE AND MAGNETIC PROPERTIES OF ELECTRICAL STEELS

INTRODUCTION

The purpose of this chapter is to review the application of crystallite orientation distribution function (ODF) analysis to the correlation of magnetic properties and texture in the soft magnetic materials. First, the mathematical formalism required for the quantitative description of crystallographic orientations of the constitutive crystallites is presented. Then, we discuss the physical principles of ferromagnetism and the factors which control the distribution of spontaneous magnetization, such as magnetic anisotropy, structure of magnetic walls, and magnetostatic energy. Studies on the influence of several structural parameters of material (grain size and orientation, stresses, thickness) on the magnetic domain structure of electrical steels are also reviewed.

The literature presents several theoretical and experimental methods of correlating texture and magnetic properties in electrical steels. These methods are discussed at the end of the chapter.

2.1. THE TEXTURE OF MATERIALS

2.1.1. Various descriptions of the crystal orientation

A polycrystalline material is textured if the orientation distribution of its grains is not random. To define the orientation "g" of a crystallite in the sample, two different coordinate systems are required.

The first right-handed cartesian system is associated with the sample. In principle, the choice of the sample reference frame K_A is arbitrary. When the sample has been deformed by rolling, it is quite natural to prefer the rolling direction (RD), the transverse direction (TD), and the normal direction (ND) for the coordinate axes of the sample. A direction in the sample reference frame will be specified by a unit vector **y** in this direction, which is defined either by its directional cosines, or by spherical polar coordinates:

$$\mathbf{y} = (\alpha_1, \alpha_2, \alpha_3) = (\chi, \eta) \tag{2.1}$$

The second coordinate system, K_B, is assigned to each crystal. It is also cartesian and right-handed, and this system can also be defined arbitrarily, but usually it is related to the crystal symmetry. In the case of cubic crystals, the most suitable choices are the [100], [010], and [001] crystallographic directions.

The orientation of a crystallite in the sample is defined by the orientation of the crystal coordinate system, K_B, with respect to the sample coordinate system, K_A. This orientation is defined by the rotation "g" which brings the two coordinate systems into coincidence, as shown in Figure 2.1.:

$$K_B = g\, K_A \tag{2.2}$$

$$K_A \xrightarrow{g} K_B$$

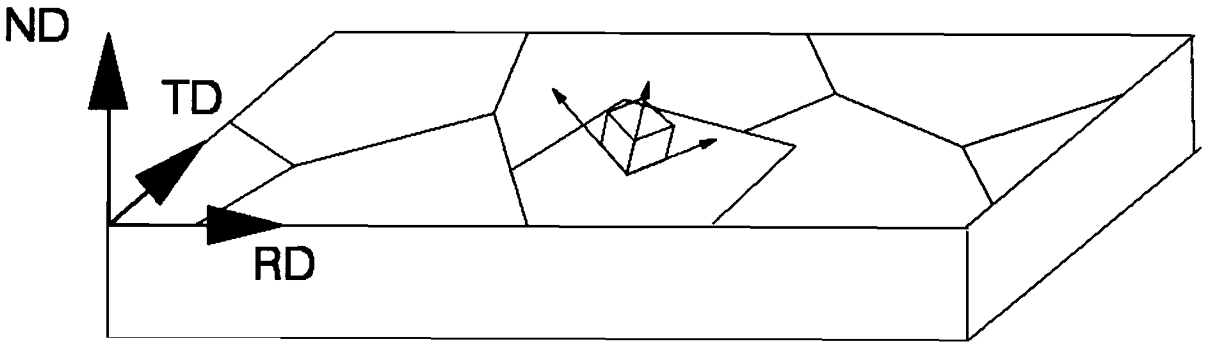

Fig.2.1. The orientation of a crystallite in a polycrystalline material

Various sets of parameters are used to describe the rotation "g" of which we shall discuss only those appearing in this work. Other orientation parameters are given, for example, in Bunge [1].

The three axes X, Y, and Z of the sample coordinate system, and the three axes x, y, and z of the crystal coordinate system form 9 angles, the cosines of which are a_{ij} (i,j=1,2,3). The orientation of the two coordinate systems can be represented in the form of a matrix:

$$g = \begin{bmatrix} a_{11} & a_{12} & a_{13} \\ a_{21} & a_{22} & a_{23} \\ a_{31} & a_{32} & a_{33} \end{bmatrix} \tag{2.3}$$

The advantage of matrix representation is that the resultant matrix of two or more rotations is expressed by matrix multiplication. For example, if the rotations "g_1" and "g_2" are carried out in this sequence, the resultant matrix is the product:

$$g = g_2\, g_1 \tag{2.4}$$

Another crystallite orientation notation, frequently used to describe texture in sheets of cubic metals, consists of the Miller indices. In this description, the crystallite orientation is specified by the crystallographic plane (hkl) parallel to the rolling plane and the crystallographic direction [uvw] that lies along the sample rolling direction. The orientation g is:

$$g = (hkl)\,[uvw] \tag{2.1}$$

In the following chapters, Euler angles are used to represent the orientation of a crystallite within the sample. According to Euler's rotation concept, a rotation g can be decomposed into three independent rotations, which are performed successively to transform K_A into K_B. Each independent rotation is related to a rotation axis, and to its associated angle. Several conventions exist for choosing the independent rotations, all of which are equally advantageous. One such widely used convention is the so called Bunge [1] convention, in which three successive rotations are conducted:

(1) φ_1 about the crystal z axis

(2) ϕ about the crystal rotated x axis

(3) φ_2 about the crystal rotated z axis

The final orientation of the crystal coordinate system K_B, with respect to the sample coordinate system K_A, is described by the three Euler angles: $g = \{\varphi_1, \phi, \varphi_2\}$. All possible orientations can be obtained within the range:

$$0 \leq \varphi_1 \leq 2\pi; \quad 0 \leq \phi \leq \pi; \quad 0 \leq \varphi_2 \leq 2\pi \tag{2.6}$$

Since the three parameters $\{\varphi_1, \phi, \varphi_2\}$ may vary independently within the specified range, it is convenient to plot them as cartesian coordinates in a three-dimensional space, called the Euler space. Each crystal orientation is represented by a point in Euler space. The elementary orientation volume is defined by:

$$dg = \frac{1}{8\pi^2} \sin\phi \, d\varphi_1 \, d\phi \, d\varphi_2 \tag{2.7}$$

which produces a distortion along the ϕ axis.

In general, this finite three-dimensional space is analyzed through simple orthogonal projections: φ_2 = constant called φ_2 - sections, or φ_1 = constant called φ_1 - sections.

It has to be emphasised that all different descriptions of the orientation are analytically related. The indices (hkl)[uvw] can be expressed by the matrix elements a_{ij}, and these in turn are functions of the Euler angles.

2.1.2. The orientation distribution function (ODF)

The texture of a polycrystalline material is defined by the orientation distribution function (ODF) of the crystallites in the material. Two variants of the definition of the ODF are considered, and must be distinguished from the experimental methods discussed later:

(1) The ODF by volume is defined by the formula:

$$\frac{dV}{V} = f(g)\,dg \qquad (2.8)$$

where dV is the volume of all the crystallites which possess the orientation g within a certain infinitesimal orientation element dg and V is the entire volume of the sample.

(2) The ODF by number is defined by the number of crystallites having the orientation g within the orientation range dg:

$$\frac{dN}{N} = n(g)\,dg \qquad (2.9)$$

where N is the total number of crystallites in the sample. These two definitions may be different if the mean grain size is orientation dependent, as it is the case in grain oriented silicon steels.

The distribution of crystal orientations within the polycrystalline sample can be random, or display preferred orientations (texture). In this study, the ODF is used as the quantitative definition of texture. According to the definitions given above, the ODF is only a function of orientation g, without consideration for size, shape or position of the crystallites.

In the case of random texture:

$$f_{random}(g) = 1.$$

The ODF is normalized according to the relation:

$$\int_g f(g)\,dg = \int_V \frac{dV}{V} = 1 \qquad (2.10)$$

where the integration is conducted over all possible orientations and, as a result of normalization, the ODF intensity is presented in random units.

In texture analysis, the description of orientation g by Euler angles has proved to be especially suited because the Euler space is the space in which the orientation distribution function f(g) can be represented. As mentioned, a point in the Euler space represents a rotation g, which unambiguously defines the orientation of a crystallite within a specimen. Alternate choices of both the crystal and the sample coordinate systems often lead to many symmetrically equivalent orientations.

In the cubic crystal there are 24 different, but symmetrically indistinguishable, representations of the coordinate system K_B of one and the same crystal. Thus, each orientation g is associated with 24 symmetrically equivalent ones which are related one to the other by the symmetry rotations g_i^c of the rotational subgroup of crystal symmetry:

$$g_i = g_i^c \, g \tag{2.11}$$

The sample symmetry originates from the symmetry of the metallurgical process, which has led to the texture formation in the material. This symmetry requires a distribution of crystallites which exhibit statistical symmetry elements. If the symmetry rotations of the sample symmetry are g_j^s, the crystal orientations:

$$g_j = g \, g_j^s \tag{2.12}$$

are symmetrically equivalent. Both crystal and sample symmetry are to be combined leading to a number of symmetrically equivalent points in the Euler space associated with an orientation g:

$$g_{ij} = g_i^c \, g \, g_j^s \tag{2.13}$$

As a consequence, the ODF has the same value in all these points:

$$f(g_{ij}) = f(g_i^c\, g\, g_j^s) = f(g) \tag{2.14}$$

2.1.3. Definition of pole figure

In a pole figure, orientation is defined by the positions of the poles (hkl) of the symmetrically equivalent lattice planes {hkl}. These positions can be visualized as the intersection points of the normal to crystallographic planes with the surface of a unit sphere whose centre coincides with the origin of the sample coordinate system. The pole figure can be graphically represented on the stereographic projection of the unit sphere. A pole figure by volume is defined as the volume fraction dV/V of crystallites having their poles (hkl) parallel to the sample direction **y** :

$$\begin{gathered}\frac{dV}{V} = \frac{1}{4\pi} P_{(hkl)}(\mathbf{y})\, dy \\ \mathbf{y} = (\chi,\eta);\quad dy = \sin\chi\, d\chi\, d\eta\end{gathered} \tag{2.15}$$

Similar to equation (2.15), a pole figure can also be defined by number:

$$\begin{gathered}\frac{dN}{N} = \frac{1}{4\pi} P'_{(hkl)}(\mathbf{y})\, dy \\ \mathbf{y} = (\chi,\eta);\quad dy = \sin\chi\, d\chi\, d\eta\end{gathered} \tag{2.16}$$

The pole figure is normalized, and pole densities are expressed in multiples of the random density:

$$\begin{gathered}P_{(hkl)}(\mathbf{y})_{random} = 1 \\ \oint P_{(hkl)}(\mathbf{y})\, dy = 4\pi\end{gathered} \tag{2.17}$$

The classical techniques for determining the orientations of crystals are based on the neutron, electron, and X-ray diffraction. Measured pole figures are related to the distribution of normal direction of the reflecting lattice plane. It must be emphasized that this direction is identical to the direction given by the Miller indices of the corresponding lattice plane, in the cubic crystal classes only . The definition of the pole figure is, however, general and is not restricted to directions normal to crystallographic planes.

In the graphical representation of the pole figure used in this study (stereographic projection), the contours connect points of equal intensity from the (hkl) diffraction peak. Heavy contour indicates the intensity that would be obtained from a random distribution of crystallite orientations. The thinner continuous contours indicate intensities greater than random, in intervals shown in the figure caption, while the dashed contours indicate intensities less than random.

2.1.4. Pole figure inversion

Generally, pole figures are the original experimental data from which the ODF is calculated. This operation is called pole figure inversion. Equation (2.15) shows that the pole density at point **y** does not depend on the rotation angle about the direction **y** because this rotation does not change the position of the reflecting lattice plane. Thus, the density $P_{(hkl)}(\mathbf{y})$ of the poles {hkl} at point **y** of the pole figure can be obtained from the ODF by integration:

$$P_{hkl}(\mathbf{y}) = \frac{1}{2\pi} \int_{0}^{2\pi} f(g)\, d\omega \tag{2.18}$$

where ω is the angle of rotation around the axis {hkl}. The solution to the above equation is pole figure inversion. Several mathematical approaches to solve equation (2.18) have been proposed, and a succinct examination of them is given by Wenk [8].

The method used in this work, the series expansion method, is based on the fact that an analytical solution for equation (2.18) can be obtained when the functions $P_{(hkl)}(\mathbf{y})$ and f(g) are represented using special functions, the spherical harmonic functions $k_l^n(\mathbf{y})$, and $T_l^{mn}(g)$. Using these functions in equation (2.18), it becomes:

$$\frac{1}{2\pi}\int_0^{2\pi} T_l^{mn}(g)\, d\omega = \frac{2}{(2l+1)}\, k_l^{*m}(\mathbf{h})\, k_l^n(\mathbf{y}) \qquad (2.19)$$

Here, $k_l^n(\mathbf{h})$ and $k_l^n(\mathbf{y})$ are the surface spherical harmonics, the former defined in the crystal coordinate system, and the latter defined in the sample coordinate system; the asterisk indicates the complex-conjugate quantity. The typical procedure of pole figure inversion in the harmonic method is the following (Wenk, [8]): any function f(g) can be composed by adding functions $T_l^{mn}(g)$ in appropriate amounts C_l^{mn}:

$$f(g) = \sum_{l=0}^{\infty} \sum_{m=-l}^{+l} \sum_{n=-l}^{+l} C_l^{mn}\, T_l^{mn}(g) \qquad (2.20)$$

Similarly, the function $P_{(hkl)}(\mathbf{y})$ can be developed into a series of harmonics $k_l^n(\mathbf{y})$ with appropriate coefficients F_l^n:

$$P_{hkl}(\mathbf{y}) = \sum_{l=0}^{\infty} \sum_{n=-l}^{+l} F_l^n\, k_l^n(\mathbf{y}) \qquad (2.21)$$

If we substitute equations (2.20) and (2.21) into equation (2.18) and take equation (2.19) into account, we obtain a relationship between the coefficients C_l^{mn} and F_l^n:

$$F_l^n = \frac{4\pi}{(2l+1)} \sum_{m=-l}^{+l} C_l^{mn}\, k_l^{*m}(\mathbf{h}) \qquad (2.22)$$

This equation represents a system of linear equations with C_l^{mn} as unknowns. The number of equations in this system is given by the number of different pole figures.

In certain cases it is necessary to determine the coefficients C_l^{mn} when the function f(g) is known. Such a situation appears in this study where the texture function f(g) of grain oriented materials has been determined directly by a discrete pole figure inversion method using iterations (Pospiech, [2]). In the case of sharp textures, this method yields better results than the series expansion method. Using the orthogonality relation of the spherical harmonics (see Bunge, [1]), one obtains:

$$C_l^{mn} = (2l+1) \int_g f(g)\, T_l^{*mn}(g)\, dg \tag{2.23}$$

which gives the coefficients C_l^{mn} in terms of the known function f(g).

2.1.5. Presentation of the results of texture analysis

The result of the ODF calculation is the distribution function f(g) which represents the relative frequency of the occurrence of crystals having the orientation g. If the orientation g is described by Euler angles, it is represented by a point in the Euler space. If every point g in the Euler space is given the value f(g) then this represents the ODF. This is the complete description of a texture.

In general, the ODF is calculated in discrete steps $\Delta\varphi_1$ $\Delta\phi$ $\Delta\varphi_2$, within the necessary range of the angular coordinates $\varphi_1, \phi, \varphi_2$. These points are presented in two-dimensional sections. On each section, lines corresponding to equal density are plotted by interpolation between grid points.

In order to better visualize the orientation relationships occurring in the ODF, the results should be presented in the simplest form. In certain cases, other descriptions of texture are possible and have, in fact, been used to rationalize a complex ODF.

In certain rare cases, the texture may consist of only one component. The texture function has a positive value at one point g_0 of the Euler space and decreases to zero within a certain angular distance from g_0. For example, a texture of this type is obtained after the secondary recrystallization in hot rolled 3% silicon steel, where all the grains have the orientation situated within a small angular interval around g = (0°,45°,0°). The orientation distribution function f(g) is often assumed to be a Gaussian function with a maximum value A and the half-maximum width Ω_0:

$$f(g) = A \exp-[(g-g_0)/\Omega_0]^2 \tag{2.24}$$

This description corresponds to the concept of an ideal orientation in a physically more realistic sense.

More familiar representation of an orientation is obtained by transforming the Euler angles into the Miller indices, especially when low integer values of the indices are involved.

In other cases, the sample symmetry may contain a rotation axis of infinite order. The ODF is then independent of a rotation about this axis. Rotationally symmetric textures are denoted as fibre textures. It directly follows from the definition of the Euler angles that, with respect to the crystal system K_B, the normal direction (ND) of the sample (Z direction) is determined only by the angles ϕ and φ_2, so that lines parallel to φ_1 at fixed ϕ, φ_2 indicate the rotations around a fixed normal direction (ND). Since ND is given by the Miller indices {hkl}, these lines also indicate a rotation around a fixed crystallographic direction [hkl].

One further identifies that the lines running parallel to the ϕ axis at fixed φ_1, φ_2 indicate different rotations around a fixed axis lying in the rolling plane and forming the angle φ_1 to rolling direction (RD), as well as in the plane {001} forming the angle φ_2 to [100]. Some of the more often used lines in Euler space are illustrated in Figure 2.2.

In some other cases, the ODF cannot be described in terms of a low number of texture components and/or fibre textures. One possibility is to represent the ODF as a continuous row of maximum density points, with a certain spread. The maximum density line is

called the skeleton line. The philosophy behind this concept is that the texture is assumed to consist of a one dimensional manyfold of ideal orientations which form a line. The representation of ODFs using skeleton lines is an attempt to simplify a complicated ODF, like the ones appearing in cold rolled materials.

2.2. MAGNETIC DOMAIN STRUCTURE IN ELECTRICAL STEELS

2.2.1. Micromagnetic characterization of materials

Magnetism in a material has its origins at atomic scale. If an electron shell of the atom is not completely filled, the sum of orbital and spin magnetic moments is not zero, and the atom will possess a spontaneous magnetization.

The basis of ferromagnetism is the ordered spontaneous magnetization within magnetic domains. This alignment is due to the collective behaviour of atoms and is opposed by thermal agitation if the temperature is finite. At 0°K the magnetic moments are perfectly oriented in one direction and the magnetization reaches a maximum value, called saturation magnetization. When the temperature increases, the energy of thermal motion increases the angular distribution of the atomic moments. This distribution becomes almost random at Curie temperature, where the value of magnetization is zero.

The alignment of atomic magnetic moments was first described by Weiss [3], who postulated the existence of a strong inner magnetic field, called the molecular field. Even though the Weiss theory described the phenomenology of ferromagnetism correctly, the origin of the molecular field was not explained. The accepted interpretation of the molecular field's nature was first presented by Heisenberg [4] in 1928. According to his theory, magnetic moments are aligned by an exchange force of quantum mechanical nature.

If the atomic magnetic moments are aligned, as is the case for all ferromagnetic materials in the temperature range below the

Curie point, a spontaneous magnetization must appear, even if the external magnetic field is absent. Since this magnetization was not experimentally proven, Weiss [3] suggested the presence of the ferromagnetic domain structure as a possible explanation. In each domain, the magnetization reaches a value equal to the saturation magnetization, but in different directions, such that the resultant magnetization is zero in the zero external field. The first experimental verification of the presence of ferromagnetic domains was indirect, and was made by Barkhausen [5].

In general, the material comprises many magnetic domains and the net magnetization is the vector sum of the magnetization within all domains. When a magnetic field is applied, the magnetization in each domain will change, either by movement of boundaries (walls) between domains, or by rotation towards the direction of the applied field. In this way, the overall magnetization of the sample is changed, as well as the domain structure. There are some energies involved in this process, the most important ones being:

(1) Exchange (or interaction) energy

As introduced by Heisenberg, this energy has an electrostatic origin, and depends on the spin orientation. The effect of the exchange energy on the atoms of a ferromagnetic material is equivalent to the introduction of a molecular magnetic field. In fact, since each atom possesses a magnetic moment, they will interact with each other. The potential energy due to interaction will depend on the orientation of each atomic magnetic moment. For two atoms having spins $\mathbf{S}_i$ and $\mathbf{S}_j$, the exchange energy is given by:

$$W_{ij} = -2J\,\boldsymbol{S}_i\,\boldsymbol{S}_j = -2J\,S^2\cos\phi_{ij} \tag{2.25}$$

where J is the exchange integral, and S is the magnitude of the spin magnetic moment. For the whole crystal, this energy is the sum of the contributions given by all the neighbouring atoms:

$$E_{ex} = -2J\,S^2 \sum_{i>j} \cos\phi_{ij} \tag{2.26}$$

(2) Magnetocrystalline (anisotropy) energy

Magnetic anisotropy describes the dependence of the internal energy of a ferromagnetic single crystal on the direction of the spontaneous magnetization. Thus, the magnetocrystalline energy represents the coupling energy between the atomic magnetic moment and the crystal lattice. As a result, the spontaneous magnetization is confined to a certain crystallographic direction, called the easy direction of magnetization. Usually, the magnetocrystalline energy is represented by the following expression:

$$E_a = K_1\left(\alpha_1^2\alpha_2^2 + \alpha_2^2\alpha_3^2 + \alpha_3^2\alpha_1^2\right) + K_2\alpha_1^2\alpha_2^2\alpha_3^2 \tag{2.27}$$

where $(\alpha_1, \alpha_2, \alpha_3)$ denote the direction cosines of the internal magnetization, and K_1 and K_2 are called the anisotropy constants of the first and second order, respectively. In iron, the value of K_1 is positive ($\approx 37 \cdot 10^3$ J/m^3), and the magnetocrystalline energy keeps the spontaneous magnetization parallel to <100> crystallographic axes.

(3) Magnetoelastic energy

The crystallographic lattice is not rigid. When a uniform tensile stress is applied, the lattice distorts. The magnetic energy associated with the lattice strains is called the magnetoelastic energy. To the first approximation, the magnetoelastic energy depends linearly on lattice strains e_{ij}. In cubic crystals this energy is (Shilling and Houze, [6]):

$$E_\lambda = -B_1\left[e_{11}(\alpha_1^2 - \frac{1}{3}) + e_{22}(\alpha_2^2 - \frac{1}{3}) + e_{33}(\alpha_3^2 - \frac{1}{3})\right] - \\ - B_2[e_{12}\alpha_1\alpha_2 + e_{23}\alpha_2\alpha_3 + e_{31}\alpha_3\alpha_1] \qquad (2.28)$$

where $(\alpha_1,\alpha_2,\alpha_3)$ are the direction cosines of the magnetization with respect to cubic axes, and B_1 and B_2 are constants.

(4) Wall energy

The transition layer between the adjacent ferromagnetic domains is called the magnetic domain wall or Bloch wall [7]. In magnetism the divergence of magnetization vector is always zero, and the normal component of magnetization has the same value across the wall:

$$\boldsymbol{n}\,(\boldsymbol{I}_1 - \boldsymbol{I}_2) = 0 \qquad (2.29)$$

where **n** is the normal to the wall and $\mathbf{I}_1$, $\mathbf{I}_2$ are the magnetizations in the two adjacent domains.

In iron, the spontaneous magnetization is confined to the <100> directions, so that two types of domain walls may exist:

- 180° domain wall between domains having antiparallel magnetizations and
- 90° domain wall when the magnetizations are in quadrature.

In a material, the wall energy equals the total domain wall area times the energy per unit area E_w. The value of E_w is deduced as the result of the competition between the effect of the exchange energy and the effect of magnetocrystalline energy on magnetic moments of atoms present in the domain wall.

If we consider that the x axis is normal to the plane of the domain wall, the azimuthal angle of the spin orientation along this axis changes from $-\Phi/2$ to $+\Phi/2$, from one domain to the other. The wall energy per unit surface is:

$$E_w = \int_{-\infty}^{\infty} \left[g(\phi) + A\left(\frac{\partial \phi}{\partial x}\right) \right] dx \tag{2.30}$$

where A is a coefficient related to the exchange energy (= $1.49 \cdot 10^{-11}$ J/m for iron), and $g(\phi)$ is the anisotropy function:

$$g(\phi) = K_1 \sin^2\phi \cos^2\phi \tag{2.31}$$

In iron, the value of E_w is evaluated to $2.76 \cdot (A \cdot K_1)^{1/2}$ for the 180° wall and to $1.42 \cdot (A \cdot K_1)^{1/2}$ for the 90° wall.

(5) Magnetostatic energy

In a magnetized body of finite dimensions, the discontinuities in magnetization ($\mathbf{n} \cdot \mathbf{I} \neq 0$) produce a demagnetizing field H_d proportional to the magnetization value, I. The proportionality factor is called the demagnetizing factor of the body, N_d:

$$H_d = -\frac{N_d}{\mu_0} I \tag{2.32}$$

where μ_0 is the permeability of vacuum.

The origin of the demagnetizing field is the "free magnetic poles" which appear inside or on the external surfaces of the body. The magnetostatic energy is caused by the interaction between magnetic free poles. Expressed in terms of magnetization and the internal demagnetizing field, this energy is:

$$E_D = -\frac{1}{2} \int_V \mathbf{I}\, \mathbf{H}_d \, dv \tag{2.33}$$

where the integration should be conducted over the volume where magnetic field H_d is present.

(6) Energy in an applied magnetic field

This is the mutual energy of a domain of magnetization I in the presence of an applied magnetic field H. Its value is:

$$E_H = -H\, I \cos\theta \tag{2.34}$$

where θ is the angle between H and I.

The total energy of the system is given by the sum of the above energies. The condition that the total energy should be minimum imposes the shape and the size of the domains present in equilibrium in a specimen. One can find detailed calculations of magnetization energy, for example, in Chikazumi [8].

2.2.2. Magnetic domain pattern in grain oriented Si-Fe

Several techniques are available for direct observation of the magnetic domains: Bitter technique, methods based on magneto-optical effects, Lorentz microscopy, etc. A comprehensive review of these techniques is given by Stewart [10].

The domain observation techniques allowed the investigators to observe the magnetic structure of the grain oriented 3% Si-Fe. The domain structure of these materials has been separated into two components (Shilling and Houze, [6]):

(a) **main domain structure** refers to large carrying slab domains whose magnetization are along the ±[001], for example, and are separated by 180° walls.

(b) **supplementary structure** refers to the remaining structure observed at flux closures and the crystal (grain) boundaries and consists of domains whose magnetization are along the ±[010] and ±[100] directions. This supplementary structure is separated by 90° walls.

The existence of the main and supplementary structures was clearly demonstrated by experiment (Kranz and Passon, [11]). It was also shown that the magnetization of a sample is realized by rearrangements of the main domain structure, with little change to the supplementary structure, at least at low inductions.

Various studies have been made on the relationship between the 3% Si-Fe domain structure and:

(1) Crystal orientation in magnetic field

It has been found [12,13] that the domain structure significantly depends on the tilt angle θ of the [001] direction out of the sheet surface. When $\theta = 0°$ only a simple 180° wall structure is observed. When $\theta > 0°$ however, the amount of supplementary structure increases with increasing θ. Depending on the magnitude of crystal misorientation, there exist many kinds of supplementary structure (lancet, lancet comb, band structure etc.) which form to minimize the normal component of magnetization across boundaries.

(2) Thickness of material

Because of the transverse components of the supplementary structure, this will depend on the sheet thickness. It has been shown by Backer [14] that different domain structures may exist in the same material when its thickness is modified (chessboard, "columnar" structure, band or sawtooth structure).

(3) Stresses

The important effects of applying tensile stress parallel to the rolling direction are the removal of the supplementary structure, and the refinement of the main domain spacing due to the balance between magnetoelastic and magnetostatic energy (Shilling and Houze, [24]).

(4) Grain size

As the magnetic domain theory predicts (Shilling and Houze, [24]), domain wall spacing increases as grain size increases. Another important effect is the micro-demagnetizing fields appearing at the boundaries. As the grain-to-grain misorientation is higher for smaller grains, and the boundary bears no special angular relationship to the [001] directions of the two grains, one might expect larger grain boundary demagnetizing fields in small grained material.

2.2.3. Magnetic domain pattern in non-oriented material

This material is characterized by small grain size (tens of μm) and weak preferred orientation. The domain structure is more complex, compared to single crystals and Si-Fe grain oriented steels. Smaller grains, structural imperfections, random orientation of one grain with respect to the other, add to the complexity of magnetic interaction in these steels.

Studies on magnetic structure in similar materials (construction steels) were performed by Szpunar and Szpunar [15] using the Bitter technique. Four different types of magnetic domain structures were described and classified as follows:

type A - antiparallel stripes of the domains

type B - lozenges or fir tree domain structure

type C - districts in the same grain having their own order in the arrangement of the domain pattern

type S - no domain walls within the grain; small grain size.

This study demonstrated that in non-oriented materials: (1) the effect of grain size on the domain pattern is significant; (2) the type of domain structure correlates with grain size; and (3) a relationship exists between the grain size and the domain wall spacing for domains of type A and B.

2.2.4. The magnetization curve and domain structure of electrical steels

When a ferromagnetic material is placed into an increasing magnetic field, its magnetization is increased and finally reaches the saturation magnetization. The magnetization process is achieved by changing the direction of domain magnetization. Starting from the demagnetized state (I = 0 at H = 0), there is a narrow range in which magnetization changes reversibly. This portion of the magnetization curve is called the initial permeability range. In this range, magnetization is achieved by reversible domain rotations, and by reversible domain wall displacements.

If the magnetic field is increased beyond the initial permeability range, the intensity of magnetization increases mainly by irreversible displacements of domain walls from one stable position to another. This range is called the irreversible magnetization range. The magnetic Barkhausen noise (Chapter 6) can be detected in this range because many discontinuous changes in magnetization are induced by irreversible domain wall displacements. The irreversible magnetization process takes place up to the knee of the magnetization curve, where the displacements of domain walls have already been completed. If the field is increased further, the magnetization is accomplished by rotation magnetization, and the process is reversible again. The magnetization gradually approaches the saturation magnetization and this portion of the magnetization curve is called the range of approach to saturation.

If the magnetic field is decreased from the saturated state, the magnetization is gradually decreased along the hysteresis curve, not along the initial magnetization curve discussed above. At zero applied field, the magnetization reaches a finite value, called the residual magnetization or remanence. If the field is then increased in a negative sense, the magnetization decreases and becomes zero at a certain value of the field. The field at this point is called the coercive field. Further increase of the field in a negative sense results in an increase of the magnetization in a negative sense and finally leads to a negative saturation magnetization. If the field is then reversed to the positive sense, the magnetization will change along a similar curve, but in the opposite direction, and the loop obtained is called the hysteresis loop. Mechanisms of magnetization along a hysteresis loop are similar to those along the curve of initial magnetization.

The magnetization process depends on the particular type of domain structure. For instance, the grain oriented metal sheet in which a strong {110}<001> texture is developed, contains two types of domains whose magnetizations are parallel or anti-parallel to the rolling direction. When the magnetic field is applied along the rolling direction, the whole magnetization process takes place exclusively by the displacement of domain walls. When the grain oriented metal sheet is magnetized in any other direction but the rolling direction, the magnetization process becomes more complex. Besides domain wall movements, changes in domain structure produced by domain nucleation and annihilation are observed under other conditions as well.

2.3. DYNAMIC PROPERTIES OF MAGNETIZATION IN ELECTRICAL STEELS

2.3.1. Dynamics of the Bloch walls

The study of domain wall mobility in a ferromagnetic material is of fundamental importance in understanding the losses which occur during the magnetization process. The mechanism of these losses is not yet completely understood, particularly in polycrystalline samples.

Two effects must be considered:

- **at a microscopic level** material defects, imperfections, and interaction fields cooperate in producing Barkhausen discontinuities, which are strictly related to the hysteresis loss. The theory of the Barkhausen noise was developed by Mazzetti and Montalenti [65] and Alessandro [17], who assumed that the Barkhausen noise is created by the domain wall motion and that individual Barkhausen jumps are grouped in large discontinuities on the power spectrum of the noise;
- **at a macroscopic level**, the irregularity in the motion of the wall affects the dynamical loss.

The behaviour of the domain wall motion is different in single crystals as compared to the polycrystalline sample. The literature results (Celasco et al., [18]) state that, in polycrystalline samples, even the motion of contiguous walls belonging to the same domain is strongly influenced by internal field interactions. In single crystals however, where the internal demagnetizing fields are nearly absent, the interaction effects are neglected, and the wall motion is dominated by the driving field.

2.3.2. Power losses

Losses in ferromagnetic materials originate from the displacement of domain walls. It is common practice to separate the losses into the sum of a hysteresis and a dynamic contribution, which are separately investigated:

$$P = P_{hyst} + P_{dyn} \tag{2.35}$$

The hysteresis loss is related to the internal structure of elementary discontinuous movements of the domain wall (Barkhausen jumps) at microscopic scale. This loss, calculated under the hypothesis of the absence of any correlation between the jumps, is equal to the area of the hysteresis loop, times the magnetizing frequency, f_m:

$$P_{hyst} = 4 I_m H_c f_m \tag{2.36}$$

where H_c is the coercive field and I_m is the peak magnetization.

The dynamic loss is associated to the space-time correlation properties of the Barkhausen jump sequence on a larger scale (presence of domain structure, clustered magnetization changes, etc.). The interpretation of dynamic loss is based on simple macroscopic domain models, ignoring the intricate fine-scale details of wall motion. In the "classical" model, the loss occurs because the materials are electrical conductors, surrounding changing magnetic fields which are perfectly homogeneous in space.

In the case of a lamination of thickness "t", and assuming sinusoidal induction, the average classical power loss is given by Bozorth [27]:

$$P_{class} = \frac{\pi^2}{6}\,\sigma\, t^2\, I_m^2\, f_m^2 \qquad (2.37)$$

where σ is the electrical conductivity of the material.

As a result of domain effects, however, the dynamic loss is generally found to be much larger than the classical loss. The difference between them is called the excess loss, and the total loss is expressed as:

$$P = P_{hyst} + P_{class} + P_{excess} \qquad (2.38)$$

The first attempt to explain the excess loss was the model proposed by Pry and Bean [28], in which the dynamic loss of an infinite slab containing a periodic array of longitudinal domains was calculated from Maxwell's equations. This model has a highly idealized character, and does not explain the non-linear dependence of the excess loss on magnetizing frequency.

A new conceptual framework based on a statistical approach to the loss phenomenology has been proposed by Bertotti [29]. Generalizing the previous models (Pry and Bean [28], Bishop [30]), the new model takes into account the spacial and temporal nonhomogeneities and the stochastic character of the elementary loss mechanisms. The most important parameter of the theory is the number of statistically independent magnetic objects (MO), each corresponding to a group of neighbouring interacting domain walls. The fundamental property of this parameter is that it is expected to be a function of peak magnetization, magnetizing frequency and some parameters characterizing the microstructure and domain structure of the material.

The main weakness of the model is that the stochastic description of the domain wall dynamics was postulated and not derived from a microscopic theory of coercivity, able to elucidate how the introduced parameters of the model depend on the microstructural properties (grain size, texture, internal and external stresses, etc.). For the first time, this model predicts the non-linear dependence of the excess loss on magnetizing frequency.

2.3.3. Rotational loss

Generally, the studies of power losses in magnetic materials are based on alternating flux measurements, where the direction of the flux remains constant. A different loss process occurs when the magnitude of the flux remains constant, and its direction varies cyclically, giving rise to rotational flux. The loss due to rotational flux is called rotational power loss, and these kind of losses are particularly important at the T-joints of three-phase transformers, and in rotating machines.

Several methods have been proposed to measure the rotational power losses in electrical steels. Among them, the method which measures the inductions B_x and B_y in two perpendicular directions of the sheet sample when the magnetic fields H_x and H_y are applied, appears to be the most convenient (Enokizono et al. [31]).

Rotational power loss is defined as the torque loss generated from the angle of lag between the **H** vector and the **B** vector caused by the rotating field. According to its definition, the rotational power loss is calculated using the following relation:

$$P_r = \frac{2\pi}{\rho} f_m^2 \int_0^T (\boldsymbol{H} \times \boldsymbol{B})\, dt = \frac{1}{\rho} f_m W_r \qquad (2.39)$$

where $f_m = 1/T$ is the magnetizing frequency, ρ is the mass density and W_r is the rotational hysteresis as defined in Cullity [32]. The rotational loss is higher than that caused by a pure alternating flux, and it increases with increasing magnetic flux density. After passing a peak value, it decreases (Narita and Yamaguchi [33]).

Other methods employ a torque magnetometer to measure rotational hysteresis W_r (Brailsford [34]). The measurements performed on single crystal discs having different orientations showed a strong correlation between the rotational hysteresis and the magnetic domain structure, specific to a certain crystal orientation. The results obtained can be explained qualitatively by the loss associated with the changing domain configuration as the field rotated. For example, in the (110) plane, the magnetic structure alternated between three possible domain patterns as the field rotated, giving rise to a higher rotational hysteresis loss than in the (100) plane where there are two equivalent easy directions of magnetization.

For a rapid evaluation of the quality of non-oriented electrical steel from the rotational loss standpoint, the conventional loss, which is the sum of the alternating power losses in the x and y directions, is often used:

$$P_t = \frac{1}{\rho}\, f_m \int_0^T \left(H_x \frac{dB_x}{dt} + H_y \frac{dB_y}{dt} \right) dt \qquad (2.40)$$

If the alternating power loss measurements are performed at constant magnetization, as they usually are, the conventional loss has the same value as the rotational power loss measured at a constant rotating flux density (Narita and Yamaguchi, [33]). This condition is partially fulfilled in non-oriented materials, where the permeability generally does not depend on the orientation of the external field in the plane of the sheet.

2.4. ANISOTROPY OF MAGNETIC PROPERTIES IN ELECTRICAL STEELS

2.4.1. Averaging the physical properties over the texture function

Many physical properties of crystalline solids are anisotropic. The corresponding property measured in a polycrystalline material is then a certain mean value depending on the single crystal property, and on the orientation distribution of crystallites in material. Thus, one of the objectives of texture investigations is to determine the mean values of anisotropic properties of individual crystallites, i.e. the resulting macroscopic anisotropy of the corresponding property in the polycrystalline material.

In some cases, the physical property, E, depends only on the orientation g of the crystallites: E = E(g). The magnetic anisotropy energy or the earring behaviour of deep drawing sheets are examples of this type of physical property. Its mean value measured on the polycrystalline sample is given by the average value of the property of individual crystallites:

$$\bar{E} = \frac{1}{V} \oint_{g} E(g) \int_{V(g)} dV = \oint E(g)\, f(g)\, dg \tag{2.41}$$

First, the integration is carried out over all the volume elements dV, which possess the orientation g, and then over all orientations g. The orientation distribution function f(g) is a weight function in this calculation. This integral can be readily expressed in terms of the series expansion coefficients. The single crystal property can be developed on the base of symmetrical generalized spherical harmonics:

$$E(g) = \sum_{l=0}^{L} \sum_{m=1}^{M(l)} \sum_{n=1}^{N(l)} e_l^{mn}\, \ddot{T}_l^{*mn}(g) \tag{2.42}$$

and f(g) is given in equation (2.20). Because of the orthogonality of the spherical harmonics, the integral yields:

$$\bar{E} = \sum_{l=0}^{L} \sum_{m=1}^{M(l)} \sum_{n=1}^{N(l)} \frac{e_l^{mn}}{(2l+1)}\, C_l^{mn} \tag{2.43}$$

In other cases, an additional effect resulting from the interaction between crystallites occurs, and the physical property, E, depends on both the crystallite orientation and on the position of crystallite in the material. Examples of such properties are the electrical conductivity, and the magnetic permeability, or the elastic stiffness. The corresponding property of the polycrystalline material depends on the orientation distribution function f(g), but also on the correlation of the orientations at different points of the material. In this case, the macroscopic property is different from the simple arithmetic average value given by equation (2.41).

We consider that two quantities, X and Y, may be linked one to the other by an arbitrary tensor property, E, which is dependent on the orientation of the crystallites and on the position r within the material:

$$Y(r) = E(r)\, X(r) \tag{2.44}$$

This relationship can be written for the components of the tensor X:

$$X(r) = E^{-1}(r)\, Y(r) \tag{2.45}$$

where the tensor E^{-1} is another representation of the same property.

It has been shown by Bunge [1] that, in this case, the actual value of the polycrystal property lies between two extremes:

$$\overline{E} \geq \overline{E'} \geq (\overline{E^{-1}})^{-1} \tag{2.46}$$

where the average value of tensor E^{-1} is:

$$\overline{E^{-1}} = \frac{1}{V} \oint_{g} E^{-1}(g) \int_{V(g)} dV = \oint E^{-1}(g)\, f(g)\, dg \tag{2.47}$$

Thus, one obtains a better approximation for the polycrystal property using the formula:

$$\overline{E'} \approx \frac{1}{2}\left[\,\overline{E} + (\overline{E^{-1}})^{-1}\right] \tag{2.48}$$

2.4.2. Magnetocrystalline energy of the polycrystalline material

As an example of polycrystalline property calculation, we will discuss the correlation between texture and magnetocrystalline energy. The cubic symmetrical functions appearing in the expression (2.27) can be rewritten as follows (Bunge [1]):

$$\begin{aligned} \alpha_1^2\alpha_2^2 + \alpha_2^2\alpha_3^2 + \alpha_3^2\alpha_1^2 &= \varphi_4(\boldsymbol{h}) \\ \alpha_1^2\alpha_2^2\alpha_3^2 &= \varphi_6(\boldsymbol{h}) \end{aligned} \tag{2.49}$$

where **h** is a direction having the cosines $(\alpha_1, \alpha_2, \alpha_3)$ in the crystal reference frame.

For polycrystalline materials, the magnetic anisotropy energy is obtained by averaging the contributions of all the crystallites using the ODF as a weight function. The functions defined in (2.49) can be also expressed using the cubic spherical harmonics $k_l^{\mu}(\mathbf{h})$ in the manner described by Bunge [1]:

$$\begin{aligned} \varphi_4(\boldsymbol{h}) &= \frac{1}{5}\,\frac{k_4^1(\boldsymbol{h})}{n_4} + \frac{1}{5} \\ \varphi_6(\boldsymbol{h}) &= \frac{1}{231}\,\frac{k_6^1(\boldsymbol{h})}{n_6} + \frac{1}{55}\,\frac{k_4^1(\boldsymbol{h})}{n_4} + \frac{1}{105} \end{aligned} \tag{2.50}$$

where n_4 and n_6 are the normalization factors. The next step, i.e. the calculation of the average of the $\varphi_{4,6}(\mathbf{h})$ functions, is made assuming the orthorhombic sample symmetry. These functions are then used to express the magnetocrystalline energy in textured specimens:

$$\overline{E_a}(\chi,\eta) = \frac{1}{9 n_4\sqrt{\pi}}\left[\frac{K_1}{5}+\frac{K_2}{55}\right] F_4(\chi,\eta) + \frac{1}{13 n_6\sqrt{\pi}}\,\frac{K_2}{231}\, F_6(\chi,\eta)$$

$$F_4(\chi,\eta) = \frac{1}{\sqrt{2}}\, C_4^{11}\, \overline{P}_4^0(\chi) + C_4^{12}\, \overline{P}_4^2(\chi)\cos 2\eta + C_4^{13}\, \overline{P}_4^4(\chi)\cos 4\eta \tag{2.51}$$

$$F_6(\chi,\eta) = \frac{1}{\sqrt{2}}\, C_6^{11}\, \overline{P}_6^0(\chi) + C_6^{12}\, \overline{P}_6^2(\chi)\cos 2\eta + C_6^{13}\, \overline{P}_6^4(\chi)\cos 4\eta + {} + C_6^{14}\, \overline{P}_6^6(\chi)\cos 6\eta$$

where χ and η are the spherical angular coordinates of the direction of the magnetization in the sample coordinate system. In the above equation, $P_l^n(\chi)$ are the normalized associated Legendre functions and C_l^{nm}'s are the ODF coefficients calculated from standard X-ray pole figure measurements.

Equation (2.51) gives for $\chi = 90°$ an expression for the magnetic torque in the plane of the metal sheet:

$$L(\eta) = -\frac{d\overline{E_a}(\eta)}{d\eta} \tag{2.52}$$

which supports the experimental data.

2.4.3. Anisotropy of permeability and power loss

It is generally agreed that the permeability or induction measured at H = 10 Oe = 800 A/m (hereafter B_{10}) is linked to the angular distribution of grains. Extensive work on this subject has concluded that B_{10} is generally insensitive to impurity content, internal stress and grain size, and is only dependent on the statistical distribution of the grain orientation (Littman [23]).

Investigations on the relationship existing between B_{10} and the average deviation of grain orientation from (110)[001] texture in 3% Si-Fe have found (Littman, [23]) that B_{10} decreases non-linearly with increasing angular spread. Other papers [24],[25] give an analytical expression for the magnetization of a single crystal at the knee of the magnetization curve. To date, no investigation which takes into account the realistic orientation distribution of grains has been undertaken to study the anisotropy of B_{10} in polycrystalline ferromagnetic materials.

Morris and Flowers [26] found that a linear relationship (to the first approximation) exists between B_{10} and the fourth order texture parameter, F_4 (from relation 2.51), but offer no theoretical explanation. They simply postulated that the variation in permeability (ΔB_{10}) is proportional to the variation in F_4, (ΔF_4). In order to predict the anisotropy of permeability, the following expression was used [26]:

$$F(\eta) = A_0 + A_4 F_4(\eta) + A_6 F_6(\eta) \tag{2.53}$$

where the functions F_4 and F_6 were defined in (2.51). The constants A_0, A_4 and A_6 are determined by fitting the experimental results obtained at various angles η with the above formula.

The same expression (2.53) was used to semi-empirically describe the correlation between the texture parameters and power losses. Hutchinson and Swift [35] found that the fourth order texture parameter F_4 describes the power losses in 1.8% Si-Fe with sufficient accuracy. In the same paper, Morris and Flowers [26] showed that the angular dependence of the total power loss in a weak textured lamination could be expressed using the linear relationship (to the first approximation) in F_4 (from rel. 2.51). Again, the experimental data were not supported by any physical grounds.

CHAPTER 3.

EVALUATION OF THE QUALITY OF ELECTRICAL STEELS

INTRODUCTION

Magnetic loss and permeability are among the most important technological parameters of electrical steels. The values of these parameters dictate the material quality, and, therefore, its price. These parameters are usually measured using the Epstein method, described in this chapter. The materials used in this study to investigate the correlation between texture and magnetic properties are characterized from the macromagnetic viewpoint.

3.1. DESCRIPTION OF MATERIALS

3.1.1. Grain oriented silicon steel

The study of the correlation between texture and magnetic properties was made on fully processed samples supplied by DOFASCO and ARMCO companies. The specimens were commercially designated as grain oriented electrical steels. The optimum magnetic properties in these alloys correspond to a composition of approximately 3 wt.

% Si. The exact process used to produce the textured Si-Fe varies from one producer to another, and is confidential. The principal stages of processing are:

(1) Prepare the Si-Fe melt as pure as economically possible and cast into large mould.

(2) Preheat the ingots at very high soaking temperature (1400°C) prior to hot rolling.

(3) Intermediate anneal of either the hot band, or after preliminary cold rolling.

(4) Cold roll the plates in one or two steps to the final thickness.

(5) Anneal in wet hydrogen at 800°C to decarburize the sheet.

(6) Final anneal at 1200°C in dry hydrogen for texture development during secondary recrystallisation process.

As mentioned previously, the detailed descriptions of the processing for these materials were not available. However, the aim of this project was centred on the analysis of texture induced magnetic properties in the final product.

3.1.2. Non-oriented silicon steel

The non-oriented silicon steel samples originated as a part of an extended research to study the effect of temper elongation on the magnetic properties of Motor Lamination Quality Steels. The specimens were supplied by DOFASCO Inc., together with their chemical composition (Table 3.1) and details of the metallurgical process.

Table 3.1. Chemical composition of non-oriented steel:

C%	Mn%	P%	S%	Si%	Al%	N%
0.026	0.36	0.03	0.005	0.594	0.06	0.003

The non-oriented steel is produced by hot rolling almost to the final thickness, pickling in 7% HCl, 82°C, 1 min. to remove the oxide scale, cold rolled to improve flatness, and batch annealed (760°C, 5 hours in 6% H_2 + 94% N_2 furnace atmosphere). Samples after batch anneal, but prior to temper, were obtained for this study. Longitudinal test coupons of 12" x 3" x thickness dimensions were sheared from the coil. Each test coupon was passed through the laboratory cold mill and elongated 2%, 6% and 12%. These test coupons were sheared into Epstein strips, and quality annealed at 770°C soak temperature, 2 1/2 hours soak time, 20% H_2 + 80% N_2 furnace atmosphere.

As the samples are tempered from 2% to 12%, stresses are induced within the material, resulting in increased dislocation density with elongation. Higher elongation implies a greater amount of time required for polygonization (rearrangement and partial elimination of dislocations) and recrystallisation. Thus, sample tempered at 2% exhibits large grain size (refer Table 3.4), which is likely caused by the secondary recrystallisation. At higher elongations (> 2%) the grains are smaller in size, suggesting that only primary recrystallisation occurred. Critical deformation is, therefore, identified as 2%. At 0% elongation, stresses are not induced to the sample, and, therefore, dislocations and nucleation sites are not created, and grain growth does not occur.

3.2. EPSTEIN METHOD FOR MACROMAGNETIC PROPERTY DETERMINATION

The standard method used for permeability and power loss measurements is the Epstein test. This test has been standardized by ASTM, and its details are described by Sanford and Cooter [36]. The material is in the form of strips 28 cm long and 3 cm wide, having a total weight of 2 kg. The strips form the cores of four solenoids arranged in a square. Figure 3.1 shows the schematic circuit of the Epstein tester. At the corners the strips overlap to assure magnetic continuity.

The instrument simulates a transformer having no load. Each

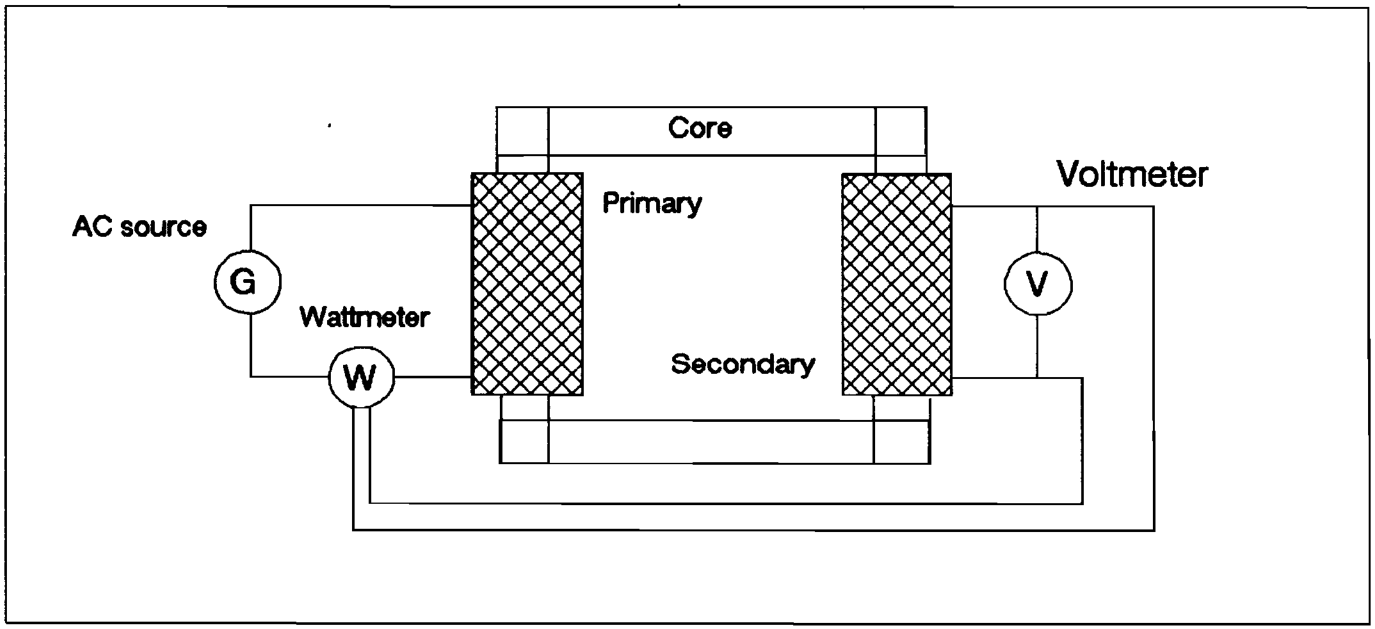

Fig.3.1. Diagram of the Epstein bridge

solenoid has an inner secondary coil of 175 turns and an outer primary coil of 175 turns. The magnetic field produced by the primary (magnetizing) coil is proportional to the current in this circuit. The transformer operates with no load in the secondary circuit, so that all the input power is dissipated as losses. The voltage in the secondary circuit is due to the changing magnetization in the core. The connected wattmeter (as shown in Figure 3.1) measures the power loss.

The maximum induction created in the core is read by the voltmeter, and as a result, both the permeability and power loss are determined simultaneously. The core loss is generally reported in units of watts/kg, obtained by dividing the total core loss by the total weight of the material. These measurements were conducted at DOFASCO Research Laboratory. The strips are generally cut with the long side parallel to the rolling direction of the sheet. When the power loss (and permeability) in the other direction is investigated, the strips are cut accordingly. For example, non-oriented steels require isotropic magnetic properties. Thus, for quality control, the power loss (and permeability) of these materials must be measured in at least two directions of the sample, usually the rolling and transverse directions.

3.3. MACROMAGNETIC CHARACTERIZATION OF MATERIALS USED FOR INVESTIGATION

3.3.1. Grain oriented silicon steel

The grain oriented samples used in the present investigation were classified as a function of the value of power losses which represents a quality parameter for these materials. According to the results of magnetic measurements, the grain oriented samples were divided into four classes: three of them were high quality, average quality and poor quality grain oriented electrical steel which were selected from the final product of the 9 mil (0.21 mm) process. The fourth class were fully processed specimens of different quality, selected from the 7 mil (0.17 mm) process. The samples were identified using a combination of numbers and letters. For the materials of the same thickness (9 mil ≈ 0.21 mm), the numbers 1, 2 and 3 used for sample notation indicate that the specimens were sampled from different lots. The letters A, B and C indicate the quality of the sample within the same lot, A corresponding to good quality, B to medium, and C to poor quality. The materials with thickness of 7 mil (≈ 0.17 mm) are represented by three specimens of different quality (power losses), identified as A, B, and C, respectively.

Magnetic measurements were conducted using the conventional Epstein test. The Epstein strips were sheared from the metal sheets along the rolling direction. The values of permeability at H = 800 A/m (10 Oe) and power losses measured for different samples are listed in Table 3.2. Quality, material specification, material thickness, and the mean grain size are also given in Table 3.2. The mean grain size of the samples was obtained from optical observation.

The magnetic properties of the polycrystalline material depend on the material texture. To correlate magnetic properties with texture, the magnetic measurements of one set of samples were performed along different directions in the rolling plane. The values of permeability and power loss obtained from Epstein strips cut from the metal sheets at different angles from the rolling direction, are listed in Tables 3.3. (a to c).

Table 3.2. Magnetic and structural properties of the grain oriented materials.

Quality	Sample	Thickness	Power loss [W/lb]		Permea	Gr.size
		[mm]	1.5 T	1.7 T	800A/m	[mm]
	9 mil					
good	GO 1A	0.21	0.376	0.551	1871	11.2
good	GO 2A	0.21	0.404	0.613	1828	2.26
good	GO 3A	0.20	0.408	0.621	1839	3.06
medium	GO 1B	0.19	0.404	0.603	1844	2.89
medium	GO 2B	0.22	0.443	0.674	1818	2.26
medium	GO 3B	0.22	0.436	0.652	1843	3.22
poor	GO 1C	0.19	0.438	0.666	1809	2.43
poor	GO 2C	0.21	0.484	0.773	1767	1.52
poor	GO 3C	0.22	0.475	0.742	1803	3.14
	7 mil					
good	GO 7A	0.17	0.362	0.543	1833	3.22
medium	GO 7B	0.17	0.369	0.572	1827	2.89
poor	GO 7C	0.17	0.390	0.591	1839	5.32

Table 3.3.a. Permeability and power loss at different angles to rolling direction for sample GO 3A.

Angle from rolling dir.	Core loss [W/lb] 1.0 T	Core loss [W/lb] 1.2 T	Core loss [W/lb] 1.3 T	Core loss [W/lb] 1.5 T	Permeability @ 800 A/m
0°	0.183	0.260	0.306	0.425	1820
10°	0.268	0.379	0.446	0.620	1748
20°	0.447	0.623	0.740	1.109	1533
30°	0.609	0.866	1.082	-	1354
40°	0.766	1.152	1.332	-	1245
50°	0.846	1.312	-	-	1197
55°	0.915	1.387	-	-	1187
60°	0.941	1.408	-	-	1196
70°	1.009	1.423	1.663	-	1229
80°	1.008	1.345	1.644	-	1289
90°	0.981	1.268	1.512	1.950	1335

Table 3.3.b. Permeability and power loss at different angles to rolling direction for sample GO 3B.

Angle from rolling dir.	Core loss [W/lb] 1.0 T	Core loss [W/lb] 1.2 T	Core loss [W/lb] 1.3 T	Core loss [W/lb] 1.5 T	Permeability @ 800 A/m
0°	0.195	0.276	0.324	0.446	1823
10°	0.328	0.460	0.541	0.777	1678
20°	0.492	0.691	0.830	1.243	1483
30°	0.657	0.940	1.176	-	1341
40°	0.810	1.219	1.430	-	1233
50°	0.881	1.311	-	-	1227
55°	0.940	1.417	-	-	1197
60°	0.983	1.459	-	-	1196
70°	0.980	1.379	1.599	-	1236
80°	0.986	1.315	1.615	-	1285
90°	0.924	1.185	1.410	-	1347

Table 3.3.c. Permeability and power loss at different angles to rolling direction for sample GO 3C.

Angle from rolling dir.	Core loss [W/lb] 1.0 T	Core loss [W/lb] 1.2 T	Core loss [W/lb] 1.3 T	Core loss [W/lb] 1.5 T	Permeability @ 800 A/m
0°	0.201	0.287	0.340	0.486	1776
10°	0.279	0.394	0.469	0.669	1713
20°	0.454	0.615	0.708	0.940	1803
30°	0.678	0.973	1.207	-	1332
40°	0.747	1.104	1.396	-	1278
50°	0.950	1.461	-	-	1194
55°	0.987	1.500	-	-	1193
60°	1.040	1.546	-	-	1184
70°	1.066	1.540	-	-	1213
80°	1.097	1.450	1.762	-	1286
90°	1.048	1.361	1.481	-	1323

3.3.2. Non-oriented silicon steel

All the magnetic tests were done after the temper elongated samples were sheared into Epstein strips packs and quality annealed. Table 3.4 lists the values of permeability and power loss measured in both the longitudinal (rolling) direction and the transverse direction of the temper elongated samples. Both the power losses and the permeability were measured at 60 Hz and 1.5 T magnetic induction. The mean grain size of the investigated samples is also given.

Table 3.4. Magnetic properties and grain size of non-oriented samples:

Percent	Longitudinal		Transverse		Grain size
elongation	Core loss [W/lb]	Perm.	Core loss [W/lb]	Perm.	[μm]
0 %	4.40	2540	4.49	1898	30
2 %	2.88	3888	2.89	1638	200
6 %	2.93	3574	2.96	1795	140
12 %	2.77	3617	2.83	2030	80

CHAPTER 4.

EXPERIMENTAL METHODS AND RESULTS OF TEXTURE ANALYSIS

INTRODUCTION

To estimate the material macroscopic properties, the orientation distribution function (ODF) is needed as input data. Experimental texture data can be obtained by a great variety of experimental methods. Most of these methods are based on X-ray or neutron diffraction, although indirect techniques based on determination of an orientation sensitive physical property such as magnetic torque are also used. Such methods allow us to determine a low order approximation to the ODF. For example, the sixth order approximation of ODF is obtained in the case of magnetic properties. Such methods are of limited scope and they are used according to the specific problem under consideration.

This chapter presents the experimental methods of texture analysis used in this study. The texture determination is based on the pole figure inversion method. The pole figures have been measured using X-ray and neutron diffraction.

When the texture of the grain oriented silicon steels is measured using neutron diffraction, the texture by number differs from the texture by volume due to the anisotropy of grain shape. Additionally, the extinction phenomenon within the grain is present. In this chapter, a correction is proposed to eliminate the effects of the orientation dependence of grain size and extinction on texture measurements. Then, following the texture data analysis, the texture and structure of grain oriented and non-oriented samples used in this study are fully described.

4.1. TEXTURE MEASUREMENT USING X-RAY DIFFRACTION

The majority of texture measurements are based on direct determination of the volume dV, or the number dN, of crystallites. Two of the three angular parameters of the crystallite orientation are fixed, and the third one takes on all possible values. This is the pole figure measurement. The orientation distribution function is calculated from several pole figures (pole figure inversion).

Pole figure measurements can be carried out by the diffraction of X-rays, neutrons, and electrons. It is not the purpose of the present work to discuss experimental methods of texture investigation based on X-ray, neutron, or electron diffraction in detail. Comprehensive summaries are given by Szpunar [16], Coulomb [37] or Underwood [38].

For texture measurements, we used the angle dispersive method which utilizes a monochromatic beam of radiation. This method allowed us to determine one pole figure after another by varying the Bragg angle. The pole densities were determined by measuring the intensities of a X-ray or neutron beam diffracted by {hkl} planes (Figure 4.1). The scattering vector of these planes remained fixed in space, and the specimen was rotated so that different directions in the sample were brought into the diffraction condition. Whenever a crystallite became so oriented that the Bragg

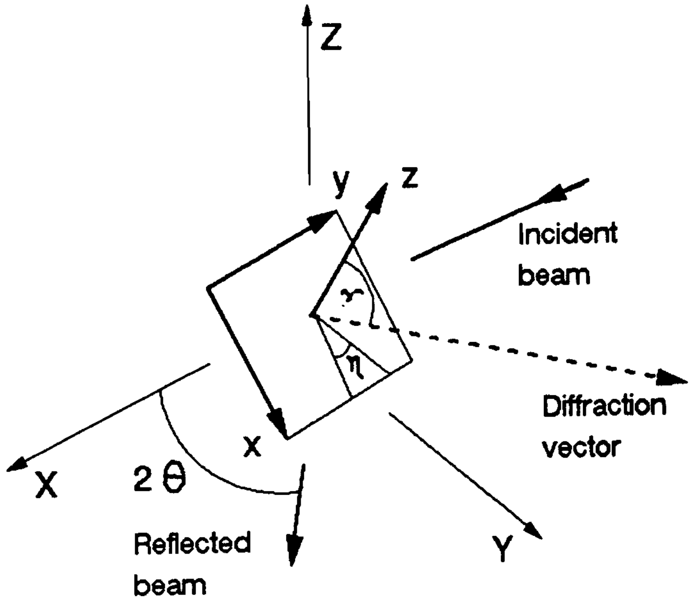

Fig.4.1. Principle of texture measurement

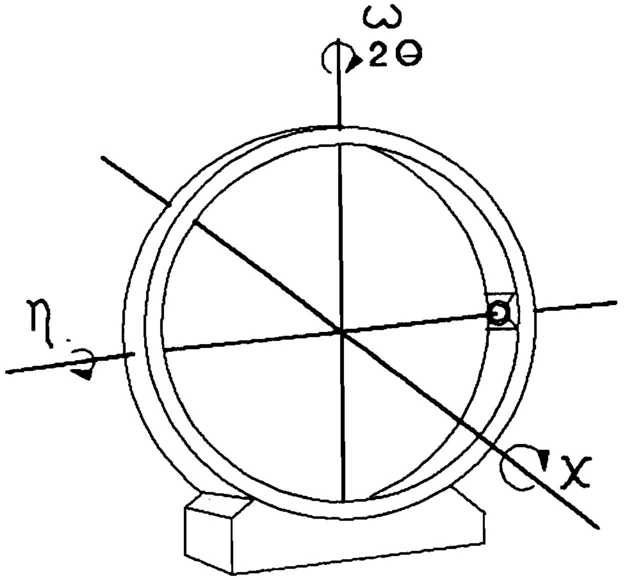

Fig.4.2. Principle axes of the texture goniometer

condition satisfied any set of the prescribed planes, a diffracted intensity was measured from that grain. The total diffracted intensity for any specified sample direction was proportional to the volume of the specimen having the set of crystallographic planes under investigation. The intensity (corrected if necessary) was proportional to the pole density at the specified sample position of that pole figure, determined by the diffraction condition. The proportionality factor was the random intensity, which is the intensity observed when a textureless sample was examined under the same experimental conditions.

For the quantitative description of material texture, the X-ray technique used in the present experiment was the Schulz reflection method whose specific features will now be described.

The specimens used for texture analysis were pieces of steel sheet cut to a size of 15 x 25 mm^2. A flat surface was prepared by grinding and chemical polishing or etching. The X-ray beam penetrates through only a thin layer at the specimen surface. The thickness of this layer depends on the material absorbtion coefficient and it has a typical value of 100 μm for iron.

The specimen was mounted in the texture goniometer (Figure 4.2) where it was subject to three types of movement:

(1) rotation about the sheet normal (angle η)

(2) rotation about an orthogonal axis (angle χ)

(3) translation to and fro, which improved the statistical averaging of texture measurement by increasing the number of grains illuminated by the incident beam.

The main problem that arises with the Schulz method is that the diffracted intensity is affected not only by the material texture but also by the geometrical setting of the goniometer. Analytical formulas for the intensity corrections which may be necessary in this method are given by Humbert [39]. They are:

(a) the geometrical correction takes into account the actual irradiated area on the sample. This area increases as the surface of the sample becomes parallel to the incident beam.

(b) the defocalization causes a reduction in the measured intensity due to the broadening of the reflected beam, with an increasing irradiated area on the specimen.

(c) absorbtion correction is due to the attenuation of the intensity of the beam, along its path through the sample.

(d) background correction eliminates the extraneous intensity due to a number of origins (non-monochromaticity of the incident beam, scattering in the air and from other materials around, non-elastic scattering, microstructural state of the material, etc.) which is measured at the same time with the useful intensity.

These basic principles of Schulz's experimental technique apply to any type of material under investigation. Depending on the specific material, the determination of texture may be altered by the presence of local texture, or by too small number of irradiated grains. We took these problems into consideration when we analyzed the experimental data.

The first problem considered is related to possible inhomogeneities of the texture in a material. The material texture is not homogeneous if different volume elements of the sample have different textures. In such cases, one must distinguish the local texture from the global texture, which is the integral over the local textures. From the magnetic properties point of view, the quantity of most interest and to be determined is the global texture. The local inhomogeneities are to be eliminated and this could be achieved, for example, by increasing the irradiated volume of the sample. As such, the X-ray beam penetrates only a small distance through the material, and as a result, the information obtained by X-rays about the material texture are correct only if the texture is homogeneous through the thickness of the sample. For example, the texture of grain oriented materials where the grains extend through the whole thickness of the sample could be considered as homogeneous, but this is not the case in non-oriented materials.

Another problem with experimental texture determination is the statistical nature of the texture function, and this is related to the total number of grains involved in the measurement. Texture can be quantitatively described only when there is reliable statistical information about the orientation of a sufficient number of grains. In coarse grained materials like grain oriented steels, even if the irradiated area is increased by sample translation, the uncertainty with which the pole densities are obtained is relatively high. Further improvement in the statistics is possible by increasing the penetration depth of the radiation, an attractive property of the neutron diffraction method.

4.1.1. X-ray texture measurement system

All the X-ray texture measurements have been done using the Siemens texture diffractometer. This instrument consists of a computer controlled vertical diffractometer and the Huber Eulerian cradle. The diffractometer provides Θ and 2Θ (Bragg angle) rotations for the specimen. The Eulerian cradle rotates the sample as previously described. The Siemens 2.0 KW X-ray tube produces molybdenum characteristic radiation when operated at 40 kV and 40 mA. The X-ray diffracted beam is measured by a scintillation detector operating at 900 V.

The defocusing effect on the measurements was limited by using a texture nose attached to the X-ray tube, in addition to the conventional slits. The texture nose is a narrow vertical slit adjacent to the specimen, and designated to decrease the spread of the irradiated area for all positions of the sample. The pole figures were collected by continually scanning over the ranges 0°-80° for angle χ, and 0°-355° for angle η. The Siemens system possesses adequate software to correct the raw data for defocusing, absorbtion, and background radiation errors using data collected on a random iron specimen. The corrected data files were then stored in the computer for further analysis and processing.

4.2. TEXTURE MEASUREMENT USING NEUTRON DIFFRACTION

An alternative type of radiation that may be used in texture measurements is provided by thermal neutrons. Thermal neutron diffraction is known to be a powerful tool, especially for volume texture analysis because of the low absorption of neutrons by the majority of materials. Neutron diffraction is essentially similar to X-ray diffraction, but there are significant differences.

Generally, the source of neutrons is a nuclear reactor. The wavelength spectrum of thermal neutrons is continuous and, contrary to X-rays, does not contain characteristic lines. A single wavelength beam is obtained by using a crystal monochromator. Since the neutron has no electric charge, the neutron scattering occurs by interaction with nuclei, rather than with electrons. The neutrons also possess a magnetic moment, so that they interact with atomic magnetic moments. This subject is discussed in Chapter 7.

The dimensions of nuclei are much smaller than the thermal neutrons wavelength, so that the atomic form factor is isotropic with the scattering angle, in contrast to X-ray scattering. The Bragg angles are comparable to those for the X-ray, but the absorbtion of neutrons by the specimen is lower than X-rays by a factor of 10^3 - 10^4. This high penetration of neutrons has the advantage of allowing examination of a large volume of material.

Texture measurements using neutron diffraction were conducted at Chalk River Nuclear Laboratory. The diffraction experiment was performed using a combined transmission-reflection technique.
If this method of pole figure registration is used, several corrections are necessary (absorption, defocalization). The absorption corrections were calculated in a similar manner to those for X-ray measurements. Primary extinction correction may be necessary in the case of anisotropic grain shape with a high perfection of grain structure. This is the subject of the next section, where a method for extinction correction in texture measurements is proposed and tested.

4.2.1. Correction of texture data obtained using neutron diffraction

The kinematic theory of the diffraction of X-rays or neutrons predicts that the intensity of the diffracted beam is proportional to the volume of the crystal. One drawback of the kinematic theory, however, is that it ignores the possibility that the diffracted beam may rescatter as it passes through the crystal. In the diffraction experiment on a perfect crystal, both the incident and diffracted beams satisfy the Bragg condition, and an interchange of energy between these two beams occurs as both beams flow through the crystal. This phenomenon is termed extinction, and it is described by the Darwin [40] energy transfer equations. Thus, in crystal structure analysis, extinction is increased reduction of the intensity of the diffracted beam from the prediction of the kinematic theory, as the crystal volume increases.

The problem of extinction is one of the major obstacles to the accuracy of coherent neutron diffraction experiments. Various methods of correction have been proposed, both experimental and theoretical. In this section, we analyze the influence of extinction and anisotropy of the grain size on texture measurements, and we propose a method of correction.

Neutrons have a lower absorbtion factor than X-rays, and this plays a very important role in the measurement of textures. Neutrons penetrate deeply into the material, and the long path of the neutrons travelling through the material increases the probability of mutual coupling between the incident and diffracted beams which causes extinction.

Extinction within a perfect crystal is termed primary. Most crystals are very far from perfect. As a result, one may think that the crystal is an aggregate of perfect domains, which are slightly misoriented with respect to each other. The phase relation between the waves diffracted by two adjacent domains is supposed to be random, and this results in an incoherent process. The statistical model of the imperfect crystal was developed by Zachariasen [41], and it is called the "mosaic model". Based on this model, one can define an ideally imperfect crystal as one comprised of very small mosaic blocks, having appreciable variations in orientation, and being so small that the primary extinction can be ignored. Even if the mosaic blocks are so small, there may be not enough disorientation between the blocks. The extinction which appears in this case is termed secondary. Both types can occur in the same material.

Zachariasen [41] developed the formalism of the extinction theory on the basis of the Darwin [40] energy transfer equations, and applied it to the analysis of the diffraction data for a number of substances (Zachariasen [42],[43]). We use this theory to interpret the experimental data obtained when the texture of grain oriented materials is measured using the neutron diffraction.

If the specimen has a misorientation between various mosaic blocks, the incident beam striking a given block differs by an angle Δ from the ideal Bragg direction. It is possible to define an angular distribution $W(\Delta)$ for mosaic blocks. Generally, $W(\Delta)$ is assumed to have a gaussian distribution of:

$$W(\Delta) = \frac{1}{\xi\sqrt{2\pi}} \exp\left[-\frac{\Delta^2}{2\,\xi^2}\right] = g\sqrt{2}\,\exp\left[-2\pi\, g^2\,\Delta^2\right] \qquad (4.1)$$

where Δ is the magnitude of the angular deviation from the mean and ξ is the standard deviation of the distribution. Normalization is such that:

$$\int W(\Delta)\, d\Delta = 1 \qquad (4.2)$$

In texture measurements, the radiation counter is placed at the Bragg angle. The counter integrates the diffracted intensities around the exact Bragg position. In a plane-wave description, the process depends only on the divergence of the incident beam, ε_1 (Cooper and Rouse, [44]). In this case, the kinematical theory of diffraction gives the following formula for the reflecting power:

$$P(\varepsilon_1) = I_0\, v\, \sigma(\varepsilon_1) \qquad (4.3)$$

where: I_0 = incident intensity of radiation

v = irradiated crystal volume

$\sigma(\varepsilon_1)$ = diffracting cross section per unit of volume and intensity.

For a crystal with a convex limiting surface, the diffracting cross section can be exactly calculated (Zachariasen, [43]):

$$\sigma(\varepsilon_1) = Q\, \alpha\, \frac{\sin^2(\pi \varepsilon_1 \alpha)}{(\pi \varepsilon_1 \alpha)^2}$$
$$\alpha = t\, \frac{\sin 2\theta}{\lambda} \qquad (4.4)$$

where Q is the average scattering cross section per unit volume of crystal, t is the thickness of the crystal parallel to the diffracted beam, and λ is the radiation wavelength. If the effective particle size t is anisotropic, the diffracting unit cross section $\sigma(\varepsilon_1)$ will also be anisotropic.

Extinction is taken into account by introducing a function $\varphi(\sigma)$, defined by the relation:

$$P(\varepsilon_1) = I_0\, v\, \sigma(\varepsilon_1)\, \varphi(\sigma) \qquad (4.5)$$

To the first approximation, the $\varphi(\sigma)$ function is the same for the two geometrically distinct situations of the diffraction experiment when the sample is placed in symmetrical transmission, or symmetrical reflection positions (Zachariasen, [43]):

$$\varphi(\sigma) \simeq 1 - \sigma(\varepsilon_1)\, t \qquad (4.6)$$

The same formalism is used to describe both primary and secondary extinction. For primary extinction, t is the thickness of a mosaic block, and $\sigma(\varepsilon_1)$ is given by equation (4.4). For secondary extinction, t is referred to as the thickness of the mosaic crystal, having a gaussian distribution of the angular orientations of the crystallites, and σ is replaced by the following expression (Cooper and Rouse, [44]):

$$\bar{\sigma}(\varepsilon_1) = Q\,\bar{\alpha}\,\exp\left(-\pi\,\varepsilon_1^2\,\bar{\alpha}^2\right)$$

$$\bar{\alpha} = \frac{\alpha}{\left(1 + \dfrac{\alpha^2}{2g^2}\right)^{1/2}} \tag{4.7}$$

where the parameter g is defined in equation (4.1).

In the experiment where the texture of grain oriented samples was measured using neutron diffraction, we expect that the values of the reflecting power are affected by extinction. Following the secondary recrystallization, the grains in 3% Si grain oriented steel are very large (several millimetres). The final annealing temperature of 1400°C eliminates the dislocations, such that the grain structure is close to the structure of perfect crystals. Additionally, the grains are very well oriented having small deviations from the ideal (110)[001] orientation. The sample used in investigation was composed of square shaped pieces 15 x 15 x 0.17 mm in dimension, cut from a grain oriented silicon steel sheet (GO-7B). The average grain size of the sample was 2.9 mm.

In texture measurements using neutron diffraction, the reflecting power is recorded in steps at points where the scattering vector is oriented in (χ,η) direction in the sample reference frame. The neutron beam is diffracted in all crystallites which are oriented so that the scattering vector satisfies the Bragg condition within the solid angular element, $d\Omega$.

In the first experiment, the microstructure of the sample was not modified. As previously mentioned, the dislocation density in each grain is very low, the mosaic blocks are large, and the misorientation between them is very small. Both primary and secondary extinction can occur in one grain. In this case, the scattering process in a grain, which is considered a mosaic

Fig.4.3. **Diffracted intensity vs. thickness**

Original crystallographic structure

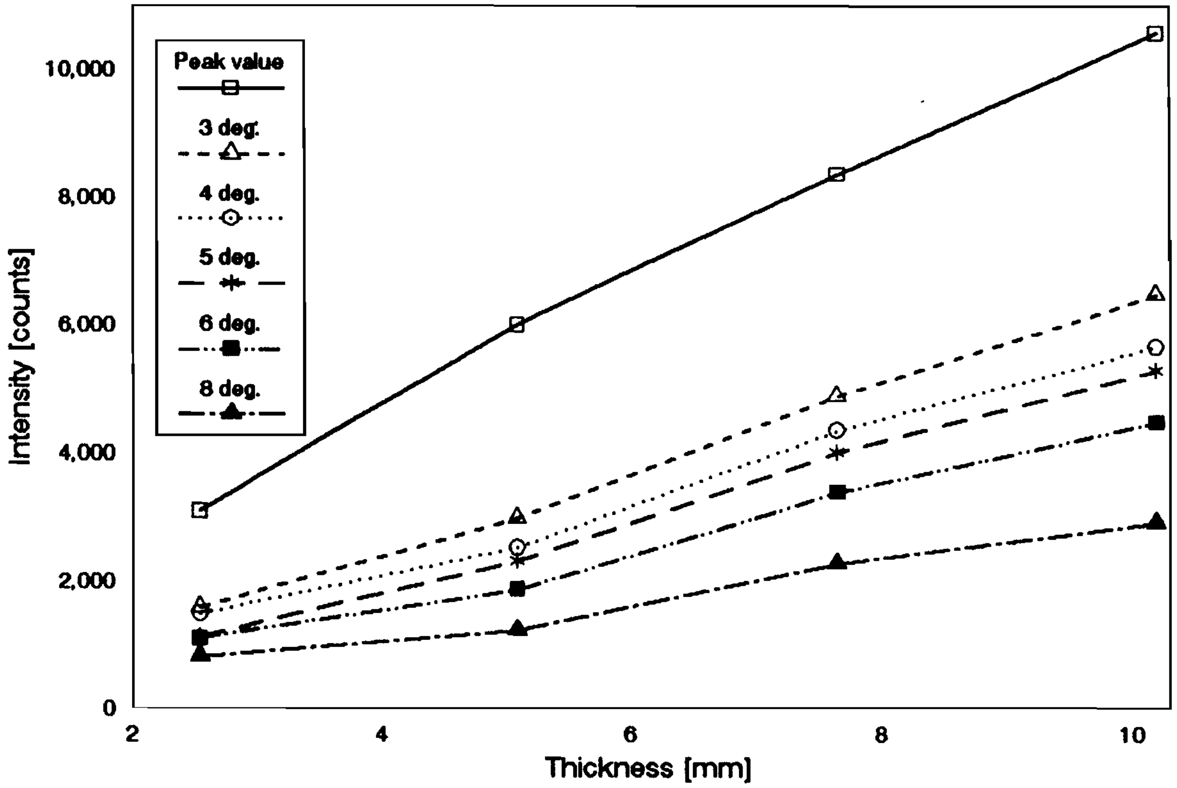

crystal, is described by the effective unit diffracting power:

$$\bar{\sigma}(\varepsilon_1) = \sigma_p(\varepsilon_1)\ W(\varepsilon_1) \tag{4.8}$$

where $\sigma_p(\varepsilon_1)$ is the scattering cross section per unit of volume and intensity corrected for primary extinction. The total reflecting power of the grain considered as a mosaic crystal is obtained by substituting relations (4.6) and (4.8) in equation (4.5):

$$\begin{gathered} P^g(\varepsilon_1) \sim I_0\ \frac{1}{S_0}\,\frac{T}{\cos\theta}\ W^g Q' \left[1 - W^g Q'\ \frac{T}{\cos\theta}\right] e^{-\mu_0 \frac{T}{\cos\theta}} \\ \textit{where:}\ \ v = \frac{1}{S_0}\,\frac{T}{\cos\theta} \end{gathered} \tag{4.9}$$

In this equation, I_0 is the intensity of the incident beam, S_0 is the cross section area of the beam, T is the thickness of the grain and μ_0 is the absorbtion factor ($\mu_0 \approx 0.08\ \mathrm{cm}^{-1}$ for neutrons in iron).

The measurements have been performed on a series of samples of different thicknesses in order to observe the variation of reflected intensity with the irradiated volume. The thickness (volume) of the sample was changed modifying the number of square shaped pieces which form the specimen: 15, 30, 45 and 60 pieces. Then, the distribution of the (110) pole density around the transverse direction (TD) was measured for each composite specimen within an angular interval of -10° to +10° (step 0.5°) of both χ and η angles. At each point of this scan a different number of grains were brought into the Bragg angle. The orthorhombic sample symmetry imposes that, at any point situated at the same angular distance from the position of maximum intensity of the pole, the number of grains is, from a statistical standpoint, the same. The maximum intensity of the (110) pole and the averaged intensities at 3°, 4°, 5°, 6°, and 8° angular distances around the pole are plotted in Figure 4.3, as a function of thickness. The linear variation of the intensity with sample thickness indicates that the diffraction inside the samples being examined supports the kinematical theory, meaning that no phase relation between the waves diffracted by different grains is present. In this case, the recorded diffracted power of the whole sample is the sum of the reflecting powers of each grain satisfying the Bragg condition:

$$P_t(\varepsilon_1) = \sum_{i=1}^{N} P_i^g(\varepsilon_1) = N\, P^g(\varepsilon_1) \tag{4.10}$$

where N is the number of grains contributing to the scattering in the (χ,η) direction of the sample. In the above formula, we assumed that the mean grain size does not depend on the grain orientation. This assumption is valid when the scattering vector is rotated within a small angular interval (χ,η), such that the orientation of grains relative to the neutron beam do not drastically change. Therefore, texture measurements are not affected by the primary and/or secondary extinction within the grain, provided that all parameters in equation (4.9) are isotropic.

In grain oriented silicon steel, the grain shape is highly anisotropic. The thickness of the grain parallel to the direction of diffraction changes when the grain orientation changes. If the grain shape is approximated by a disc of diameter D, and thickness d, the path lengths of the neutron beam, parallel to the direction of diffraction, will be: $T_{33} = D/\cos\theta$ when the diameter of the disc lies in the scattering plane, $T_{22} = d/\cos\theta$ when the scattering vector is parallel to the thickness of the grain and $T_{11} = d/\sin\theta$ when the scattering vector is perpendicular to the thickness of the grain. The grain shape, as seen by the beam, turned into an ellipsoid with the dimensions of the principal axes T_{11}, T_{22} and T_{33}. For a direction (χ,η), the thickness of the crystal, parallel to the direction of diffraction, can be expressed by means of spherical surface harmonics of second order (Bunge, [1]):

$$T(\chi,\eta) = \frac{1}{3}(T_{11} + T_{22} + T_{33}) + \frac{2\sqrt{\pi}}{3\sqrt{5}}\, k_2^1(\chi)\,(2T_{33} - T_{11} - T_{22}) + \\ + \frac{2\sqrt{3\pi}}{3\sqrt{5}}\, k_2^2(\chi,\eta)\,(T_{11} - T_{22}) \tag{4.11}$$

The effect of the anisotropy of grain shape on texture measurements was investigated using three (110) pole figures from the composite specimen with 60 pieces of material. The sample was placed in the texture goniometer with the rolling direction (RD) in (χ=0°,η=0°) direction, the transverse direction (TD) in (χ=90°,η=90°) direction, and the measurement was done using an pseudo-equal area scan with 1020 points per pole figure. For the first (110) pole figure measurement, the scan started from that position of the sample where the scattering vector was oriented in the (χ=0°,η=0°) direction. For the next measurements, the starting value of angle χ was shifted by 0.125° after the first pole figure measurement, and again after the second measurement. As a result, each of the measured (110) pole figures investigates the orientation of the grains from different volumes of material. This was an attempt to improve the statistical errors due to the number of irradiated grains.

From these three pole figures, the average intensities of the poles situated at (90°,0°), (90°,90°) and (45°,45°) were calculated. This data is presented in Table 4.1, together with the corresponding thicknesses of the crystallite, parallel to the direction of the diffracted beam.

Table 4.1. Diffracted intensities and effective grain thicknesses at different symmetrical <110> poles.

Direction (χ,η)	Intensity [counts]	Thickness [mm]
(90°,0°)	890	0.487
(90°,90°)	380	0.181
(45°,45°)	560	1.766

These results clearly indicate the presence of primary and/or secondary extinction within the grain, in addition to the effect of the anisotropy of grain shape on the pole figure density. This method of texture measurement yields a pole figure by volume which was defined using equation (2.15). We assume that all grains have the same mean volume. Since the mean grain size is orientation dependent, the pole figure by volume and the pole figure by number will differ. The relationship between the two pole figures is obtained from the relationship between the volume of the sample (ΔV) and the number of grains having the same orientation of an individual crystal direction with respect to the sample reference frame:

$$\begin{aligned} P^V(\chi,\eta) &= P^N(\chi,\eta)\ \Delta V(\chi,\eta)\ f_{ext}(\Delta V) = \\ &= P^N(\chi,\eta)\ S_0\ T(\chi,\eta)\ f_{ext}(\Delta V) \end{aligned} \tag{4.12}$$

where f_{ext} is a factor related to extinction.

Obviously, the pole figure by number, as it is defined, does not depend on extinction and/or the anisotropy of the grain shape effects. The quantitative comparison between the pole figure by number and the pole figure by volume may yield information on the orientation dependence of the mean grain size, which is an information on the polycrystalline structure beyond the texture.

As far as the texture of a material with grains of the same volume is concerned, the pole figure by number is the quantity of interest. To obtain this pole figure in terms of reflecting power, each point on the pole figure by volume must be multiplied by the amount:

$$E(\chi,\eta) = \frac{1}{T(\chi,\eta)\ f_{ext}(\Delta V)} = \frac{1}{T(\chi,\eta)\ W^g\,Q'[1 - T(\chi,\eta)\ W^g\,Q']} \tag{4.13}$$

where $T(\chi,\eta)$ is given by equation (4.11) and the quantity, ($W^g \cdot Q'$), representing the unit diffracting power in the grain, is unknown.

We can calculate this quantity from equations (4.9) and (4.10). The densities of (110) poles in the (90°,0°), (90°,90°), and (45°,45°) directions of the sample are produced by the same number of grains. Since no coherent relationship exists between the beams diffracted by individual grains, we can use equation (4.10) written for the particular three directions indicated above in which the reflecting power $P^g(\epsilon_1)$ is given by equation (4.9). In this way, we obtain three equations, each of them dependent on the unknown parameter, N. Dividing these relations to eliminate N, we obtain a system of three equations, each having the product ($W^g\,Q'$) as the unknown, and found by least-squares fitting. The best fit of the experimental data given in Table 4.1 is obtained for a value $(W^g \cdot Q') = 4.1\ \mathrm{cm}^{-1}$.

As an example of how the anisotropy of grain shape and/or extinction affects the texture measurements, we calculate the texture coefficients C_l^{nm} from the (110) pole figure by volume (experimental) and from the (110) pole figure by number (corrected). Since one pole figure is used, only low order coefficients ($l \leq 6$) are calculated. The results are presented for comparison in Table 4.2 where we also calculated the percentage difference between them:

$$Diff\ [\%] = \frac{C_{l\ exper}^{mn} - C_{l\ corr}^{mn}}{C_{l\ exper}^{mn}}\ 100 \qquad (4.14)$$

Table 4.2. Texture coefficients for experimental and corrected intensities:

(110) pole	C_4^{11}	C_4^{12}	C_4^{13}	C_6^{11}	C_6^{12}	C_6^{13}	C_6^{14}
Experim.	5.640	-.058	-4.702	-3.434	.407	-9.019	.151
Corrected	5.201	-.071	-4.616	-3.886	.254	-8.727	.099
Differ [%]	8.4	18.3	1.8	11.6	60.2	3.3	52.5

In the second experiment, the perfection of the crystals' structure was destroyed by soaking the sample in liquid nitrogen

Fig.4.4. Diffracted intensity vs. thickness

After soak in liquid nitrogen

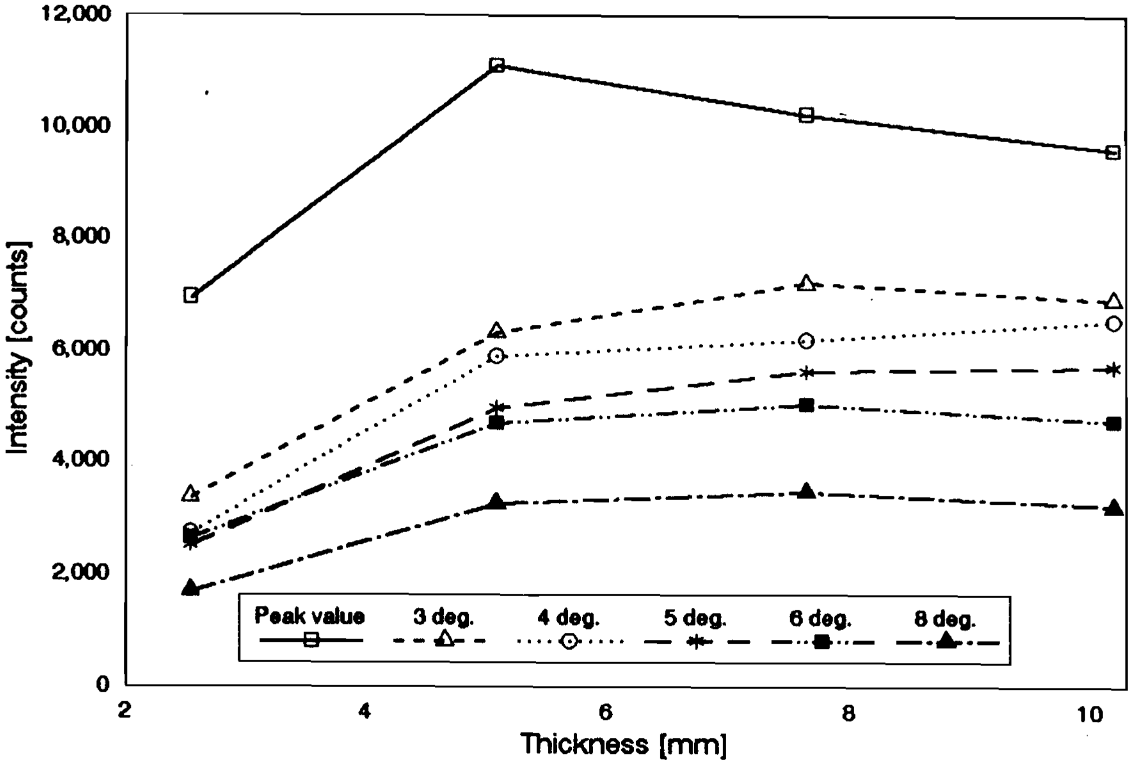

for 10 minutes. The high dislocation density introduced in each grain practically eliminates the primary and/or secondary extinction within the grain. The equivalent of secondary extinction in a polycrystalline material is multiple scattering. In an experiment, multiple scattering manifests itself as an apparent absorbtion.

The same (110) pole around the transverse direction in the (-10°,+10°) interval of both the χ and η angles with step 0.5°, was measured versus the thickness of the sample. The maximum intensity of this pole, and the average intensities calculated for 3°, 4°, 5°, 6°, and 8° angular distances from the centre of the pole are plotted in Figure 4.4, versus sample thickness. This graph clearly shows that the reflecting power is reduced as the volume of the sample increases, or in other words, that multiple scattering is present in the sample. The dependence of the reflecting power on the thickness T′ of the sample could be described by a formula similar to the one used in the true absorbtion case:

$$P(\varepsilon_1) = I_0 \, v \, \sigma(\varepsilon_1) \, e^{-\mu_m T'} = I_0 \, S_0 \, T' \, \sigma(\varepsilon_1) \, e^{-\mu_m T'} \qquad (4.15)$$

where μ_m is the coefficient accounting for multiple scattering. If $\sigma(\varepsilon_1)$ is assumed to be constant inside the crystal, the value of μ_m calculated from the experimental data is $\mu_m = 1.7\ \mathrm{cm}^{-1}$.

To investigate the influence of the anisotropy of grain shape on texture measurements, the (110) pole figure of the sample having the maximum thickness (= 10.2 mm) was measured. Contrary to the previous experiment, the pole densities for symmetrical equivalent directions have approximately the same values. This experimental result indicates that the dimension of the mosaic blocks are very small, and their angular distribution function is very broad, as expected after soaking the sample in liquid nitrogen. In this case, the diffracting unit cross section given in equation (4.4) is isotropic and no correction of the measured pole figure is necessary.

4.3. TEXTURE ANALYSIS

Following texture measurements, the (110), (200), and (211) pole figures were obtained for each specimen. Depending on the diffraction method used, these raw data represent incomplete pole figures (up to $\chi = 80°$) in X-ray measurements, or complete pole figures (up to $\chi = 90°$) in neutron diffraction. The pole figure inversion, i.e. the calculation of the orientation distribution function (ODF) from pole figure data was performed using a iterative method implemented with a software package developed at the McGill Texture Laboratory. The particularity of this pole figure inversion method is that the ODF calculation problem is treated directly on the basis of the discrete form of the equation (2.18), by applying iterations (Pospiech, [2]).

In the present study, the results are discussed in terms of ODF's, and not the pole figures, the latter offering incomplete information about the orientation distribution of crystallites. The accuracy of the ODF is characterized by two parameters. The first one is the angular resolution $\Delta\varphi_1$ $\Delta\phi$ $\Delta\varphi_2$, which was 5° in the present investigation. The second one is the statistical relevance, $\Delta f(g)/f(g)$, which differs from one sample to the other. The numerical procedure involved in ODF's calculation led to the general accepted error of approximately 20%. This error varied from sample to sample, depending on the spread of texture components, and on the shape, size, and arrangement of the individual grains.

The two classes of material under investigation, grain oriented and non-oriented electrical steels, have different textures. Often, simpler parameters can be proposed and used for their characterization from the texture point of view. These parameters should illustrate the relationship between the actual texture developed in these materials and the ideal texture which provides the required magnetic anisotropy. Some of these parameters were used in this study to evaluate the proposed models. For example, in grain oriented materials the texture parameters should illustrate the deviation of the distribution of grain orientations from the ideal {110}<001> orientation which provides the optimum magnetic properties in the rolling direction of the sample. The ideal texture for non-oriented steels is {100}<uvw> because such texture assures the presence of the maximum number of easy magnetization directions in the sheet plane. This texture is usually accompanied by other textures which are known to be responsible for a deterioration of magnetic properties. The results of the texture analysis of non-oriented steels should be presented to facilitate the identification and evaluation of these textures.

The grain oriented samples under investigation show a texture of {110}<001> type. This texture is represented by the physical (110)[001] point in the Euler space, i.e. the texture function deviates from zero in a certain region centred about the ideal (110)[001] orientation. Several texture parameters were chosen to describe the strength of this orientation:

- ODF intensity of (110)[001] orientation, f(goss)
- volume fraction of (110)[001] orientation, V(goss)%
- intensity of the (100) pole figure at rolling direction (RD)
- in-plane angular distribution of [001] direction about RD
- out-of-plane angular distribution of [001] direction about RD.

In non-oriented samples, the grain orientations are distributed along a tube in Euler space, which corresponds approximately to rotations about a common crystallographic direction. Since <100>, <110>, and <111> directions represent easy, medium and hard magnetization directions of iron respectively, it is of practical importance for non-oriented steels to determine the distribution of these directions in the sheet plane. These distributions are given by the fibre texture components having the <100>, <110>, and <111> fibre axes perpendicular to the sample normal direction. They will be termed μ, α, and γ fibres of the ODF, respectively. In the Euler space, these fibres are parallel to the φ_1 axis, and located at $\varphi_2 = 45°$ and $\phi = 0°$, 90° and 55°, respectively. Thus, a concise description of texture in non-oriented steels is given by:

- skeleton line locations and intensities
- volume fraction of the main texture components
- μ, α, and γ fibres.

The orientation distribution function f(g) is analytically expressed as a sum of symmetrical spherical harmonics with appropriate coefficients. Knowledge of these coefficients is the basis of texture analysis and of anisotropy studies. The texture and the structure of the specimen are not homogeneous, so the information on the average texture is important when studying the influence of texture on the anisotropy of certain physical properties. Thus, the texture coefficients should correspond to the overall texture of the sample, and they will be used for the prediction of the macroscopic magnetic properties of the polycrystalline materials.

4.3.1. Texture of grain oriented silicon steels

Grain oriented samples have been measured using the X-ray diffraction technique. The X-ray method is often used in texture studies, but it encounters difficulty when measuring a coarse grained specimen. Reliable statistical texture information requires knowledge of orientation from volumes which contain approximately 10^4 grains (Humbert [39]). In our investigation, ODF analysis was made using the pole figure data obtained from 5 specimens of the same material. This was an attempt to improve statistical accuracy. In the analyzed samples, the average grain size ranged from 0.6 mm to 3.5 mm, and this corresponds to approximately 400 grains from each specimen, and a total of 2000 grains from 5 measurements used to obtain the ODFs. The texture measurements of GO-1A sample, having the largest grain size of approximately 12 mm, was made on a composite specimen containing 125 layers.

Because grain oriented steels display nearly identical preferred orientations, with only slight variations from the ideal (110)[001] orientation, one representative of each quality has been

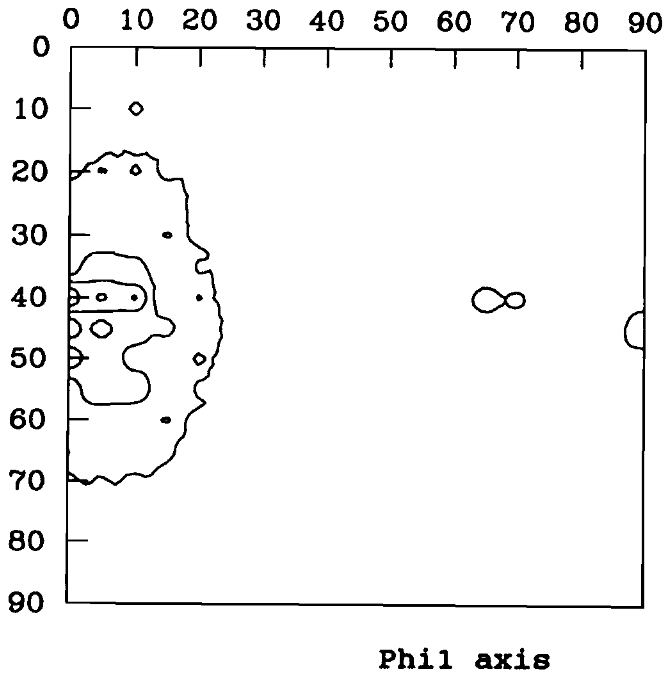

Fig.4.5.a.
ODF Phi2=0° section of sample OR-1A
(contour separation 30 x random)

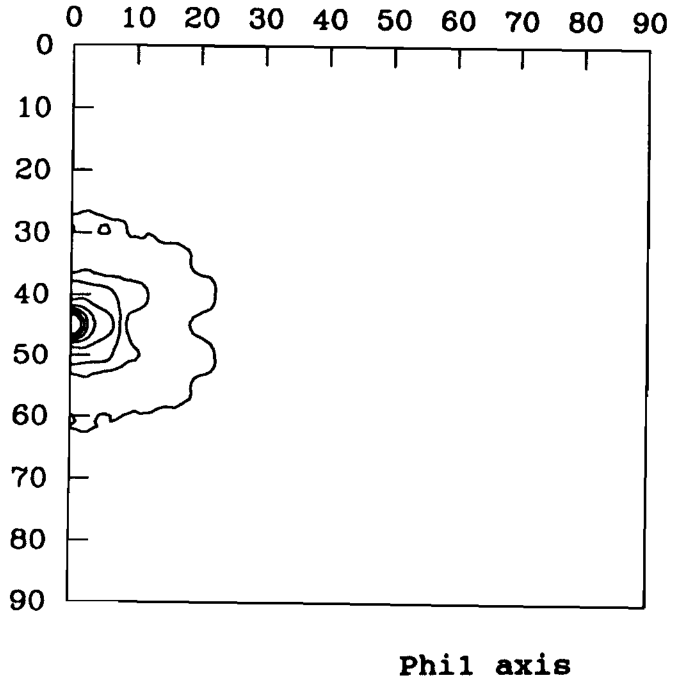

Fig.4.5.b.
ODF Phi2=0° section of sample OR-1B
(contour separation 50 x random)

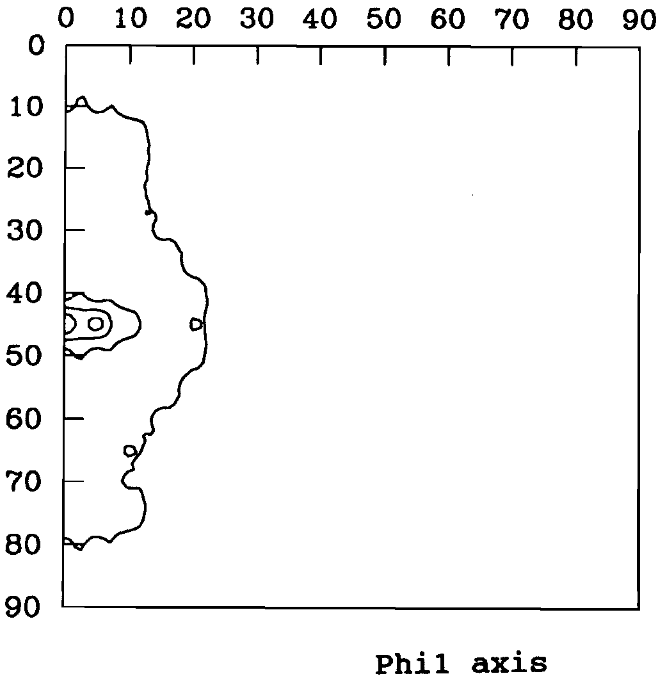

Fig.4.5.c.
ODF Phi2=0° section of sample OR-1C
(contour separation 50 x random)

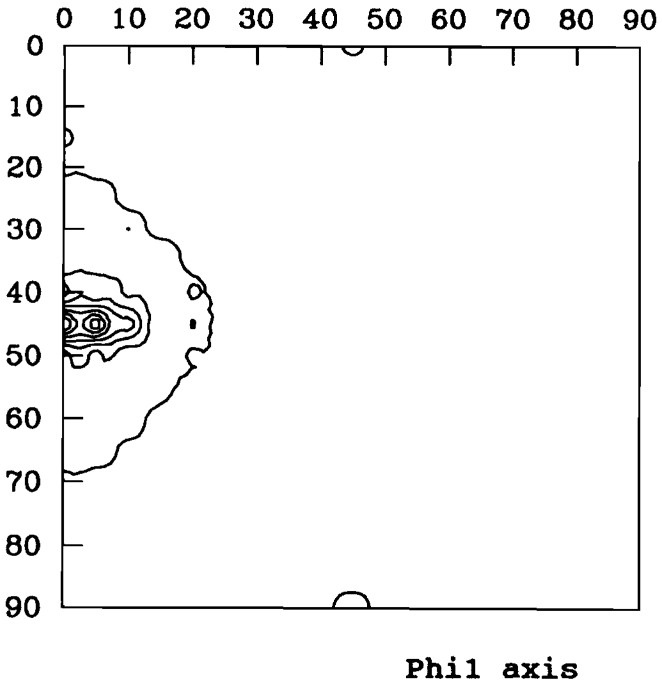

Fig.4.5.d.
ODF Phi2=0° section of sample OR-7A
(contour separation 50 x random)

Table 4.3. Texture coefficients with $l \leq 8$ for grain oriented samples.

Sample	C_4^{11}	C_4^{12}	C_4^{13}	C_6^{11}	C_6^{12}	C_6^{13}	C_6^{14}	C_8^{11}	C_8^{12}	C_8^{13}	C_8^{14}	C_8^{15}
9 mil												
GO 1A	-1.64	-6.34	3.41	5.46	-3.02	-5.89	-4.63	5.22	4.11	6.63	-5.50	3.24
GO 1B	-1.53	-6.55	3.56	5.86	-3.15	-5.95	-4.59	5.07	3.22	7.06	-6.17	3.35
GO 1C	-1.33	-6.09	3.40	5.06	-2.78	-5.05	-4.02	4.28	2.60	5.81	-5.13	2.94
GO 2A	-1.10	-6.04	3.64	4.97	-2.91	-4.80	-4.24	3.16	1.10	5.38	-5.77	3.50
GO 2B	-1.50	-6.47	3.37	5.82	-3.19	-5.43	-3.83	4.92	3.07	6.29	-5.25	2.64
GO 2C	-1.09	-5.70	3.08	4.93	-2.69	-4.18	-3.12	3.31	1.09	4.92	-4.49	2.21
GO 3A	-1.49	-6.53	3.46	5.98	-3.27	-5.56	-4.00	4.94	3.09	6.59	-5.60	2.77
GO 3B	-1.32	-5.66	3.04	4.70	-2.80	-4.51	-3.09	3.49	2.17	4.41	-4.47	2.07
GO 3C	-1.32	-5.95	2.77	5.64	-2.96	-4.28	-2.38	4.31	2.09	5.03	-3.63	1.25
7 mil												
GO 7A	-1.55	-6.49	3.45	5.81	-3.12	-5.68	-4.25	5.12	3.46	6.66	-5.52	2.82
GO 7B	-1.12	-6.04	3.42	5.14	-2.91	-4.78	-3.81	3.37	1.11	5.45	-5.25	2.70
GO 7C	-1.23	-6.21	3.49	5.67	-3.12	-4.98	-3.67	3.93	1.48	5.86	-5.51	2.87

Table 4.4. Texture parameters for grain oriented samples.

Sample	f(goss) (x random)	V(goss)%	I<100> @ RD (x random)	Half-width in-plane angle [deg.]	Half-width out-of-plane angle [deg.]
9 mil					
GO 1A	72.5	79 %	16.6	8.8°	8.1°
GO 2A	46.8	79 %	23.8	7.3°	8.4°
GO 3A	57.9	81 %	9.8	15.7°	11.0°
GO 1B	143.7	82 %	41.1	7.1°	4.2°
GO 2B	61.7	78 %	14.9	13.7°	9.1°
GO 3B	51.8	83 %	18.6	6.8°	5.5°
GO 1C	73.3	77 %	21.9	9.2°	6.6°
GO 2C	68.9	72 %	16.8	11.1°	7.4°
GO 3C	89.7	76 %	17.0	9.6°	5.2°
7 mil					
GO 7A	107.7	72 %	23.7	11.3°	4.8°
GO 7B	77.4	69 %	16.4	13.7°	8.4°
GO 7C	93.6	72 %	34.6	9.2°	4.3°

Fig.4.6.a. In-plane alignment (9 mil specimens)

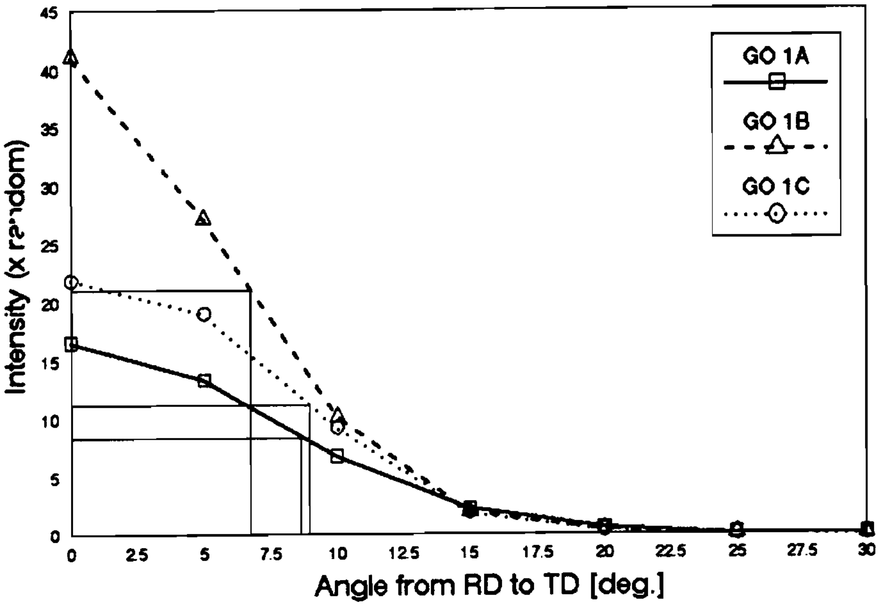

Fig.4.6.b. In-plane alignment (9 mil specimens)

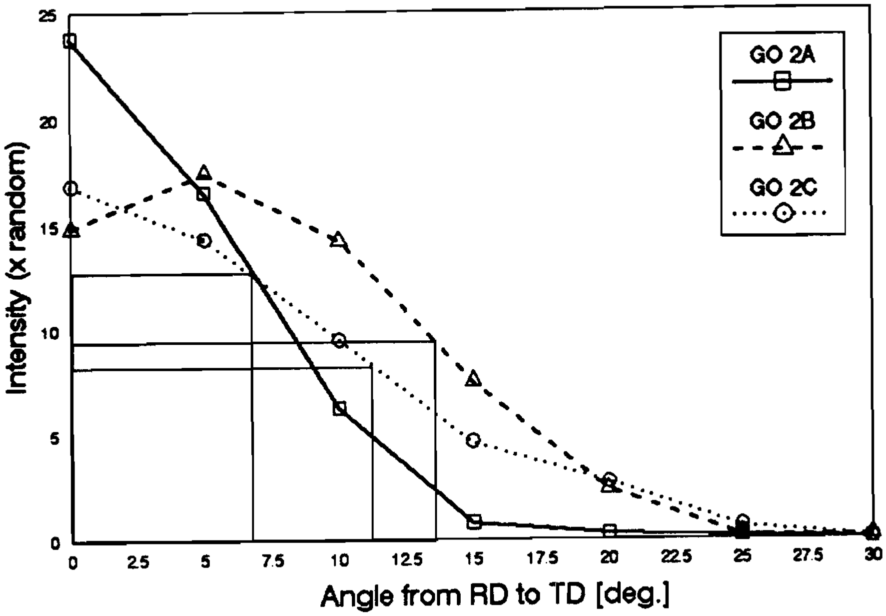

Fig.4.6.c. In-plane alignment (9 mil specimens)

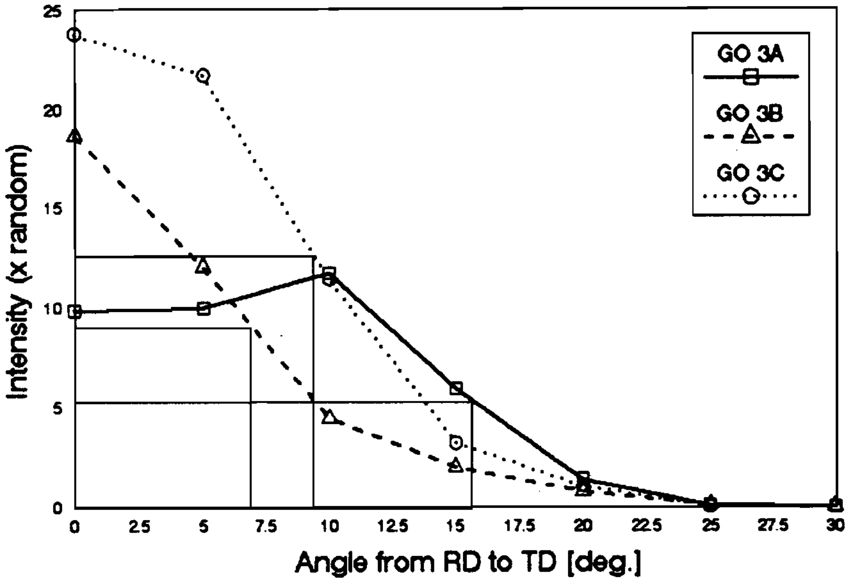

Fig.4.6.d. In-plane alignment (7 mil specimens)

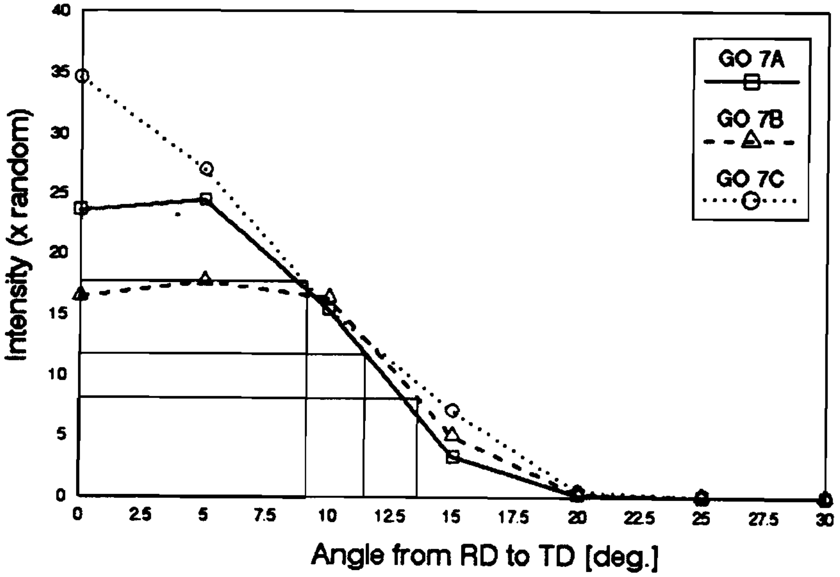

Fig.4.7.a. Out-of-plane alignment (9 mil specimens)

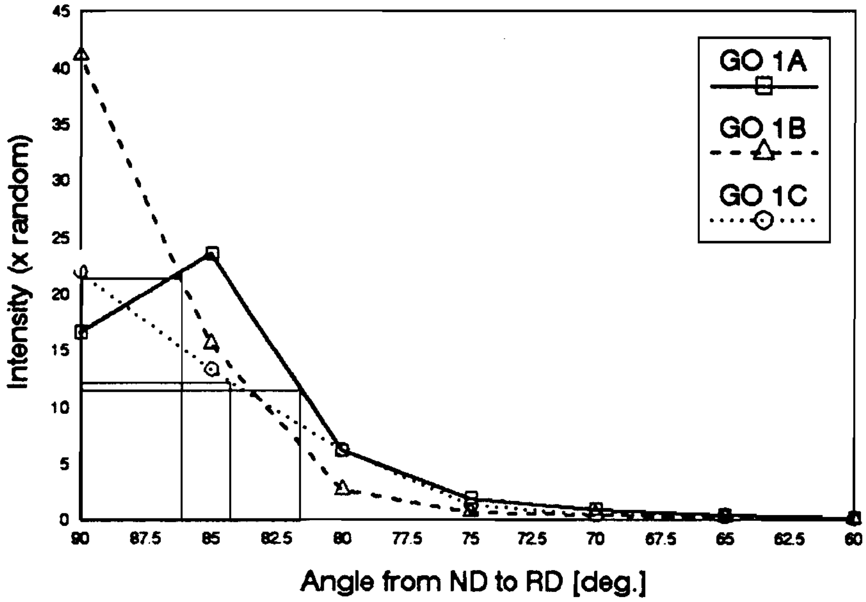

Fig.4.7.b. Out-of-plane alignment (9 mil specimens)

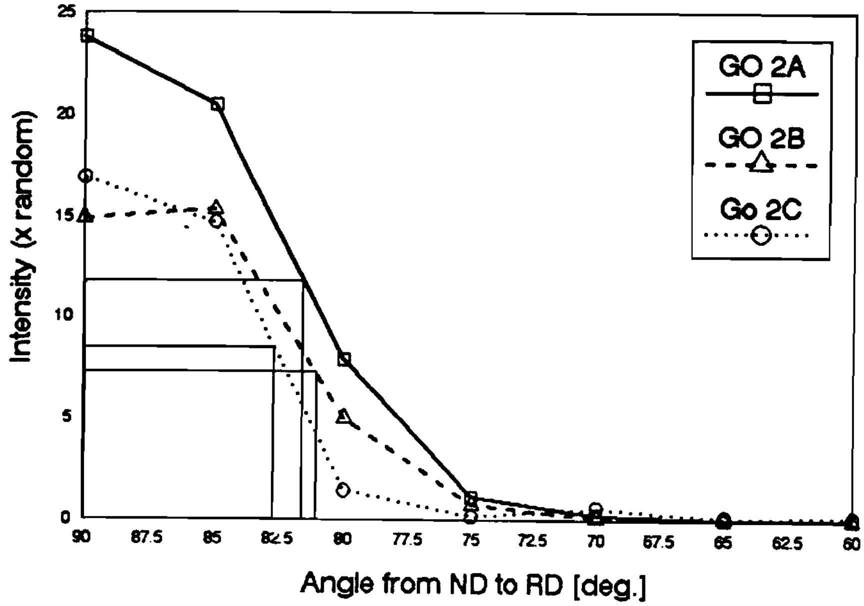

Fig.4.7.c. Out-of-plane alignment (9 mil specimens)

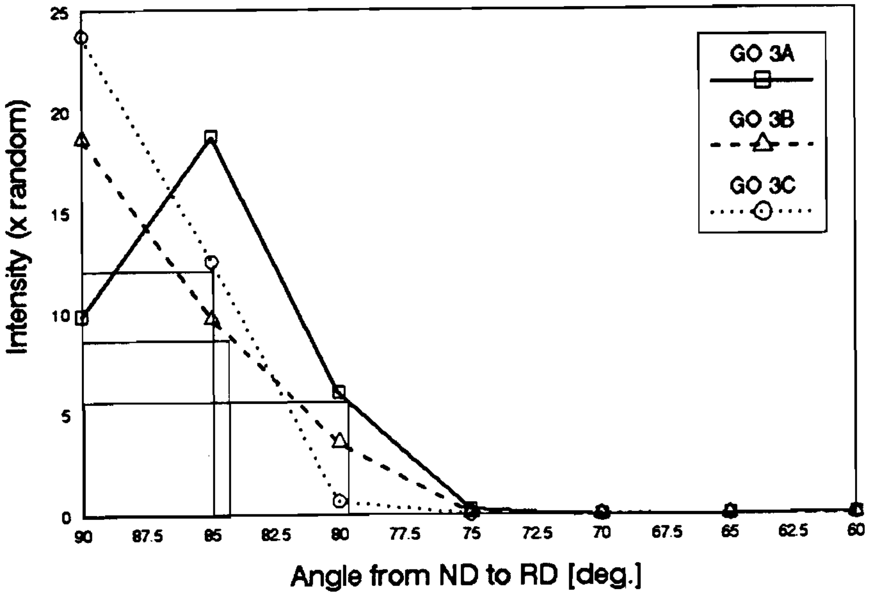

Fig.4.7.d. Out-of-plane alignment (7 mil specimens)

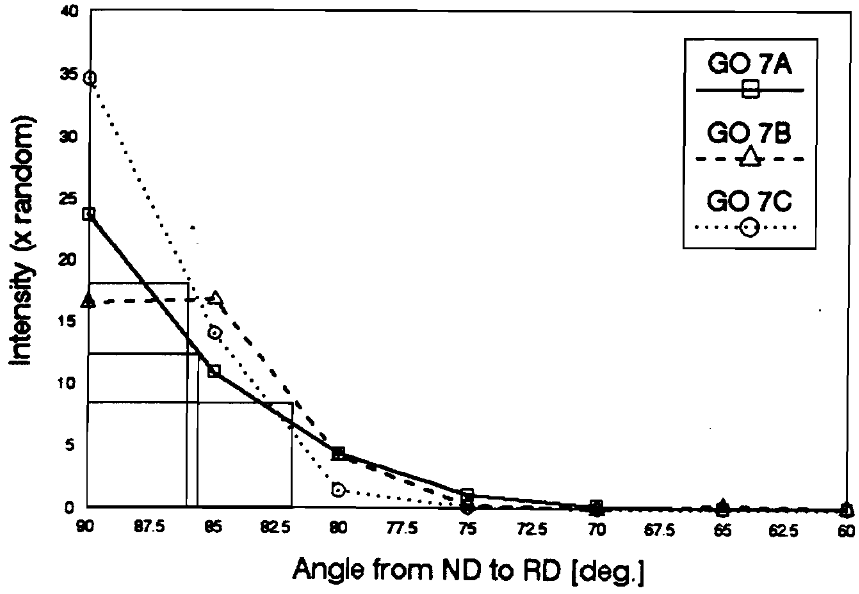

selected. Due to the symmetrical equivalent positions of (110)[001] orientation in Euler space, a concise description of the texture function in these materials is given in the ϕ_2= 45° ODF section. These ODF sections, calculated from the measured textures of one steel of each quality, are shown in Figure 4.5. A more quantitative description of texture is given in terms of texture coefficients which are presented, for $l \leq 8$, in Table 4.3.

The complete (100) pole figures recalculated from the ODF's give information about the alignment of <100> directions around rolling direction. Figure 4.6 (a to d) shows the alignment within the rolling plane (in-plane alignment), while Figure 4.7 (a to d) indicates the out-of-plane alignment. We have marked on each of these figures the angular value corresponding to half of the I<100> intensity observed at rolling direction. This is referred to as the half-width angle. The data obtained from these figures are summarized in Table 4.4. The volume fraction (V%) of (110)[001] orientation for these samples was measured at the Dofasco Research Laboratory, using a method based on torque magnetometry. The ODF intensity at (100)[001] orientation, f(goss), is the average value of ODF intensities within a 5° interval in Euler space around the ideal orientation.

4.3.2. Texture of non-oriented electrical steels

The X-ray texture measurements of non-oriented materials revealed the through-thickness inhomogeneity of grain orientation in these samples. The texture data obtained for different layers is not representative for the whole sample, and, therefore, the texture of non-oriented composite samples was measured using neutron diffraction. The ODFs calculated from the measured texture of temper elongated materials are shown in Figure 4.8. (a to d). These ODFs could be also described using the texture coefficients which, for $l \leq 6$, are displayed in Table 4.5.

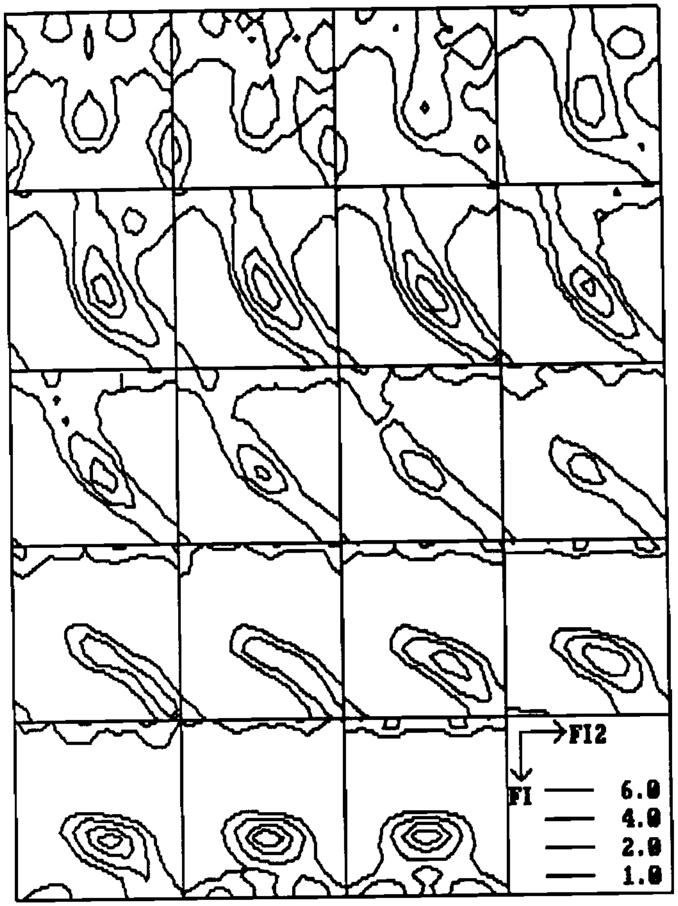

Fig.4.8.a. ODF of 0% elongated sample

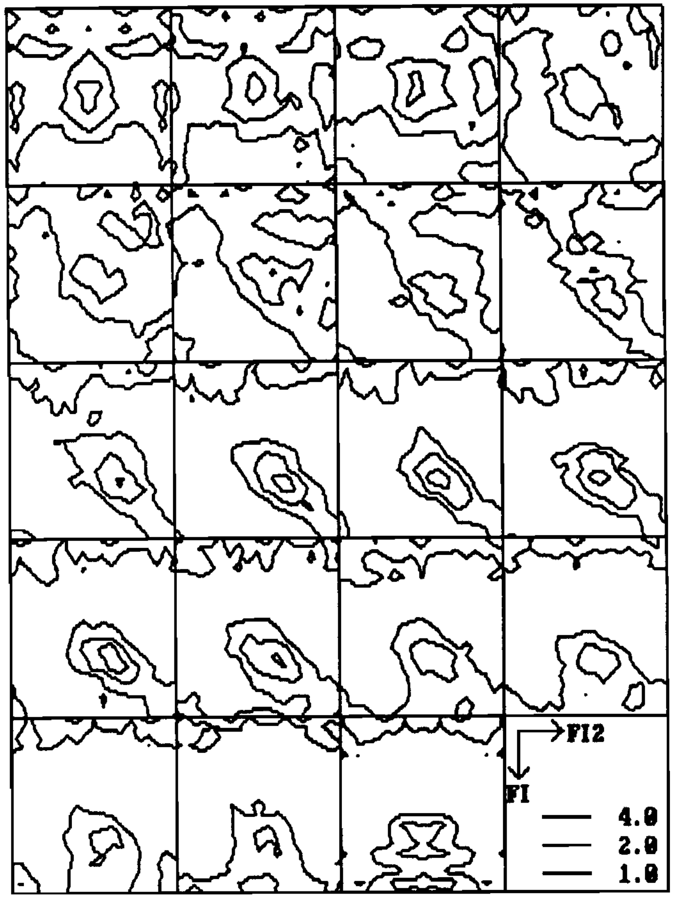

Fig.4.8.b. ODF of 2% elongated sample

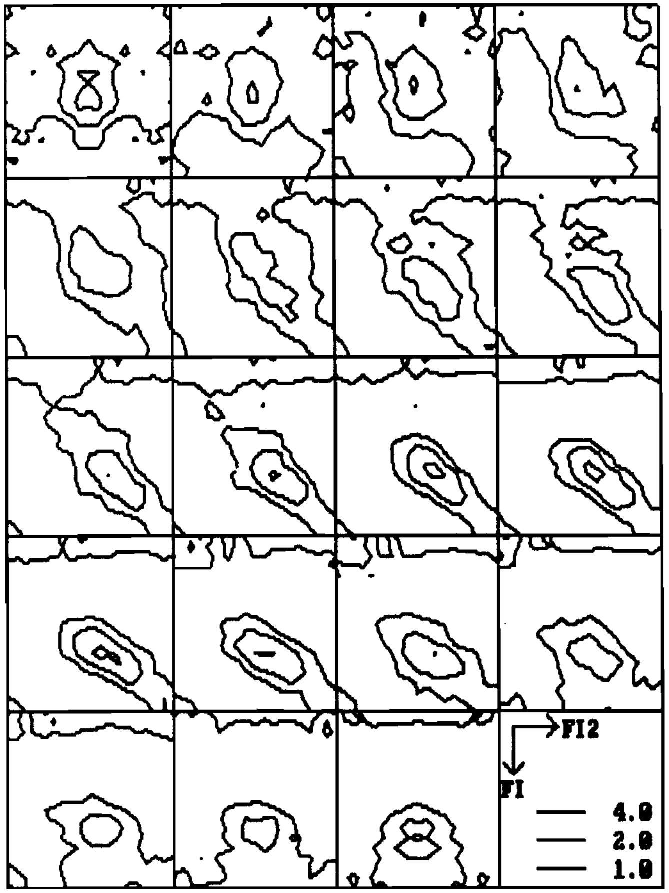

Fig.4.8.c. ODF of 6% elongated sample

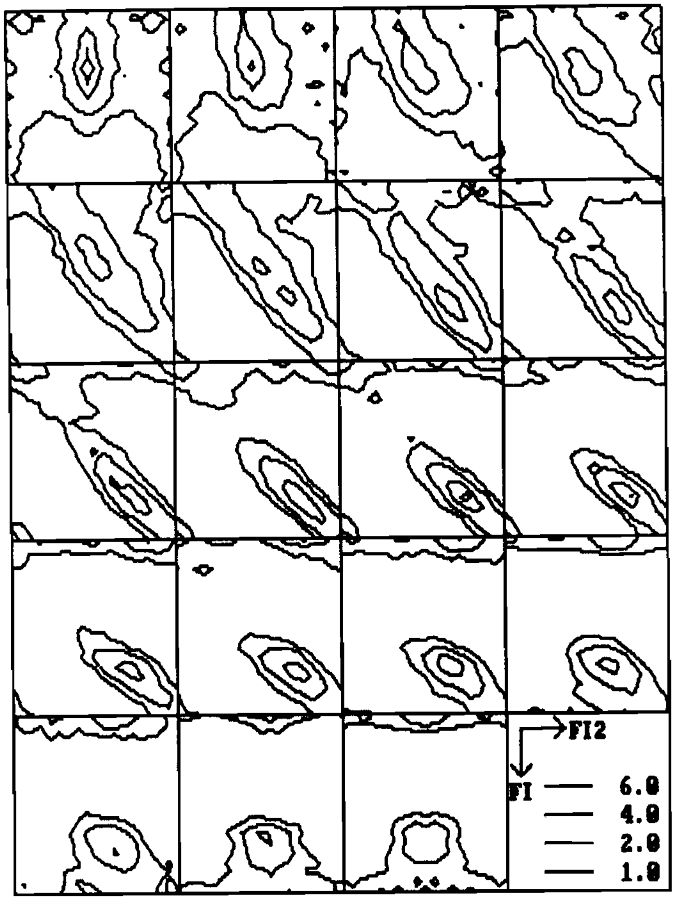

Fig.4.8.d. ODF of 12% elongated sample

Fig.4.9. Skeleton lines of non-oriented samples

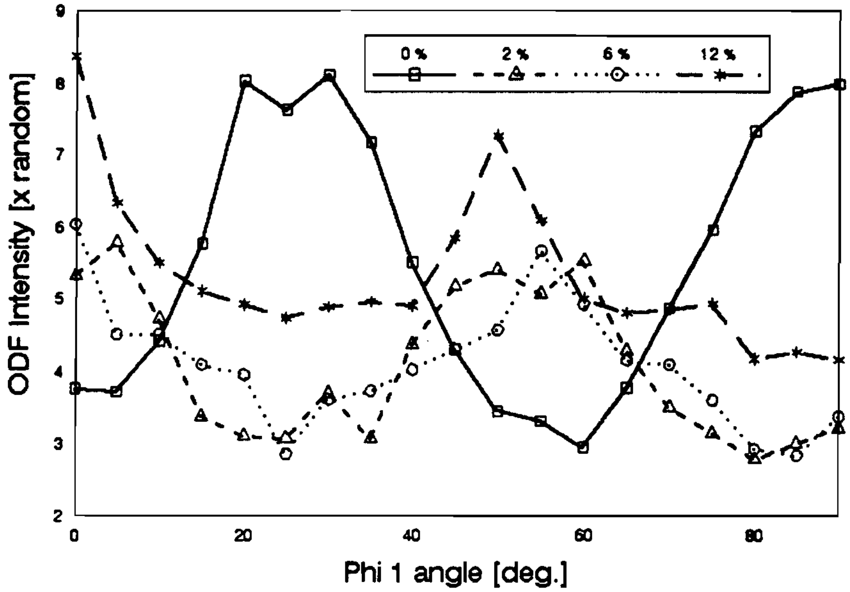

Fig.4.10.a. Miu fibres of non-oriented samples

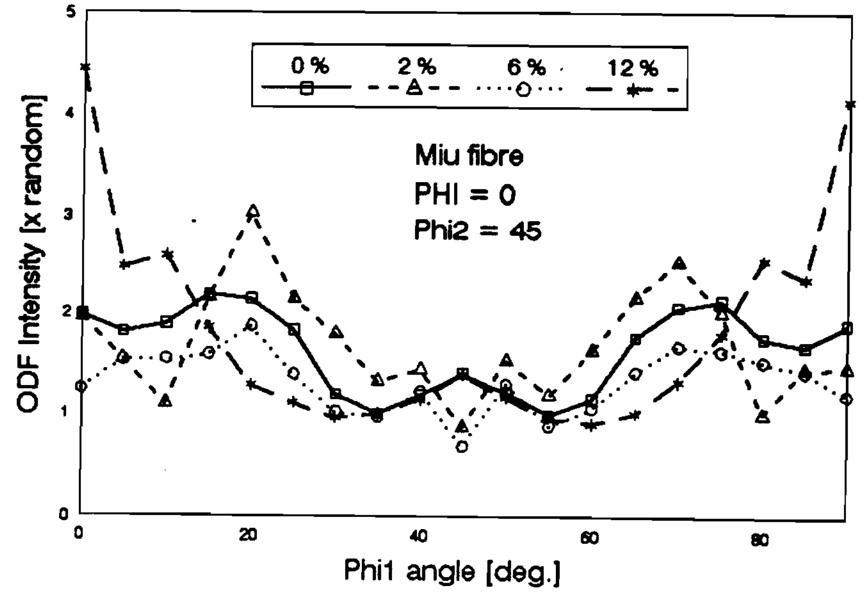

Fig.4.10.b. Gamma fibres of non-oriented samples

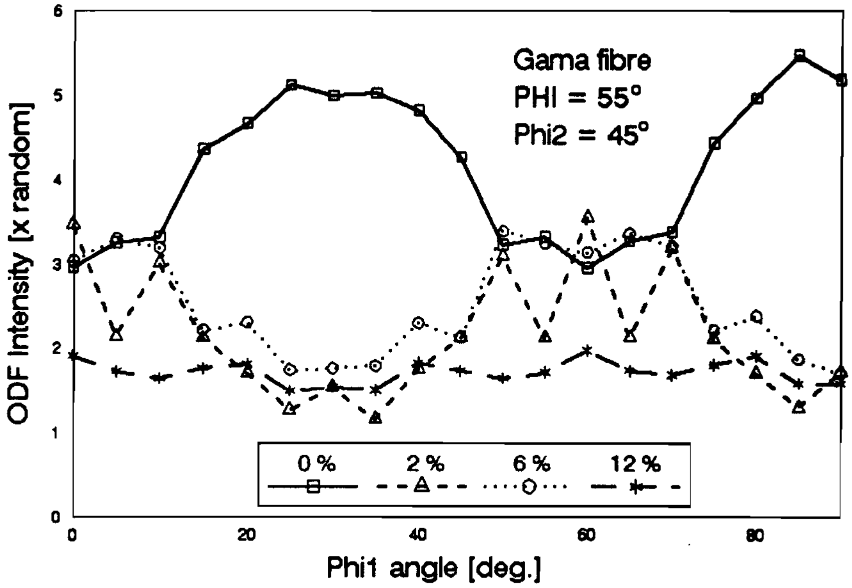

Fig.4.10.c. Alpha fibres of non-oriented samples

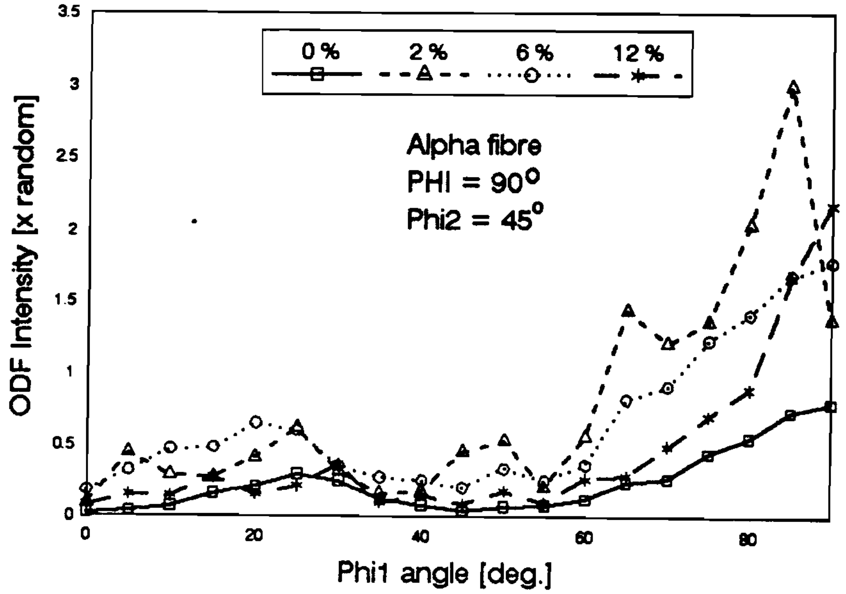

Table 4.5. Texture coefficients of non-oriented materials.

Percent elongation	C_4^{11}	C_4^{12}	C_4^{13}	C_6^{11}	C_6^{12}	C_6^{13}	C_6^{14}
0%	-0.52	-0.97	0.57	-2.23	1.53	-0.41	-1.19
2%	-0.38	-1.12	0.15	-1.06	0.83	-0.24	0.06
6%	-0.49	-0.92	0.11	-1.42	1.09	-0.29	-0.07
12%	-0.08	-1.41	-0.06	-1.40	1.94	-0.73	-0.47

A more detailed description of ODF's can be given in terms of the skeleton line and the fibres. On the skeleton lines plotted in Figure 4.9, one could identify the main texture components. The original 0% temper elongated sample has the grains' preferred orientation around the (111)[1 -2 1] orientation, while all plastically deformed specimens have approximately the (112)[1 -1 0] orientation as the main texture component, but with different intensities. The μ, α, and γ fibres are plotted in Figure 4.10. (a to c).

CHAPTER 5.

METHODS OF CORRELATING TEXTURE AND MAGNETIC ANISOTROPY ENERGY

INTRODUCTION

Magnetocrystalline energy refers to that part of the crystal free energy which is dependant on the magnetization direction relative to the crystallographic axis. For a polycrystalline material, the magnitude of the magnetocrystalline energy reflects the anisotropy of the specimen, and is expressed in terms of texture function (ODF). There are several methods to determine the magnetocrystalline energy. Among them are the analysis of energy required to magnetize the sample in a certain direction, the microwave ferromagnetic resonance, magnetostrictive measurements, and torque magnetometry.

In torque magnetometry, the differential of the magnetocrystalline energy with respect to angle is inferred from the measured torque experienced by a specimen in a magnetic field large enough to magnetize the material to saturation. The instrument used for magnetic torque measurements, data analysis and interpretation are presented in this chapter.

When the magnetic field strength gradually increases toward the value of the saturation field, the magnetization vector rotates toward the direction of the applied field against the magnetocrystalline energy. This is the saturation approach process, and it reflects the magnetic anisotropy of the material. The magnetic torque measured under these conditions provides information about the orientation of the magnetization vector with respect to the easy magnetization direction of the sample. In this chapter, a model-based method is developed to correlate texture and the coefficient representing the contribution of the magnetic anisotropy to the rotation process. The theoretical values of the magnetization rotation process obtained using this model are compared to experimental data. Industrial application of this method is also suggested.

5.1. CONSTRUCTION OF A TORQUE MAGNETOMETER

5.1.1. Basic principles of torquemagnetometry

In this paragraph, the torque magnetometer designed and built as part of this academic project is described. This instrument was used to investigate the correlation between texture and magnetic anisotropy energy of the material in two cases: where the magnetization is forced to line up with the applied magnetic field strong enough to saturate the sample, and where the magnetization is gradually rotated toward the direction of the field.

The sample measured is shaped in the form of a disc. Assuming that the magnetization and the magnetic field make angle η and η_0 with a coplanar easy magnetization direction in the sample, the energy density is composed of the magnetic anisotropy of the sample E_a, and the energy E_H, due to the presence of the field:

$$E = E_a + E_H = E_a - HI_s \cos(\eta_0 - \eta) \tag{5.1}$$

where I_s is the saturation magnetization of the sample.

At equilibrium, the torque per unit volume due to the magnetic field H acting on the sample is balanced by the torque created by the magnetocrystalline energy:

$$\frac{\partial E}{\partial \eta} = 0 = -I_s H \sin(\eta_0 - \eta) + \frac{\partial E_a}{\partial \eta} \tag{5.2}$$

Magnetic torque is measured by suspending the sample from a torsion wire in a magnetic field which causes magnetic saturation. The torsion constant of the suspension wire is known. The torque acting on the sample in the direction normal to the plane of relative rotation between the sample and applied magnetic field is recorded versus field angle.

The instruments used for these measurements are known as torque magnetometers. There exist a large variety of such devices, all of which are homemade, and their design varies from one laboratory to the other. Depending on the material under investigation, any particular measurement requires its own instrument. When constructing new equipment, one must consider the following factors which influence the choice of instrument:

(A) <u>physical dimensions of the magnetic sample</u>: These dictate the sensitivity and the dimensions of the torque magnetometer, namely the size and the shape of the sample, and the probable anisotropy. The sample volume is imposed by the material thickness and the electromagnet gap. The anisotropy factor is given by the cubic anisotropy constants, and by the material texture. Based on texture data, the values of the effective anisotropy constants for the two classes of electrical steels, oriented and non-oriented, were in the range 10^2 to $3 \cdot 10^4$ J/m^3 (10^3 to $3 \cdot 10^5$ dyne-cm/cc). Using samples of volume 10^{-2} to 10^{-3} cm^3, an instrument with sensitivity in the range 10^{-6} - 10^{-4} N-m (10 to 10^3 dyne-cm) was found to be suitable.

(B) magnetic field value: This is determined by the necessity to saturate the sample. The magnetic saturation is achieved by rotating the magnetization vector towards the direction of the applied magnetic field against the magnetocrystalline energy E_a. In order to rotate the magnetic moments, the magnetic field must be higher than a certain value called the anisotropy field of the material. The fictitious anisotropy field is parallel to the easy magnetization direction of the specimen and of magnitude that it exerts the same torque on magnetization as the crystal anisotropy itself. For cubic crystals having positive anisotropy constants like iron, the anisotropy field derived by Chikazumi [9] is:

$$H_{anisotropy} = 2\ K_1/I_s$$

where I_s is the saturation magnetization.

This requirement is easily fulfilled by a typical electromagnet with a pole face diameter of 5.5 cm which produce fields of 1.5 T (15 kG) in a 2.5 cm gap. These fields are adequate for torque measurements on most soft magnetic materials, including electrical steels.

5.1.2. Description of the constructed magnetometer

The instrument described here is based on the one developed by Aldenkamp, Marks and Zijlstra [46] with which torque measurements up to 10^{-2} N-m were performed. The transducer shown in Figure 5.1 is made from two circular discs which are attached to each other by three symmetrically placed flat springs. In this arrangement, the transducer is highly sensitive to twisting, but shows great resistance to bending. In the present design, the specimen is placed in a rotating field at the end of a rod attached to the lower disc, while the upper disc is rigidly screwed. The displacement of the two discs, relative to each other, is detected by a cross-coil mutual inductance of direct angular sensitivity.

This transducer was chosen because:

- instrument sensitivity can be varied from 10^{-6} - 10^{-4} N-m
- mechanical construction ensures the robustness in operation

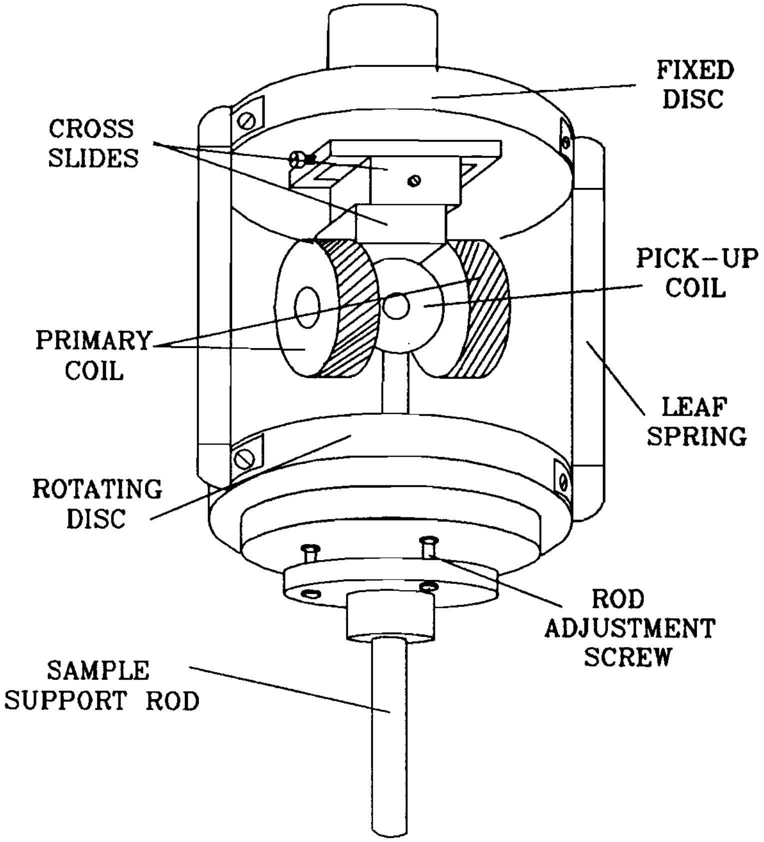

Fig.5.1. Torquemeter head

- it is easy to calibrate because the torsional constant is fixed
- the collected data can be processed automatically using a personal computer.

The design of this instrument imposed some limitations on its sensitivity. Mechanical sensitivity is limited by the large moment of inertia of the lower disc. Electronic sensitivity is limited by the elastic after effect in the transducer.

A block diagram of the electronics is illustrated in Figure 5.2. The instrument operates automatically using a computer controlled Lock-in Amplifier. The transducer coil system is driven by the Lock-in Amplifier internal oscillator. The cross-coil transducer produces a signal having a phase and amplitude proportional to the applied torque. The Lock-in Amplifier links this signal to the signal supplied by the position potentiometer on the magnet base. These two signals constitute one set of data, and are recorded by the computer. The magnet is rotated automatically by a DC motor electronically controlled.

5.1.3. Mechanical details of the magnetometer

The leaf-springs were made of brass and of dimensions 10 mm x 75 mm x 0.2 mm. The lower disc was 10 mm in thickness and made of plastic, producing a low moment of inertia; its diameter was 7 cm. This dimension, together with the leaf-spring elastic constants and dimensions, dictate the transducer torsional constant according to the equation due to Birss and Shepherd [47]:

$$K = \frac{\theta[rad]}{T[N\text{-}m]} = \frac{l_e^3}{6ESb^2R^2} + \frac{l_e}{M_s S(a^2+b^2)} \tag{5.3}$$

where E is the Young's modulus, M_s the shear modulus, S the cross-sectional area of the springs, 2a their width, 2b their thickness, l_e their effective length, and R the distance of their centres from the suspension axis.

The primary coils of the transducer were mounted on a cross-

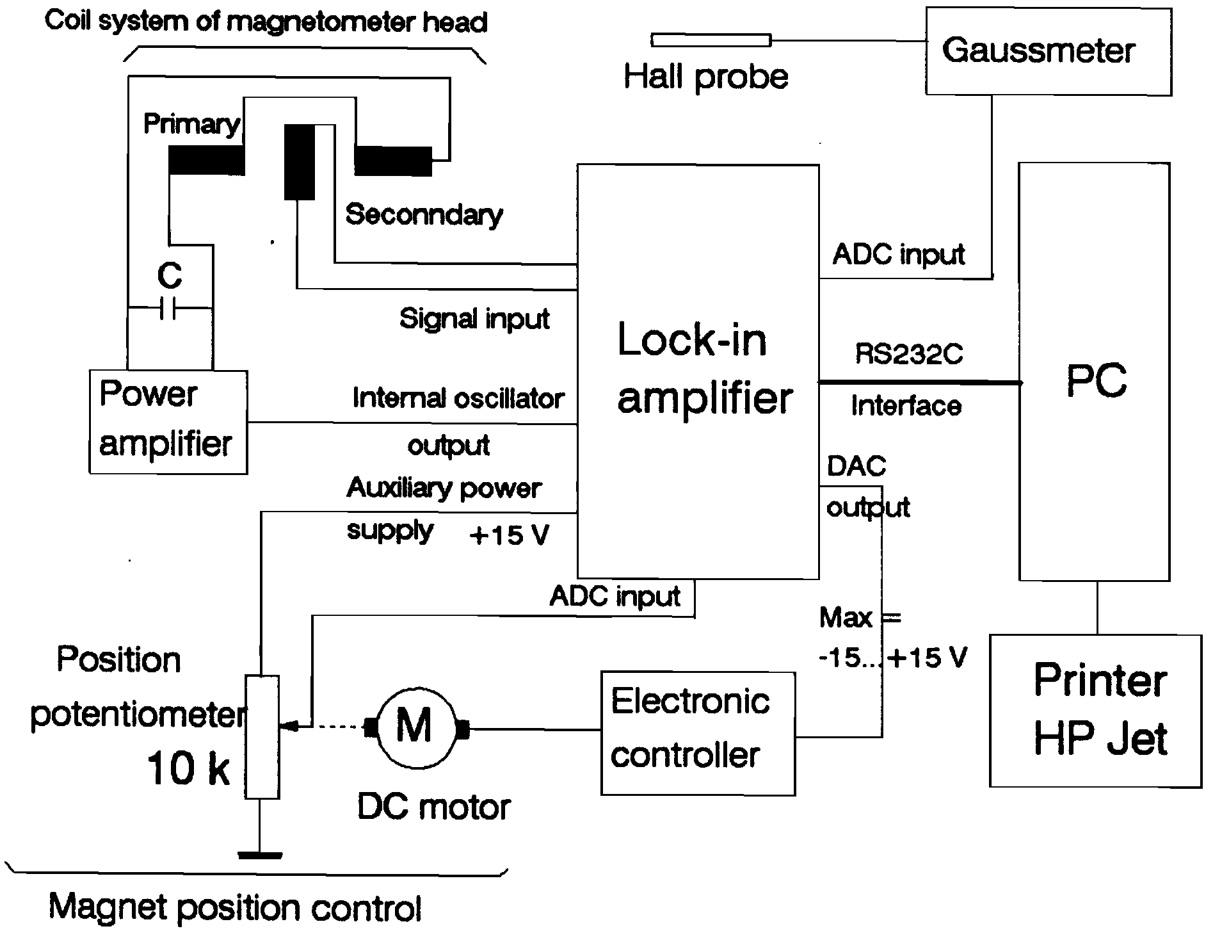

Fig.5.2. Electronic diagram of the torque magnetometer

slide combination, as shown in Figure 5.1. Thus, the pick-up coil was accurately centred, minimizing the artificial signal when no torque was applied.

The sample support rod was made of glass pipe 6 mm in diameter having a length of approximately 30 cm. The sample was glued on a plastic end-piece attached to the rod, and this rod was attached to the transducer by an adjustable plastic mount. Three brass screws symmetrically disposed around the base allowed adjustment of the rod orientation. With these screws one can fix the central position of the sample on the rotation axis of the magnetometer.

5.1.4. Electrical details of the magnetometer

For this application, we used the EG&G PARC Model 5210 Two-Phase Lock-in Amplifier. The signal measured by the instrument is made to appear at a reference frequency. The signal is then amplified and applied to a phase-sensitive detector operated at the reference frequency. Because of the phase-sensitive detector frequency translation effects, the result is a detector output that includes a value representing the amplitude of the signal of interest, as well as AC components which may be due to noise. The AC resulting from the noise is then reduced to any arbitrary degree by low pass filters. This instrument has four auxiliary Analog-to-Digital Converter (ADC) Inputs which allow voltages in the range of ±15 V to be applied, digitized, and stored internally. It also has one Digital-to-Analog Converter (DAC) Output having a full scale of ±15 V. The provision of both RS232C and IEEE-488 GPIB interfaces allows one to control all of the functions of the Lock-in Amplifier from an external computer.

The transducer coil system has two primary coils consisting of 3000 turns of 0.1 mm copper wire and the pick-up coil consisting of 4500 turns of 0.02 mm copper wire. The primary coils were operated in resonance using a 0.01 μF capacitor. They were fed with a 1500 Hz signal supplied by a power amplifier which buffers the output of the Lock-in Amplifier internal oscillator. The power amplifier did not reverse the phase of the input signal, therefore, the primary signal had the same phase as the signal generated by the internal oscillator.

The induced signal in the pick-up coil had an amplitude proportional to the rotation of the lower disc. Depending on the sense of rotation, the phase of this signal was either +180° or -180° relative to the phase of primary signal. Thus, if the secondary signal was fed to the Lock-in Amplifier and the internal oscillator used as a reference, a DC output proportional to the magnitude and sense of the torque was obtained.

The magnet position was controlled using a potentiometer attached to the magnet turning table. The potentiometer was of ten-turns type, having a resistance of 10 kΩ and constant linearity (2%). It was fed with 15 V by an auxiliary power supply available as output at Lock-in Amplifier. The DC signal provided by the potentiometer was applied to one of the ADC Inputs to be read by the computer. To improve the angular resolution, instructions were included within the software which read the position potentiometer voltage before and after recording the torque signal. The actual angular position for the given torque was the average position voltage obtained.

The magnet was rotated automatically. The DC motor which moved the magnet turning table was driven by an electronic controller. The sense and velocity of rotation was set by software via DAC auxiliary output.

The electromagnet was constructed by Walker Scientific Inc., and was of conventional design. The coils wound on the tapered pole pieces were water cooled, and the DC power supply provided 70 V and an adjustable current from 0 to 35 A. The field obtained with a pole-piece gap of 3 cm and maximum power dissipation of 2.5 kW was approximately 1.6 T.

5.1.5. Software used to operate the instrument

The torque magnetometer works automatically. All the operations needed for data acquisition are implemented by the Lock-in Amplifier which, in turn, is fully controlled by an external PC. To operate the instrument, a computer program was written which performs the following tasks:

- interfaces the computer and the Lock-in Amplifier
- brings the magnet to initial (arbitrary) position
- set the sense and velocity of magnet rotation for measurement
- rotates the magnet 360° clockwise or counter-clockwise
- reads the angular position and the torque value with step 10°
- Fourier analyses of the raw data
- displays the experimental torque curve on the screen
- saves the collected data for subsequent analysis.

This program was written for data acquisition only. The raw data was then corrected for errors and analyzed using another computer program. The corrections which were introduced are discussed in the next section.

5.1.6. Analysis of experimental results

In the mathematical formula describing the magnetic anisotropy energy, the energy is expressed in terms of the angle of magnetization, rather than the angle of the external applied field. The theoretical magnetic torque, as the derivative of the magnetic anisotropy energy, is also expressed in terms of the angle of magnetization. When the magnetic torque is measured, the experimental data are recorded as a function of the angle of the external field. The magnetization direction may lag behind the magnetic field direction with the result that each point on the experimental torque curve is slid or 'sheared' from its actual position. Thus, the first stage in the treatment of the experimental data is to convert the experimental curves of torque versus angle of applied field to curves of torque against magnetization direction.

The experimental curve can be corrected if the sample magnetization and applied field are known. From equation (5.2) one obtains:

$$\eta_0 - \eta = \sin^{-1}\left(\frac{L}{HI_s}\right) \tag{5.4}$$

where $(\eta_0-\eta)$ is the angle between field and magnetization. $(\eta_0-\eta)$ can be computed for each point of experimental torque which can then be replotted against the magnetization direction.

Another problem arising in any torque experiment is that the strength of the true field H is not equal to that of the applied field H_a, due to the demagnetizing field ΔH, determined by the magnetization and dimensions of the specimen. The demagnetizing field ΔH parallels the sample magnetization, and adds vectorially to H_a, forming the true field H. In the first approximation, for small angle $(\eta_0-\eta)$, the component of ΔH along H_a was subtracted from H_a giving:

$$H = H_a - \Delta H \cos(\eta_0-\eta) = H_a - \frac{N_d I_s}{\mu_0}\cos(\eta_0-\eta) \tag{5.5}$$

where N_d is the sample demagnetizing factor in the magnetization direction.

Thus, the experimental torque curve was corrected from the 'sheared' and demagnetizing field errors by numerically solving the equation having the unknown η:

$$\begin{aligned} L(\eta) &= HI_s\sin(\eta_0-\eta) = \\ &= H_a I_s \sin(\eta_0-\eta) - \frac{1}{2\mu_0} N_d I_s^2 \sin 2(\eta_0-\eta) \end{aligned} \tag{5.6}$$

for each point η_0 . The torque curve was then replotted versus η.

The next step in the treatment of experimental data is separating the components of the corrected torque curve caused by the sample texture from those caused by the systematic errors in the torque measurements. A common method used is based on the Fourier analysis of the data:

$$L(\eta) = \frac{a_0}{2} + \sum_{n=1}^{N}[a_n\cos(n\eta) + b_n\sin(n\eta)] \tag{5.7}$$

with the coefficients a_n, b_n given by:

$$a_n = \frac{2}{K}\sum_{k=0}^{K-1} L_k \cos(2\pi kn/K)$$
$$b_n = \frac{2}{K}\sum_{k=0}^{K-1} L_k \sin(2\pi kn/K) \tag{5.8}$$

where K is the number of torque readings.

Torque is generally expressed in terms of sine functions:

$$L(\eta) = \frac{a_0}{2} + \sum_{n=1}^{N} A_n \sin n(\eta - \alpha_n) \tag{5.9}$$

where:

$$A_n = (a_n^2 + b_n^2)^{\frac{1}{2}}$$
$$\alpha_n = \tan^{-1}\left(\frac{a_n}{b_n}\right) \tag{5.10}$$

This formula corrects the systematic error caused by the misalignment of the sample easy magnetization direction from the zero direction of the magnetic field.

In practice, the Fourier terms are influenced by irrelevant torques which may be related to the following factors:

(A) Position of the sample in the magnet. If the centre of the sample does not coincide with the axis of the magnetometer, parasitic effects of period π and 2π may be observed.

An additional error is introduced by a non-horizontal disc shaped sample, whose diameter makes a small angle α_0 with the external field. The free magnetic poles on the disc surfaces tend to keep the magnetization lying in the plane, thereby introducing torque having a $\sin(2\eta)$ type variation, as derived by Phillips and Shephard [48]:

$$L = -I_s H\,(1 - \cos\alpha_0)\, sin2\eta \tag{5.11}$$

(B) Shape effects in sample. The shape anisotropy of the sample may generate additional torque. For a sample of arbitrary shape placed in a saturating magnetic field, the shape anisotropy energy contains harmonic terms, depending only on the second power of the magnetization direction cosines. Thus, the torque produced by the shape anisotropy introduces only terms in $\sin(2\eta)$, where η gives the direction of the magnetization relative to a reference direction in the sample. As an example, an elliptical disc having an elongation of a diameter by amount ε and the thickness to diameter ratio R, produces a torque per unit volume given by the following expression [48]:

$$L = \frac{3}{16}\mu_0 I_s^2 \pi R \varepsilon \sin 2\eta \qquad (5.12)$$

(C) Instrumental errors. These errors are always present and usually can be detected by making torque measurements in the absence of the sample. In case of the constructed instrument, such an error is caused by the mechanical hysteresis which is due to elastic after-effect in the leaf-springs of the magnetometer head. The mechanical hysteresis modifies the harmonic content of a particular set of torque curves if these curves are obtained by clockwise or counter-clockwise rotation of the magnet. To account for the elastic after-effect, both clockwise and counter-clockwise torque curves were recorded for the same sample. The curve corrected for the mechanical hysteresis was the average between these two curves. This correction is particularly important in torque measurements of materials with low magnetic anisotropy, such as non-oriented steels. As a result of the artificial torques which appear during the measurements, only the A_4 and A_6 terms are expected to be unaffected by experimental error, and can therefore, be used for further analysis.

5.1.7. Calibration of the instrument

The calibration of the torque magnetometer was made gravimetrically. The magnetometer was deflected with a known torque produced by a weight which was attached to the lower suspension using a rod of known length, as shown in Figure 5.3. The applied torque varied between 0 and $9 \cdot 10^{-4}$ N-m, and the voltage output

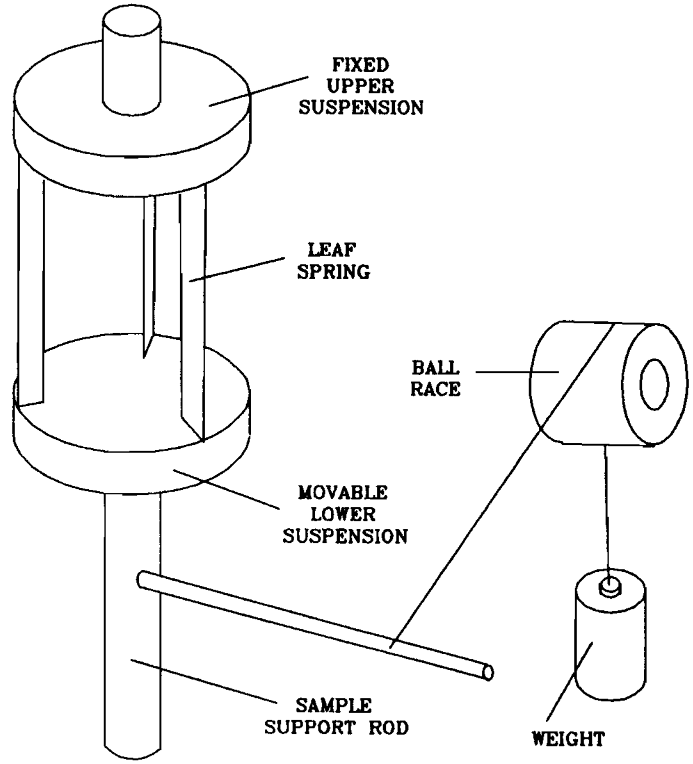

Fig.5.3. Calibration method

measured with the voltmeter of the Lock-in Amplifier. The resulting graph is shown in Figure 5.4. From this graph, the magnetometer calibration factor is:

$$\alpha_{mag} = (0.54 \pm 0.01)\ N\text{-}m/V \tag{5.13}$$

A test was then performed on a standard sample which was a disc shaped 3% Si-Fe single crystal having (110)[001] orientation, 1 cm in diameter, and 0.20 mm thickness. The literature states that the anisotropy constants of 3% Si steels have values lying in a large interval. For K_4, the range is from $28.0 \cdot 10^3$ $J \cdot m^{-3}$ (Cullity, [49]) to $38.0 \cdot 10^3$ $J \cdot m^{-3}$ (Benford, [50]), while for K_6, the values are more questionable. In Cullity [49] its value is $+10.0 \cdot 10^3$ $J \cdot m^{-3}$, but very accurate measurements performed by Benford [50] on a single crystal having (111)[121] orientation gives the value $K_6 = -7.2 \cdot 10^3$ $J \cdot m^{-3}$. Following our torque measurements on the 3% Si-Fe single crystal, we found that the torque curves are best fitted using the values: $K_4 = 36.0 \cdot 10^3$ $J \cdot m^{-3}$ and $K_6 = -6.0 \cdot 10^3$ $J \cdot m^{-3}$. These values of anisotropy constants were used in further calculations, and the single crystal specimen was used as a standard sample to calibrate the instrument, when necessary.

5.2. RESULTS OF MAGNETIC TORQUE MEASUREMENTS

Discs were punched from each material sheet to produce the samples used in magnetic torque measurements. For grain oriented materials the discs were 1.5 cm in diameter, while for non-oriented steel, where the grain size is much smaller, discs of 1.0 cm in diameter were used. To eliminate the parasitic free magnetic poles which could appear, the edges of the discs were carefully polished.

The magnetic anisotropy measurements were conducted using the torque magnetometer presented in the previous paragraph. Samples were attached to the magnetometer holder using glue, and all torque measurements were made at a single magnetic field strength of 1.4T. The field was determined using a gaussmeter produced by Walker

Fig.5.4. Torquemeter head calibration curve

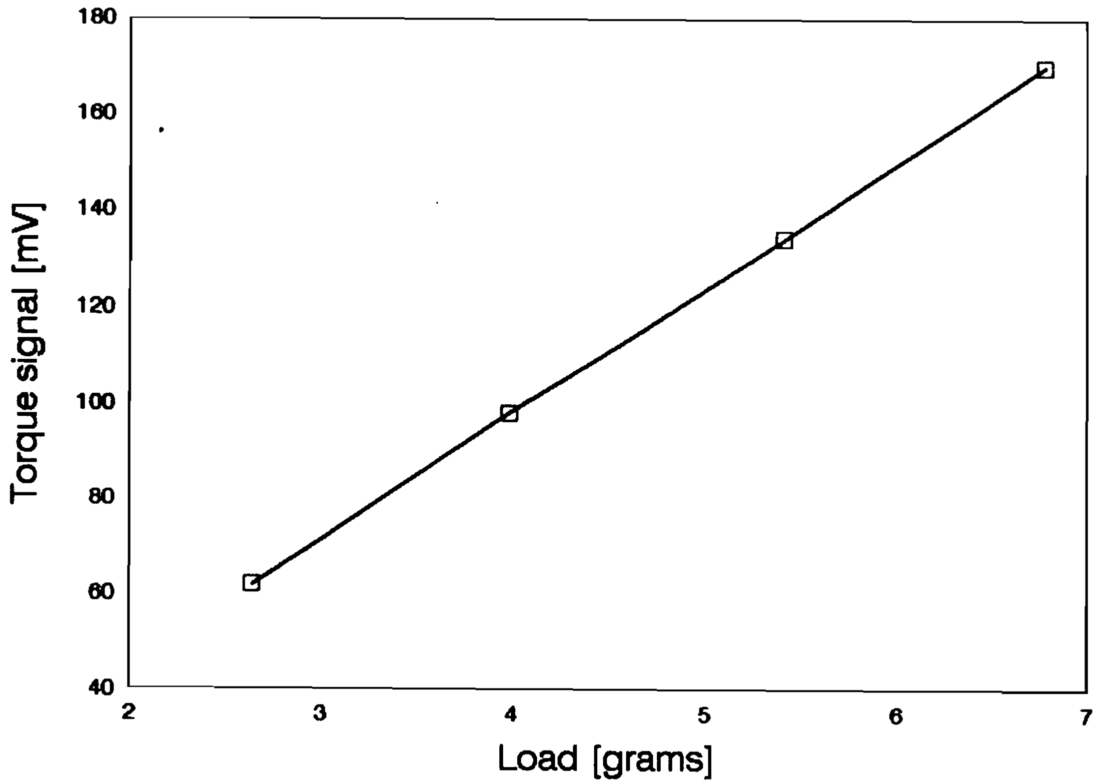

Scientific Laboratories. The magnetic field transducer was a calibrated Hall probe which was applied to the central homogeneous region of the field of interest.

For one set of data, the electromagnet was rotated 360° clockwise and counter-clockwise, starting from an arbitrary position. The torque data were recorded every 10°, and the resulting clockwise and counter-clockwise torque curves were averaged to correct for elastic after-effect. Then, the experimental data were corrected for non-ideal magnetic behaviour (shear and demagnetizing corrections). As a result of the applied corrections, the torque data are a function of the magnetization direction, and the angular interval between two successively recorded data will be different from 10°. Thus, the Fourier analysis of the harmonic content solved a linear system of equations (5.7) for data spaced unevenly along the abscissa. The first eight harmonics were determined as an average of the values obtained for each of the three torque curves. In the case of the textured specimen exhibiting orthorhombic sample symmetry, the Fourier series contained only even-η terms of order, less or equal to six.

In order to reject parasitic effects in the torque curve, the phase of each harmonic of interest, with respect to the easy magnetization direction, was examined, and only that component having a node at the easy magnetization direction of the sample was used in torque analysis. The harmonics which are out of phase with the easy axis cannot be legitimate since they do not reflect the orthorhombic sample symmetry. The procedure used to correct for the phase errors was the following:

First, the torque was expressed in terms of sine functions:

$$L(\eta) = A_2 \sin 2(\eta+\alpha_2) + A_4 \sin 4(\eta+\alpha_4) + A_6 \sin 6(\eta+\alpha_6) \qquad (5.14)$$

where α_2, α_4, and α_6 are the magnitudes of the misalignment with respect to the easy direction or phases of the corresponding harmonic. They were introduced because the torque measurements started from an arbitrary position, which differed from the easy direction. For an ideal curve, they should be equal:

$$\alpha_2 = \alpha_4 = \alpha_6 \tag{5.15}$$

For a real torque curve, they may have different values. One of these values must be chosen as a reference, representing the angle between the easy direction of the sample and the direction of magnetization at the starting position. Usually, the reference is taken the phase of the fourth harmonic component, α_4, on the basis that this component is the lowest order harmonic not affected by systematic errors. Relation (5.14), therefore, becomes:

$$\begin{aligned} L(\eta) &= A_2\sin 2(\eta+\delta_1) + A_4\sin 4\eta + A_6\sin 6(\eta+\delta_2) = \\ &= A_2\sin 2\eta\cos\delta_1 + A_4\sin 4\eta + A_6\sin 6\eta\cos 6\delta_2 + \textit{other terms} \end{aligned} \tag{5.16}$$

where $\delta_1 = \alpha_2 - \alpha_4$ and $\delta_2 = \alpha_6 - \alpha_4$ are the phase errors. Therefore, the corrected Fourier components are:

$$\begin{aligned} A_2^* &= A_2 \cos\delta_1 \\ A_4^* &= A_4 \\ A_6^* &= A_6 \cos\delta_2 \end{aligned} \tag{5.17}$$

Examples of the torque curves produced by the magnetometer are given in Figures 5.5 and 5.6. Figure 5.5 (a to c) shows the experimental (continuous lines) and the corrected (square marks) torque curves for the first three grain oriented samples (OR-1A, OR 1B and OR-1C). As these two curves practically coincide, it can be concluded that the field of 1.4 T used throughout the present investigation was strong enough for producing the single domain state in the samples. Figure 5.6 illustrates the experimental torque curves of the non-oriented samples.

The harmonic components of the torque curves normalized to the volume of the sample are presented in Table 5.1 for the grain

Fig.5.5.a. Torque curve of sample OR-1A

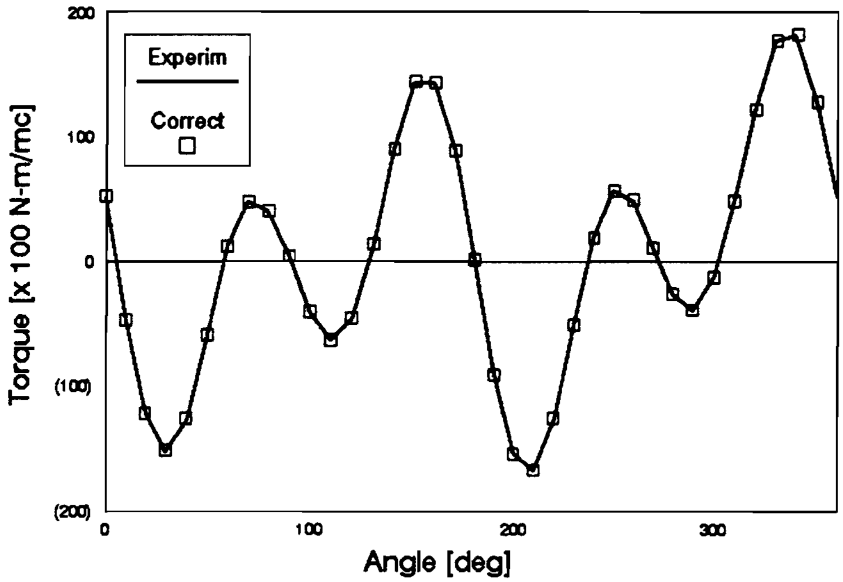

Fig.5.5.b. Torque curve of sample OR-1B

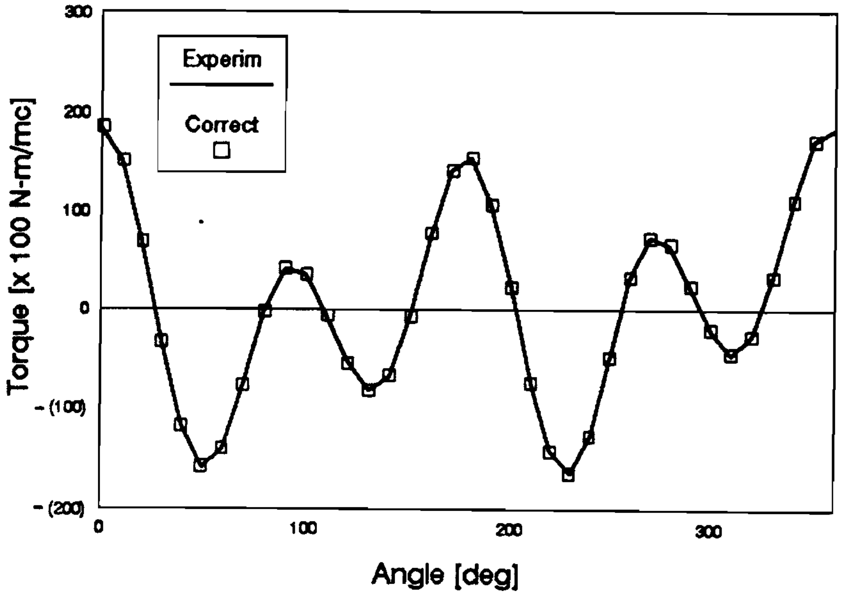

Fig.5.5.c. Torque curve of sample OR-1C

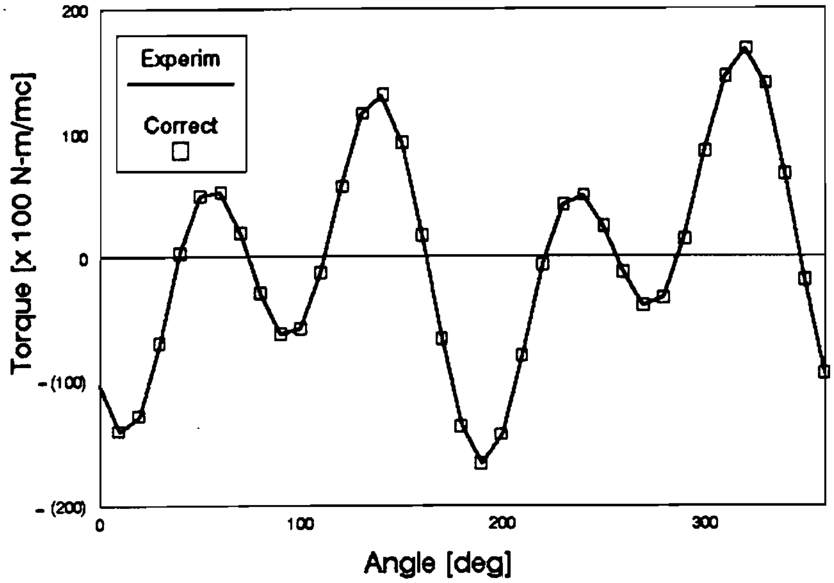

Fig.5.6. Torque curves of non-oriented samples

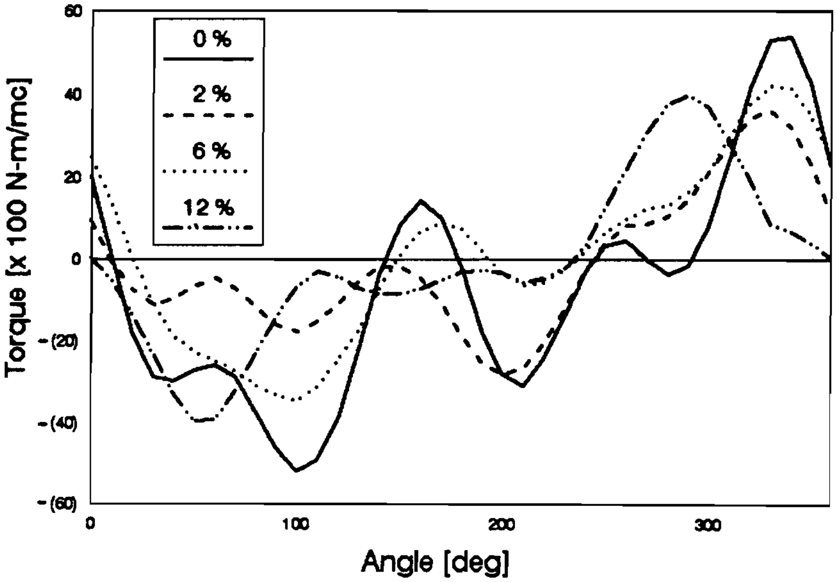

oriented materials, and Table 5.2 for non-oriented materials. The volume of non-oriented samples was 35.4 mm^3.

5.3. CORRELATING TEXTURE AND MAGNETOCRYSTALLINE ENERGY

As described in Chapter 2, the influence of texture on magnetocrystalline energy is calculated by averaging the crystal magnetic anisotropy energy over the orientation distribution function. The result of this calculation is equation (2.51). From this formula, by differentiation, one obtains an expression for

Table 5.1. Fourier coefficients of torque curve for grain oriented samples in $10^2 \cdot [N\text{-}m/m^3]$.

Sample	Volume [mm^3]	F 2	F 4	F 6
9 mil				
GO 1A	32.3	-78.7	-104.7	0.9
GO 1B	28.3	-59.8	-110.1	2.2
GO 1C	29.3	-70.1	-99.6	1.1
GO 2A	32.3	-79.1	-113.9	1.9
GO 2B	33.8	-87.1	-113.4	1.8
GO 2C	32.3	-76.6	-107.9	-2.2
GO 3A	30.7	-78.9	-106.2	1.4
GO 3B	33.8	-64.6	-82.9	1.8
GO 3C	33.8	-80.3	-105.4	3.2
7 mil				
GO 7A	26.1	-72.9	-101.2	1.4
GO 7B	-	-	-	-
GO 7C	26.1	-77.9	-103.1	2.2

Table 5.2. Fourier coefficients of torque curves for non-oriented samples in $10^2 \cdot [\text{N-m/m}^3]$:

Percent elongation	F 2	F 4	F 6
0 %	-17.3	-17.7	-0.007
2%	-13.0	-7.8	0.18
6 %	-11.5	-5.7	0.36
12 %	-14.8	5.1	-0.03

magnetic torque exerted on a sample with a circular cross-section, when a homogeneous magnetic field sufficient to saturate the sample is applied in the plane of the sheet in a direction **y** = (χ = 90°,η):

$$
\begin{aligned}
L(\eta) &= \frac{1}{9 n_4 \sqrt{\pi}} \left[\frac{K_1}{5} + \frac{K_2}{55} \right] F_4'(\eta) + \frac{1}{13 n_6 \sqrt{\pi}} \frac{K_2}{231} F_6'(\eta) \\
F_4'(\eta) &= 2 C_4^{12} \overline{P_4^2}(90°) \sin 2\eta + 4 C_4^{13} \overline{P_4^4}(90°) \sin 4\eta \qquad (5.18) \\
F_6'(\eta) &= 2 C_6^{12} \overline{P_6^2}(90°) \sin 2\eta + 4 C_6^{13} \overline{P_6^4}(90°) \sin 4\eta + \\
&\quad + 6 C_6^{14} \overline{P_6^6}(90°) \sin 6\eta
\end{aligned}
$$

This relationship directly relates the magnetic torque to the cubic anisotropy coefficients and the texture coefficients, C_l^{nm}, calculated from standard X-ray pole figure measurements.

The harmonic components of the torque curve are readily identified in the above formula:

Fig.5.7.a. Harmonic coefficients of torque curves
Experimental and calculated with texture data

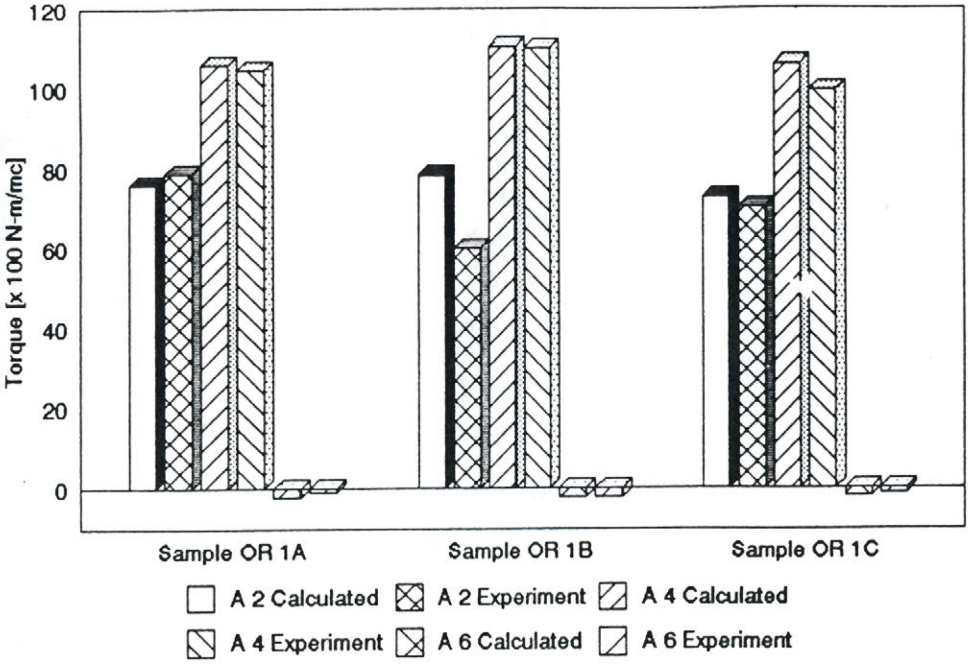

Fig.5.7.b. Harmonic coefficients of torque curves
Experimental and calculated with texture data

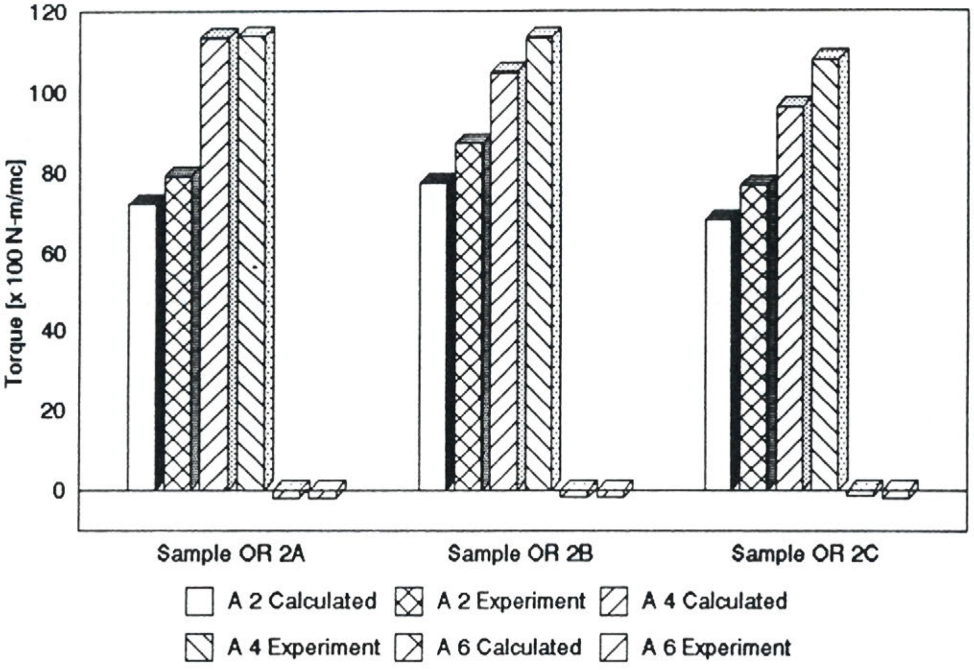

Fig.5.7.c. Harmonic coefficients of torque curves
Experimental and calculated with texture data

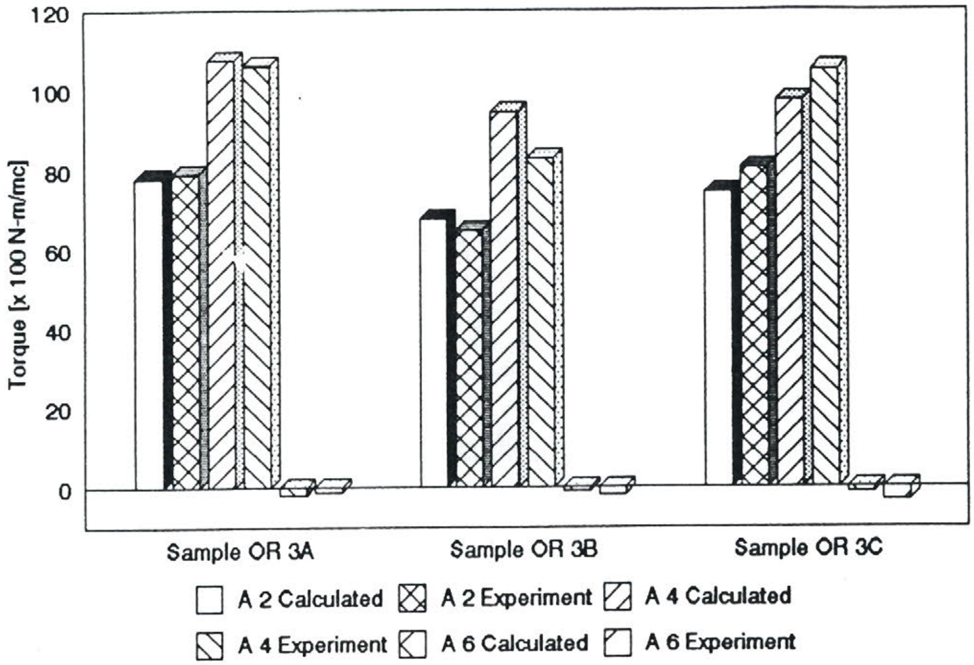

Fig.5.7.d. Harmonic coefficients of torque curves
Experimental and calculated with texture data

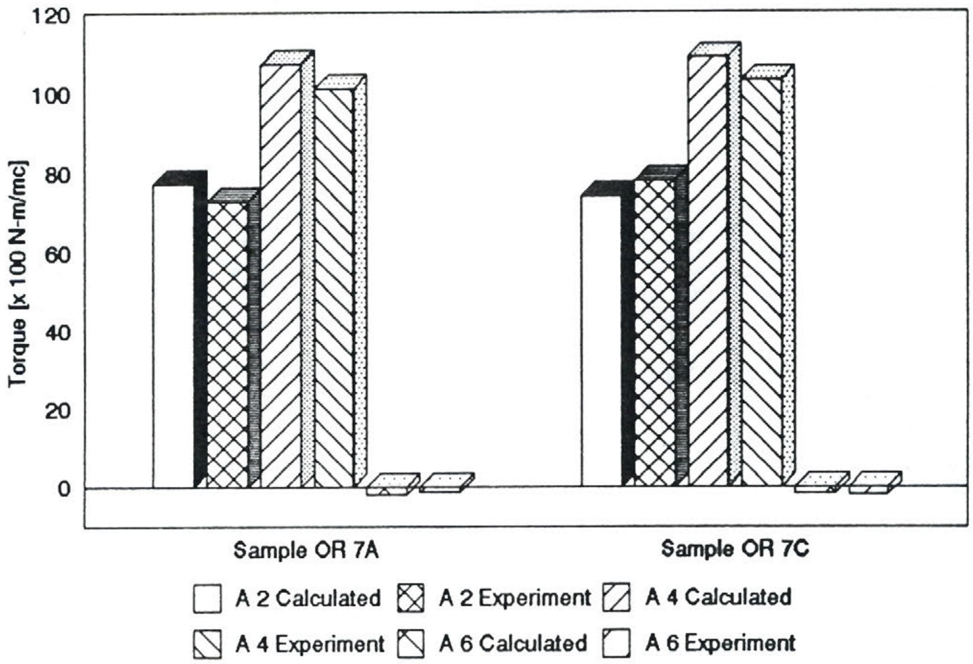

Fig.5.8. **Harmonic coefficients of torque curves**
Experimental and calculated with texture data

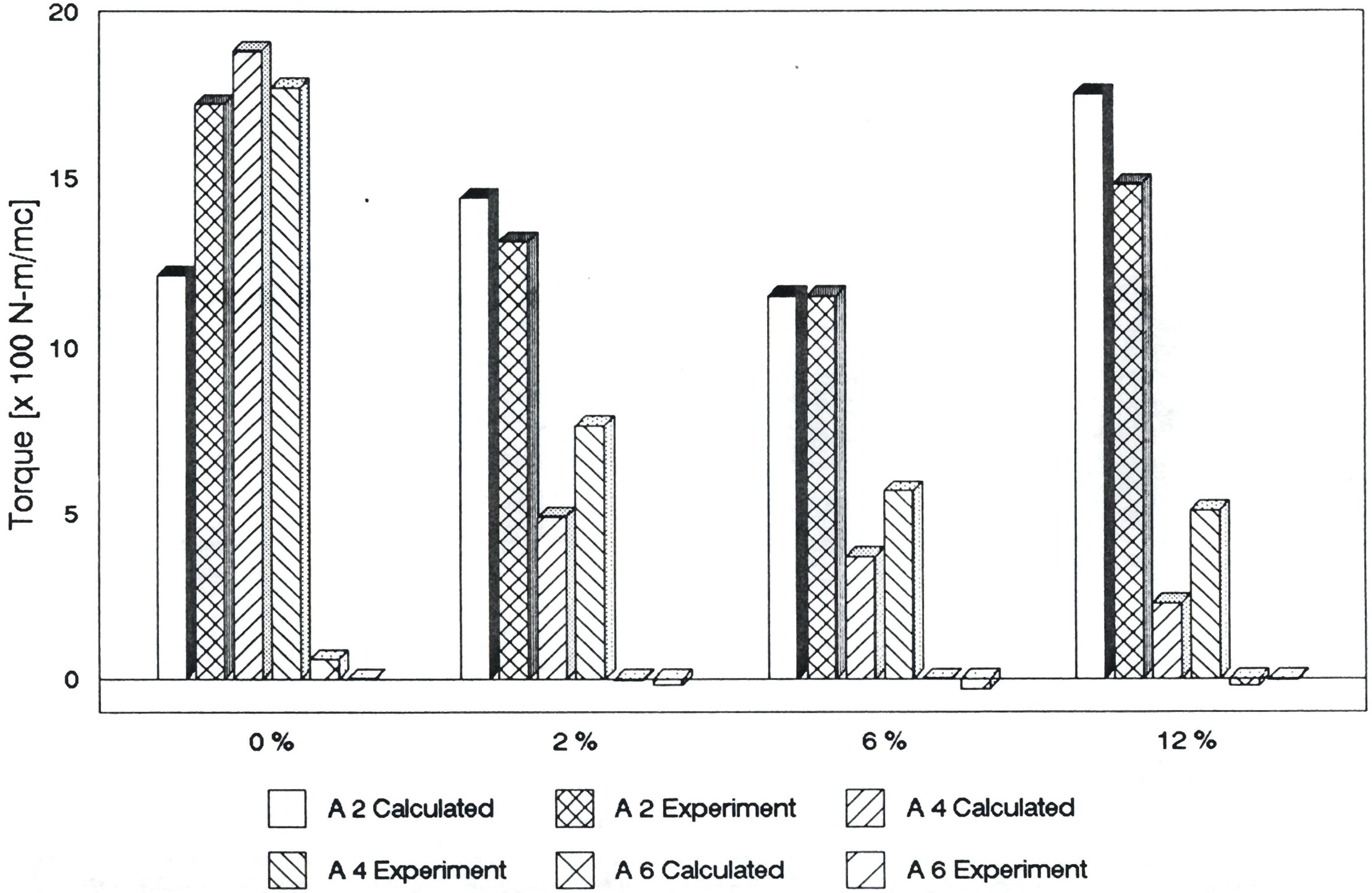

$$
\begin{aligned}
T_2 &= \frac{1}{9n_4\sqrt{\pi}}\left[\frac{K_1}{5} + \frac{K_2}{55}\right] 2C_4^{12}\overline{P_4^2}(90°) + \frac{1}{13n_6\sqrt{\pi}}\frac{K_2}{231}\,2C_6^{12}\overline{P_6^2}(90°) \\
T_4 &= \frac{1}{9n_4\sqrt{\pi}}\left[\frac{K_1}{5} + \frac{K_2}{55}\right] 4C_4^{13}\overline{P_4^4}(90°) + \frac{1}{13n_6\sqrt{\pi}}\frac{K_2}{231}\,4C_6^{13}\overline{P_6^4}(90°) \qquad (5.19) \\
T_6 &= \frac{1}{13n_6\sqrt{\pi}}\frac{K_2}{231}\,6C_6^{14}\overline{P_6^6}(90°)
\end{aligned}
$$

These coefficients were calculated using the texture data presented in Table 4.3 for grain oriented samples and in Table 4.5 for non-oriented samples. The comparison between the values of these coefficients and the Fourier coefficients of the experimental torque curves given in Tables 5.1 and 5.2 is shown in Figures 5.7 (a to d) and 5.8. The agreement between measured values and those calculated from the texture is quite strong. The differences are due to a number of factors affecting both the magnetic torque measurements and the calculation of texture coefficients. Some of these are:

- in grain oriented materials, there exists a statistical error due to an insufficient number of grains under investigation;
- the sharp texture of grain oriented materials causes a truncation error in the calculation of ODF;
- the weak magnetic anisotropy of non-oriented materials increases the error in measuring torque because the instrument works at its lower limit of sensitivity.

5.4. THE INFLUENCE OF TEXTURE ON THE REVERSIBLE MAGNETIZATION ROTATION IN GRAIN ORIENTED MATERIALS

In this section, we propose a model relating the torque measured when the sample is magnetized from remanence to saturation to the spread of grain orientations. The model is then experimentally tested on two specimens of different texture qualities. The results obtained suggest an industrial application of magnetic torque measurements to evaluate the quality of texture.

5.4.1. The model

In grain oriented 3% Si-Fe, the magnetization curve from saturation to remanence is primarily determined by the crystallographic texture. In this range of the hysteresis curve, the displacements of domain walls have already been completed and the magnetization takes place by rotation magnetization.

For soft magnetic materials, the process of magnetization rotation starts at a moderately strong magnetic field. Initially, the magnetization in each grain is pointing in that direction of easy magnetization which is nearest to the direction of the external magnetic field. Starting from this point the approach to saturation is realized by rotation of magnetization against the anisotropy energy. For a grain-oriented material, this process depends on the value of cubic anisotropy constants K_1 and K_2, on the grain orientation distribution (texture) and on the direction in which the specimen is magnetized.

Assuming that α is the angle between a easy magnetization direction in the crystal and the magnetization and α_0 is the angle between the same easy magnetization direction and the magnetic field, the energy density is composed of the magnetic anisotropy of the crystal E_a and the energy E_H due to the presence of the field:

$$E = E_a + E_H = E_a - H\, I_s \cos(\alpha_0 - \alpha) \tag{5.20}$$

where I_s is the saturation magnetization, and E_a is given in equation (2.27).

The torque per unit volume due to the magnetic field H acting on the sample is balanced by the torque created by the magnetocrystalline energy:

$$I_s\, H \sin(\alpha_0 - \alpha) = -\frac{\partial E_a}{\partial \alpha} = +\frac{\partial E_a}{\partial \theta} \tag{5.21}$$

where $\theta = (\alpha_0 - \alpha)$ is the angle between the magnetization and the magnetic field. The magnetization component along the direction of the magnetic field is:

$$I = I_s \cos\theta \tag{5.22}$$

For a very small value of angle θ, the saturation approach law of the magnetization in the direction of the field is given by Chikazumi [51]:

$$I = I_s \left(1 - \frac{C^2}{2 I_s^2 H^2}\right) \tag{5.23}$$

where the coefficient C represents the contribution of the magnetic anisotropy to the rotation process. For the cubic symmetry, the coefficient C can be expressed as a function of the magnetic anisotropy constant K_1 and of the direction cosines $(\alpha_1, \alpha_2, \alpha_3)$ of the magnetization, as deduced by Chikazumi [51]:

$$\begin{aligned} C^2 = 4K_1^2\ [\,1-2(\alpha_1^4+\alpha_2^4+\alpha_3^4)+(\alpha_1^6+\alpha_2^6+\alpha_3^6)\,] \ - \\ - \ 4K_1^2\ [\,1-(\alpha_1^4+\alpha_2^4+\alpha_3^4)\,]^2 \end{aligned} \tag{5.24}$$

The cubic symmetrical functions appearing in the expression (5.24) were rewritten as follows:

$$\begin{aligned} \alpha_1^4 + \alpha_2^4 + \alpha_3^4 &= 1 - 2\varphi_4(\boldsymbol{h}) \\ \alpha_1^6 + \alpha_2^6 + \alpha_3^6 &= 1 - 3\varphi_4(\boldsymbol{h}) + 3\varphi_6(\boldsymbol{h}) \end{aligned} \tag{5.25}$$

where the functions $\varphi_4(\mathbf{h})$ and $\varphi_6(\mathbf{h})$ were previously defined in equation (2.49). Here, $\mathbf{h}$ is a direction having the cosines $(\alpha_1, \alpha_2, \alpha_3)$ in the crystal reference frame.

The functions $\varphi_4(\mathbf{h})$ and $\varphi_6(\mathbf{h})$ are expressed using the cubic spherical harmonics $k_l^{m}(\mathbf{h})$ given in relation (2.50). In equation

(5.24) the function $[\varphi_4(\mathbf{h})]^2$ also appears which is represented as a function of cubic spherical harmonics in Bunge ([1], equation 14.281):

$$[\varphi_4(\boldsymbol{h})]^2 = -\frac{1}{65}\,\frac{k_8^1(\boldsymbol{h})}{n_8} + \frac{52}{15015}\,\frac{k_6^1(\boldsymbol{h})}{n_6} + \frac{10}{143}\,\frac{k_4^1(\boldsymbol{h})}{n_4} + \frac{5}{105} \qquad (5.26)$$

where n_4, n_6 and n_8 are the normalization factors.

The coefficient C, defined by equation (5.24), now has the following form:

$$C^2 = 4K_1^2\,[\varphi_4(\boldsymbol{h}) + 3\varphi_6(\boldsymbol{h}) - 4\varphi_4^2(\boldsymbol{h})] =$$

$$\simeq 4K_1^2\left[\frac{4}{105} - \frac{4}{143}\,\frac{k_4^1(\boldsymbol{h})}{n_4} + \frac{1}{1100}\,\frac{k_6^1(\boldsymbol{h})}{n_6} + \frac{4}{65}\,\frac{k_8^1(\boldsymbol{h})}{n_8}\right] \qquad (5.27)$$

Using the procedure of averaging a crystal property in a polycrystalline sample outlined in Bunge [1], one can calculate the mean square value of the coefficient C, over the crystal orientation distribution:

$$|\overline{C^2}| = K_1^2\,[\frac{16}{105} - \frac{1}{9n_4\sqrt{\pi}}\,\frac{1}{9}\,F_4(\chi,\eta) +$$

$$+ \frac{1}{13n_6\sqrt{\pi}}\,\frac{1}{275}\,F_6(\chi,\eta) + \frac{1}{17n_8\sqrt{\pi}}\,\frac{1}{4}F_8(\chi,\eta)]$$

where: (5.28)

$$F_8(\chi,\eta) = \frac{1}{\sqrt{2}}C_8^{11}\overline{P_8^0}(\chi) + C_8^{12}\overline{P_8^2}(\chi)\cos 2\eta +$$

$$+ C_8^{13}\overline{P_8^4}(\chi)\cos 4\eta + C_8^{14}\overline{P_8^6}(\chi)\cos 6\eta + C_8^{15}\overline{P_8^8}(\chi)\cos 8\eta$$

and the other functions are defined in equation (2.51).

Substituting this coefficient into equation (5.23) we obtain:

$$I = I_s\left(1 - \frac{|\overline{C^2}|}{2I_s^2\,H^2}\right) \qquad (5.29)$$

where the information concerning the influence of texture on the magnetization rotation is fully contained in the C^2 coefficient.

This formula can be used in the range of magnetic fields where the saturation approach law is valid (angle Θ is very small) and magnetic interactions among grains can be neglected. In 3% Si-Fe steel, the anisotropy constant value $K_1 = 36 \cdot 10^3$ J/m^3 has been assumed. In the same way, one could introduce in relation (5.24) terms in $(K_1 \cdot K_2)$ and (K_2^2) representing the higher order spherical harmonics. These terms, however, contribute less than 3% to the total value of C^2, as demonstrated by Celasco and Mazzetti in [53]. It is also possible to correct equation (5.29) using factors which take into account the magnetic interactions among grains and the internal stresses (Celasco and Mazzetti, [4]).

5.4.2. Experimental method and results

Two specimens were used in this study, both of them conventional grain-oriented silicon steels with differing strengths of texture. We called these two specimens OR-1B (medium quality), and OR-1C (poor quality). The OR-1B specimen has a smaller dispersion angle of the <001> directions around the rolling direction than specimen OR-1C. The first eight texture coefficients of these two samples are documented in Table 4.3.

The material thickness is 9 mil (0.21 mm) and, therefore, we can assume that the over-all magnetization is confined to the sheet plane. The magnetic field vector **H** and the magnetization vector **I** are, therefore, co-planar, i.e. the magnetization rotation occurs in the sheet plane.

For the range of the magnetic field where the magnetization is almost parallel to the field, the rotation of magnetization in the vicinity of **H** is determined by the coefficient C^2 which changes with angle η. A plot of $C^2(90°, \eta)$ versus η is represented in Figure 5.9, for both specimens OR-1B and OR-1C, and for a random sample.

Fig.5.9. C^2 coefficient as function of angle from rolling direction

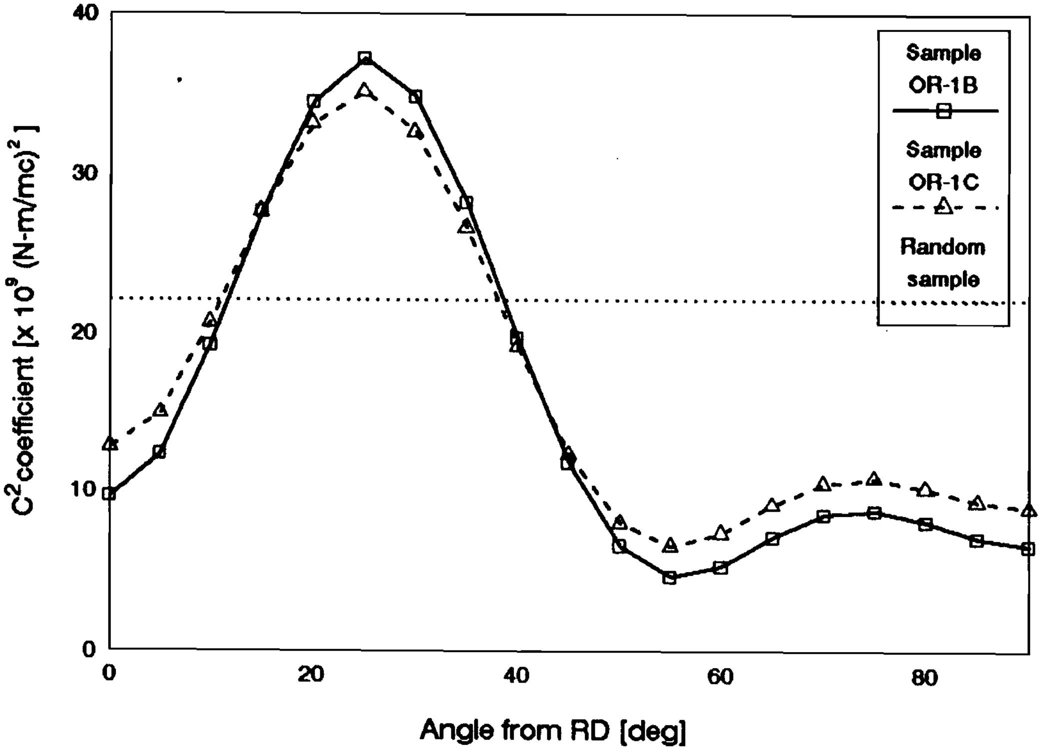

This plot reflects the anisotropy of the saturation approach law and its dependence on the specimen texture.

For lower values of the magnetic field H, the orientation of the magnetization vector is obtained by minimizing the energy density of the whole sample. The equilibrium relationship expresses the torque on the whole sample as the resultant of the torques on all of the crystallites:

$$L(\chi,\eta) = H(\eta_0)\,\bar{I}(\chi,\eta)\,\sin\theta'$$

where:

$$\bar{I}(\chi,\eta) = I_s \frac{1}{N}\sum_{j=1}^{N}\cos\beta_j = I_s\langle\cos\beta\rangle \tag{5.30}$$

In the above equation, the torque $L(\chi,\eta)$ is given in equation (5.1), and $I(\chi,\eta)$ is the magnetization of the sample. Its value is given by the sum of all the projections on the (χ,η) direction of each magnetization I_s in crystallite j and $\theta' = \eta_0 - \eta$ is the angle between the magnetization and the magnetic field. In the following calculation we assume that the magnitude of the sample magnetization $I(\chi,\eta)$ is constant during the rotation process. This assumption is valid in the range of magnetic fields where the angle θ' is large, and the saturation approach law does not apply. The cosine of the angle between rolling direction (RD) and the crystallographic [100] direction described by the Euler angles is:

$$\cos\beta = \cos\varphi_1\cos\varphi_2 - \sin\varphi_1\sin\varphi_2\cos\phi \tag{5.31}$$

Its average value is determined by the orientation distribution function (ODF):

$$\langle\cos\beta\rangle = \oint\cos\beta\, f(\varphi_1,\phi,\varphi_2)\,\sin\phi\; d\varphi_1 d\phi d\varphi_2 \tag{5.32}$$

The orientation of the magnetization vector relative to the magnetic field was determined as follows: Discs of 15 mm in diameter were punched from the two specimens. The shape of the sample introduces an additional term to the total energy density

(5.1). In general, the shape anisotropy energy has the form:

$$\begin{aligned} E_s(\chi,\eta) &= \frac{1}{\mu^*}\,\frac{4\pi}{2}\,N(\chi,\eta)\,\overline{I^2}(\chi,\eta) \approx \\ &\approx \frac{2\pi}{\mu^*}\,N(\chi,\eta)\,I_s^2 \end{aligned} \tag{5.33}$$

where $N(\chi,\eta)$ is the demagnetizing factor, and μ^* is the coefficient for the μ^* correction in the magnetized state of the sample, deduced by Imamura et al. [54] ($\mu^* = 45.2$ for 3% Si-Fe). For an ellipsoid of revolution having the demagnetizing factors along its principal axes N_{11}, N_{22}, and N_{33}, the demagnetizing factor $N(\chi,\eta)$ can be expressed by means of the orthorhombic (sample symmetry) spherical harmonics of the second order:

$$\begin{aligned} N(\chi,\eta) = \frac{1}{3}(N_{11}+N_{22}+N_{33}) + \frac{\sqrt{2\pi}}{3}\sqrt{\frac{2}{5}}\,\dot{k}_2^{1}(\chi)\,(2N_{33}-N_{11}-N_{22}) + \\ + \frac{2}{3}\sqrt{\frac{3\pi}{5}}\,\dot{k}_2^{2}(\chi,\eta)\,(N_{11}-N_{22}) \end{aligned} \tag{5.34}$$

For a disc shaped specimen $N_{11} = N_{22}$, and the shape anisotropy energy does not depend on angle η. In our experiment, the ratio of diameter to thickness is approximately 70, giving the demagnetizing factors for the corresponding oblate ellipsoid equal to: $N_{11} = N_{22} = 0.01$ and $N_{33} = 0.98$. For sample OR-1B, lines of constant magnetocrystalline energy (E_a/K_1) are plotted in stereographic projection in Figure 5.10, substituting the C_l^{mn} coefficients from Table 4.3 in equation (2.51). In the real disc shaped specimen, the shape anisotropy energy is added to the magnetocrystalline energy. The equipotential lines of the resultant energy density (over K_1) are plotted in Figure 5.11. It is clear that the minimum value of energy density is in the rolling direction (RD), which is the sample easy magnetization direction.

When the disc is placed in a magnetic field parallel to its plane, the torque exerted on the disc by the increasing field

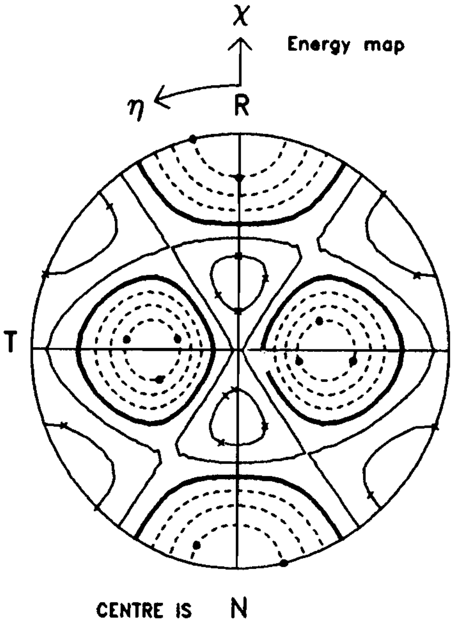

Fig.5.10. Magnetocrystalline energy (over K_1) for sample OR-1B

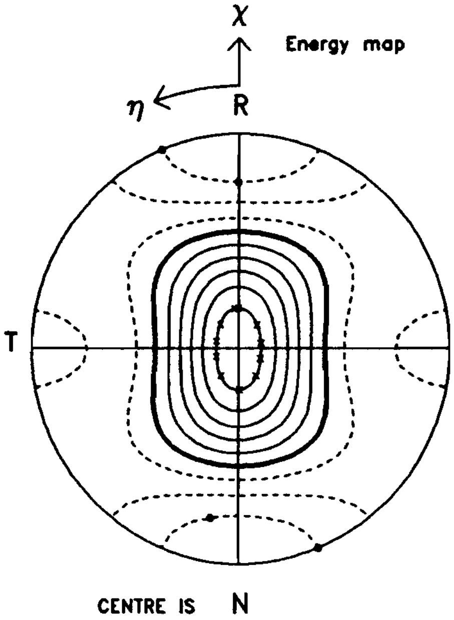

Fig.5.11. Magnetocrystalline plus shape anisotropy energy (over K_1) for sample OR-1B

gradually increases with the strength of the field. The magnetization rotates from the sample easy magnetization direction towards the direction of the field, and the path followed by the magnetization **I** can be determined from the equilibrium condition (5.21). The equilibrium value of η is not always single valued because the shear angle θ' between the magnetization **I** and the applied field may lag, or lead **H**, and discontinuous irreversible changes may occur (Hoon and Lowe, [55]). If the increasing magnetic field has an orientation given by the polar coordinates (χ,η) in the sample reference frame, the path followed by the magnetization **I** rotating from the rolling direction (RD) towards **H** could be determined graphically, in a similar manner to the one described by Bozorth and Williams [56] in the case of single crystals. In Figures 5.10 or 5.11, one could draw circles of various diameters around the point (χ,η). The points at which these circles are tangent to the equipotential lines satisfy the minimum energy density condition. The locus of such points is the required path. Discontinuous irreversible changes may occur for values of angle η higher than 45°, where the relative minimum of energy density around the transverse direction may create an instability in the magnetization rotation process.

In our experiment, the magnetic field was confined in a direction lying between easy magnetization direction (rolling direction) and the $(\chi=90°,\eta=45°)$ direction, where the solution of equation (5.21) is unique. In this range of angle η, the calculation of torque $L(\eta)$ and magnetization **I** can be made by solving equations (5.21) and (5.22) simultaneously.

The position of the maximum value of torque is determined by the derivative of equation (5.18):

$$\frac{\partial L(\chi,\eta)}{\partial \eta} = 0 \qquad (5.35)$$

and depends on the texture coefficients C_l^{mn}. For both samples, the maximum value of torque is situated near η = 26°. Therefore, the **L** versus **H** curves will have a maximum whenever the direction of **H** lies between $\eta = 26°$ and $\eta = 45°$.

The torque measurements were made with the increasing magnetic field applied at the ($\chi=90°,\eta=22.5°$) and ($\chi=90°,\eta=45°$) directions of the sample, using the automated torque magnetometer presented in this chapter. These directions were chosen as a function of the maximum position of the torque curve. For the $\eta=22.5°$ direction of the field, the **L** versus **H** curve should not present any maximum, while the torque measured with the field applied in the $\eta=45°$ direction should present a maximum value. In both cases, the torque measured versus the applied field depends on the material texture due to the anisotropy of the magnetization rotation process.

The true field applied to the disc was considered in the first approximation as the difference between the external field H_{app} and the projection of the demagnetizing field on the direction of the external field:

$$H_{true} \approx H_{app} - N\, 4\pi I_s \cos(\eta_0 - \eta) \qquad (5.36)$$

where the demagnetizing factor $N = N_{11} = 0.01$.

Theoretical curves for $H_d = N \cdot I_s \cdot 4\pi \approx 200$ Oe ($= 16 \cdot 10^3$ A/m) demagnetizing field calculated using equations (5.30) and (5.36) are plotted together with the experimental curves in Figures 5.12 and 5.13. There is a close similarity between these graphs, which demonstrates that the theory supports the experimental data.

The calculation of the theoretical curves is not exact because:

(a) the value of the true magnetic field applied on the sample was roughly approximated in equation (5.36);

(b) the finite thickness of the sample does not confine the magnetization in the sheet plane so that the magnetization vector **I** may have a slight deviation out of the sheet plane;

(c) in the range of magnetic fields higher than 4000 Oe ($320 \cdot 10^3$ A/m), the differences between the theoretical and experimental torque curves are due to the dependence of anisotropy constants on the magnitude of the applied field. In 1939, Tarasov [57] realized that the experimental torque curve amplitude does not show a

Fig.5.12. Theoretical and experimental torque for sample OR-1B

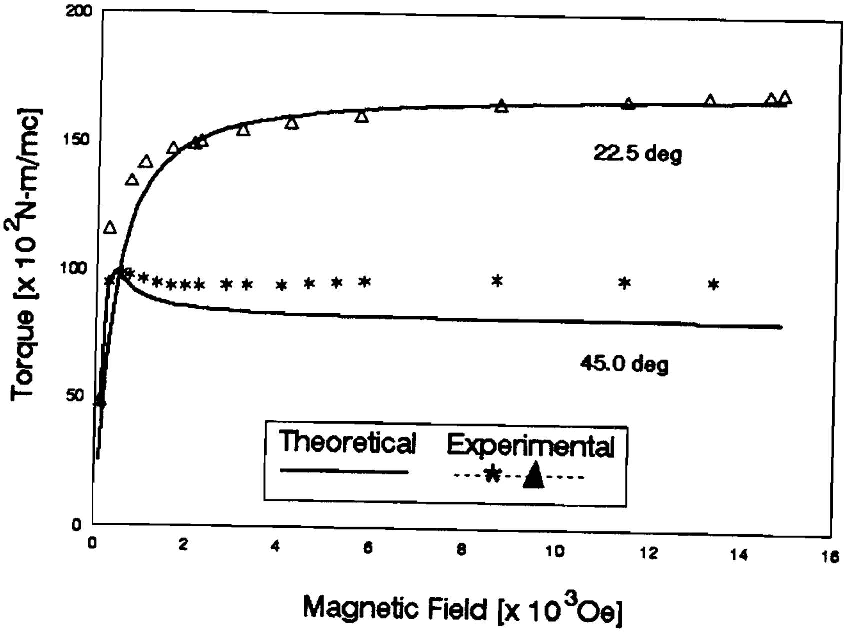

Fig.5.13. Theoretical and experimental torque for sample OR-1C

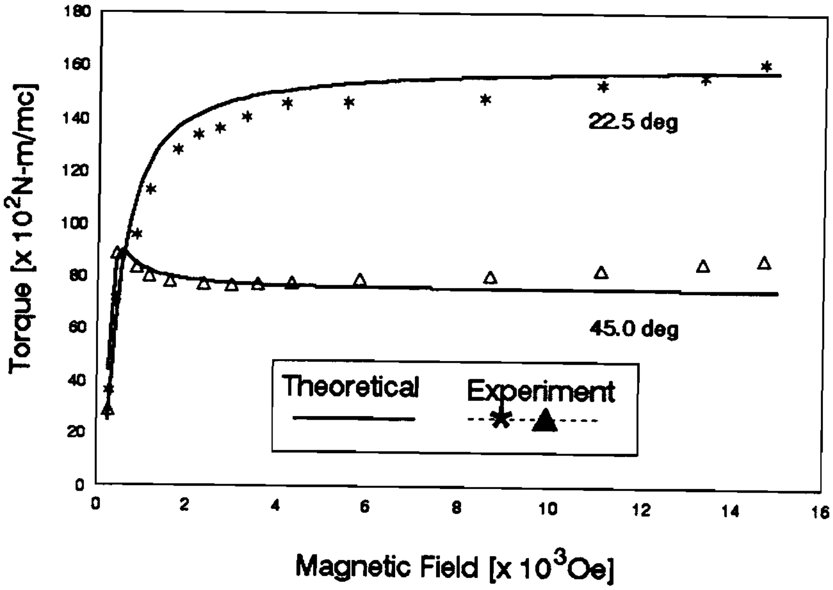

Fig.5.14. The influence of demagnetizing field Hd on magnetic torque for sample OR-1B

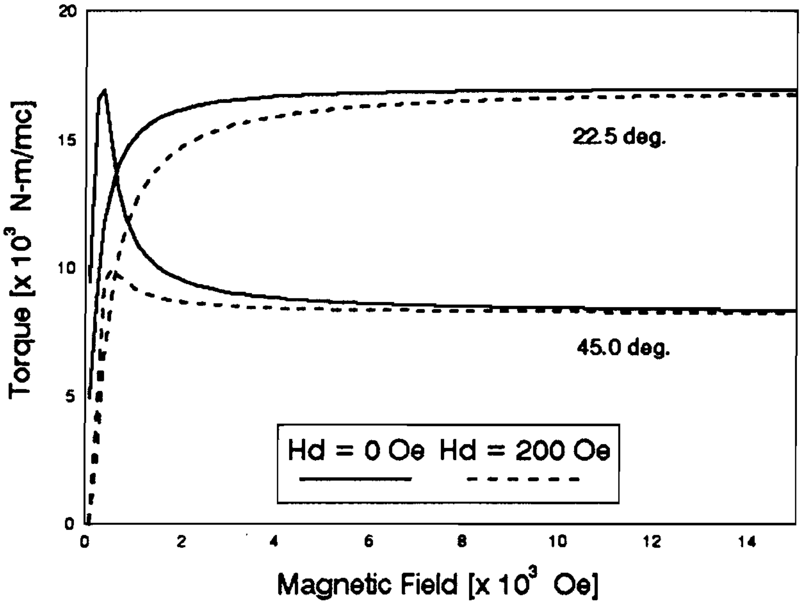

Fig.5.15. The influence of demagnetizing field Hd on magnetic torque for sample OR-1C

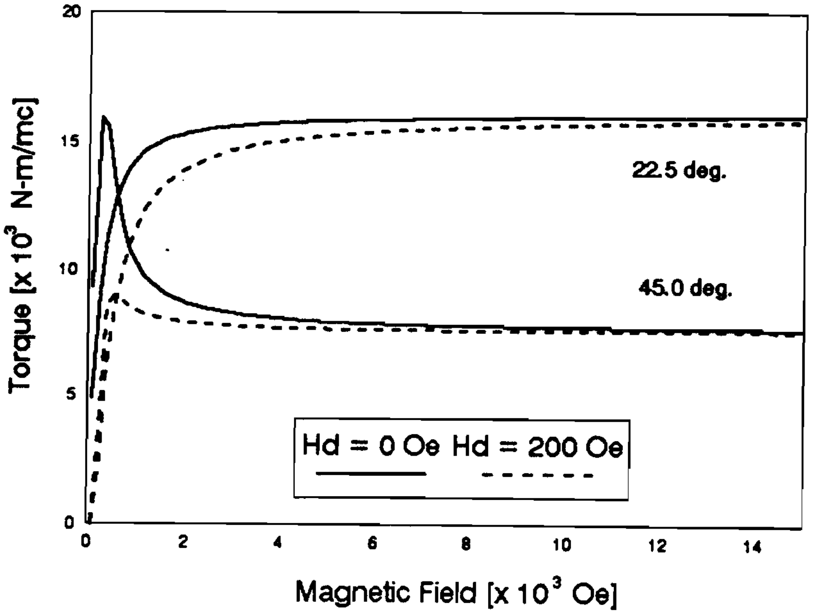

limiting value when the external field is increased, as the theory predicts. During the time, several models [58- 60] were proposed to describe this situation, but no satisfactory results were obtained.

The contribution of the demagnetizing field to the magnetic torque in intermediate fields for the two specimens is shown in Figures 5.14 and 5.15. This contribution, which is negligible in the low field region where the magnetic domains still exist, was calculated at intermediate fields, assuming that all magnetic moments are aligned in one direction, and that the rotational process dominates. The torque at $\eta = 22.5°$ and $\eta = 45°$ directions of the applied field was calculated as a function of H, using the equilibrium condition (equation 5.30). The demagnetizing field was neglected ($H_d = 0$) in the first case and considered as having the value of 200 Oe, in the second case. From these plots, one can see that the demagnetizing field considerably lowers the value of **L** in the range of small **H** values ($H < 1{,}000$ Oe $= 80 \cdot 10^3$ A/m). The difference in torque value between the two specimens is significant for higher values of **H**, where the influence of texture is strong. For the two examples considered here, the difference in magnetic torque measured at 22.5° between samples OR-1B and OR-1C at H = 3,000 Oe is approximately 1000 N-m/m^3.

This analysis describes the quantitative correlation between the magnetization rotation process and the material texture, characterized by the orientation distribution function (ODF). It is shown that the coefficient C^2, used to characterize the approach to saturation is not constant, but depends on the distribution of grain orientation; it also changes with the direction of magnetization. The saturation approach law provides useful information about the angular spread of grain orientation. Using the theoretical background developed in this chapter, it is demonstrated that the magnetic torque measured at a given direction of the external field is a sensitive method, describing the texture related anisotropy of magnetization rotation. This method is used to determine the angular and magnetic field ranges where the influence of texture on magnetic torque is the strongest. It is also shown that the demagnetizing factor decreases the sensitivity of the method in the lower range of H values.

This analysis allows us to apply the results to evaluate different texture qualities, using a magnetic instrument which could be implemented on-line.

5.4.3. Method of inspecting the texture quality in grain oriented materials

In the previous section, we demonstrated how the texture of material influences the process of magnetization rotation. In a constant magnetic field, strong enough to align the magnetic moments in each crystallite in one direction, the direction of the sample magnetization is determined by its crystallographic texture through the magnetic anisotropy energy.

Based on this theoretical background, we devised a simple instrument which gives information about the quality of the texture by measuring the angle between the direction of magnetization in the sample and the direction of a fixed applied field. The measurement is indirect because the instrument measures the torque exerted by the sample magnetization on the external field produced by a permanent magnet.

The instrument is a modified torque magnetometer of the same type as the one described in this chapter. In the magnetic torque measurements, the horizontal magnetic field produced by the electromagnet was rotated relative to the sample which was fixed on the magnetometer head through the rigid glass rod. The transducer measured the torque exerted by the magnetic field on the magnetization of the sample.

This arrangement could be reversed: a magnet producing the horizontal field is fixed in the sample position and the sample is rotating in front of the magnet around the normal direction (ND). In this case, the magnetometer records the torque produced by the sample magnetization acting on the fixed permanent magnetic field. The electromagnet was removed and the new setup is illustrated in

Figure 5.16. A strong permanent Nd-Fe-B magnet ($H_c = 500\cdot10^3$ A/m = 6000 Oe) attached to the magnetometer rod magnetized the sample above the value of the magnetization knee. If the magnetic field is not oriented along the easy direction of magnetization, the magnetization direction in the sample does not coincide with the direction of the field due to the magnetocrystalline energy. For a magnetic field of constant direction and magnitude, the direction of magnetization depends only on the texture of the sample, as was previously illustrated. According to the proposed theory, when the applied field lies between $\eta = 0°$ and $\eta = 45°$ directions of the sample, a higher value of the lag angle between the magnetization and magnetic field corresponds to a better orientation of the crystallite easy magnetization directions along the sample rolling direction. Since the torque measures the sine of the angle between the magnetization and the magnetic field, it provides information about the perfection of grain orientation in the sample. This instrument could be readily implemented to monitor the quality of the grain oriented materials on-line.

The material used for analysis is a coarse grain oriented metal sheet placed horizontally underneath the permanent magnet which is hung through the glass rod on the lower suspension of the torquemeter head. The permanent magnet produces a constant magnetic field, which is a function of the distance between the permanent magnet and the sample plane. To obtain comparable information about the texture quality of different materials, the tests must be performed at constant magnetic field, which means a constant distance between the permanent magnet and the surface of the sample. The large dimensions of the metal sheet, practically infinite size in comparison with the dimensions of the permanent magnet, exclude the possibility of the free magnetic poles appearing inside the sample, so that the demagnetizing field can be considered zero.

We assumed that the magnetization process occurs in the plane of the sheet, minimizing the magnetostatic energy caused by free magnetic poles on the sheet surfaces.

If the magnetic field is oriented in a direction lying in the sheet plane, and with an angle η_0 to the sample easy magnetization direction, the magnetization direction in the sample plane is determined by the equilibrium condition (5.30):

$$L(\eta) = H(\eta_0)\ I(\eta)\ \sin(\eta_0 - \eta) \tag{5.37}$$

where the left term is a function of the texture coefficients of the material.

Let us assume that the relative permeability of the sample in the direction (90°,η) is $\mu(\eta)$. The problem of permeability variation with the angle from the easy magnetization direction of the sample is discussed in chapter 8.2. We anticipate that the permeability is described, to the first approximation, as a function of $F_4(\eta)$, defined in equation (2.51) and, as a result, one can write:

$$\mu(\eta) \approx \mu_2 \cos 2\eta + \mu_4 \cos 4\eta \tag{5.38}$$

where μ_2 and μ_4 are material constants.

The magnetization in direction (90°,η) is related to the component of the magnetic field in this direction through the relationship:

$$I(\eta) = \mu(\eta)\ H(\eta_0)\ \cos(\eta_0 - \eta) \tag{5.39}$$

Substituting equations (5.38) and (5.39) in (5.37), we obtain:

$$\begin{aligned} L(\eta) &= \frac{1}{2}\ \mu(\eta)\ H^2(\eta_0)\ \sin 2(\eta_0 - \eta) \approx \\ &\approx L_0 + L'_2\cos 2\eta + L''_2\sin 2\eta + L'_4\cos 4\eta + L''_4\sin 4\eta + \dots \end{aligned} \tag{5.40}$$

where the coefficients of the series are expressed as functions of η_0, H, and texture coefficients.

The instrument was experimentally tested in the laboratory on two pieces of grain oriented metal sheets of different texture qualities, namely the OR-1B and OR-1C samples.

Starting from a position where the direction of the magnetic field coincides with the rolling direction (RD) of the sample, the

Fig.5.16.
Schematic diagram for texture inspection

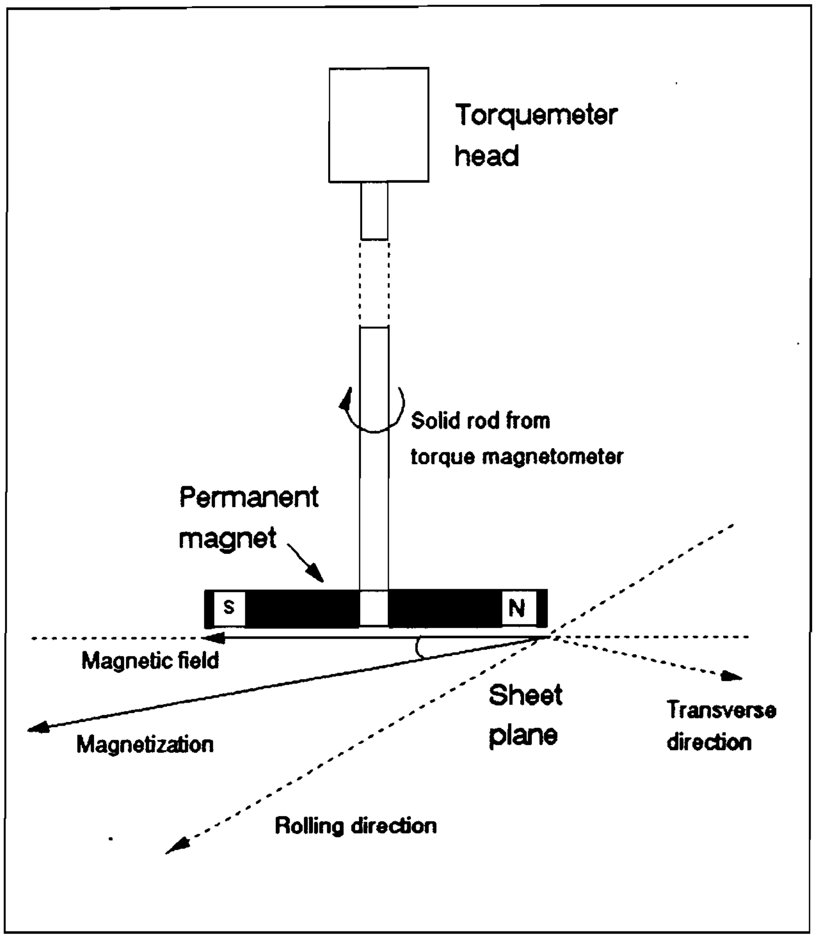

Fig.5.17. Torque signal recorded from two samples with different texture quality

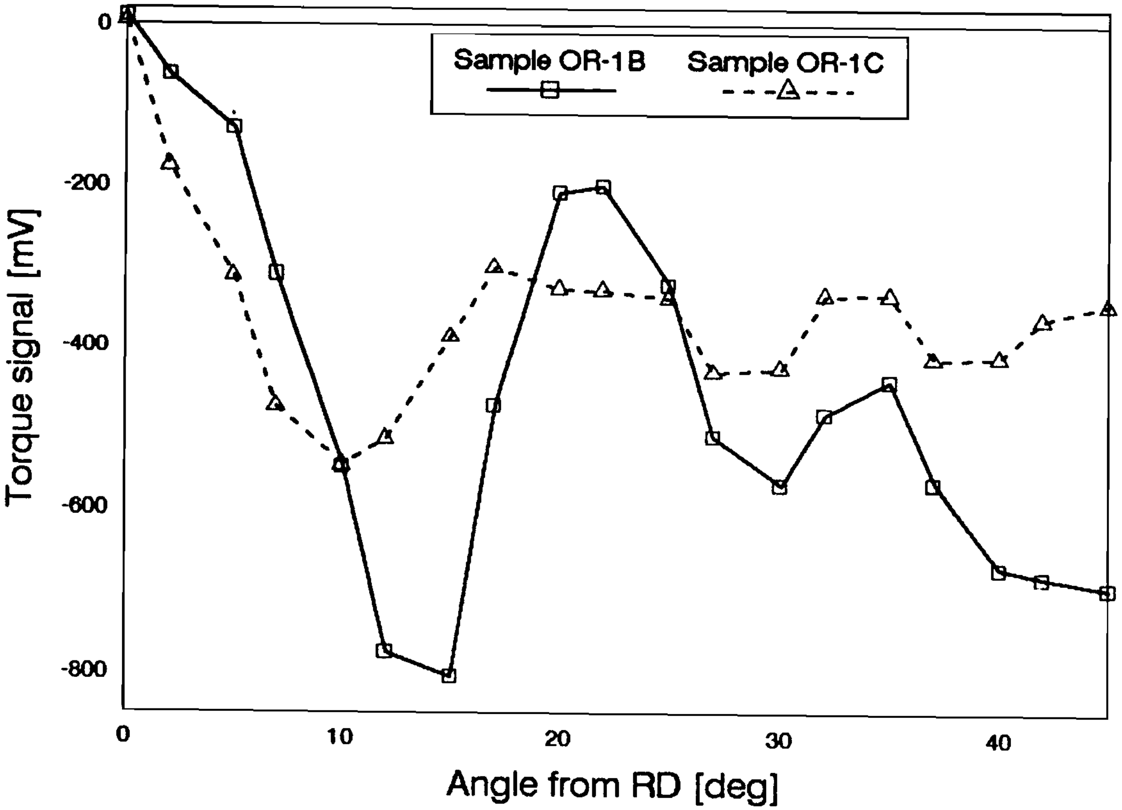

metal sheet was rotated 45°, and the signal proportional to the torque was recorded by the instrument in 2.5° step. The results obtained for the two samples are shown in Figure 5.17. The shape of these curves is less important for our purposes. What is important is that these curves reflect the differences in texture between the two materials.

In the proposed industrial application of the instrument, the direction of the magnetic field created by the permanent magnet should be constant relative to the lamination rolling direction, for example, at 12.5° where the difference in torque signal is maximum. The instrument must be calibrated using a material of known texture.

The simplicity and robustness of this instrument are remarkable. When implemented on the processing line, the designed instrument would indicate the variation in the texture of the final product.

CHAPTER 6.

NON-DESTRUCTIVE METHODS OF CORRELATING TEXTURE, MICROSTRUCTURE AND POWER LOSSES IN ELECTRICAL STEELS

INTRODUCTION

From the applicative point of view, the power loss in electrical steels is a quality parameter. From the physical standpoint, however, the power loss represents a macroscopic parameter which provides valuable average information on the microscopic processes contributing to the total magnetization. An external magnetic field applied to a specimen with homogeneous magnetic structure produces a homogeneous magnetization in the sample cross-section. The power loss value is given by its classical formula (2.38). In reality, there always exist a magnetic domain structure which opposes the action of the external magnetic field. As a result, the magnetization process is inhomogeneous and characterized by strong interaction fields.

It is known that the basic physical mechanism responsible for power loss in soft magnetic materials is the competition between the external applied field and the local internal fields due to coercive, magnetostatic, and eddy current effects. The phenomenology is very complex. The internal fields interact each other in an intricate fashion due to the strong correlation existing between magnetic domains. Establishing simple relationships between the loss behaviour and the various microstructural, metallurgical, and magnetic parameters of material is not an easy task, therefore. Nevertheless, statistical investigation of the microscopic processes contributing to the total power loss can be done through detection and analysis of the Barkhausen noise.

In the present chapter, a method based on the measurement of clustered Barkhausen transitions in electrical steels is proposed and tested, to non-destructively investigate the statistical correlation between the Barkhausen phenomenon and the total power losses. It is shown that the correlation reflects a relationship between Barkhausen noise power and the irreversible permeability of the material. The Barkhausen noise instrument was devised to rapidly monitor the quality of the grain oriented and non-oriented electrical steels.

The most important origin of losses accompanying the magnetization of electrical steels is the eddy current. In a material containing many domain walls, the eddy currents are localized at the wall. Calculating the distribution of eddy currents is very difficult because it depends not only on the shape and the distribution of the domain walls, but also on the shape of the specimen. For the simple case of an infinite slab containing a periodic array of longitudinal domains, Pry and Bean [28] calculated the eddy current loss and found it to be proportional to the domain wall spacing. Using the Bitter technique, we measured the domain wall spacing in several grain oriented samples, in an attempt to identify the mechanisms of losses in these materials.

The method and the results are presented in this chapter.

6.1. CORRELATION BETWEEN TEXTURE, DOMAIN WALL SPACING AND POWER LOSSES IN GRAIN ORIENTED MATERIALS

The Bitter technique was used to visualize the domain walls in grain oriented 3% Si steels. Based on this method, an instrument called the Magnetic Domain Viewer was developed by the British Steel Corporation Research Laboratory. The Magnetic Viewer contains an aqueous suspension of colloidal particles of iron. The suspension is held in a cylindrical container having a membrane 10^{-3} inch thick at the bottom, a glass at the top and a magnetizing coil wound around the cylinder surface. The surface to be examined must be thoroughly cleaned to remove all traces of dirt and grit. The Magnetic Viewer is placed with the membrane on the surface and the magnetizing coil is activated. Magnetized particles are attracted by the stray fields and the obtained image reveals the Bloch walls.

The magnetic structures of several grain oriented samples in the demagnetized state revealed by the assembly of the colloidal particles was recorded on the film. On these photos, it was possible to measure the domain spacing of individual grain. Then, on the same area, a photo showing only the grain boundaries was taken. These photos allowed us to map the grains, and to measure the surface area of each grain.

Pictures taken from an area of 15x10 mm^2 are shown in Figure 6.1 (a to e). The magnification of the presented photos is 6. Parameters characterizing magnetic domains, such as directions and spacings of main domain walls and densities of closure domains, differed from grain to grain, and from sample to sample, due to differences in the spread of grain orientations. Domain wall spacing is related to the local magnetic flux: wall displacements in regions with wider wall spacing are bigger than those in regions with narrower wall spacing. Bishop [61] demonstrated that overloading the more permeable wider slab domain regions by flux bypassing the less permeable narrower wall spacing regions, leads

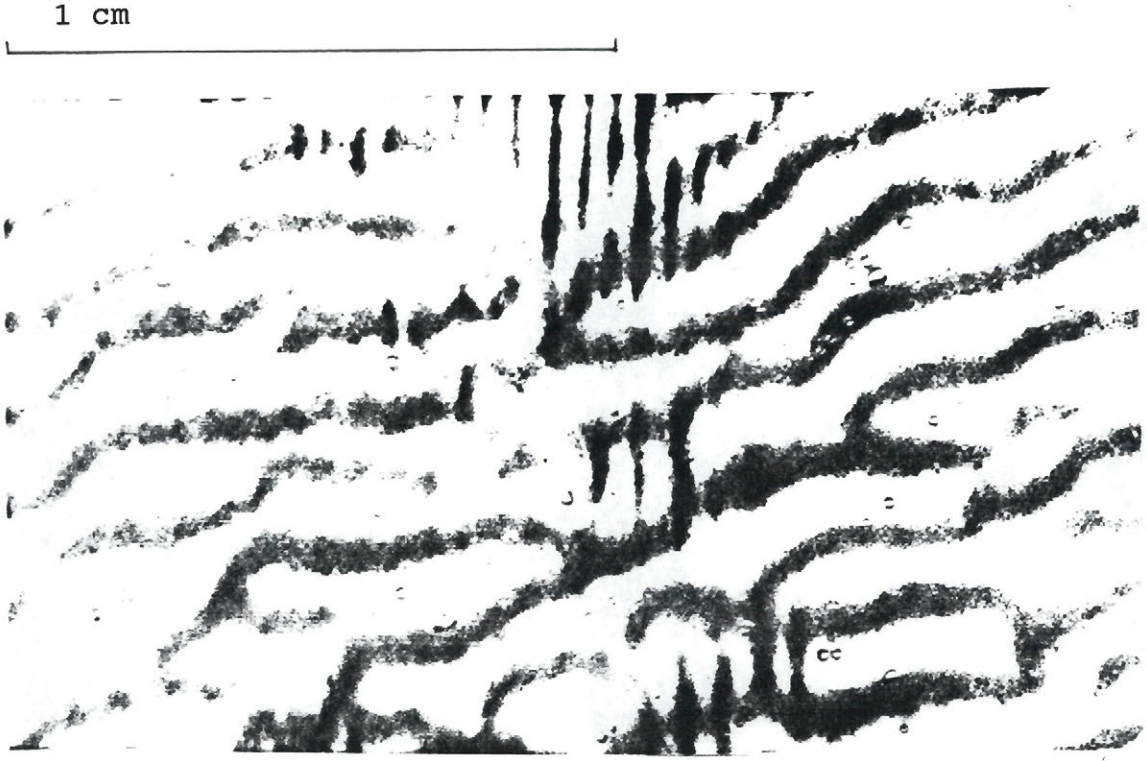

Fig.6.1.a. Magnetic domain pattern in sample OR-1A

Fig.6.1.b. Magnetic domain pattern in sample OR-1B

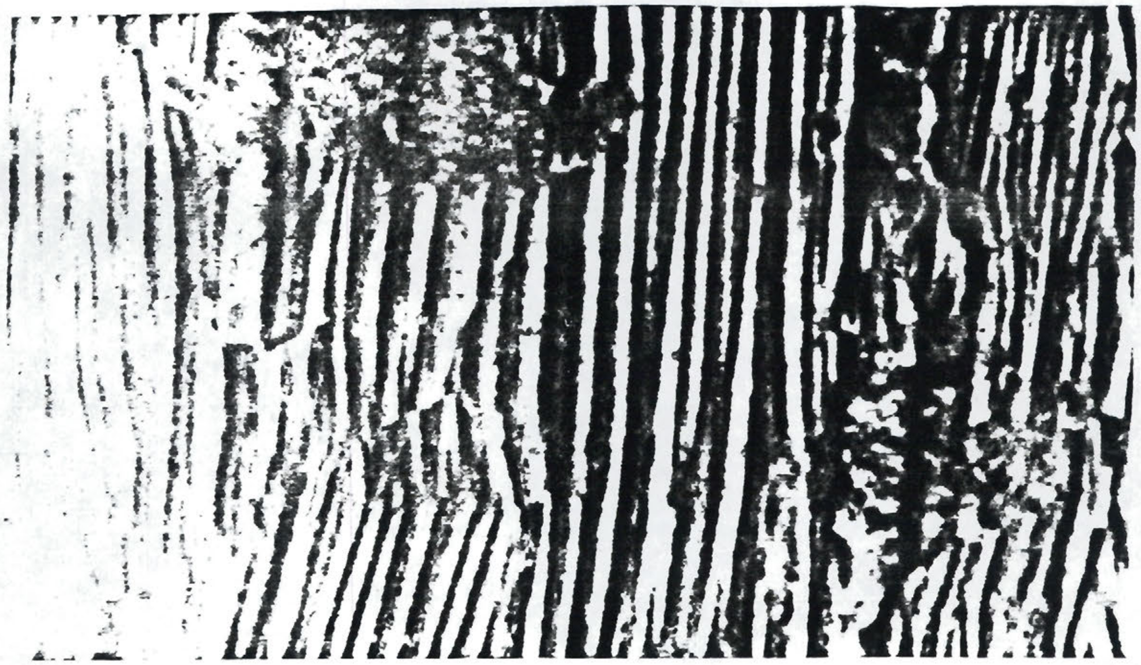

Fig.6.1.c. Magnetic domain pattern in sample OR-1C

Fig.6.1.d. Magnetic domain pattern in sample OR-7A

Fig.6.1.e. Magnetic domain pattern in sample OR-7C

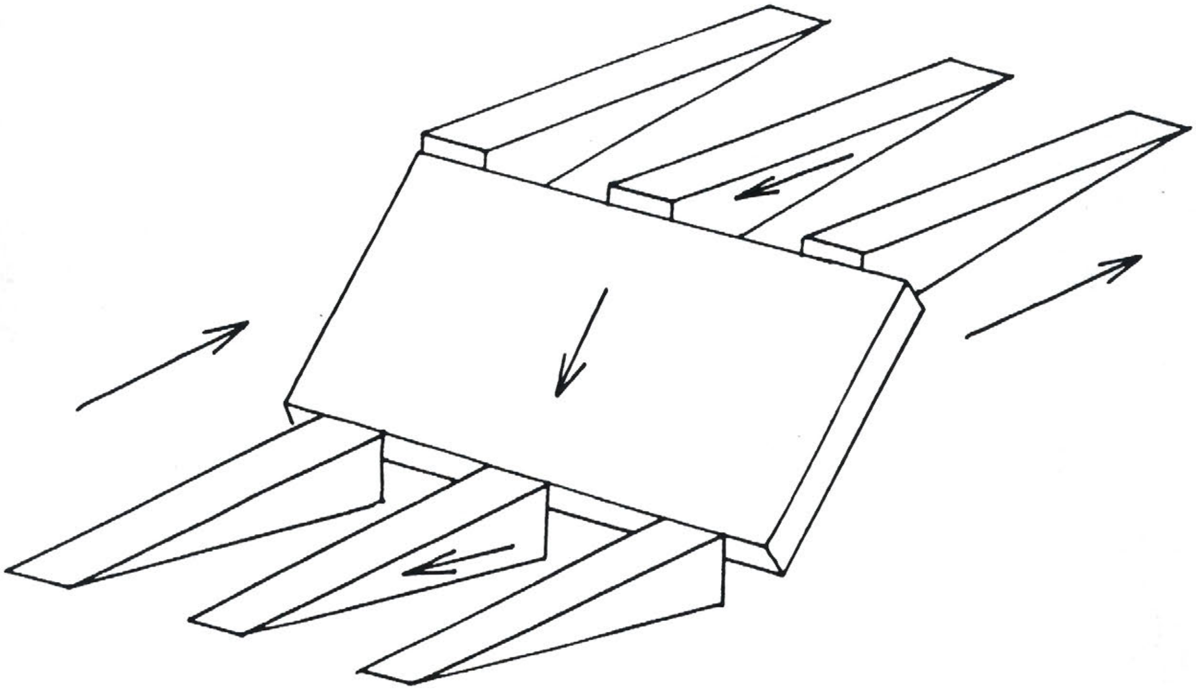

Fig.6.2. Proposed domain structure for band domains

to excess power losses. Therefore, to decrease losses, the magnetic flux must be uniformly distributed over the sample. This is accomplished by a uniform domain structure, obtained using a domain refining technique (eg., mechanical or laser scribing). As a result of domain refinement, the number of walls which move effectively under alternating field increases, and the velocity (eddy current loss) of an individual wall in a constant flux density decreases. We use this information to interpret the experimental data relating the domain wall spacing to the magnetic Barkhausen noise, and to power losses.

For each sample under investigation, the average domain spacing was calculated using the formula:

$$<d> = \frac{\sum_{i=1}^{N} d_i A_i}{\sum_{i=1}^{N} A_i} \tag{6.1}$$

where d_i is the domain spacing in the grain "i", which has the surface area A_i. N is the total number of grains contained in the investigated area of 30x100 mm^2 for each sample. This number varies from 130 to 200 grains as a function of the mean grain size of the sample.

The magnetic domain pattern of several grain oriented samples of different thicknesses (9 and 7 mil) were investigated using the Bitter technique. The average domain wall spacing of each specimen is correlated with the results obtained from texture analysis and power loss measurements.

The three 9 mil (0.21 mm) samples which were analyzed, have different textures and grain sizes (see Table 3.2). Table 6.1 presents the values and the positions in the Euler space of the maximum ODF intensities of these samples.

Out of the three 9 mil samples, the sample termed OR-1C has the poorest orientation and the highest power loss (see Table 3.2); the differences in the domain structure between grains was greatest for this sample. There are grains with large domain spacing and grains having only a maze domain structure. For sample OR-1C, the average domain spacing calculated from 138 grains is <d> = 0.49 mm.

Table 6.1. ODF intensity and position for grain oriented samples:

Sample	Maxim ODF (x random)	φ_1	ϕ	φ_2
OR 1C	221	90°	90°	45°
OR 1B	522	90°	90°	45°
OR 1A	461	90°	85°	45°

Sample OR-1B has good orientation and lower loss. There were smaller differences in domain structure between grains and the average domain wall spacing <d> = 0.52 mm was larger than in sample OR-1C. The average domain spacing was calculated using formula (6.1) with N = 131.

Sample OR-1A has a refined domain structure with very low loss. Despite very large grains, the tilt angle for [001] directions out of the sheet plane generates a fine magnetic structure formed by 180° spike surface domains connected by a 90° body. Figure 6.1.c illustrates the surface flux closure domains which appear as bands, together with small regions where slab domains prevail. The proposed magnetic domain structure for the band regions is shown in Figure 6.2.

The other two samples which were investigated (Figures 6.1. d and e) belong to the 7 mil class. They are OR-7C and OR-7A, respectively. These samples are characterized by a (110)[001] texture with the same ODF intensity and angular spread, but with different grain size. The differences in the magnetic domain patterns and in the magnetic properties are due to the differences in magnetostatic energy existing at grain boundaries. Sample OR-7A has lower power loss and smaller grain size. Its domain wall spacing was calculated by averaging the values obtained from 199 grains and it is <d> = 0.45 mm.

Sample OR-7C has higher power loss, and approximately the same distribution of grain orientation as sample OR-7A, but it has larger grain size. The average domain wall spacing calculated from 128 grains is <d> = 0.37 mm.

The results of this investigation are interpreted using the model developed by Pry and Bean [28], which predicts a direct proportionality between domain spacing and the eddy current loss. The eddy current loss is the dominant loss in grain oriented materials at low magnetizing frequency; therefore, the Pry and Bean model should predict the power losses of the materials under investigation. The proportionality between power losses and domain wall spacing has, however, not been experimentally observed, in fact, the samples with lower power loss have higher mean domain wall spacing. The relationship between the mean domain spacing and the total power loss proved that the domain wall spacing determined in static conditions may not be a relevant parameter related to power losses in electrical steels. From this point of view, one can presume the existence of another mechanism which may affect the loss in dynamic conditions. This mechanism could be related to the structural parameters of the material, like pinning centres affecting the domain wall movement and/or the homogeneity of the magnetic flux distribution in the material cross section.

There is another interesting result of this investigation. Let us consider an isolated cubic crystallite of grain oriented material containing two sorts of domains having magnetizations parallel or anti-parallel to its length. The 180° domain wall spacing, d, of the crystallite in the demagnetized state is given by the relation established by Kittel [62] :

$$d = \sqrt{\frac{\gamma L}{1.7\, I_s^2}} \tag{6.2}$$

where γ is the domain wall energy per unit area of the wall, I_s is the saturation magnetization, and L is the length of the crystallite. This relationship was obtained by minimizing the total magnetization energy of the crystallite, which is the sum of the magnetostatic and wall energies:

$$E_T = E_{ms} + E_{wall} = 1.7\, I_s^2\, d + \gamma\, \frac{L}{d} \tag{6.3}$$

where the magnetostatic energy is due to the interaction between magnetic free poles at the crystallite surface.

Free poles are expected to appear on the grain boundaries but the magnetostatic energy is greatly decreased when the domain distribution in each grain is closely related to that of the neighbouring grain. In a polycrystalline material, the effect of the magnetic interaction between neighbouring grains on the magnetostatic energy of one grain can be taken into account by introducing an effective field parameter describing the demagnetizing field from a polycrystalline matrix , $\delta < 1$, in the expression of magnetostatic energy in equation (6.3). Assuming a cubic grain in a polycrystalline material, the expression for the demagnetizing energy per unit surface has been deduced by Szpunar [15]:

$$E_{ms} = 1.7\, \delta^2\, I_s^2\, d \tag{6.4}$$

Thus, the magnetostatic energy of the magnetic poles appearing on the grain boundary is smaller than in an isolated crystallite, but still finite, so that the domain wall spacing is essentially determined by the mean size of the grain.

To analyze the influence of the magnetostatic energy of the free poles appearing at grain boundaries on the magnetic domain

Fig.6.3.a. Grain size - domain wall spacing correlation sample OR-1C

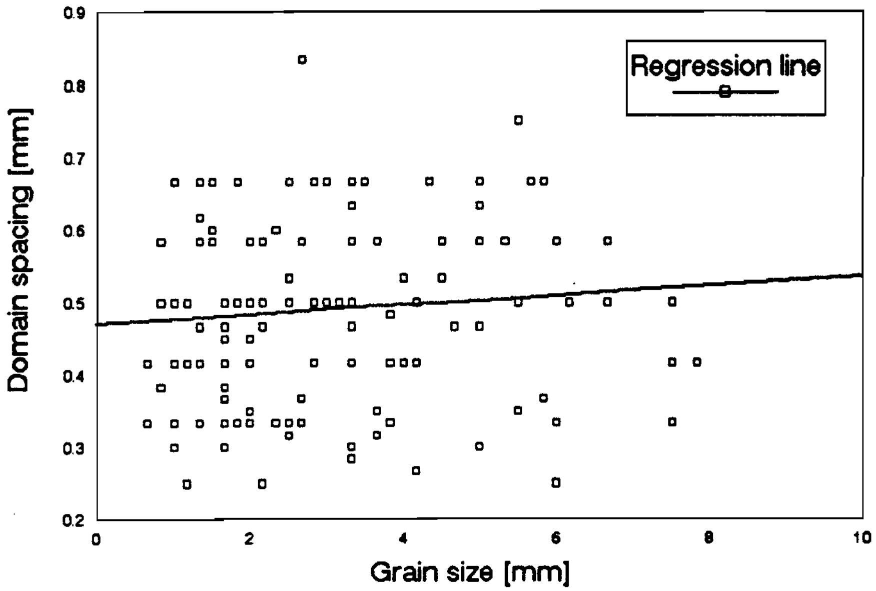

Fig.6.3.b. Grain size - domain wall spacing correlation sample OR-1B

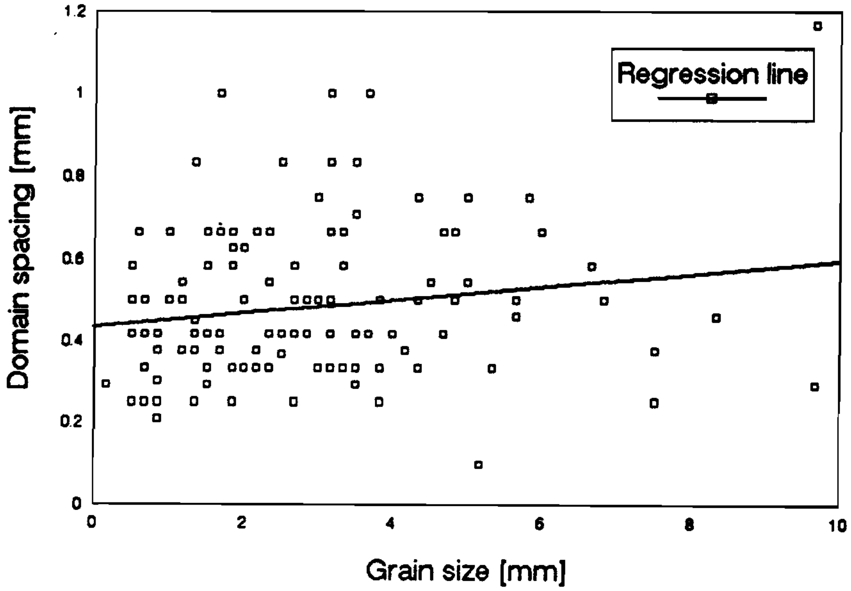

Fig.6.4.a. Grain size - domain wall spacing correlation
sample OR-7A

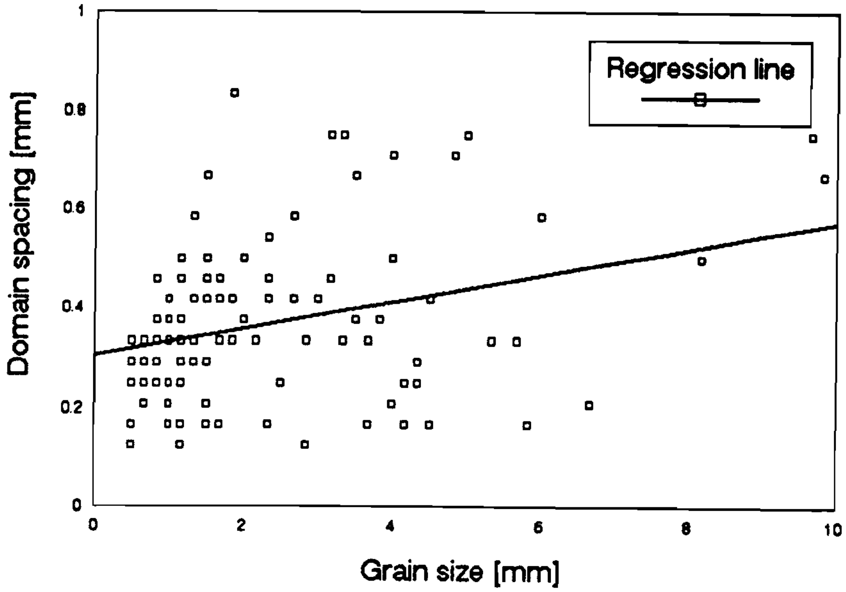

Fig.6.4.b. Grain size - domain wall spacing correlation
sample OR-7C

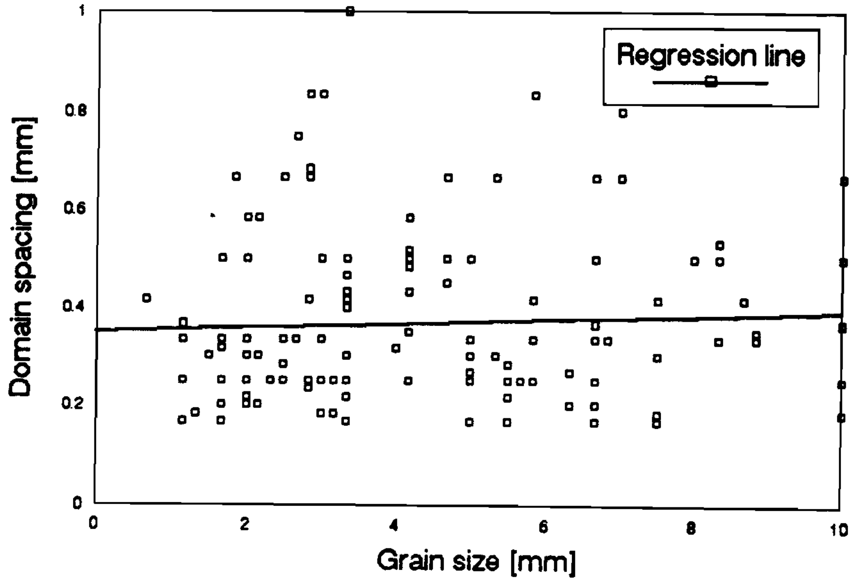

pattern, we plotted the domain wall spacing as a function of grain size. Graphs of the four samples are shown in Figures 6.3 (9 mil samples), and 6.4 (7 mil samples). From these graphs, one may say that there is no correlation between domain spacing and grain size. The regression analysis, however, demonstrates that, as the theory predicts, there may be a proportionality between these parameters, even if the correlation coefficient of the regression is very small. The conclusion is that the magnetostatic energy appearing at the grain boundaries has little influence on the magnetic domain pattern. As Imamura et al. [54] states, the important factor determining the size of domain wall spacing in each grain seems to be the magnetostatic energy created on the surface of the grain when the <100> direction is inclined with a small angle out of the sheet plane.

6.2. METHOD BASED ON BARKHAUSEN NOISE MEASUREMENTS TO CORRELATE TEXTURE, MICROSTRUCTURE AND POWER LOSSES

In this section, a method is proposed and tested to study the effects of crystallographic structure on magnetic Barkhausen noise (MBN), and its relation to power losses of electrical steel laminates. The method relates the MBN to power losses through a model based on domain wall displacement after they are released from pinning centres. Several specimens of the same class of materials with different power losses have been investigated using this method. The experimental results show that there is a clear correlation between the MBN power and the material quality (power loss). Since the magnetizing core and the pick-up coil are placed directly on the sample surface, this method offers the possibility for rapid and non-destructive evaluation of the power losses. The method is of practical importance, characterizing the magnetic properties of electrical steels.

6.2.1. Experimental method and apparatus

The setup employed in Magnetic Barkhausen Noise (MBN) experiments is quite simple. An external sweep field produced by a ferrite core magnet is applied to the specimen and the Barkhausen signal induced in a pick-up coil mounted on the specimen is amplified and analyzed. Measurements were performed at Queens's University using the experimental apparatus shown in Figure 6.5.

The MBN is released as a result of the change in the magnetic dipole moment caused by an external magnetic field. Neglecting the demagnetizing effect inherent in every magnetization discontinuity, the variation of the magnetic moment in the direction of the magnetizing field is expressed in the reduced form:

$$\Delta m_{\parallel} = I_s\,(2\Delta\nu\,\cos\gamma + \nu\,\Delta\cos\gamma) \tag{6.5}$$

where I_s is the saturation magnetization, ν is the volume of the magnetic domain and γ is the angle between the assumed magnetic dipole moment and the direction of the magnetizing field. The resulting change of flux in the sample is basically of the form given by Heiden and Storm [63]:

$$\Delta\Phi_{\parallel} = \frac{\mu_{rev}}{D}\,I_s\,(2\Delta\nu\,\cos\gamma + \nu\Delta\cos\gamma) \tag{6.6}$$

where μ_{rev} is the reversible permeability of the sample and D is the distance between the pole pieces of magnetizing core.

The effective change in the magnetic dipole moment in the direction perpendicular to the field is:

$$\Delta m_{\perp} = I_s\,(2\Delta\nu\,\sin\gamma + \nu\,\Delta\sin\gamma) \tag{6.7}$$

and the flux change produced in the sample in this direction is:

$$\Delta\Phi_{\perp} = \frac{1}{T}\,I_s\,(2\Delta\nu\,\sin\gamma + \nu\,\Delta\sin\gamma) \tag{6.8}$$

where T is the thickness of the sample. If the thickness T is much

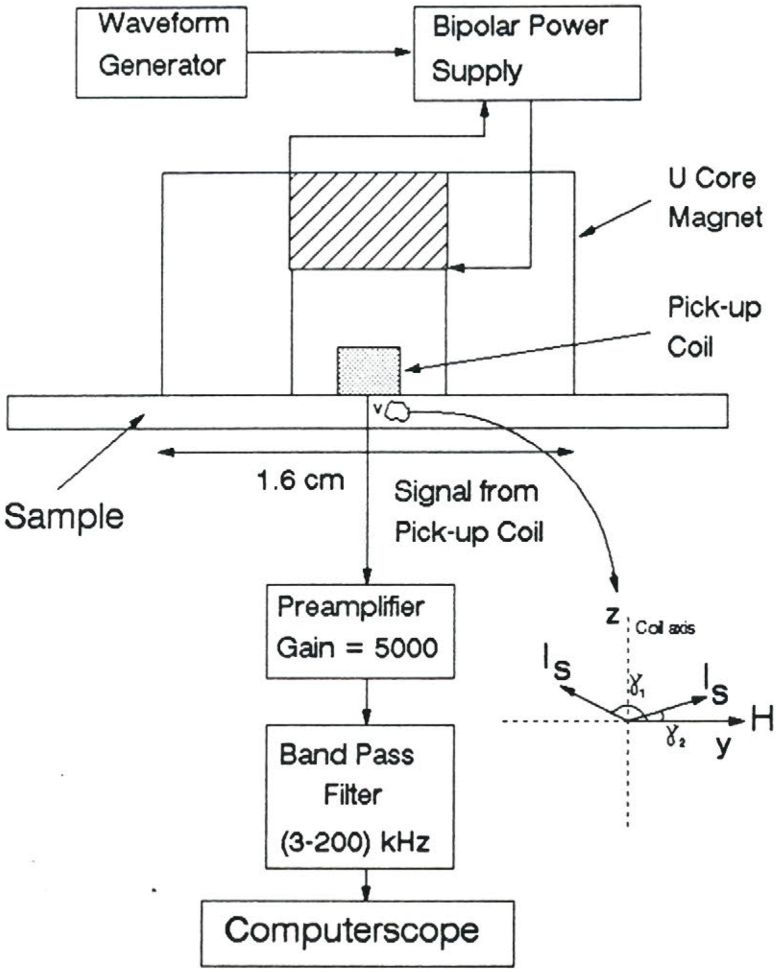

Fig.6.5. MBN instrument

smaller than the other two dimensions of the sample, $\mu_{rev} = 1$ in the sample normal direction.

Changing the magnetic moment causes a corresponding flux through the pick-up coil placed perpendicular to the direction of the magnetizing field (Saynajakangas, [64]):

$$\Phi_{\perp} = N \frac{R_{ms}}{R_{mc}+R_{ms}} \frac{1}{T} I_s \left(2\Delta\nu \sin\gamma + \nu \Delta\sin\gamma\right) \tag{6.9}$$

where:

N = number of turns of the coil

R_{ms} = reluctance of the sample between the pole pieces of the core

R_{mc} = reluctance of the coil.

In the case of a single 180° wall displacement, the relationship between the variation of the flux in the direction of the field and the same variation in a direction perpendicular to the field is obtained from equations (6.6) and (6.8):

$$\Delta\Phi_{\perp} = \Delta\Phi_{\parallel} \frac{D}{\mu_{rev} T} \tan\gamma \tag{6.10}$$

The voltage V(t) induced in the pick-up coil, due to the movement of a single wall, is caused by the variation of the flux:

$$V(t) = \frac{d\Phi_{\perp}}{dt} = \frac{d\Phi_{\parallel}}{dt} \frac{D}{\mu_{rev} T} \tan\gamma = C \frac{2 I_s}{T} \frac{\Delta\nu}{\Delta t} \sin\gamma \tag{6.11}$$

where C is the coupling constant.

These equations relate the MBN measurements generated in a direction perpendicular to the field to the theory used to interpret the MBN data based on the description of the bulk flux rate in the direction of the magnetizing field.

In practice, the simple model of changing local magnetization associated with a magnetic Barkhausen event as described by equation (6.11), does not take into account the resultant complicated coupling existing between the sample surface and the small normally oriented pick up coil. Nevertheless, the presented model outlines the basic principle of the instrument.

The apparatus used in the experiments consisted of a magnetic transducer, a magnetization generator, a preamplifier, and output equipment. The waveform generator produces a sinusoidal signal which is amplified by the bipolar power supply and applied to the ferrite sweep field coil. The sweep field frequency was 12 Hz, having an amplitude up to ±200 A/m (±250 mV). The voltage induced by the MBN at the sample surface was detected by an induction type probe whose axis is normal to the sample. This signal was amplified 5,000 times and passed through a wide band filter of flat response between 3 kHz and 200 kHz. The magnetic Barkhausen noise (MBN) signal waveform was monitored with a digital oscilloscope (computerscope). The signal was sampled at a rate of 2 μsec over a trace of 8 K samples (buffer size). This took place over a 16 msec time scale and constituted one trace. Eight traces were recorded at each measurement for subsequent retrieval and analysis.

The total gain of the amplifier is very large and the output voltage has a noise component caused by the magnetizing current, external magnetic stray fields in the transducer and the instrument itself. To eliminate the noise, only voltages above a certain threshold, here set at ±10 mV, were considered in the analysis. Then, the voltages V(t) measured in each of the time intervals were squared and the area below this spectrum calculated. A sum over all 8 traces of this squared voltage area was performed, and this value is referred to as the MBN power, P_{MBN}.

The theory of the power spectrum of MBN is presented by Mazzetti and Montalenti [65], taking into account the correlation between single Barkhausen pulses. It is also shown that this correlation is fully controlled by the demagnetizing field (i.e. by the sample permeability). Due to the space-time correlation between the magnetization transitions, the elementary Barkhausen jumps cluster into a large pulse which has the average duration $<\tau_{av}>$, and carries out the average flux $<\Delta\Phi_{av}>$. The area of the MBN power spectrum (Barkhausen noise power) can also be expressed as in Bertotti et al. [66]:

$$P = \int_0^\infty F(\omega)\, d\omega/2\pi = \dot{\Phi}\, \langle\dot{\phi}_{av}\rangle \qquad (6.12)$$

$$\textit{where:} \quad \langle\dot{\phi}_{av}\rangle = \frac{\langle\Delta\phi_{av}\rangle}{\langle\tau_{av}\rangle}$$

is the flux rate associated with a Barkhausen avalanche, $(d\Phi/dt)$ is the macroscopic flux rate, and $F(\omega)$ is the power spectrum. In the samples investigated within the induction range of interest, the bulk flux rate $(d\Phi/dt)$ is entirely caused by discontinuous movements of the domain walls, so that one can set:

$$\dot{\Phi} = n\, \Delta\phi \qquad (6.13)$$

where n is the average number of elementary events in unit time and $\Delta\Phi$ is the average flux change carried by an elementary event. On the other hand, the average flux change carried by a cluster is:

$$\langle\Delta\phi_{av}\rangle = \rho\, \Delta\phi \qquad (6.14)$$

where ρ is the average number of elementary events in a cluster. If we express the flux variation caused by an elementary event through the pick-up coil, using equation (6.10), the quantity measured in our experiment is related to the Barkhausen noise power measured in the direction of the field through the relationship:

$$P_{MBN} = C^{*}\, \dot{\Phi}\, \langle\dot{\phi}_{av}\rangle \langle\tan\gamma\rangle^{2} \qquad (6.15)$$

where $\langle\tan\gamma\rangle$ is the average value of $\tan\gamma$ over the number of elementary events and all the proportionality factors are combined into C^{*}. Relation (6.15) was deduced for a general case, where the sample magnetization rate had a constant average value, and the MBN was averaged over the whole hysteresis loop. Using this approach, the nonstationary character of MBN along the hysteresis loop was not taken into account (Bertotti, [69]).

In the present experiment, the duration of integration was higher than the period of the applied signal; the MBN, therefore, was averaged over the whole hysteresis loop. These measurements were performed with different sweep field amplitudes along the rolling direction (RD), and with constant field amplitude at various angles with respect to the rolling direction (RD).

6.2.2. Statistical interpretation of MBN

Magnetic Barkhausen Noise (MBN) analysis relates the magnetization process to the discontinuous movements of the domain walls. These wall movements reflect the interaction of Bloch walls with pinning centres at grain boundaries, dislocations, inclusions and precipitates. As a result, the domain wall energy has a component which fluctuates, depending on the structure of defects in material.

In grain oriented 3% Si steel, the magnetization process takes place predominantly through the 180° domain wall displacement caused by the driving force exerted on the wall:

$$F_d = 2 I_s H \cos\gamma \tag{6.16}$$

where γ is the angle between the external magnetic field H and the direction of spontaneous magnetization.

The presence of the pinning centres modifies the wall energy E_w with its position x. The perturbations encountered by the domain wall in its motion are assumed to have a random fluctuation. The gradient of this energy $dE_w/dx = F_r(x)$ acts as a retarding force to wall motion. The wall passes over a pinning centre if the driving force exceeds the retarding force $F_r(x)$ of the defect.

By means of this model one can correlate the MBN experimental data with factors related to the sample structure, which are responsible for the appearance of the pinning centres in the material (local stresses, precipitates, grain boundaries, etc). The local critical field by which the wall can get over one pinning centre is obtained from the equilibrium condition between the forces acting on the wall:

$$H_0 = \frac{F_r(x)_{max}}{2 I_s \cos\gamma} \tag{6.17}$$

According to Chikazumi [9], the number of pinning centres having a critical field from H_0 to (H_0+dH_0) is $f(H_0)\cdot dH_0$, where $f(H_0)$ has the dimension of a density of pinning centres per unit critical field. In general, $f(H_0)$ varies according to a gaussian distribution which is spread about $H_0 = 0$. Since H_0 is limited to a small range (dH_0), $f(H_0)$ is considered constant, $f(H_0) = f_0$. If the external field is increased from H to (H+dH), the irreversible magnetization produced in the sample is:

$$dI_{irr} = p\, f_0^2\, H\, dH \tag{6.18}$$

where p is a proportionality factor, $(f_0\cdot dH)$ is the number of displaced walls at each stroke of displacement, and the quantity $(f_0\cdot H)$ is proportional to the displacement of these walls.

To relate the irreversible change in magnetization produced by the sweep field H to the sample magnetic properties we will refer to the theory and experimental method developed by Alessandro et al. [67, 68]. In these papers, the statistical properties of MBN were predicted analytically by the solution of a Langevin equation. The MBN measurements were limited to a narrow magnetization interval ($\Delta B = 0.4$ T) centred around $B = 0$, where μ is generally constant. The dominant magnetization process is domain wall motion. Under these conditions, $d\Phi/dt$ is a stationary process having a constant average value $\langle d\Phi/dt\rangle = S\, dB/dt$. The expression deduced for the MBN power is similar to relation (6.12), but the noise parameters entering this equation depend linearly on the differential permeability $\mu = dB/dH$ of the material. $\langle \Delta\Phi_{av}\rangle$ and $\langle \tau_{av}\rangle$ were found proportional to $\mu^{3/2}$ and μ respectively. Thus, the MBN power is approximately described by the law:

$$P \propto \dot{\Phi} \left(\frac{\mu}{\mu_0} \right)^{1/2} \tag{6.19}$$

The differential permeability μ, as a measure of magnetostatic effects, changes along the hysteresis loop, thus affecting the MBN behaviour. For this reason, the MBN power in relation (6.19) will depend on the region of the hysteresis loop where the permeability μ is considered.

Let us analyze relation (6.19). One term of the right side of this equation is the differential permeability μ. Since in our experiment the MBN was averaged over the whole hysteresis loop at constant magnetic field (H=const.), we have to introduce in (6.19) an average value for the differential permeability. The expression for the average differential permeability when the field changes from 0 to H, is given by Chikazumi [9]:

$$<\mu> = \frac{I_{irr}}{H} = \frac{1}{2} p\ f_0^2\ H \tag{6.20}$$

and it represents the Raileigh's law.

The other term of the right side of equation (6.19) is the average macroscopic induction rate (dB/dt). This quantity is obtained from the frequency response of the specimen relative to the reversible permeability (Mazzetti and Montalenti, [65]). The frequency response of a specimen represents the r.m.s. voltage induced in the detecting coil by an a.c. current of constant r.m.s. value in the magnetizing coil plotted versus the magnetization frequency. Using this method, the macroscopic flux rates were experimentally determined for each sample.

Two sets of experiments were performed. In the first experiment, the intensity of the sweep field directed along the rolling direction (RD) was gradually increased. Substituting relation (6.20) in (6.19), and using equation (6.15), we obtained the dependence of MBN power on the sweep field H at a constant induction rate:

$$P_{MBN} \propto f_0 \, \langle \tan\gamma \rangle^2 \, H^{\frac{1}{2}} \approx f_0 \, \langle \gamma \rangle^2 \, H^{\frac{1}{2}} \qquad (6.21)$$

which is valid for small values of angle γ.

In the second set of experiments the MBN power was measured with constant H applied at different angles β from the rolling direction (RD) in the specimen plane. The results reflect the angular change of the driving force.

6.2.3. MBN in grain oriented materials

It is known that texture influences the bulk magnetic properties of grain oriented materials but little attention has been paid to the influence of texture on the domain wall dynamics at different stages of magnetization. The MBN experiments were performed on 3% Si-Fe laminates of different quality (power losses). The specimens are identified as OR-1A, OR-1B and OR-1C. The results obtained for these samples are presented in Figures 6.6 and 6.7.

The statistical parameters characterizing the Barkhausen noise are related to the macroscopic magnetic properties of the material (Bertotti, [29]). Equation (6.19) relates the MBN power to the average macroscopic induction rate and the differential permeability of the sample. The average macroscopic induction rate (dB/dt) can be obtained from the frequency response of the specimens, as it was previously presented. The measured induction rates for the three samples at 12 Hz are:

$$\left(\frac{dB}{dt}\right)_{OR\text{-}1A} = 1.01 \left(\frac{dB}{dt}\right)_{OR\text{-}1B} = 1.06 \left(\frac{dB}{dt}\right)_{OR\text{-}1C} \qquad (6.22)$$

This allows us to consider that the macroscopic induction rate (dB/dt) is approximately constant for the three investigated samples. In this case (constant induction rate), the MBN power is

Fig.6.6. **MBN power vs. magnetizing field**

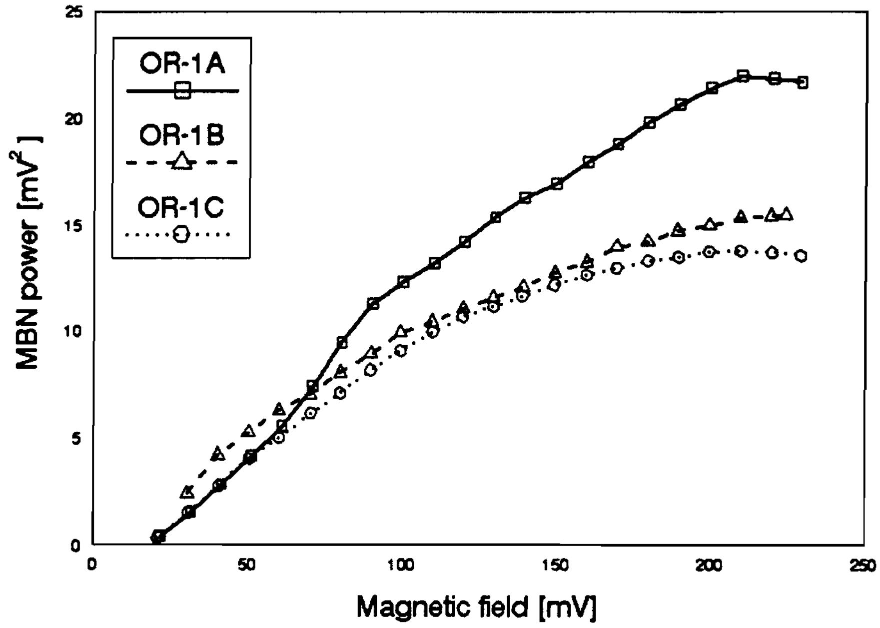

Fig.6.7. **MBN power vs. angle from RD**

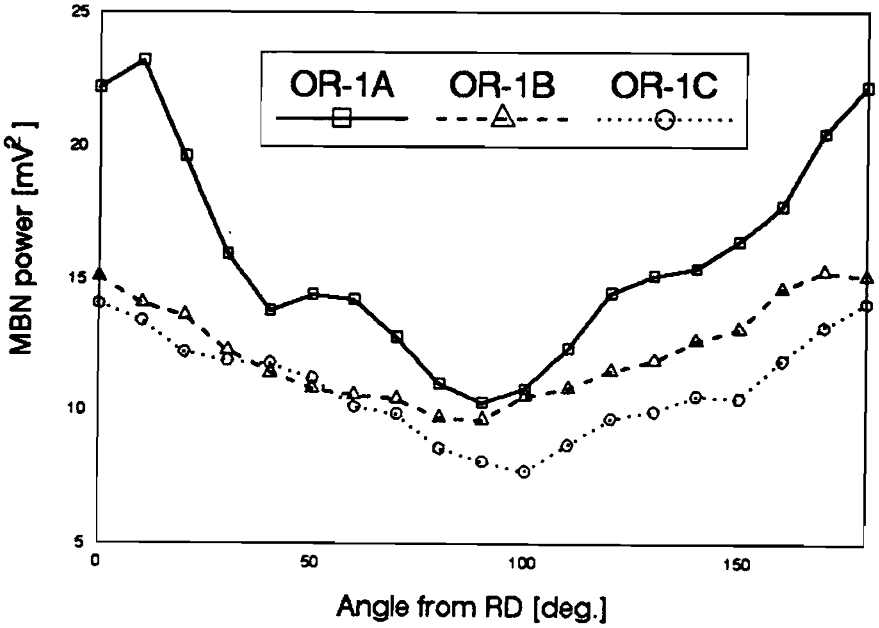

described by equation (6.21) and the results presented in Figure 6.6 illustrate the dependence of MBN power on the applied magnetic field for the three specimens. From these graphs, one can see that the relationship (6.21) is strongly supported by the experimental data. It is remarkable that equation (6.21) holds far beyond the Raileigh region, supporting the previous results published by Bertotti [69].

The differences between the three curves presented in Figure 6.6 are explained using equation (6.21), which describes the MBN power. In this expression, there are two terms related to material structure which are analyzed: $<\gamma>^2$ is a texture parameter, and f_0 is a structural parameter characterizing the material.

The texture parameter is calculated using the averaging over the grain orientation distribution function. If the grain orientation in the sample reference frame is represented by the three Euler angles $(\varphi_1, \phi, \varphi_2)$ and the grain orientation distribution function $f(g) = f(\varphi_1, \phi, \varphi_2)$ is known, the average value of $\tan\gamma \approx \sin\gamma$ (for small values of angle γ), is given by:

$$<\sin\gamma> = \frac{1}{8\pi^2} \oint \sin\gamma(g) f(\varphi_1, \phi, \varphi_2) \sin\phi \; d\varphi_1 d\phi d\varphi_2 \qquad (6.23)$$

where:

$$\sin\gamma(g) = \cos\phi \qquad (6.24)$$

For the three samples, the values of $<\tan\gamma> \approx <\cos\phi>$ calculated using equation (6.23) are presented in Table 6.2, together with the average domain spacing measured using the powder pattern technique.

The other term analyzed in equation (6.21) is the structural parameter f_0. First, let us assume a constant value of f_0 for the three samples, which means that the density of pinning centres is the same.

Table 6.2. Calculated average values of <sinγ> and measured domain wall spacing of the investigated specimens.

Sample	<sinγ>	Domain spacing
OR-1A	0.14	-
OR-1B	0.07	0.52 mm
OR-1C	0.11	0.49 mm
OR-7A	0.09	0.45 mm
OR-7C	0.10	0.37 mm

One can see in Figure 6.6 that sample OR-1A has, at constant value of the magnetizing field H, the highest value of MBN power (or $f_0 \cdot \langle\gamma\rangle^2$). The value of <tanγ> is larger in the OR-1A sample than in samples OR-1B and OR-1C. This result supports the data presented in Table 6.2. In samples OR-1B and OR-1C, the correlation between the MBN power and the texture parameter is no longer valid, which means that the structural parameter f_0 is not constant for the three samples, as was previously assumed.

According to the proposed model, the MBN power depends on the product $f_0 \cdot \langle\gamma\rangle^2$. Taking the calculated values of the texture parameter $\langle\gamma\rangle^2$ into consideration (Table 6.2), the experimental results of MBN power in Figure 6.6 should imply that the density of pinning centres per unit critical field, f_0, is higher in the OR-1B sample than in the OR-1C sample. The higher value of f_0 is equivalent to a higher number of walls contributing to magnetization when the magnetic field increases from H to (H+dH), because the number of moving walls is proportional to $f_0 \cdot dH$. In conclusion, the magnetization process is more homogeneous in the OR-1B sample than in the OR-1C sample, even when the domain wall spacing in Table 6.2 does not indicate this. We call this phenomenon the dynamic homogenization of the magnetization process.

For the samples investigated, the power losses presented in Table 3.2 are inversely proportional to the MBN power. It was demonstrated by Imamura et al. [54] that, in a single crystal of silicon iron, there is an inverse proportionality between the domain wall spacing d, and the out-of-plane angle of <100> easy magnetization direction. Generalizing this relationship to a polycrystalline material, one could write that the average domain wall spacing is:

$$\langle d \rangle \propto \frac{\sqrt{T}}{I_s \langle \sin\gamma \rangle} \tag{6.25}$$

where T is the sample thickness and $\langle \sin\gamma \rangle$ is an average value calculated using equation (6.23), and whose values for the investigated samples are presented in Table 6.2. Calculating the domain wall spacing with equation (6.25), we found that there exists a proportionality between the calculated values and the values obtained from direct measurements using the powder pattern technique. Thus, the texture data can be used for calculating the mean domain wall spacing in a grain oriented material.

As previously mentioned, the power losses decrease if there is a more uniform distribution of magnetic flux over the sample. Accordingly, the OR-1A sample with the most uniform domain structure (refined domain structure) has the lowest losses. However, one can see from Table 6.2 that the power losses in the other samples are not correctly predicted by domain wall spacing, in the sense that there is not a direct proportionality between these two parameters. This observation applies to both cases where the average domain spacing is either calculated from the texture function (ODF), or measured directly.

The present model developed to interpret the MBN power represents a relationship between the hysteresis and dynamic losses. Using it, one could explain the discrepancy between the experimental results and the values predicted by the Pry and Bean [28] model.

To verify the proposed method, the investigation of grain oriented materials using Barkhausen noise was extended, and other 9 mil samples were studied, namely OR-3A and OR-3B. New sets of results were obtained following investigation of the 7 mil samples OR-7A, OR-7B, and OR-7C. Clearly, these results (presented in chapter 8.6) indicate that the simple correlation between power losses and MBN power is valid over a large range of power losses for the same class of materials with thicknesses of either 9 mil (= 0.22 mm) or 7 mil (= 0.17 mm). The basic result of this study is that the lower power losses in grain oriented materials are obtained in samples where the dynamic conditions of domain wall movement make the distribution of the magnetic flux more homogeneous.

In the second series of experiments, the MBN power was measured with H applied at different angles β from the rolling direction (RD); the results are shown in Figure 6.7. The amplitude of the magnetic field was constant and much lower than the anisotropy field, which is approximately $37 \cdot 10^3$ A/m for the studied material. At such field values, no magnetic rotation occurs regardless of the direction of the field. The number of Barkhausen noise events decreases as the angle β increases, due to the reduced driving force with the angle, and an increase in the number of impassable pinning centres.

The angular dependence of the driving force is expressed by relation (6.16). Using the Euler angles $(\varphi_1, \phi, \varphi_2)$, the cosine of the angle between the <100> direction of the grain and a direction lying in the sheet plane at angle β from RD is:

$$\begin{aligned} \cos\gamma(\beta) = {} & (\cos\varphi_1 \cos\varphi_2 - \sin\varphi_1 \sin\varphi_2 \cos\phi) \cos\beta + \\ & + (\sin\varphi_1 \cos\varphi_2 + \cos\varphi_1 \sin\varphi_2 \cos\phi) \sin\beta \end{aligned} \tag{6.26}$$

The average value of the above cosines for the whole specimen is obtained using the orientation distribution function $f(\varphi_1, \phi, \varphi_2)$ as a weight function:

$$\langle\cos\gamma(\beta)\rangle = \oint \cos\gamma(\beta)\, f(\varphi_1, \phi, \varphi_2) \sin\phi \, d\varphi_1 \, d\phi \, d\varphi_2 \tag{6.27}$$

Fig.6.8. The dependence of MBN power on <cos(gamma)>

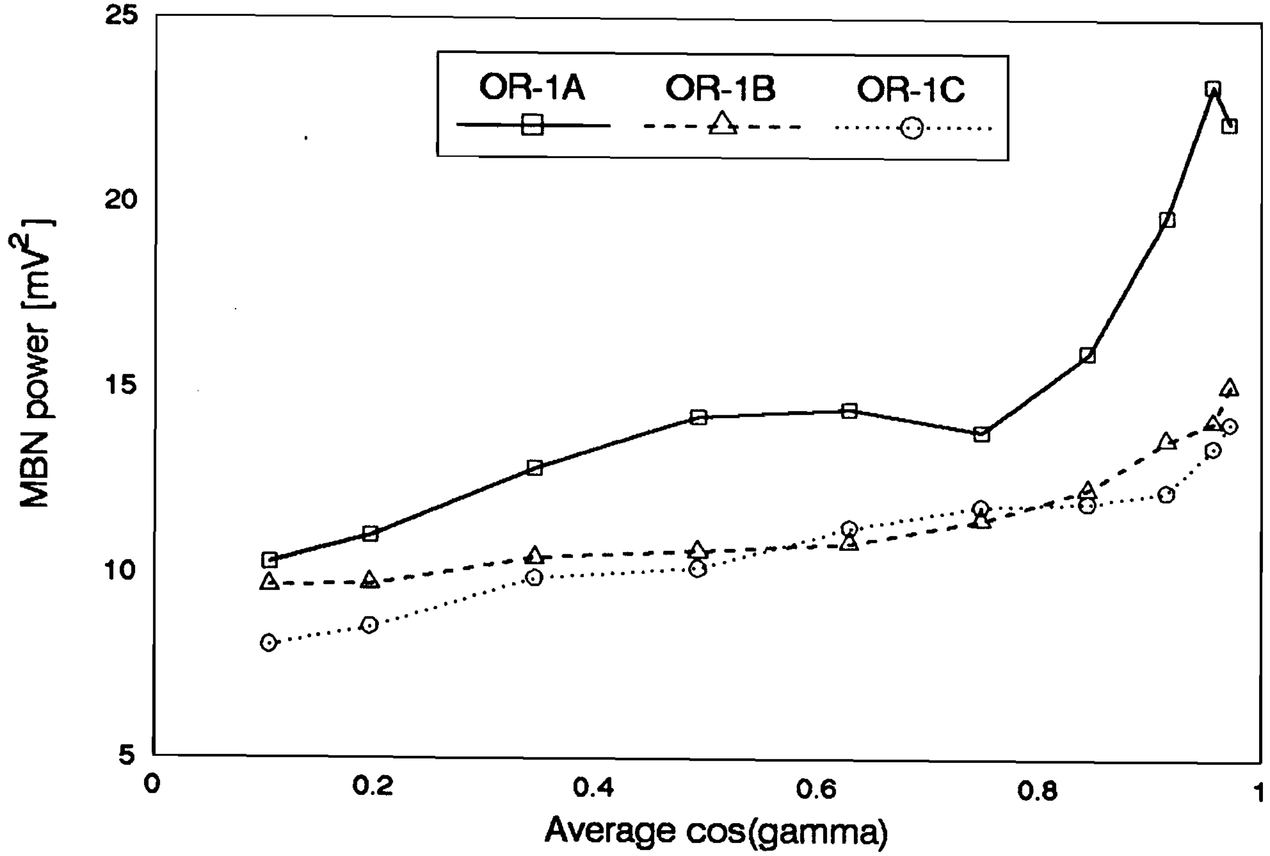

The plot of the MBN power versus <cos $\gamma(\beta)$>, calculated using relation (6.27) for the three samples, is shown in Figure 6.8. For the OR-1C and OR-1B samples, a linear relationship between the differential permeability and <cos Θ> is observed. This confirms that the driving force obeys the angular dependence law given by equation (6.16). The presence of the supplementary domain structure in sample OR-1A makes this relationship more complicated.

In summary, the method proposed for analyzing the anisotropy of the MBN power is useful for:

- detecting the presence of the crystallographic texture in a ferromagnetic material;
- identification of the easy magnetization direction;
- obtaining quantitative information about the magnetization anisotropy.

6.2.4. MBN in non-oriented materials

Magnetic Barkhausen noise (MBN) measurements were performed on four samples of non-oriented silicon steel which had been elongated by 0%, 2%, 6% and 12%, respectively. Following elongation, the crystallographic texture and the grain size of these samples were modified and, as a result, the power losses and the permeability changed. As demonstrated by Bertotti [70], the change of the macroscopic magnetic behaviour of the material is reflected in a profound modification of the microscopic dynamics of the domain walls to which MBN is related. Barkhausen noise investigation of the four samples gives the MBN power as a function of sweep field amplitude, and as a function of angle with respect to the rolling direction. The results are presented in Figures 6.9 and 6.10.

The measurements of the MBN power illustrate that the magnetic anisotropy in all four samples is small, despite an observed variation in the background of the MBN signal. Samples elongated by 2% to 12% demonstrated a lower MBN signal than the sample which was not elongated. Figure 6.10 demonstrates that the anisotropy of the

Fig.6.9. MBN power vs. sweep field for non-oriented samples

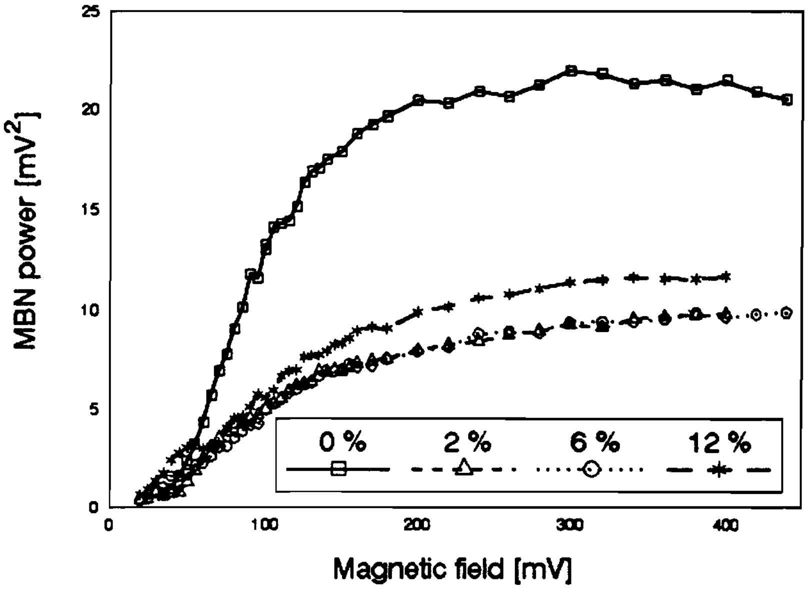

Fig.6.10. MBN power vs. angle from RD for non-oriented samples

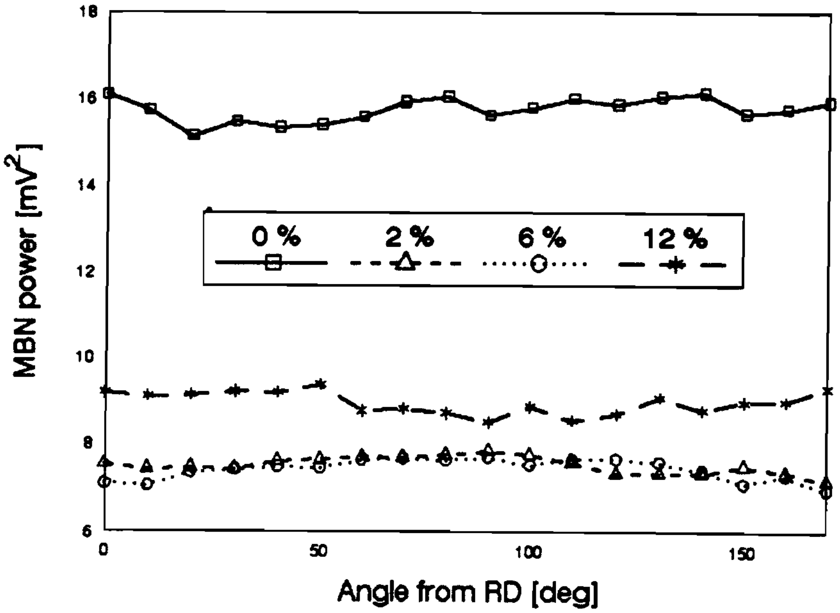

Barkhausen noise in all four samples is negligible when compared to the relative changes of the background MBN signal. The sample with 0% elongation has the highest MBN background signal, followed by the sample with 12% elongation. Samples with 2% and 6% elongation, have the smallest signal. The MBN power measured as a function of sweep field (Figure 6.9) demonstrates the same features in the level of MBN in the different samples as the results presented in Figure 6.10.

In interpreting these results, we use the model developed in this chapter, in which the MBN power is proportional to the product $f_0 \cdot \langle\gamma\rangle^2$. For a randomly oriented ferromagnetic sample with positive anisotropy constant K_1, the average value of angle γ is calculated as follows:

We assume that the magnetic flux within the induction range of interest results from discontinuous movements of the domain walls, so that the domain magnetizations stay in one of the three <100> directions closest to the direction of the applied field. The maximum deviation of magnetization from the applied field direction occurs when the <111> axis of a crystallite is parallel to the direction of the field. Therefore, the angle between the <100> easy axis and the direction of applied field cannot exceed $\gamma_{max} = 54.73°$. The distribution of easy magnetization directions in a random sample is, thus, confined to the solid angle the vertical half-angle of which is 54.73°. In this case, the average value of $\cos\gamma$ over all possible orientations of the <100> direction in the indicated region is calculated in Chikazumi [9], and has the value $\langle\cos\gamma\rangle = 0.832$, from where $\langle\sin\gamma\rangle = 0.554$.

One notices that there is a proportionality between the values of the power losses of non-oriented samples presented in Table 3.4 and the corresponding values of MBN power. As previously demonstrated, the MBN power is proportional to the product $f_0 \cdot \langle\gamma\rangle^2$. If we now consider that the average value $\langle\gamma\rangle^2$ is constant for all four samples, the power losses are proportional to f_0, the density of pinning centres per unit magnetic field. This structural parameter is associated with the grain size because the grain boundaries represent places with high density pinning points. The relationship between the grain size and the value of power losses in non-oriented samples demonstrates that the main source of loss in these materials is the hysteresis loss. Similar results were reported by Saynajakangas and Otala [106].

6.2.5. Possible application of the developed method for measurements of losses

The main purpose of this chapter was to demonstrate that the proposed method of investigation based on MBN measurements is capable of predicting the behaviour of losses in all analyzed materials. For both grain oriented and non-oriented electrical steels, the loss behaviour in the useful induction range is basically governed by f_0. This parameter contains all the relevant information required to correlate the losses with the dynamics of domain structure.

The physical origin of this parameter is not clear. In non-oriented materials, f_0 could be related to the grain size because of the domain wall pinning at the grain boundaries. In grain oriented materials, f_0 may be related to other structural factors such as dislocations, stresses, precipitates, scratches on the material surface, supplementary magnetic domain structure, etc. Thus, understanding the relationship between the structure and the value of f_0 is of great importance in developing methods of loss reduction in electrical steels.

Using the MBN measurements, the power losses of different electrical steels could be readily compared. Quantitative measurements of power losses are also possible if the instrument is calibrated using the specimens with known values of the power losses.

CHAPTER 7.

NEUTRON SCATTERING METHODS FOR MAGNETIC TEXTURE DETERMINATION

INTRODUCTION

Neutrons are scattered by interaction with nuclei and atomic magnetic moments. Due to the latter interaction, neutron diffraction has become a unique tool for analyzing the magnetic structures. In this chapter, we discuss various possibilities for using neutrons to investigate the orientation distribution of atomic magnetic moments in ferromagnetic materials. The main advantage of these methods is that the neutrons, penetrating deeply into the material, reveal the arrangement of atomic magnetic moments inside the sample.

The possibility of using neutron diffraction to measure the orientation distribution of the magnetic moments has attracted researchers for some time. The first attempt to measure magnetic texture by Szpunar et al. [19] and the research work which followed [20-22], were not conclusive. The work presented here is an attempt to solve this age-old problem, and to propose methods which can be used to obtain the statistical distribution of the magnetic moments from the magnetic part of neutron diffraction data.

7.1. MAGNETIC TEXTURE

The concept of crystallographic texture can be generalized to describe the density distribution of the atomic magnetic moments in a polycrystalline material. This distribution is called the magnetic texture.

In iron, the magnetocrystalline energy keeps the atomic magnetic moments aligned along the <100> easy magnetization directions. In several situations, the relationship between the magnetic texture and the crystallographic texture can be readily determined (Bunge, [22]):

(a) In the demagnetized state, the magnetic moments are distributed with equal probability along the six <100> directions. Under this assumption, the magnetic texture is identical to the (100) crystallographic texture.

(b) In weak magnetic fields, the spontaneous magnetization is still aligned along the easy magnetization directions. Thus, the magnetic texture is still related to the crystallographic texture, but the symmetry of the orientation distribution of magnetic moments is no longer cubic.

(c) In high magnetic fields, the spontaneous magnetization is no longer parallel to the <100> crystallographic directions. In this case, the magnetic texture is related only to the sample coordinate system.

7.2. METHOD OF MEASURING MAGNETIC TEXTURE USING NON-POLARIZED NEUTRON DIFFRACTION

7.2.1. Experimental method

When the neutron beam is unpolarized, the diffracted intensity from the lattice plane {hkl} is proportional to the differential scattering cross section of an atom containing a nuclear and a magnetic part (Bacon, [71]):

$$d\sigma = b^2 + q^2 p^2 \tag{7.1}$$

In this formula, b is the coherent scattering amplitude of the atomic nuclei and p is the magnetic scattering amplitude of atoms. The factor q is the magnitude of the magnetic interaction vector, and is equal to $\sin\psi$, where ψ is the angle between the magnetic moment and the direction of the diffraction vector. The diffraction vector (**Δk**) bisects the incident and diffracted neutron beams. The relationship between various vectors involved in the neutron diffraction is illustrated in Figure 7.1. Vector **m** is a unit vector parallel to the atomic magnetic moment. The magnitude of vector **q** is equal to the projection of vector **m** onto the plane perpendicular to vector **Δk**, and the direction of **q** is parallel to this plane.

The total elastic scattering of neutrons is a function of the reflecting plane (hkl), neutron wavelength (λ = 1.05 Å), and the magnetic scattering amplitude of atoms. To calculate the maximum magnitude of possible magnetic scattering from a single domain, we used the neutron diffraction data given in Bacon [71]. The nuclear scattering length for iron is b_{Fe} = 9.45 fm, and the magnetic scattering is given by the formula:

$$p^2 = [\, s_m F(\Delta k) \langle S \rangle \,]^2 \tag{7.2}$$

where the magnetic scattering length is:

$$s_m = 5.39\ fm \tag{7.3}$$

the magnetic form factor for the (110) reflection is:

$$F(\Delta k) = 0.77$$

and the effective spin is calculated as:

$$\langle S \rangle = \frac{I_s}{N} \frac{1}{2\mu_B} \tag{7.4}$$

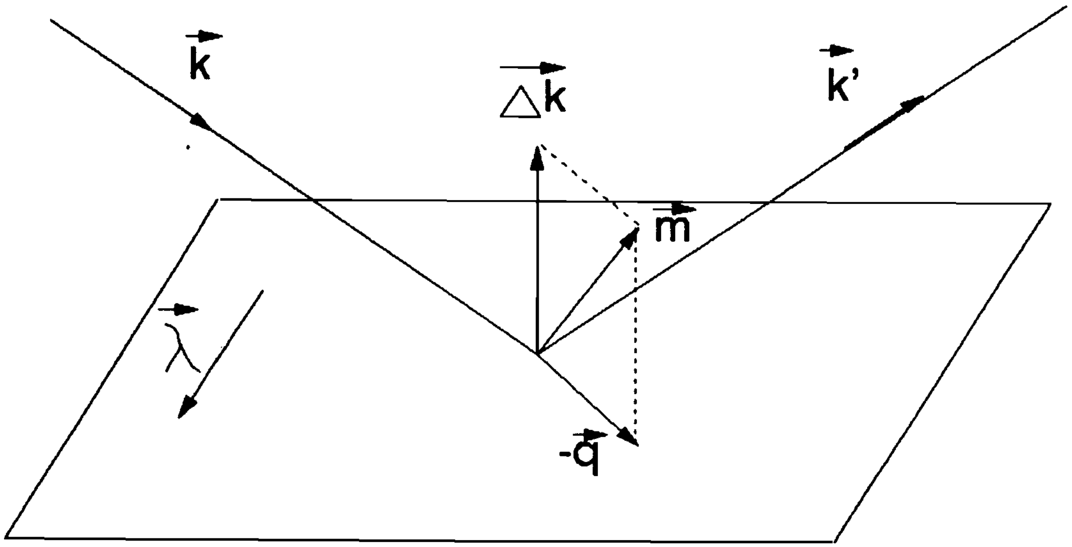

Fig.7.1. Relation between various vectors involved in neutron diffraction

where I_s is the spontaneous magnetization (= 1707 Gauss for iron), N is the number density of iron atoms in steel ($N = (4/3.591^3)\cdot 10^{24}$ ions/cm^3), and $\mu_B = 9.274\cdot 10^{21}$ erg/gauss. With these values, we then get:

$$b^2 = 89.3\ \text{fm}^2$$
$$p^2 = 19.5\ \text{fm}^2\ .$$

In the diffraction experiment, neutron intensity is measured as a function of scattering angle, 2θ. The neutron wavelength is denoted as λ. The magnetic scattering amplitude, p, decreases rapidly with increasing $(\sin\theta)/\lambda$ and this dependency has been tried previously to analyze the magnetic contribution to the total scattering [19],[20]. When this method is used, both the (110) and (220) pole figure were measured. The (220) pole figure represents essentially the sample crystallographic texture because the contribution of the magnetic scattering to the total diffracted intensity is negligible, while the (110) pole figure contains both the crystallographic and magnetic textures. The disadvantage of using this method of magnetic scattering separation is that the geometry of the experiment differs from one pole figure measurement to another and errors are possible. We also attempted to separate the magnetic contribution of the total diffracted intensity by measuring and analyzing the (110) and (220) pole figures. This method of separation has, however, not produced reliable results because various geometrical corrections which must be introduced made interpretation of the obtained data questionable.

To obtain the magnetic contribution to the total scattering, (110) pole figures were measured for the demagnetized sample, and also for the sample magnetized at a certain value of the external magnetic field. The geometry of this experiment is shown in Figure 7.2. Initially, this method was tested using a soft iron rod which was carefully demagnetized using a varitran. The orientation distribution of the grains in this sample was practically random. During the experiment, the sample was tilted around an axis

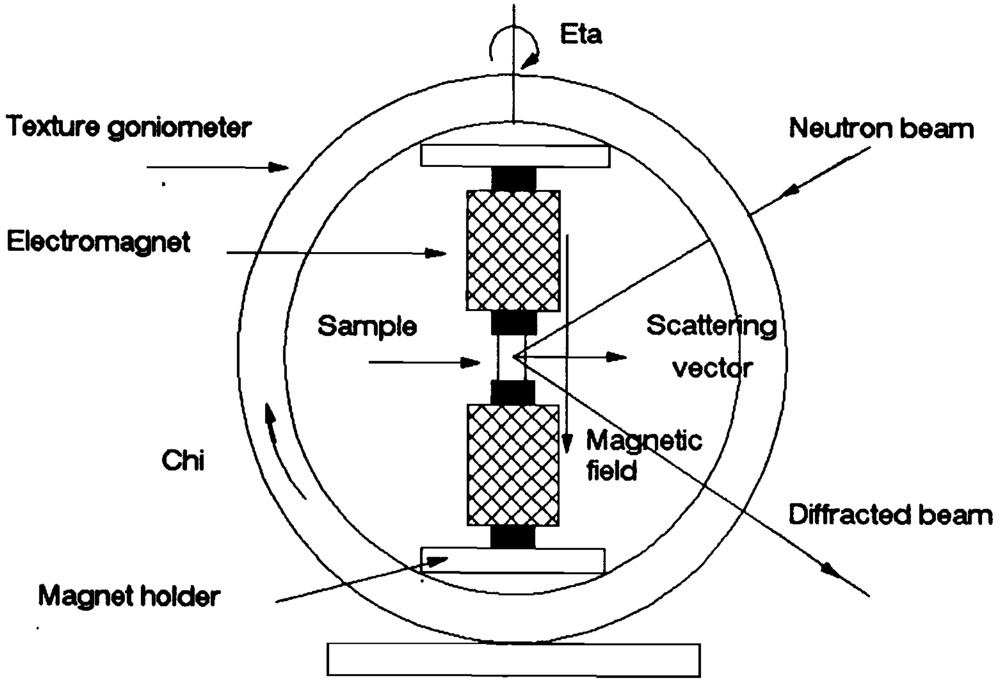

Fig.7.2. Setup for magnetic texture measurements using non-polarized neutrons

Fig.7.3. Regression of magnetic signal
Test sample

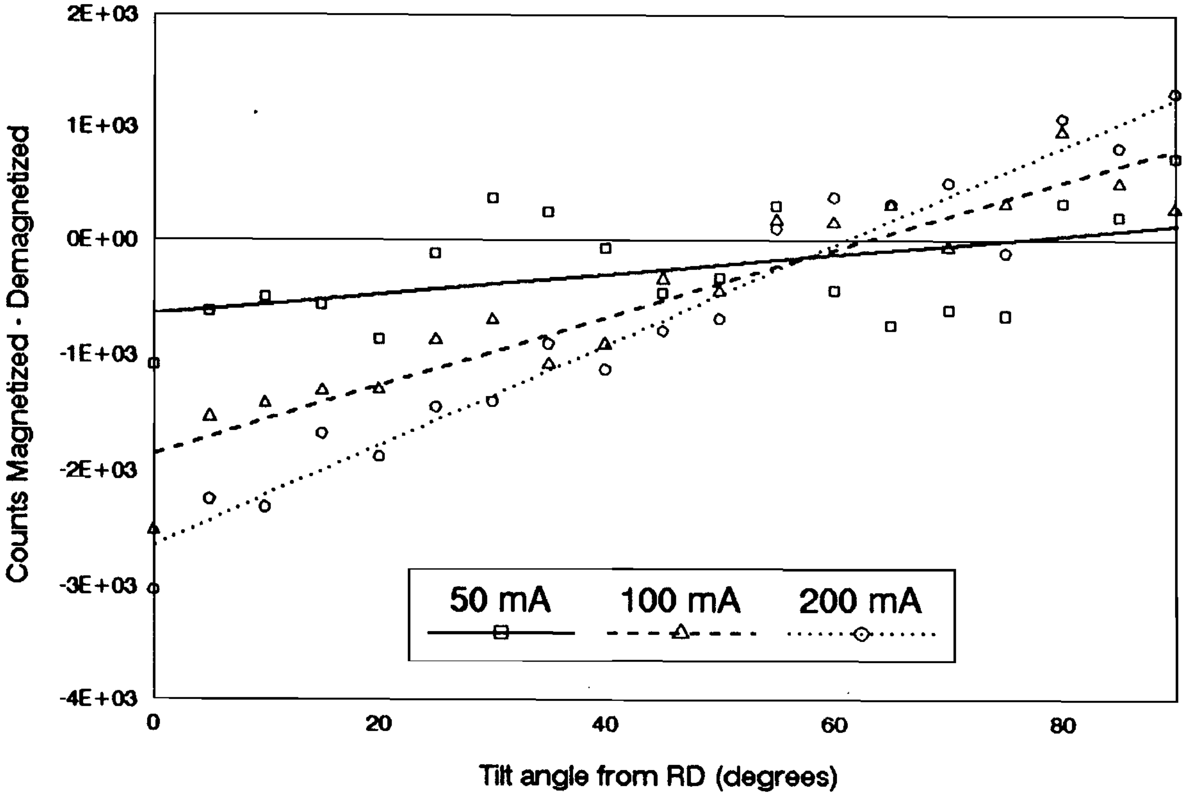

perpendicular to the rolling direction. The magnetic field was oriented parallel to the rolling direction, and was incrementally increased as the current was increased through the magnetizing coils; the (110) diffracted intensity was recorded at every 5° angular step. Figure 7.3 shows the count difference between the diffracted neutron intensities obtained from the magnetized and demagnetized samples. This test clearly demonstrated the practical possibility of separating the magnetic scattering by measuring the total elastic scattering from the demagnetized and magnetized sample.

It is of practical interest to determine the sensitivity of the method, i.e. the maximum and minimum values of the magnetic signal contained in the diffracted intensity measured in this experiment. If we assume that the distribution of atomic magnetic moments for the demagnetized sample is completely random, the average value of $q^2 = \sin^2\psi$ over all possible orientations of magnetic moment is 2/3. In this case, the differential scattering cross section is:

$$d\sigma_{demag} = b^2 + \frac{2}{3} p^2 = 102.3 \ fm^2 \qquad (7.5)$$

When the magnetic moment vector is parallel to the scattering vector, $\sin^2\psi = 0$ and the difference:

$$d\sigma_{|} - d\sigma_{demag} = b^2 - d\sigma_{demag} = -13.0 \ fm^2 \qquad (7.6)$$

represents -12.7% of $d\sigma_{demag}$. The other extreme value of the scattering cross section is obtained when the magnetic moment vector is perpendicular to the scattering vector. In this case, $\sin^2\psi = 1$ and the scattering cross section

$$d\sigma_{\perp} = b^2 + p^2 = 108.8 \ fm^2 \qquad (7.7)$$

Then, the difference:

$$d\sigma_{\perp} - d\sigma_{demag} = 6.5\ fm^2 \tag{7.8}$$

represents a +6.4% change from the scattering cross section of the demagnetized sample. In practice, the magnetic part of the total scattering lies anywhere between these two extreme values. Because the measurable signal from the magnetic texture is a small fraction of the total intensity, long counting times are required to determine the magnetic portion of the pole figure with unpolarized neutrons.

The experiments measuring the magnetic texture using non-polarized neutron diffraction were performed at Chalk River Nuclear Laboratory on non-oriented silicon steel. The average grain size of the material was 30 μm. The statistical error of neutron diffracted intensity related to an insufficient number of grains in the examined specimen is, therefore, negligible.

Strips having dimensions of 10 x 50 x 0.4 mm^3 were cut from the sheet and clamped together forming a parallelepiped with a cross section area of 10 mm^2. The long dimension of the sample is parallel to the sheet rolling direction (RD). This sample was placed between the pole pieces of an electromagnet, and the whole ensemble was mounted in the texture goniometer. The pole figure measurement was conducted using a pseudo-equal area scanning routine with 1020 points per pole figure. The background pole figure was measured with the neutron radiation detector shifted 3° from the (110) Bragg angle, $2\theta = 49.6°$.

In this experiment, the sample was rotated 90° from the standard position used for texture measurements, such that the centre of the pole figure represents now the sheet rolling (RD) direction. As a result, we have to redefine the angular coordinates of the sample reference frame. Thus, χ is the angle between the diffraction vector and rolling direction (RD) and η is the angle between the diffraction vector and the plane defined by the normal and rolling directions.

7.2.2. Separating the magnetic part from the total neutron scattering

Two major problems must be solved before any information about the magnetic texture can be obtained. The first problem, which is discussed in this paragraph, is to separate the magnetic and nuclear scattering components in the whole angular space which is scanned during the measurements of the crystallographic texture. The second problem to be solved is to relate the experimentally obtained magnetic scattering data to the actual distribution of magnetic moment orientations. This problem will be treated in the next paragraph.

In order to separate the magnetic part from the total scattering, we used pole figures obtained from different magnetic field strengths. The procedure was as follows:

The first (110) pole figure was measured with the sample carefully demagnetized by a varitran. In this state, the specimen does not display remanent magnetization in any direction. However, the distribution of magnetic moments may not necessarily be random, but it is expected to follow the distribution of easy magnetic directions which coincides with (100) pole figure for the demagnetized specimen, $P_{(100)}(\chi,\eta)$. Thus, for the demagnetized specimen, the magnetic contribution is estimated by calculating the average value of q^2 using the equation:

$$<q^2> = \frac{1}{2\pi}\int_0^{\frac{\pi}{2}}\int_0^{2\pi} \sin^2\psi \; P_{(100)}(\chi',\eta') \sin\chi' \, d\chi' \, d\eta' \approx \frac{2}{3} \qquad (7.9)$$

which proved to be approximately constant (= 2/3) for any point of the pole figure of the investigated sample (weak textured). In the above equation, the magnitude of q^2 is:

$$\sin^2\psi = 1 - [\, \sin\chi \, \cos(\eta-\eta') \, \sin\chi' + \cos\chi \, \cos\chi' \,]^2 \qquad (7.10)$$

Thus, we can assume that the pole figure given in Figure 7.4

represents the sample crystallographic texture because the contribution of magnetic scattering in the pole figure angular space is the same.

A second pole figure was measured with an electromagnet current of 150 mA, which produced an estimated internal magnetic induction of 1.1 T. The direction of the applied magnetic field was parallel to the rolling direction (RD) of the sample. In this case, the pole figure represents a sum of both the crystallographic and magnetic textures. All measured pole figures were corrected for the background (point by point subtraction), but were not normalized using the random sample intensity.

The separation of the magnetic part from the total diffracted intensity was accomplished by subtracting the (110) pole figure of the demagnetized sample from the (110) pole figures of the magnetized sample. The magnetic scattering is always associated with the total elastic scattering intensity (see the expression for the cross section, equation 7.1). Therefore, in a textured material, the experimental magnetic pole figure is to be weighted with the pole density of the measured pole figure (hkl). The magnetic scattering in each direction of the pole figure angular space, $D(\chi,\eta)$, is related to the magnetic texture existing in the sample at the specific field ($H \neq 0$) through the following equation:

$$D(\chi,\eta) = \frac{W_{(110)}(\chi,\eta)}{2\pi}\left[\int_0^{\frac{\pi}{2}}\int_0^{2\pi}\sin^2\psi\, M(\chi',\eta')\,\sin\chi'\,d\chi'\,d\eta' - \frac{2}{3}\right] \tag{7.11}$$

where $M(\chi,\eta)$ is the unknown magnetic texture and $W_{(110)}(\chi,\eta)$ is the weighting function obtained from the (110) crystallographic pole figure.

The experimental magnetic scattering, which is proportional to $D(\chi,\eta)$, measured at a magnetizing current equal to 150 mA is plotted in Figure 7.5.

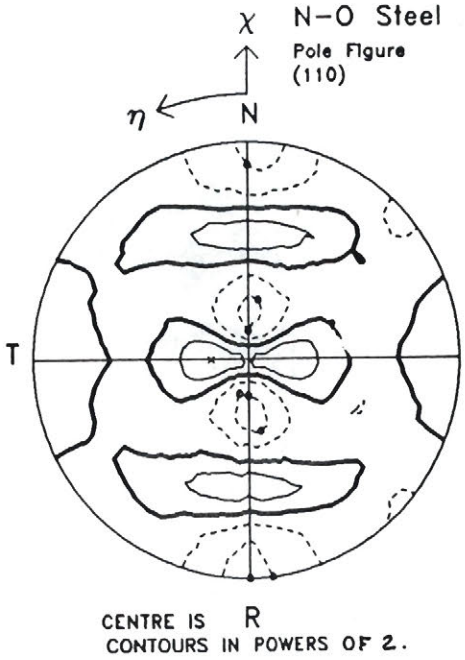

Fig.7.4. (110) pole figure of the demagnetized sample

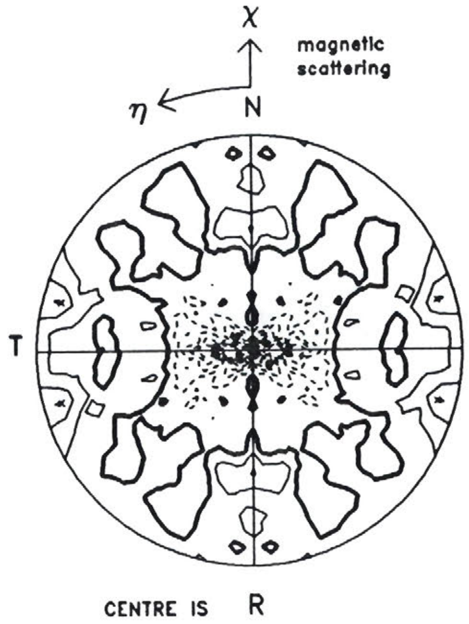

Fig.7.5. Magnetic scattering at 150 mA magnetizing current

7.2.3. Magnetic texture determination

The second problem which must be solved is to relate the experimental magnetic pole figure to the underlying distribution of magnetic moment orientations. Unlike diffraction from crystal planes, the scattering from a magnetic domain yields intensity over all specimen orientations, weighted by q^2. Thus, the measured magnetic pole figure is always a broad distribution from which the underlying magnetic texture must be calculated. We propose for the restoration of the underlying magnetic texture the maximum entropy method which yields the underlying distribution of magnetic moment orientations with the least possible structure, consistent with the measured magnetic signal. In other words, the resulting distribution is the most uniform, by definition of maximum entropy. This method is well described in the context of image reconstruction [72 - 74], NMR spectral analysis [75,76] and in more general works [77,78].

To obtain information about the magnetic texture, equation (7.11) must be solved. We shall discuss the general case where the magnetic texture is described in the sample coordinate system. The sample has orthorhombic symmetry and the magnetic field is applied along the rolling direction which is one of the symmetry axis. Thus, it is reasonable to assume that the magnetic texture also has orthorhombic symmetry. The measured differences between the magnetized and demagnetized sample have been symmetrized in quadrants to produce Figure 7.5.

The system of equations represented by relation (7.11) is, therefore, reduced to the first quadrant of the pole figure. In a discrete representation of the pole figure, using a 5° interval for both angles χ and η, the first quadrant contains $19 \times 19 = 361$ points. The first attempt to solve equation (7.11) as a system of 361 equations with 361 unknowns $M(\chi,\eta)$ failed. The matrix of this system is nearly singular due to the slow variation of the $\sin^2\psi$ coefficients.

For this reason, we proposed a different method of solving the magnetic texture problem. In this method, the least-biased magnetic pole figure to be restored from experimental magnetic scattering data, has maximum entropy. The magnetic pole figure is represented as a sequence of positive values in the angular space of the sample reference frame:

$$M(\chi_j, \eta_j) = M(\boldsymbol{x}_j) \geq 0 \tag{7.12}$$

where the unit vector $\boldsymbol{x}_j$ denotes the direction (χ_j, η_j).

The entropy E of this set of values is defined as:

$$E = -\sum_{j=1}^{J} M(\boldsymbol{x}_j) \ln M(\boldsymbol{x}_j) \tag{7.13}$$

and it is a measure of the amount of information represented by a $M(\chi_j, \eta_j)$ distribution. Positivity is assured since entropy does not exist if any $M(\chi_j, \eta_j)$ are negative. We aim to maximize E subject to the constraints of experimental observations.

Using the discrete representation, equation (7.11) becomes:

$$D(\boldsymbol{y}_n) = \sum_{j=1}^{J} M(\boldsymbol{x}_j)\, S(\boldsymbol{y}_n, \boldsymbol{x}_j) - \frac{2}{3} \tag{7.14}$$

where:

$$S(\boldsymbol{y}_n, \boldsymbol{x}_j) = \frac{\Delta\chi\, \Delta\eta}{2\pi} W_{110}(\boldsymbol{y}_n) \sin^2\psi \sin\chi_j \tag{7.15}$$

Following the maximum entropy formalism, we constructed the variational principle for the solution set $M(\chi_j, \eta_j)$ subject to constraint equation (7.14):

$$-\sum_{j=1}^{J} M(\boldsymbol{x}_j) \ln M(\boldsymbol{x}_j) - \sum_{n=1}^{N} \lambda_n \left\{ \left[\sum_{j=1}^{J} M(\boldsymbol{x}_j)\, S(\boldsymbol{y}_n, \boldsymbol{x}_j) - \frac{2}{3} \right] - D(\boldsymbol{y}_n) \right\} = \max \tag{7.16}$$

where λ_n are undetermined multipliers.

The magnetic texture solution is deduced from the above equation by differentiation with respect to $M(\mathbf{x}_j)$:

$$M(\mathbf{x}_j) = \exp\left[-1-\sum_{n=1}^{N}\lambda_n\, S(\mathbf{y}_n,\mathbf{x}_j)\right] \qquad (7.17)$$

Differentiation with respect to λ_n produces the constraint equations (7.14) which constitute, together with equation (7.17), the restoring formulas proposed in this paper. Since y_n and λ_n are not related each other, equation (7.14) represents a non-linear system of M (= number of experimental data points) equations with N (= number of undetermined multipliers) unknowns. This system was numerically solved using the Newton-Raphson method. To solve the system with a non-square matrix (M > N), we modified the Newton-Raphson method and combined it with the linear least squares fitting procedure [79]. Since this algorithm differs from the classical Newton-Raphson method, we present it briefly.

Our problem gives M functional relations to be zeroed, involving a number N (< M) of variables λ_n:

$$f_m(\lambda_1,\lambda_2,\ldots\;,\lambda_N) = 0 \quad ; \quad m = 1,2,\ldots\;,M \qquad (7.18)$$

The Newton-Raphson set of linear equations for the corrections $\delta\lambda_n$ is:

$$\sum_{n=1}^{N}\alpha_{mn}\,\delta\lambda_n = \beta_m \qquad (7.19)$$

where:

$$\alpha_{mn} = \frac{\partial f_m}{\partial\lambda_n}\;; \qquad \beta_m = -f_m \qquad (7.20)$$

Since M > N, the matrix equation (7.19) was solved using a linearized least squares method. The new variables are obtained by

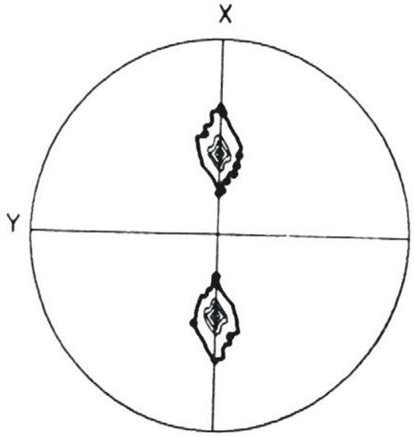

Fig.7.6.a. Computer simulated magnetic texture

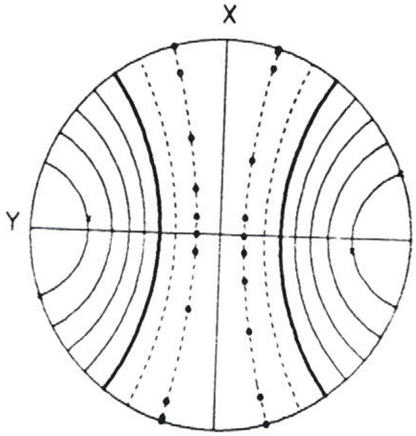

Fig.7.6.b. Magnetic signal generated by computer simulation

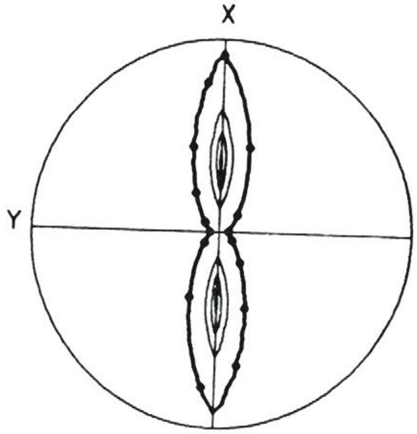

Fig.7.6.c. Reconstructed magnetic texture

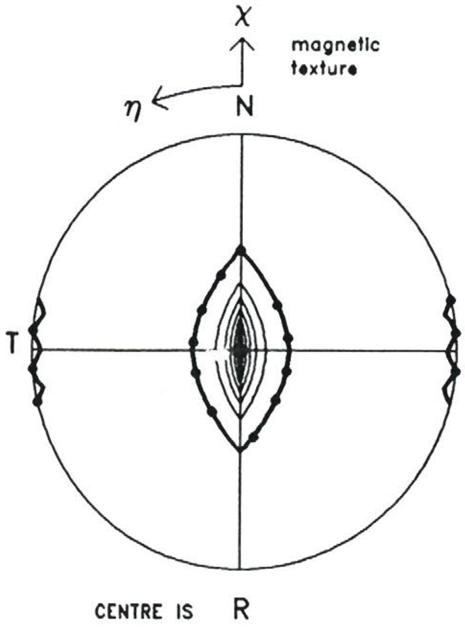

Fig.7.7. Calculated magnetic texture at 150 mA magnetizing current

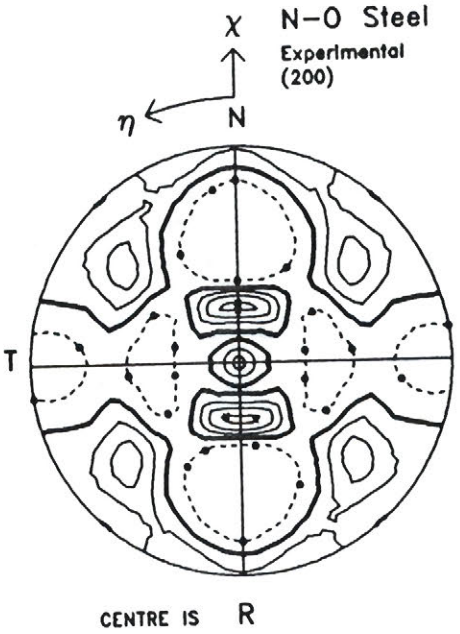

Fig.7.8. (200) pole figure

adding the corrections to the solution vector:

$$\lambda_n^{new} = \lambda_n^{old} + \delta\lambda_n \; ; \quad n = 1,2,\ldots,N \tag{7.21}$$

and the process is iterated to convergence.

The restoring equations (7.14) and (7.17) were tested by computer simulation. We generated a magnetic texture, as shown in Figure 7.6.a. The magnetic scattering data points were calculated using equation (7.11) with $W_{(110)}(\chi,\eta) = 1$ and they were plotted in the same stereographic projection that was used for pole figure representation in Figure 7.6.b. The magnetic pole figure restored with maximum entropy as obtained using the outlined method with N=16, J=360 (step 10°) and M=361 is shown in Figure 7.6.c. The magnetic texture was also normalized, such that:

$$1 = \frac{1}{2\pi} \oint M(\chi,\eta) \sin\chi \, d\chi \, d\eta \tag{7.22}$$

As an example of magnetic texture calculation, the experimental data representing the magnetic scattering obtained at 150 mA magnetizing current were used to calculate the magnetic texture, as shown in Figure 7.7. For comparison, the (200) pole figure which describes the orientation distribution of the easy magnetic directions, was measured and plotted in Figure 7.8.

An interesting feature of the magnetic texture is the shape of the peak around the position of the maximum magnetic pole density which, as expected, is located in the rolling direction. However, as one can see by comparing the magnetic texture with the (200) pole figure, the magnetic distribution is elongated towards the directions of maximum density of <100> easy directions.

7.3. METHOD TO ANALYZE THE MAGNETIC TEXTURE USING POLARIZED NEUTRON DIFFRACTION

7.3.1. Experimental method

The effect of the polarization state of the neutrons on the differential scattering cross section of a magnetic system in which all the magnetic moments are aligned parallel (or antiparallel) to a certain direction is seen from the expression derived by Halpern and Johnson [80]:

$$d\sigma = b^2 + 2bp\, \mathbf{q}\cdot\lambda + q^2\, p^2 \tag{7.23}$$

where λ is the unit vector parallel to the polarization direction, and $\mathbf{q}$ is the interaction vector defined together with the other factors in the previous section.

The magnetic measurements using polarized neutron diffraction were performed at Chalk River Nuclear Laboratory with the experimental setup shown in Figure 7.9. The neutrons were polarized in a direction perpendicular to the beam by reflection from the Co-Fe single crystal which is magnetized to saturation. The input spin-flipper offers the possibility of changing the polarization direction from spin-down to spin-up. The polarized neutron beam was then adiabatically guided by a vertical magnetic field created by a set of permanent magnets and then it faced the sample. We call the field produced by the magnetic guides the "local magnetic field". The sample was magnetized using an external magnetic field of different intensities, produced by the Helmholtz coils. The output spin-flipper can also change the polarization of the beam. The neutrons were then analyzed by a similar Co-Fe single crystal, similar to the one used to polarize the beam.

In this experiment, the Helmholtz coils were allowed to rotate along with the axis of the specimen, such that the magnetization of the sample was fixed in the transverse direction (TD). The magnetic field produced by the Helmholtz coils was approximately 1000 Oe (= $80\cdot10^3$ A/m). The neutron analyzer was placed in the Bragg position

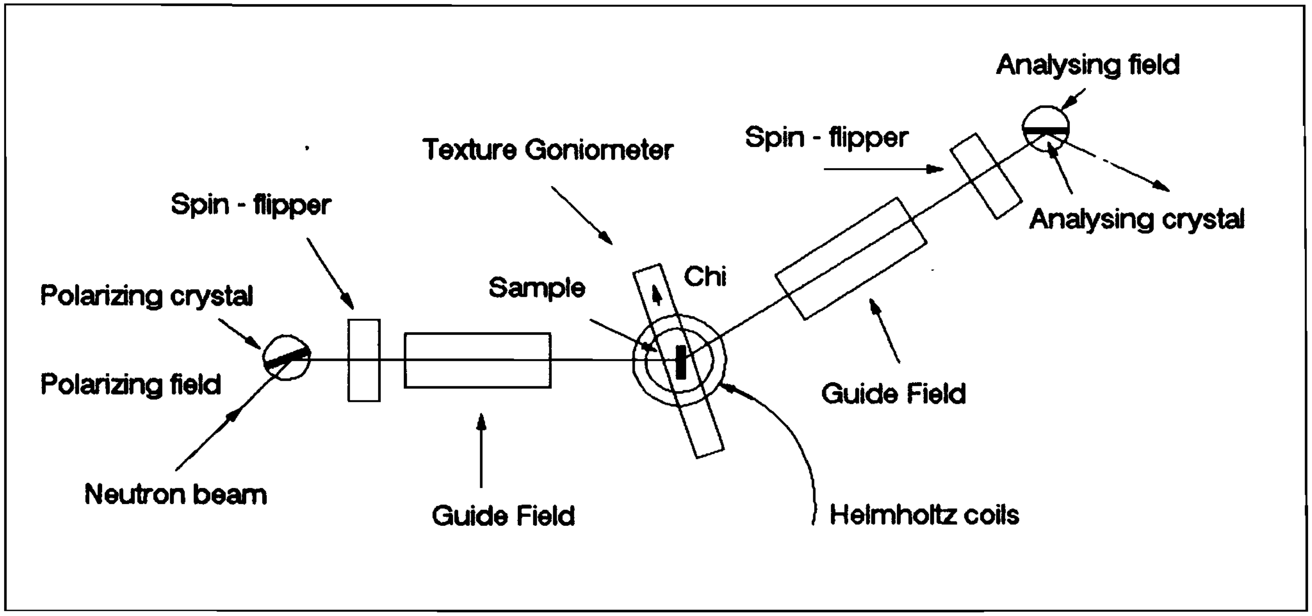

Fig.7.9. Setup for polarized neutron diffraction

to record the intensity of the (110) diffracted beam. At each (χ,η) direction of the scattering vector with respect to the sample coordinate system, the intensity was measured in the Up-Up configuration of polarizers, and then in the Down-Down configuration. Then, the next (χ,η) point was examined, and so on. Polarization analysis was made in both the incident and diffracted beams. The pole figure measurement was accomplished by using the pseudo-equal area scanning routine, with 1020 points per pole figure.

Polarized neutrons experiments were performed on a sample of grain oriented 3% silicon steel. A single sheet of oriented steel was shaped in the form of a disc 5 cm (= 2") in diameter. The sample was mounted in the texture goniometer in the standard position. An external magnetic field acting on the sample was produced using a set of Helmholtz coils mounted inside the CHI circle of the texture goniometer. The Helmholtz coils imposed a large-volume field to provide a smooth gradient between the guide fields and the applied field on the specimen.

7.3.2. Magnetic scattering in polarized neutron diffraction

The spin of the neutron is represented by a vector **S**. A neutron beam is polarized if the average value of a component of the spin vectors along an arbitrary direction is unequal to zero. The maximum value of the average spin component determines the direction of polarization of the beam; this direction is defined by a unit vector λ.

The neutron spin state is defined in relation to the "local magnetic field", which represents the environment where the polarized neutron experiment takes place. In the present experiment, the local magnetic field vector was oriented vertically in the laboratory reference frame, and the sense of this vector was downwards. We denote the spin states of the neutron by U = "spin-up" if the orientation of the spin coincides with the direction of local magnetic field, and D = "spin-down" for the opposite direction of the spin.

The spin states of the scattered neutrons are, in general, analyzed in the polarization direction of the incident neutrons. To take into account the polarization of both the incident and scattered beams, the scattering amplitude was described in terms of the spin matrices (Bacon, [71]). The four types of spin transition which can be examined in the experiment give rise to four spin-state cross sections of the atomic nucleus. They correspond to:

U → U, D → D, U → D, D → U.

The experimental procedure and instrumental setup were previously described. Two (110) pole figures were measured corresponding to the (U → U) and (D → D) cross sections of the atoms in the grain oriented sample magnetized by a strong magnetic field oriented along the sample transverse direction (TD). The density of the orientation distribution of the <110> poles was proportional to the corresponding spin-state cross section. Using the results derived by Bacon [71], the two differential cross sections for the transitions without spin flip are:

$$\begin{aligned} d\sigma_{U\text{-}U} &= (b - p\,\mathbf{q}\,\lambda)^2 \\ d\sigma_{D\text{-}D} &= (b + p\,\mathbf{q}\,\lambda)^2 \end{aligned} \tag{7.24}$$

where the parameters b and p were defined in equation (7.1). In texture measurements, the direction of the scattering vector **Δk** varies in the sample coordinate system. As a result, the directions of vectors **q** and λ also change in the sample reference frame. To calculate these spin-state cross sections (7.24), we must determine first the scalar product $\mathbf{q}\cdot\lambda$ in the reference frame of the sample.

Let us consider that in the sample coordinate system the magnetization unit vector **m**, which is parallel to the atomic magnetic moment and the scattering unit vector **Δk**, have the directions given by the angular coordinates (χ_0,η_0) and (χ,η), respectively. The components of these two vectors along the coordinate axes are:

$$m_x = \sin\chi_0 \cos\eta_0$$
$$m_y = \sin\chi_0 \sin\eta_0 \qquad (7.25)$$
$$m_z = \cos\chi_0$$

and similar relations exist for Δk_x, Δk_y and Δk_z.

As in the previous section, ψ is the angle between the magnetization direction and the scattering vector whose cosine is:

$$\cos\psi = m_x\,\Delta k_x + m_y\,\Delta k_y + m_z\,\Delta k_z = $$
$$= \sin\chi\,\cos(\eta_0-\eta)\,\sin\chi_0 + \cos\chi\,\cos\chi_0 \qquad (7.26)$$

The interaction vector **q** is given by the formula (Bacon, [71]):

$$\mathbf{q} = \Delta\mathbf{k}\,(\Delta\mathbf{k}\,\mathbf{m}) - \mathbf{m} \qquad (7.27)$$

It is decomposed into the components:

$$q_x = \Delta k_x \cos\psi - m_x$$
$$q_y = \Delta k_y \cos\psi - m_y \qquad (7.28)$$
$$q_z = \Delta k_z \cos\psi - m_z$$

It can be readily shown that the magnitude of the vector **q** is:

$$q^2 = q_x^2 + q_y^2 + q_z^2 = \sin^2\psi \qquad (7.29)$$

Now, we must establish the direction of the vector λ in the sample reference frame, knowing that in the laboratory or in the instrument reference frame, this direction was perpendicular to the scattering plane. The generally accepted convention (see, for example, Bacon [71]) is that the positive direction of the vector **q** is oriented in the opposite direction to the projection of the magnetization vector **m** onto the plane perpendicular to the vector **Δk** (as shown in Figure 7.1). Since the polarization vector λ is perpendicular to the scattering vector **Δk**, which is oriented in the (χ,η) direction, the direction of λ in the right-handed cartesian coordinate system of the sample is given by the angular coordinates (χ+90°,η). In this case, the components of the unit vector λ along the coordinate axes are:

$$\begin{aligned} \lambda_x &= \cos\chi\ \cos\eta \\ \lambda_y &= \cos\chi\ \sin\eta \\ \lambda_z &= -\ \sin\chi \end{aligned} \qquad (7.30)$$

The scalar product is then:

$$\begin{aligned} \boldsymbol{q}\ \boldsymbol{\lambda} &= \cos\xi = \\ &= \cos\chi\ \cos\eta(\sin\chi\ \cos\eta\ \cos\psi - \sin\chi_0\ \cos\eta_0) + \\ &+ \cos\chi\ \sin\eta(\sin\chi\ \sin\eta\ \cos\psi - \sin\chi_0\ \sin\eta_0) - \\ &- \sin\chi\ (\cos\chi\ \cos\psi - \cos\chi_0) = \\ &= \cos\chi\ \cos(\eta-\eta_0)\ \sin\chi_0 + \sin\chi\ \cos\chi_0 \end{aligned} \qquad (7.31)$$

which has the value cosξ = +1, when the direction of neutron polarization is opposite to the magnetization direction ($\chi_0 = \chi - 90°$ and $\eta_0 = \eta$), thereby supporting the above mentioned convention.

The differential spin-state cross sections are rewritten:

$$\begin{aligned} d\sigma_{U\text{-}U} &= (b - p\cos\xi)^2 = b^2 - 2bp\cos\xi + p^2\cos^2\xi \\ d\sigma_{D\text{-}D} &= (b + p\cos\xi)^2 = b^2 + 2bp\cos\xi + p^2\cos^2\xi \end{aligned} \qquad (7.32)$$

The reflected intensities when the polarization analysis was performed for the (U → U) and (D → D) transitions of the spin were proportional to the corresponding differential spin-state cross sections (Figure 7.10.a). Separating the magnetic part of the scattered intensity is accomplished by subtracting the above

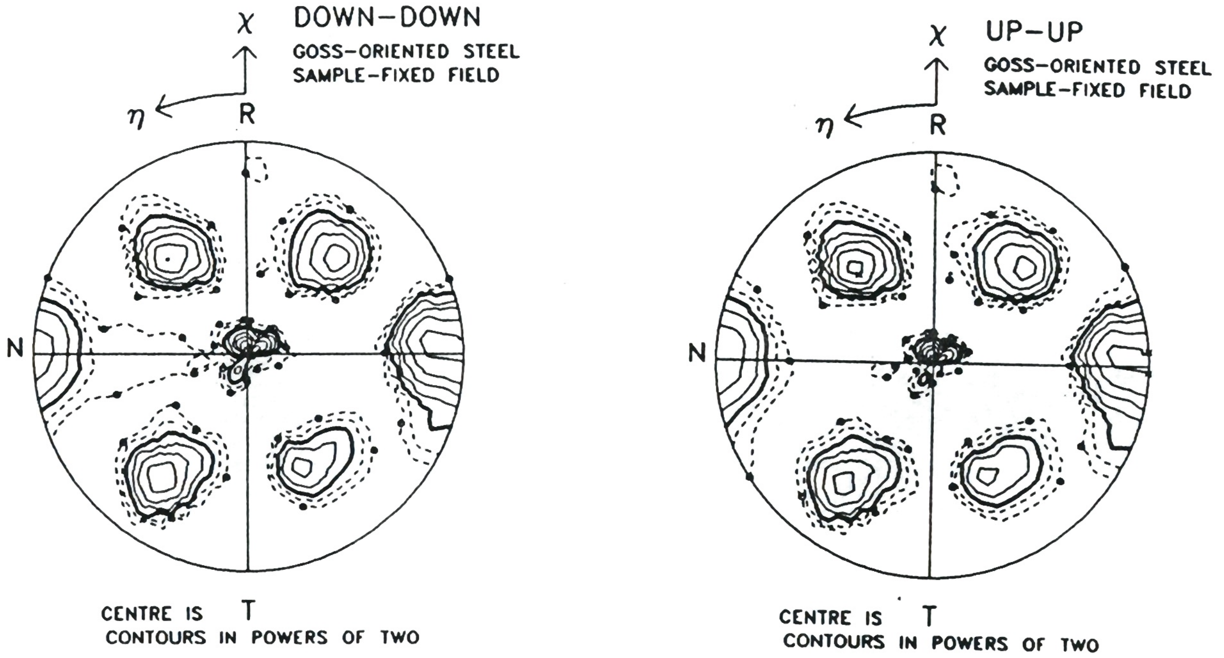

Fig.7.10.a. Non-spin-flip (110) pole figures

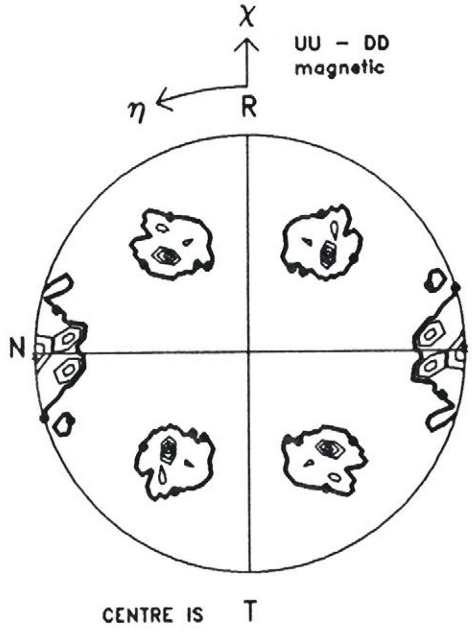

Fig.7.10.b. UU - DD pole figure

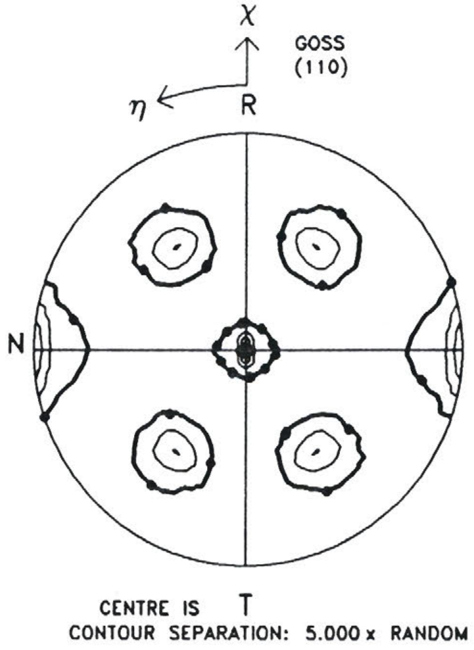

Fig.7.11. (110) pole figure of grain oriented sample

equations:

$$I_{D\text{-}D} - I_{U\text{-}U} \sim 4b\, p \cos\xi \tag{7.33}$$

If the orientations of the atomic magnetic moments are distributed in the sample according to the orientation distribution function M(χ,η), the magnetic scattering in each direction of the pole figure obtained as the difference of the (U → U) and (D → D) (110) pole figures is given by:

$$D^{diff}(\chi,\eta) = \frac{W_{(110)}(\chi,\eta)}{2\pi} \int_0^{\frac{\pi}{2}}\int_0^{2\pi} \cos\xi \; M(\chi',\eta')\,\sin\chi'\, d\chi'\, d\eta' \tag{7.34}$$

where the weight function W(χ,η), obtained from (110) crystallographic pole figure, appears as a result of the correlation existing between the magnetic and the nuclear scattering.

The magnetic scattering representing the difference of the (U → U) and (D → D) pole figures is shown in Figure 7.10.b. For comparison, the crystallographic (110) pole figure measured with non-polarized neutron beam is presented in Figure 7.11. One notices on the pole figure representing the magnetic signal, that the central (χ = 0°) pole which represents direction parallel to the applied magnetic field is now absent because cos ξ ≈ 0 within this angular range.

In principle, one could solve equation (7.34) for the unknowns M(χ,η) using a similar procedure to that used in non-polarized neutron diffraction investigation of magnetic texture (see the previous paragraph). However, for magnetic analysis of polarized neutron diffraction data, this method is not applicable if the magnetic texture has orthorhombic symmetry. Orthorhombic symmetry of magnetic texture implies that:

$$M(\chi,\eta) = M(\chi,180°+\eta) \tag{7.35}$$

From equation (7.31), one sees that:

$$\cos\xi(\eta) = -\cos\xi(180°+\eta) \tag{7.36}$$

In this case, the integral (7.34) does not depend on angle η:

$$D^{diff}(\chi,\eta) = D^{diff}(\chi) \tag{7.37}$$

The conclusion is that the experimental data representing the magnetic part of polarized neutron diffraction intensity obtained from a distribution of magnetic moment orientations, and having orthorhombic symmetry, does not uniquely determine the solution of equation (7.34). As a consequence, the underlying magnetic texture cannot be restored using the maximum entropy method.

The polarized neutron diffraction offered a better method of separating magnetic signal from the total scattering than the non-polarized neutron diffraction. Restoring magnetic texture from the magnetic signal using the maximum entropy method is possible only for lower symmetries than orthorhombic, such that the condition expressed in the equation (7.35) is not satisfied.

7.4. ANALYSIS OF NEUTRON DEPOLARIZATION IN A GRAIN ORIENTED ELECTRICAL STEEL

7.4.1. Experimental method

The magnetic measurements using neutron depolarization were performed with the experimental setup shown in Figure 7.12. Comparing this setup with the diffraction experiment, one can notice some differences in the geometry of the experiment. The neutron analyzer is placed in the direction of the beam and the axis of the texture goniometer circle coincides with the direction of the neutron beam. The grain oriented sample is oriented with the normal direction (ND) parallel to the direction of the beam which is also the rotation axis for the specimen. In this experiment, the sample was magnetized at constant magnetic field applied in different directions in the plane of the sheet and at constant magnetization in rolling direction. The magnetic field was produced by the Helmholtz coils which were fixed on the frame of the texture goniometer cradle.

This instrumental arrangement allowed us to measure the depolarization of the neutrons passing through the magnetized sample. If the incident beam is polarized spin-down and the counter counts only the neutrons having the polarization spin-down, the difference between the intensities recorded with the sample removed from the beam and with the sample placed in the beam represents the intensity of neutrons which have been depolarized by the magnetization inside the sample. The intensity of the depolarized neutrons depends on the direction and magnitude of the magnetization of the sample, i.e. on the orientation of the magnetic moments. The intensity of depolarized neutrons is anisotropic if the magnetic properties of the sample are anisotropic.

It should be mentioned that the results obtained from neutron depolarization yield only statistical information about the orientation distribution of magnetic domains. This is due to the fact that the depolarization of the whole beam is obtained as an average of neutron depolarization in the magnetic field of each domain.

7.4.2. Analysis of neutron depolarization

The magnetic interaction between thermal neutrons and matter offers one of the best means for investigating the magnetic properties of ferromagnetic specimens. Part of this interaction is the polarization change of a polarized neutron beam transmitted through the investigated material. Information obtained from the neutron depolarization studies is of special interest since the magnetic structure in the bulk, rather than on the surface of the sample determines the magnetic properties and should be investigated.

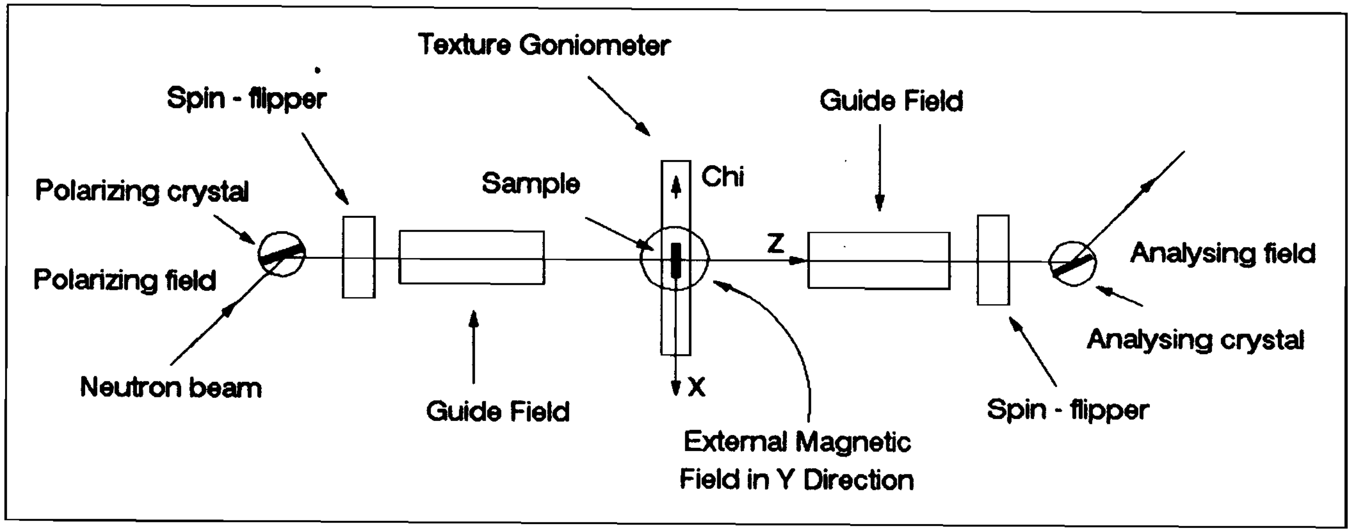

Fig.7.12. Setup for magnetic measurements using polarized neutrons

As stated by Halpern and Holstein [81], the depolarization of the neutron beam in a ferromagnetic material results from uncorrelated spin rotations of the neutrons in oriented magnetic domains. This theory was extended by Rekveldt [82], who developed a model for magnetic domain arrangement and demonstrated that the depolarization of a neutron beam passing through a ferromagnetic polycrystalline sample could be described by a (3 x 3) rotation matrix, depending only on the interaction time and the orientation of the magnetic field.

The work undertaken by Akselrod et al. [83] measured magnetic texture using polarized neutrons. The interpretation of results was based on the depolarization formula derived by Maleyev and Ruban [84] in terms of the correlation function of magnetization fluctuations. This formula is valid only for small domains (i.e. small neutron spin rotation within a domain) and was successfully applied on polycrystalline ferrite.

As in the previous chapter, **S** and λ denote the neutron spin vector, and a unit vector in the direction of polarization, respectively. The degree of polarization is given by the average value of the spin component in the polarization direction divided by its maximum value (= 1/2). The polarization vector is defined by its direction λ and magnitude P as:

$$\boldsymbol{P} = \frac{\langle \boldsymbol{S} \rangle}{\frac{1}{2}} = \frac{I_+ - I_-}{I_+ + I_-} \lambda = P \lambda \tag{7.38}$$

where I_+ and I_- are the intensities of the neutrons with + and - spin component along the direction λ. One sees that the magnitude of the polarization vector is in the range $P \in [-1, 1]$.

Under the action of an external magnetic field, the neutron spin performs a precession motion described by the Landau - Lifshitz equation:

$$\frac{d\boldsymbol{P}}{dt} = -\gamma \left[(\boldsymbol{P} \times \boldsymbol{H}) - \frac{\alpha}{\gamma P} \frac{d\boldsymbol{P}}{dt} \right] \tag{7.39}$$

where γ is the gyromagnetic ratio for neutrons and α is the dumping term. Solving this equation describes the polarization change of a polarized neutron beam passing through a single ferromagnetic domain, where the magnetic field vector is constant in orientation and magnitude. In this case, the magnetic field acting on the neutron spin is given by:

$$\boldsymbol{H} = \frac{\boldsymbol{B_s}}{\mu_0} \tag{7.40}$$

where B_s is the spontaneous magnetic induction in one domain, and μ_0 is the permeability in vacuum. If the initial inclination of the spin axis relative to the external magnetic field is Θ_0, the final orientation Θ of the spin axis is a function of the interaction time t, as was given by Chikazumi [9, § 16.3]:

$$\tan\frac{\theta}{2} = \tan\frac{\theta_0}{2}\, e^{\frac{t}{\tau}} \tag{7.41}$$

where τ is the relaxation time. The interaction time depends on the magnetic domain size (δ) in the direction of the neutron beam divided by the neutron velocity (v):

$$t = \frac{\delta}{v} \tag{7.42}$$

In the particular case where the domain size in the direction of propagation of the neutron beam is the same as the material thickness, one assumes that the interaction time is high enough to rotate the spins toward the direction of the internal field of the domain, irrespective of the initial direction of polarization.

We must emphasize that, according to the minimum energy principle, the direction of the spin vector can be either parallel or antiparallel to the direction of the magnetization vector. When a polarized neutron beam propagates through a magnetic field, the beam polarization is preserved either parallel or antiparallel to the direction of the field as far as the magnetic field is constant or the gradient of the field in the direction of propagation is smooth. The construction of the magnetic guides which assure the preservation of beam polarization between the polarizer, specimen, and analyzer, is based on this principle (adiabatic process). As in the previous section, we call the field produced by the magnetic guides the "local magnetic field".

The neutron spin state is defined in relation to the local magnetic field. Thus, the spin polarization is +1 if the orientation of the spin coincides with the direction of the local magnetic field, and -1 in the opposite case.

If the gradient of the local field in the direction of propagation of the beam is high, the neutron spin vector flips in the direction parallel to the magnetic field, following the precession rotation; this is how the electronic spin flippers work. From this point of view, the thin magnetic domain interposed in the path of the polarized neutron beam plays the role of a spin flipper. According to these theoretical considerations, the neutron spin state is preserved when the magnetic domain has the magnetization parallel to the local field, such that the neutron passes adiabatically through the domain. The spin state is reversed in the opposite case.

Usually, polarization analysis of the transmitted beam is effected in the direction of the polarization of the incident beam. In this experiment, the initial polarization of the beam was either +1 or -1, and the analyzer detected the neutrons having +1 spin state, so that only one component of the polarization vector was counted.

After passing through the domain, the resultant polarization can be written:

$$P = m\,P_0 \tag{7.43}$$

where m is the reduced magnetization of the domain:

$$m = \frac{1}{B_s} (\pm B_s) = \pm 1 \tag{7.44}$$

also defined in relation with the local magnetic field, and P_0 is the initial polarization. Relation (7.43) does not specify the orientation of the magnetization within the domain relative to the local magnetic field, as if the domain magnetization is either parallel or antiparallel to the local field. If the direction of domain magnetization makes an angle δ with the direction of local field, the spin of the neutron passing through the sample is oriented in the direction of magnetization within the domain. After passing through the sample, this inclination is eliminated by the second magnetic guide. Since the local magnetic field preserves the ±1 spin states, the orientation of the domain magnetization relative to the local field is not taken into account. The reduced magnetization of the domain (equation 7.44) can be rewritten as:

$$m = \frac{1}{B_s} [\mathit{sign}\ (\cos\delta)\ B_s] = \pm 1 \tag{7.45}$$

or, we can consider it a vector:

$$\mathbf{m} = \mathit{sign}(\cos\langle \mathbf{B_s}, \lambda\rangle)\ \lambda \tag{7.46}$$

oriented along the direction of the local magnetic field.

In general, a ferromagnetic material consists of many domains, in which magnetization is homogeneous and constant in size. The mean magnetization of the whole body is the sum of the spontaneous magnetization vectors of individual domains:

$$\mathbf{B} = \frac{1}{N} \sum_{i=1}^{N} (\mathbf{B_s})_i \tag{7.47}$$

We studied the particular case where the magnetic domains extended across the sample thickness. The neutron beam can be subdivided into a large number of smaller beams, each of them having a cross section area equal to the surface area of a domain. Such a small beam passes through one domain and its polarization is changed or not by the domain spontaneous magnetization, according to relation (7.43). The resulting polarization of the whole neutron beam passing through the sample with this particular magnetic domain structure is expressed as the average:

$$P = \frac{P_0}{N} \sum_{i=1}^{N} m_i = \frac{P_0}{NB_s} \sum_{i=1}^{N} [\ sign(\cos <B_s, \lambda>)\ B_s\ ]_i \qquad (7.48)$$

If the magnetization of each domain is either parallel or antiparallel to a certain direction of the sample, the vectorial summation given in equation (7.47) is reduced to an algebraic summation of the domain magnetizations. In this case, the relationship between the polarization of the transmitted beam and the formula expressing the sample magnetization <B> has the simple form:

$$P = P_0 \frac{<B>}{B_s}$$
$$<B> = \frac{1}{N} \sum_{i=1}^{N} (B_s)_i \qquad (7.49)$$

where $(B_s)_i$ could have a positive or negative value depending on the sense of its direction.

This method was proposed to investigate the magnetization anisotropy in a grain oriented sample, where the domain structure is very simple, containing two sorts of domains whose magnetizations are parallel or anti-parallel to the rolling direction. The intensity of the incident beam is the same for both spin states of beam polarization:

$$|I_{+1}| = |I_{-1}| = I_0 \qquad (7.50)$$

The analyzer diffracts neutrons into the counter only if they have

Fig.7.13. Neutron depolarization in the sample magnetized at constant magnetization

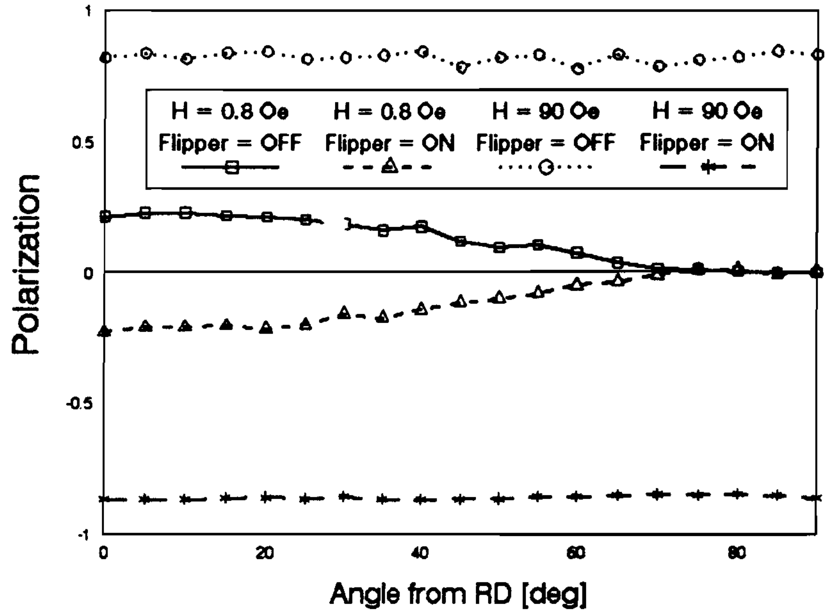

Fig.7.14. Neutron depolarization in the sample magnetized at constant magnetic field

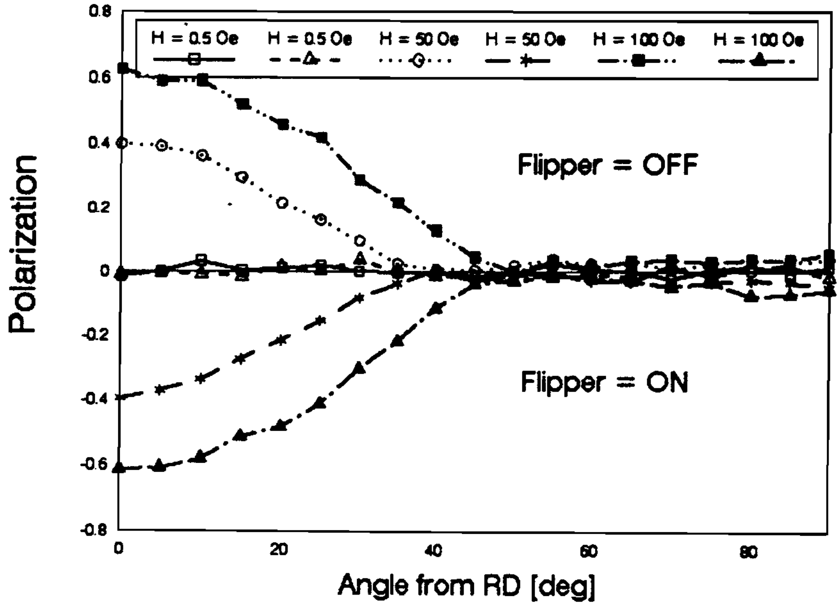

the +1 spin. We call this number the recorded intensity, I_r. In this case, the magnitude of the resultant polarization is:

$$P = \frac{2I_r - I_0}{I_0} \in [-1,+1] \tag{7.51}$$

Measurements were performed using the experimental setup previously presented. The sample was rotated about the normal direction which is parallel to the neutron beam. In the initial position of the sample, the rolling direction (RD) coincides with the vertical (Y) direction of the laboratory coordinate system (Figure 7.12).

According to equation (7.49), the value of polarization should be constant when the sample is magnetized at a constant B, regardless of the direction of the magnetization relative to the direction of the local magnetic field. Figure 7.13 presents the polarization values when the sample was rotated 90° from the initial position and the magnetization of the sample was constant. Initially, the sample was in the demagnetized state and then it was magnetized in the rolling direction using a magnetic field of approximately $4 \cdot 10^3$ A/m (= 50 Oe). The initial polarization was +1 and -1, respectively. This graph clearly shows that the demagnetized specimen has completely depolarized the beam. When the external magnetic field was applied, the sense of the magnetic field inside the sample coincided with the sense of the local magnetic field, so that the initial polarization of the beam was not changed (see equation 7.48).

Due to the strong texture, the sample magnetization depends on the direction of the magnetic field. The study of magnetization anisotropy was effected with a field of 0, 55, and 110 Oe, applied in different directions of the sheet plane for both polarizations of the incident beam. The results are described by equation (7.47) and are shown in Figure 7.14.

For the particular case considered here, the described method of magnetic analysis using the neutron depolarization effect offers the possibility of:

- directly relating the neutron polarization to the sample magnetization in static conditions (with equation 7.49);
- obtaining quantitative information about the magnetization anisotropy (using equation 7.48);
- identifying the presence of the crystallographic texture;
- identifying the easy magnetization direction.

CHAPTER 8.

MODEL-BASED METHODS OF CORRELATING TEXTURE AND MAGNETIC PROPERTIES IN ELECTRICAL STEELS

INTRODUCTION

Power loss, rotational loss, and permeability are of major importance for application of the electrical steels in various magnetic equipments. It is well known that there is a direct relationship between the material texture and these properties. For instance, a semi-empirical correlation was established between the permeability or the power loss, and the fourth order texture parameter $F_4(\eta)$. There is, however, not enough evidence to demonstrate that such a correlation is valid for a variety of textures existing in the same material, or if it can be applied to very sharp textures like the ones observed in grain oriented electrical steels.

In this chapter, we propose and deduce analytical formulae which describe the anisotropy of the permeability and power loss in textured materials. Both properties are compared to experimental data. Also, a model is proposed which relates the textural and structural parameters to the excess power loss in grain oriented and non-oriented materials. Using this model, we show that the magnetization process in electrical steels is governed by the minimum entropy production principle.

In an attempt to work out a unified interpretation of the observed rotational loss in polycrystalline materials, a model previously developed to explain the rotational loss in single crystals with different orientations is used to correlate the texture and rotational power loss in non-oriented electrical steels.

8.1. ANISOTROPY OF PERMEABILITY IN TEXTURED SOFT MAGNETIC MATERIALS

This paragraph addresses the problem of theoretical determination of the effective magnetic permeability of textured materials, in terms of the orientation distribution function (ODF), and permeabilities of constituting grains.

It is generally agreed that the permeability, or induction, measured at H = 800 A/m = 10 Oe (hereafter termed B_{10}) is linked to the angular distribution of grains. Extensive work on this subject has concluded that B_{10} is generally insensitive to impurity content, internal stress, and grain size, and is only dependent on the statistical distribution of the grain orientation, as shown, for example, by Littmann [85]. These results make it possible to calculate B_{10} as a function of texture parameters.

Other authors, like Shilling and G.L.Houze [86], and Craik and McIntyre [87], give an analytical expression for the magnetization of a ferromagnetic single crystal at the knee of the magnetization curve, and we use these results to analyze the permeability at H = 10 Oe in textured materials. At present, no investigation takes into account a realistic orientation distribution of grains to study the anisotropy of B_{10} in polycrystalline electrical steels.

Polycrystalline material can be considered, from a magnetic permeability viewpoint, as a multiphase material. Studies on the magnetic permeability of a multiphase material undertaken by Brown [88], Hashin and Shtrikman [89], and Woodside and Messner [90], concluded that permeability is not completely determined by the volume fractions and magnetic permeabilities of the phases, but that the statistics of phase distribution influenced the result. Therefore, instead of deriving an expression for the effective permeability of a multiphase material, only the upper and lower bounds for this quantity were calculated.

These bounds were first derived by Wiener [91], who demonstrated that the permeability μ of a material containing N magnetic phases lies within the interval:

$$\sum_{i=1}^{N} v_i \, \mu_i \geq \mu \geq \left[\sum_{i=1}^{N} \left(\frac{v_i}{\mu_i} \right) \right]^{-1} \tag{8.1}$$

where v_i and μ_i are the volume fraction and the permeability of the phase "i", respectively. The upper bound corresponds to the case where all the phases conduct magnetic flux in parallel, and the lower bound corresponds to the serial case.

To calculate the magnetization in a cubic single crystal it is necessary to know the distribution of domains among the six <100> easy directions of magnetization for each value of the applied field. Considering a strip of grain oriented steel placed in a magnetic field (H = 10 Oe = 800 A/m) lying in the plane of the sheet, one introduces a constraint on the domain structure such that only the three easy directions closest to the applied field can be occupied. This field cannot rotate the magnetic moment out of the easy direction because it is much smaller than the anisotropy field (H_{an} = 560 Oe for silicon iron). In order to avoid high demagnetizing energy in each crystallite, the magnetization distributes itself between the easy directions, so that the component of magnetization perpendicular to the specimen surface is zero.

In this case, the volume fractions in a single crystal which are magnetized along each of the easy directions are uniquely determined. The net component of magnetization (or induction), B_p, of the specimen which is parallel to the applied field is only a function of crystal orientation:

$$\frac{B_p}{B_s} = \frac{1}{(\alpha_1 + \alpha_2 + \alpha_3)} \tag{8.2}$$

where the applied field has direction cosines α_1, α_2, and α_3 with the three closest easy directions, and $B_s = 4\pi \cdot I_s$ [Gauss] (= I_s [T]), I_s being the saturation magnetization.

The experimental results are in a relatively good agreement with this equation. The measurements of the induction at H = 10 Oe performed by Swift et al. [92] on 3% Si-Fe single crystals are somewhat larger than those predicted by equation (8.2), and the same tendency is observed in our experiment.

The measurements of the induction at 10 Oe were effected on Epstein strips cut from the metal sheet at a angle η from rolling direction (RD). The results for three grain oriented samples, namely OR-3A, OR-3B and OR-3C, are shown in Table 3.3 (a to c).

If the orientation of a crystallite is given by the Euler angles $g = (\varphi_1, \phi, \varphi_2)$, and the internal induction vector **B** is parallel to the applied field direction **H** making the angle η with the rolling direction, the direction cosines α_1, α_2, and α_3 are deduced from the rotation matrix [g] defined in Bunge [1], and they are given by the formulae:

$$\begin{aligned}
\alpha_1(\eta) &= |(\cos\varphi_1 \cos\varphi_2 - \sin\varphi_1 \sin\varphi_2 \cos\phi) \cos\eta + \\
&\quad +(\sin\varphi_1 \cos\varphi_2 + \cos\varphi_1 \sin\varphi_2 \cos\phi) \sin\eta| \\
\alpha_2(\eta) &= |(-\cos\varphi_1 \sin\varphi_2 - \sin\varphi_1 \cos\varphi_2 \cos\phi) \cos\eta + \\
&\quad +(-\sin\varphi_1 \sin\varphi_2 + \cos\varphi_1 \cos\varphi_2 \cos\phi) \sin\eta)| \\
\alpha_3(\eta) &= |(\sin\varphi_1 \sin\phi \cos\eta - \cos\varphi_1 \sin\phi \sin\eta)|
\end{aligned} \tag{8.3}$$

With these direction cosines, equation (8.2) gives the magnetization of grain "i" having the orientation $g_i = (\varphi_1, \phi, \varphi_2)_i$ when the direction of the field makes the angle η with the rolling direction :

$$B_{10}(g_i, \eta) = \frac{B_s}{\alpha_1(\eta) + \alpha_2(\eta) + \alpha_3(\eta)} \tag{8.4}$$

Since the property depends on the crystallite orientation, g, to obtain its average value we integrate over the Euler space using the orientation distribution function f(g) as a weight function. If all the grains conduct flux in parallel, the overall magnetization of the sample in the direction of the magnetic field is:

$$B_{10}^{p}(\eta) = \oint B_{10}(g, \eta)\, f(g)\, dg \tag{8.5}$$

For the case where all the grains conduct flux in series, we calculate the average value (see § 2.5):

$$\left[B_{10}^{s}(\eta)\right]^{-1} = \oint B_{10}^{-1}(g, \eta)\, f(g)\, dg \tag{8.6}$$

These two averages yield limiting values for the permeability of the polycrystalline material. The actual permeability is expected to lie between these two extremes, so that we can set:

$$\overline{B_{10}}(\eta) \approx \frac{1}{2}\left[B_{10}^{p}(\eta) + B_{10}^{s}(\eta)\right] \tag{8.7}$$

The calculated and experimental permeabilities are plotted in Figure 8.1 (a to c) for samples OR-3A, OR-3B, and OR-3C, respectively. As anticipated, the experimental results are somewhat larger than those predicted by the theory. However, it should be stressed that the variation of the values experimentally obtained versus angle from the rolling direction strongly supports the one describing the theoretical magnetization. Some differences may be caused by statistical error of measurements: the experimental magnetic permeability is the average value of 10 different Epstein strips, while the X-ray ODF determination involved 5 specimens, each on of approximately 4 cm^2 surface area. For these samples, the theoretical and experimental data have the same features: in the sample OR-3C the maximum permeability is not in the rolling direction (RD) as experimentally tested, while in samples OR-3A and OR-3B the permeability is higher than in OR-3C, and it has the maximum in the rolling direction (RD). The major contributing factor to these differences is a different amount of material near the ideal (110)[001] orientation.

It is interesting to compare the predicted values of permeability given by the above equations with those obtained semi-empirically by Morris and Flowers [26], who assumed that a linear relationship exists between the permeability and the magnetic anisotropy function $F_4(\chi,\eta)$, defined in equation (2.51). Accordingly, the variation in permeability (ΔB_{10}) with the angle η is proportional to the variation in $F_4(\eta)$, (ΔF_4). If two test values of permeability are available, the following equation was used by Morris and Flowers [26] to calculate the induction B_{10} in the (90°,η) direction of the sample:

$$B_{10}(\eta) = B_{10}(RD) + [F_4(\eta) - F_4(RD)]\,\frac{\Delta B_{10}}{\Delta F_4} \tag{8.8}$$

We will justify this relationship. In general, we express the cosine function by expanding it in Legendre polynomials:

$$\begin{aligned}\cos\vartheta &= \sum_{l=0}^{\infty} c_l\,\overline{P_l}(\vartheta) = \\ &= c_0 + c_2\,(\cos^2\vartheta - \frac{1}{3}) + c_4\,(\cos^4\vartheta - \frac{6}{7}\cos^2\vartheta + \frac{3}{35}) + \ldots\end{aligned} \tag{8.9}$$

If we let (α_1, α_2, α_3) denote the direction cosines of the internal magnetization, in equation (8.9) $\cos\vartheta$ can be replaced by α_1 for those atomic magnetic moments which are parallel to the x axis, by α_2 for y magnetic moments, and by α_3 for z magnetic moments, and we calculate the sum:

Fig.8.1.a. Permeability of sample OR-3A

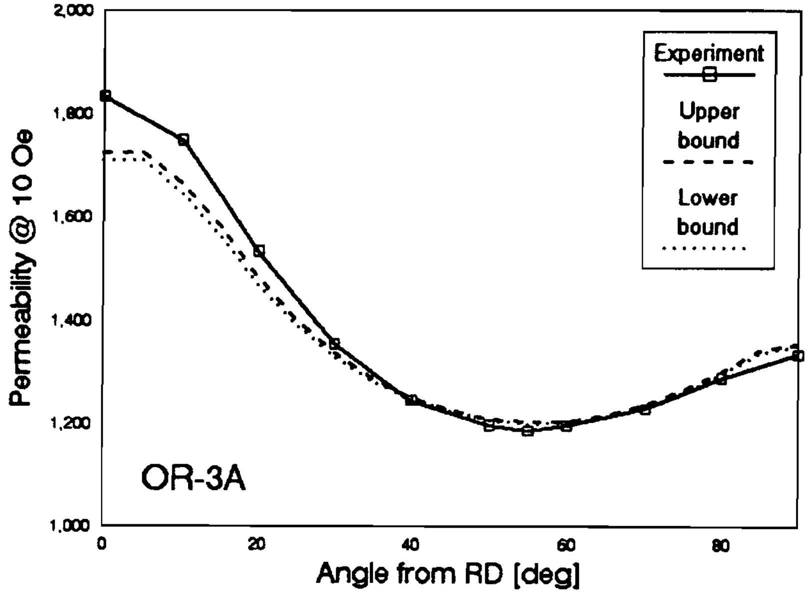

Fig.8.1.b. Permeability for sample OR-3B

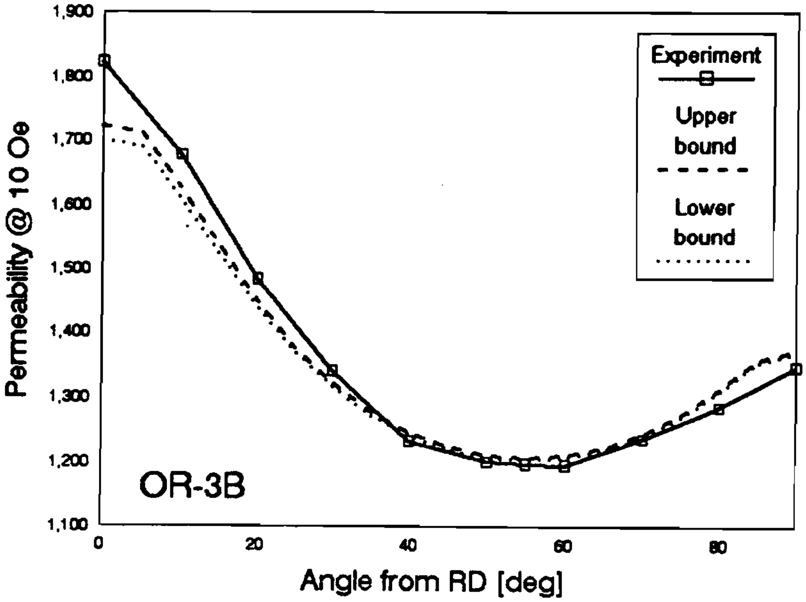

Fig.8.1.c. Permeability for sample OR-3C

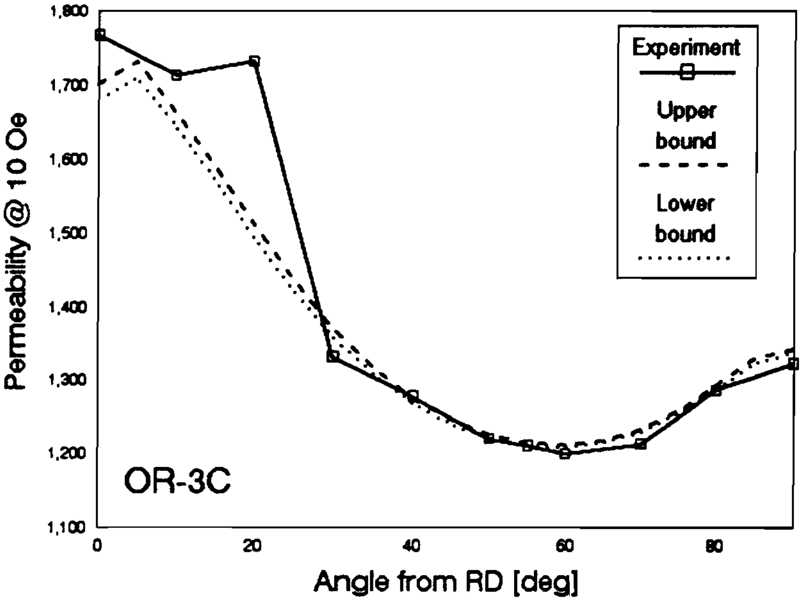

Fig.8.2.a. **Grain oriented sample**

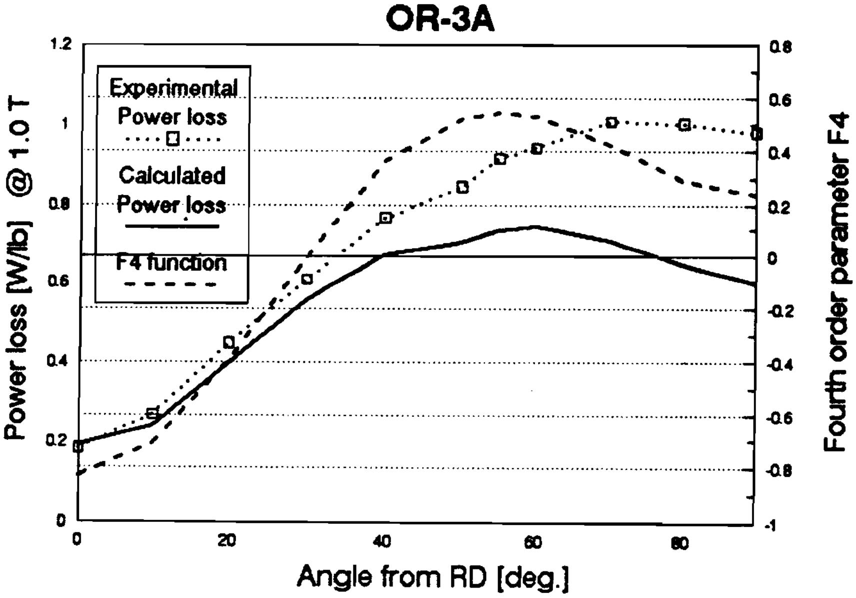

Fig.8.2.b. **Grain oriented sample**

OR-3B

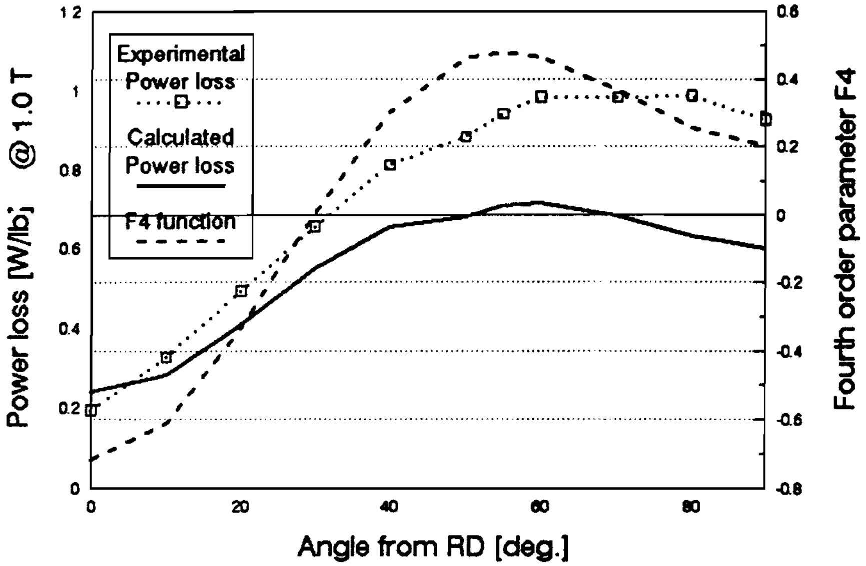

Fig.8.2.c. **Grain oriented sample**

OR-3C

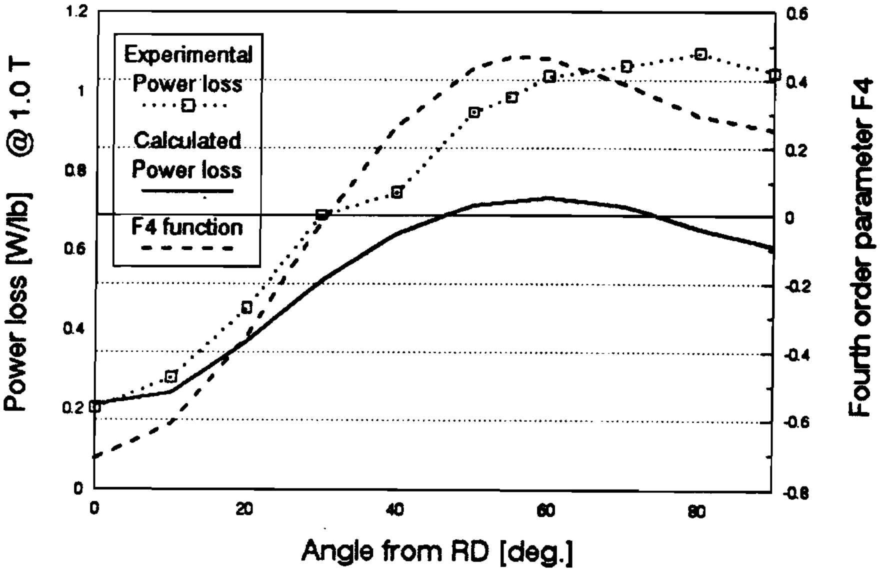

$$\begin{aligned} &\alpha_1 + \alpha_2 + \alpha_3 = \\ &= c_0 + c_2\left(\alpha_1^2 - \frac{1}{3}\right) + c_4\left(\alpha_1^4 - \frac{6}{7}\alpha_1^2 + \frac{3}{35}\right) + \\ &+ c_0 + c_2\left(\alpha_2^2 - \frac{1}{3}\right) + c_4\left(\alpha_2^4 - \frac{6}{7}\alpha_2^2 + \frac{3}{35}\right) + \\ &+ c_0 + c_2\left(\alpha_3^2 - \frac{1}{3}\right) + c_4\left(\alpha_3^4 - \frac{6}{7}\alpha_3^2 + \frac{3}{35}\right) = \\ &= const. + c_4(\alpha_1^4 + \alpha_2^4 + \alpha_3^4) = \\ &= const. - 2c_4(\alpha_1^2\alpha_2^2 + \alpha_2^2\alpha_3^2 + \alpha_3^2\alpha_1^2) \end{aligned} \tag{8.10}$$

Equation (8.2) becomes:

$$\begin{aligned} &\frac{B_p}{B_s} = \frac{1}{\alpha_1 + \alpha_2 + \alpha_3} \approx \\ &\approx \frac{1}{const. - c_4(\alpha_1^2\alpha_2^2 + \alpha_2^2\alpha_3^2 + \alpha_3^2\alpha_1^2)} = \frac{1}{const. - c_4\,\varphi_4(\mathbf{h})} \end{aligned} \tag{8.11}$$

where $\varphi_4(\mathbf{h})$ is the magnetic anisotropy function corresponding to a single ferromagnetic crystal.

Averaging the above equation over all orientations using the distribution function of grain orientations f(g) as a weight function, we obtained a relationship which justifies, to the first approximation, the intuitive approach of Morris and Flowers [26]. Obviously, in this case, it is not specified which value of permeability is considered, the lower or upper bound.

8.2. ANISOTROPY OF POWER LOSSES IN TEXTURED SOFT MAGNETIC MATERIALS

As mentioned in chapter 2.5, the studies of power losses in weak textured materials performed by Hutchinson and Swift [35] and by Morris and Flowers [26] did not give any theoretical ground in describing the angular dependence of power losses using a linear equation in $F_4(\chi,\eta)$ texture parameter, defined in relation (2.51). The fourth order texture parameter $F_4(\chi,\eta)$ expresses the variation of the magnetocrystalline energy in the sample reference frame. This function was calculated assuming the state of magnetization saturation of the sample when the magnetization in each grain is oriented in the (χ,η) direction, which coincides with the direction of the applied field. Obviously, the power losses are measured at much lower inductions where the spontaneous magnetization is not rotated out of the easy magnetization directions. From this point of view, there is no physical reason, other than the symmetry of texture, to relate the power losses to the $F_4(\chi,\eta)$ function.

Let us consider a single crystal of ferromagnetic material having the easy directions of magnetization along the x, y, and z axes which coincide with the <100> directions. In the demagnetized state, the magnetic moments are distributed with equal probability along the six <100> directions. When a magnetic field is applied in a direction making angles a_1, a_2, and a_3 with the x, y, and z axes, respectively, the probability that the <100> directions closer to the field to be occupied by magnetic moments are higher, compared with the other <100> directions.

Usually, the power losses measurements are performed at constant magnetization (or induction) measured in the direction of the external field. We call this magnetization the parallel component of magnetization, and it is constant during the power loss measurement, $B_\parallel$ = const. Thus, the magnetic moments are distributed along the nearest easy directions to the field, such that the components of magnetization are:

$$\begin{aligned} B_x &= B_\parallel \cos a_1 \\ B_y &= B_\parallel \cos a_2 \qquad (8.12) \\ B_z &= B_\parallel \cos a_3 \end{aligned}$$

We must emphasize that the constraint introduced by the external field on the domain structure does not imply that the magnetic moments occupy only the three easy directions closest to the applied field. They may also occupy the other three easy directions but with less probability, meaning that:

$$B_x + B_y + B_z < B_s \tag{8.13}$$

where B_s is the saturation induction (= 2.03 T for iron).

Magnetocrystalline energy confines the spontaneous magnetization to the six easy magnetization directions. When the field is applied, the component of magnetization lying along the easy direction can be decomposed into two parts:

$$\begin{aligned} \vec{B}_x &= \vec{B}_x^a + \vec{B}_x^r \\ \vec{B}_y &= \vec{B}_y^a + \vec{B}_y^r \\ \vec{B}_z &= \vec{B}_z^a + \vec{B}_z^r \end{aligned} \tag{8.14}$$

The first component, $\mathbf{B}^a$, is parallel to the magnetic field and contributes to the measured sample magnetization, $B_{|}$. Similar to an electrical circuit, we call this component the active component of magnetization which has the magnitudes:

$$\begin{aligned} B_x^a &= B_x \cos a_1 = B_{|} \cos^2 a_1 \\ B_y^a &= B_y \cos a_2 = B_{|} \cos^2 a_2 \\ B_z^a &= B_z \cos a_3 = B_{|} \cos^2 a_3 \end{aligned} \tag{8.15}$$

and

$$B^a = B_x^a + B_y^a + B_z^a = B_{|} \tag{8.16}$$

The second component, $\mathbf{B}^r$, is perpendicular to the direction of applied field. Using the same analogy, we call it the reactive component of magnetization:

$$\begin{aligned} B_x^r &= B_x \sin a_1 = \frac{1}{2} B_1 \sin 2a_1 \\ B_y^r &= B_y \sin a_2 = \frac{1}{2} B_1 \sin 2a_2 \\ B_z^r &= B_z \sin a_3 = \frac{1}{2} B_1 \sin 2a_3 \end{aligned} \tag{8.17}$$

and

$$B^r = B_x^r + B_y^r + B_z^r = \frac{1}{2} B_1 (\sin 2a_1 + \sin 2a_2 + \sin 2a_3) \tag{8.18}$$

The energy per unit volume of the sample supplied by the external field to create the reactive components of magnetization is equivalent to a loss:

$$E_r = \frac{1}{2} H B^r = \frac{1}{4} H B_1 (\sin 2a_1 + \sin 2a_2 + \sin 2a_3) \tag{8.19}$$

and it is called the reactive energy.

First we notice that this energy is anisotropic depending on the direction of applied field. The anisotropy function which describes the angular dependence of the reactive energy is written as:

$$e_4(\boldsymbol{h}) = |\sin 2a_1| + |\sin 2a_2| + |\sin 2a_3| \tag{8.20}$$

It is expressed in absolute values to emphasize that it is always defined in the angular range a_1, a_2, $a_3 \in [0, 90°]$. A similar function was already defined in equation (2.27), and was called the magnetic anisotropy function:

$$\begin{aligned} \varphi_4(\boldsymbol{h}) &= \cos^2 a_1 \cos^2 a_2 + \cos^2 a_2 \cos^2 a_3 + \cos^2 a_3 \cos^2 a_1 = \\ &= \sin^2 2a_1 + \sin^2 2a_2 + \sin^2 2a_3 + \mathit{const.} \end{aligned} \tag{8.21}$$

Comparing these two functions (8.20 and 8.21), one can understand why $\varphi_4(\mathbf{h})$ describes, with reasonable accuracy, the angular variation of power losses.

Obviously, when the external field is applied along one of the easy magnetization directions, the reactive component of magnetization is zero, and the losses are due to other dissipation mechanisms: eddy currents, hysteresis, etc. (this situation is described in the subsequent paragraph). When the magnetic field is applied along a direction other than the easy magnetization direction, the magnetic domain structure becomes very complex. The magnetization process takes place by local rearrangements of the magnetic moments, and the loss due to the reactive component of magnetization prevails. The reactive energy is mainly used to create new domain walls and its value is directly related to the domain wall energy ($\approx 1.8\cdot10^{-3}$ J/m^2 for iron).

For textured materials, calculating the average value of the reactive energy over the orientation distribution function is determined by simply representing the energy in equation (8.20) as a function of orientation $g = (\varphi_1, \phi, \varphi_2)$. We are particularly interested in studying the angular variation of power loss in the sheet plane of a grain oriented material. If a grain orientation is given by the Euler angles $(\varphi_1, \phi, \varphi_2)$, the rotation matrix [g] as defined in Bunge [1] is used to determine the cosines α_1, α_2, and α_3 of a direction making the angle η with the rolling direction of the sample:

$$\begin{aligned}
\alpha_1(\eta) &= |(\cos\varphi_1 \cos\varphi_2 - \sin\varphi_1 \sin\varphi_2 \cos\phi) \cos\eta + \\
&\quad +(\sin\varphi_1 \cos\varphi_2 + \cos\varphi_1 \sin\varphi_2 \cos\phi) \sin\eta\,| \\
\alpha_2(\eta) &= |(-\cos\varphi_1 \sin\varphi_2 - \sin\varphi_1 \cos\varphi_2 \cos\phi) \cos\eta + \\
&\quad +(-\sin\varphi_1 \sin\varphi_2 + \cos\varphi_1 \cos\varphi_2 \cos\phi) \sin\eta)| \\
\alpha_3(\eta) &= |(\sin\varphi_1 \sin\phi \cos\eta - \cos\varphi_1 \sin\phi \sin\eta)|
\end{aligned} \tag{8.22}$$

Now, we calculate the sine functions which appear in equation (8.20):

$$\sin 2a_1 = \sin(2 \arccos \alpha_1)$$
$$\sin 2a_2 = \sin(2 \arccos \alpha_2) \qquad (8.23)$$
$$\sin 2a_3 = \sin(2 \arccos \alpha_3)$$

The average value of $E_r(\mathbf{h})$, as given in equation (8.19), calculated in the sample direction $\mathbf{y}$ = (90°, η) over all orientations g of crystallites is:

$$\overline{E}_r = \oint E_r(g)\, f(g)\, dg \qquad (8.24)$$

where f(g) is the orientation distribution function.

The experimental power losses measured at different inductions B_m in different directions in the sheet plane of three grain oriented materials are displayed in Table 3.3 (a to c). The total energy required to magnetize the sample is:

$$E_T(\eta) = \frac{1}{2}\, H(\eta)\, B_m = \frac{1}{2}\, H\, B^a + \frac{1}{2}\, H\, B^r \qquad (8.25)$$

and it produces both the active and reactive components of magnetization. Since we do not know the values of the magnetic field H(η) used to produce the constant magnetization in the sample (90°,η) direction, we consider this term of equation (8.25) a constant. In this case, the average of the reactive energy calculated using equation (8.24) describes the angular variation of the anisotropy function (8.20) in the sheet plane. To illustrate the relationship between the anisotropy of the reactive energy and the angular variation of power loss, we plotted the experimental power losses and the calculated values of the reactive energy on the same scale. These plots are shown in Figure 8.2 (a to c), together with the fourth order texture parameter F_4, plotted on a different scale. On these graphs one observes that the difference between the experimental and theoretical curves increases with an increased angle from the rolling direction (RD). These differences are due to the fact that the external field necessary to create a constant magnetization in the sample is not constant, as was assumed, but increases with the angle from rolling direction compensating for the increase of the magnetostatic energy created by the free magnetic poles on the sample surface. Since the angle between the magnetic field and <100> easy direction is continuingly increasing from 0° at RD, to 45° at TD, an additional term which has the form (Imamura et al. [54]):

$$E_{ms}(\eta) = \frac{1}{2\overline{\mu^*}\,\mu_0} B_m^2 \sin^2\theta(\eta) \tag{8.26}$$

is introduced on the right side of the energy expression (8.25) to account for the dissipated energy by free magnetic poles creation on the sample surface. This term also explains the increase of power losses with increasing peak induction B_m. The approach of Morris and Flowers [26] does not predict the dependence of power loss on the peak magnetization, which is an important technological parameter.

The most important aspect of the theoretical approach proposed, is its practical applicability. When power loss is measured in the rolling direction of a grain oriented sample, the reactive energy is not zero, but depends on the texture function (ODF), and it is calculated using equation (8.24). The lowest values of power losses obtained in high permeability (H-B) grain oriented steels where the texture is very sharp and approaches to the ideal (110)[001] orientation are partially explained by the decreasing reactive component of magnetization in these materials.

8.3. NEW INTERPRETATION OF THE EXCESS LOSS

In this section, a new approach is proposed for understanding the relationship between the excess loss and textural and structural parameters of polycrystalline soft magnetic materials. As mentioned in chapter 2.4, several models have been developed to interpret the excess loss in soft magnetic materials. In the case of single crystals, the model proposed by Pry and Beam [28] was extended to include various effects, like the presence of irregularities in the wall motion (Shilling, [93]), statistical distribution of the domain population (Bishop, [61]), domain multiplication (Sakaki, [94]) and wall bowing (Bishop, [95]). The case of fine-grained non-oriented soft magnetic materials was treated by Mazzetti [96], who proposed a model which related the excess loss to the Barkhausen noise.

In a series of articles [97]-[100], Bertotti proposed an unified theoretical explanation of power losses based on a statistical approach of this phenomenon. The main concept of his theory is describing the magnetization process in a given cross section of the material in terms of "n" active correlation regions, termed magnetic objects (MO). A magnetic object (MO) can be identified with a single Bloch wall in grain oriented materials, or with a group of neighbouring interacting domain walls in microcrystalline materials. The excess loss is expressed as a function of a fictional field H_{exc} acting on each magnetic object:

$$P_{excess} = \dot{B}\, H_{exc} = 4 B_m\, f_m\, H_{exc} \qquad (8.27)$$

where B_m is the peak induction, f_m is the magnetizing frequency and S is the cross section area. The number of active magnetic objects deduced by Bertotti from dimensional and qualitative considerations is:

$$\tilde{n} = \frac{H_w}{H_{exc}} \qquad (8.28)$$

$$\text{where:} \quad H_w = 4 \sigma\, G^w\, S\, B_m\, f_m$$

represents the dynamic field existing when the material is magnetized by the movement of a single wall. In the above relation, σ is the electrical conductivity of the material, and G^w is the dumping coefficient of a single plan wall:

$$G^{w} = \frac{4}{\pi^{3}} \sum_{odd} \frac{1}{n^{3}} \tag{8.29}$$

Bertotti found that several iron-based alloys including oriented and non-oriented silicon steels obey the linear law:

$$\tilde{n} = n_0 + \frac{H_{exc}}{V_0} \tag{8.30}$$

where n_0 is the number of magnetic objects when $f_m \rightarrow 0$, and the field V_0 is controlled by the material microstructure.

Bertotti's model leads to the non-linear expression for the excess loss as a function of magnetizing frequency:

$$P_{exc} = \dot{B} \frac{n_0 V_0}{2} \left(\sqrt{1 + \frac{4 \sigma G^{w} S \dot{B}}{n_0^2 V_0}} - 1 \right) \tag{8.31}$$

$$\textit{where:} \qquad \dot{B} = 4 \, B_m \, f_m$$

and S is the lamination cross section area.

This expression describes the excess loss in both oriented and non-oriented silicon steels, but the characteristic magnetic field V_0 which governs the number of domain walls participating in the magnetization process has different interpretations for the two cases. Even if this model correctly describes the experimental data, the parameters involved in equation (8.31) are not related to the material structure.

Bertotti's model led to the conclusion that the magnetization process is controlled by a general physical principle through the simple characteristic field V_0. In this connection, the principle of minimum entropy production used by Haller and Kramer [101] offers the possibility of identifying some structural parameters which directly affect the excess loss. Our simple model, depicted here in Figure 8.3, is very similar to the Pry and Bean model,

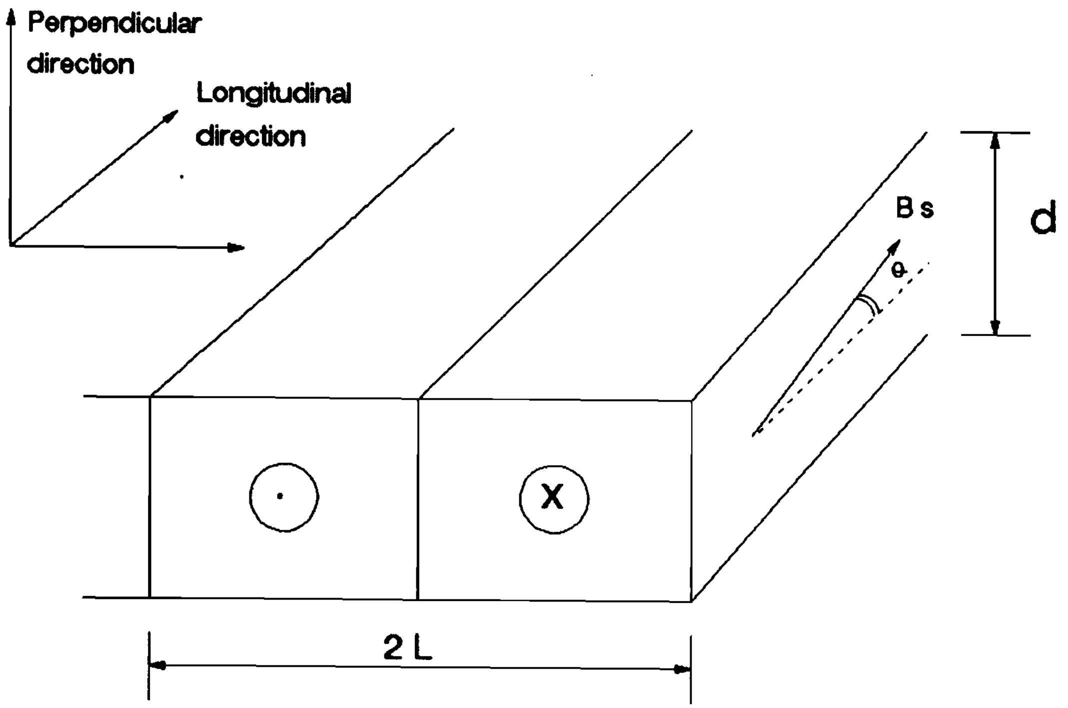

Fig.8.3. Model for magnetic domain structure

invoking an infinite regular parallel array of walls spanning a lamination of infinite width. The easy magnetization direction, however, is slightly inclined from a specimen surface. It constitutes a good first approximation to the domain structure in grain oriented materials. In the proposed model, the magnetization process is accomplished by domain wall motion and domain wall nucleation. The energy dissipation is assumed to be related to the following mechanisms:

(1) eddy current loss E_{eddy} dissipated as heat

(2) domain wall nucleation requires additional energy E_{wall} which must be supplied by the external field

(3) the appearance of free magnetic poles on the material surfaces is also dissipative, E_{ms}.

During one half-cycle of magnetization, the total energy dissipated in the sample is:

$$E_T = E_{eddy} + E_{wall} + E_{ms} \tag{8.32}$$

In a slab material of thickness d, width l and length > l, the number of domain walls present at a certain stage of magnetization process is:

$$N = \frac{l}{2L} \tag{8.33}$$

where 2L is the magnetic domain spacing. This number includes the number of walls existing in the specimen in the demagnetized state, and the number of walls nucleated during the magnetization process. In the model presented in Figure 8.3, the number of domain walls can vary, but they remain parallel one to the other.

The energy dissipated in the sample during one half-cycle of magnetization through eddy currents is given by the expression developed by Pry and Beam [28] for the case of constant average magnetization rate:

$$E_{eddy} = 16\sigma\, d\, G^{w} B_{m}^{2} f_{m} \left(\frac{l}{N}\right) \tag{8.34}$$

where the domain spacing (2L) was substituted by (1/N), and all other symbols were previously defined.

The energy of domain walls per unit volume of the sample is:

$$E_{wall} = \frac{1}{l}\, \gamma_{w} N \tag{8.35}$$

where γ_w is the wall energy per unit surface.

Since the magnetostatic energy along the longitudinal direction is negligible for a long slab (length > 1), only the magnetostatic energy for the direction perpendicular to the surface is considered. The expression for this energy was derived by Kooy and Enz [102]:

$$E_{ms} \simeq \frac{2}{\bar{\mu}^{*}} \frac{B_{m}^{2} \sin^{2}\theta}{4\mu_{0}} + \frac{1}{\bar{\mu}^{*}} \frac{B_{s}^{2} \sin^{2}\theta\, G^{w}}{\mu_{0}\, d} \left(\frac{l}{N}\right) \tag{8.36}$$

In this equation, B_s is the saturation induction of the material, θ is the out-of-plane angle of the magnetization direction, and μ^* (= 46 for iron) is the coefficient accounting to the μ^* correction in both the magnetized and demagnetized states (Imamura et al. [54]).

The total energy dissipated in the sample is minimized with respect to the number of domain walls N:

$$\frac{\partial E_{T}}{\partial N} = 0 \tag{8.37}$$

and the result is:

$$N^2 = \frac{16}{\gamma_w} \sigma d\, G^w l^2\, B_m^2\, f_m + \frac{1}{\bar{\mu}^*} \frac{B_s^2 \sin^2\theta\; G^w\, l^2}{\mu_0\, d\, \gamma_w} = \tag{8.38}$$
$$= N_f^2 + N_0^2$$

where N_f is the number of domain walls present in the sample at a certain magnetizing frequency, f_m. In the low frequency range ($f_m \rightarrow 0$), this model predicts a value of the number of domain walls N_0 which gives the domain spacing as a relationship identical to that derived by Imamura [54] using the minimum energy principle:

$$\frac{1}{2L} = \frac{N_0}{l} = \frac{B_s \sin\theta\, \sqrt{G^w}}{\sqrt{\mu_0\, \bar{\mu}^*\, \gamma_w\, d}} \tag{8.39}$$

The excess power loss per cycle is calculated substituting the expression deduced for N in the energy formula (8.32):

$$\frac{P_{exc}}{f_m} = \frac{1}{\bar{\mu}^*} \frac{B_m^2 \sin^2\theta}{2\mu_0} + 2\sqrt{\gamma_m}\, \sqrt{A\, f_m + B}$$
$$A = 16\, \sigma d\, G^w\, B_m^2 \tag{8.40}$$
$$B = \frac{1}{\bar{\mu}^*} \frac{B_s^2 \sin^2\theta\; G^w}{\mu_0\, d}$$

which is similar in form to equation (8.27), derived by Bertotti. Thus, the two models, one based on the phenomenology and the other on structural parameters, describe the same magnetization mechanism. Both models predict similar dependence on the number of active walls in the sample on the peak induction B_m, and on the square root of magnetizing frequency, supporting the experimental results published by Haller and Kramer [101].

From equations (8.31) and (8.40), one can identify the characteristic field V_0, when the terms which do not depend on n_0

are compared (no analytical expression is given for n_0). It turns out that V_0 is:

$$V_0 = \frac{\gamma_w d}{4S B_m} \tag{8.41}$$

The fact that the field V_0 is found to be dependent of B_m makes it a parameter related to the magnetization process, so that it is not an intrinsic parameter of the material, connected to the microstructural properties. We conclude that the presented model correctly predicts the variation of domain wall spacing and power loss with the frequency and the peak magnetization. It also gives a correct value for the static domain wall spacing, and it was built on a solid theoretical background, but it does not predict the characteristic field. In the following, we try to improve this situation.

In our model describing the excess loss, the hysteresis loss as a mechanism of energy dissipation was not considered. On the basis of dimensional and qualitative considerations, Bertotti suggested [99] that the microstructural interpretation of V_0 should involve a relation of the form:

$$V_0 \sim \frac{H_c}{N_0} \tag{8.42}$$

where H_c is the coercive field, and N_0 is the number of magnetic objects present in a given cross section of the material. We assume again (see § 6.3 in this work) that the number of pinning centres having a critical field from H_0 to (H_0+dH_0) is $f_0 \cdot dH_0$. The quantity f_0 represents the pinning centre density per unit critical field dH_0, which is an intrinsic parameter of material. To move an isolated wall, we must apply a field higher than the coercive field:

$$H = H_c + \Delta H = H_0 + H_{exc} \tag{8.43}$$

where ΔH represents the excess field required to balance the opposite field produced by eddy currents surrounding the moving wall. Generalizing the above relation to the whole sample, the number of walls which move when the external field is increased with $\Delta H = H_{exc}$ is:

$$\tilde{n} = f_0 H_{exc} = \frac{H_{exc}}{\frac{1}{f_0}} = \frac{H_{exc}}{V_0} \tag{8.44}$$

and the excess field acting on a single domain wall is decreased accordingly. In this way, the characteristic field V_0 is related to a microstructural parameter, $1/f_0$, which represents the critical field per unit pinning centre in the interval from H_0 to $(H_0+\Delta H_0)$. If the critical field H_0 depends on the angle γ between the external magnetic field H and the direction of spontaneous magnetization, as expressed by equation (6.16), the characteristic field V_0 is expected to have an opposite variation (higher value of critical field corresponds to a fewer number of pinning centres in that interval):

$$V_0 = \frac{\cos\gamma}{f_0} \tag{8.45}$$

Bertotti's experimental results [99] prove that V_0 decreases with increasing sample cross section (f_0 increases), decreasing grain size (f_0 increases), and decreasing degree of magnetic orientation ($\cos\gamma$ decreases); no analytical relationship between the characteristic field and these microstructural parameters was suggested.

There are several factors determining the number of moving walls in a grain oriented sample, among which our simple model identified: the magnetizing frequency, the peak magnetization and the characteristic field. The influence of these factors on the magnetization process can be inferred from the minimum entropy production principle. Since the characteristic field acts on a microscopic scale, it is expected to have a greater influence on the minimization of the entropy production than the magnetizing frequency and the peak magnetization, which influence the magnetization process on a macroscopic scale.

In non-oriented silicon steel, the average size of magnetic domains is certainly smaller than the grain size which, in turn, is much smaller than the thickness of the steel sheet. In this case, the active magnetic object refers to the whole domain structure inside a single grain.

Bertotti's model for calculating the excess power loss in non-oriented steels [103] is equivalent to our model based on the minimum entropy production principle when we assume that the mechanism of energy dissipation in the sample is only the hysteresis loss. To demonstrate this, let us consider that the total number of magnetic objects (MO) which are present in the lamination cross section S is:

$$N_0 = \frac{S}{s^2} \tag{8.46}$$

where s is the average dimension of the grain.

When a magnetic object completely reverses its flux, it gives a contribution of

$$\Delta B = \frac{2<B_s>}{N_0} \tag{8.47}$$

to the total magnetization, where $<B_s>$ is the induction corresponding to the condition where each grain is saturated along its easy magnetization direction. For an isotropic iron sample, it was demonstrated by Chikazumi [9] that $<B_s> \approx 0.85\ B_s = 1.7$ T.

In dynamic conditions, at each point of the magnetization loop the applied field is greater that its static value by an amount ΔH

$= H_{exc}$. The additional energy supplied to the sample during a cycle of peak magnetization B_m equals the energy required by N magnetic objects to overcome the local coercivity H_c :

$$2\,H_{exc}\,B_m = N\,H_c\,\Delta B = 2N\,H_c\,\frac{<B_s>}{N_0} \tag{8.48}$$

From the above equation, we obtain:

$$N = \frac{H_{exc}}{\dfrac{H_c\,<B_s>}{B_m\,N_0}} = \frac{H_{exc}}{V_0} \tag{8.49}$$

and

$$V_0 = \frac{H_c\,<B_s>}{B_m\,N_0} \tag{8.50}$$

This equation is identical to the equation for V_0 proposed by Bertotti [103], but the characteristic field is derived from a different theoretical approach.

It was demonstrated in this section that the principle of minimum entropy production controls the global features of the magnetization dynamics in ferromagnetic materials. The advantage of this approach is that it relates the excess power loss to parameters characterizing the microstructure and the magnetic domain structure of material. Even if the model is very simple, it offers direction for reduction of losses in electrical steels.

The number of domain walls contributing to the magnetization process is correlated with the coercive field. In the theoretical frame corresponding to the presence of a number of strongly correlated magnetic objects, the characteristic field V_0 makes the dynamic homogenization of the magnetization process easier (see equation 8.30). It was demonstrated by experiments in § 6.2 that this factor, V_0, significantly contributes to loss reduction, and its contribution is more important than decreasing the average wall spacing in static conditions.

8.4. CORRELATION BETWEEN TEXTURE AND ROTATIONAL LOSS IN NON-ORIENTED STEELS

The study of Narita and Yamaguchi [104], [105] on rotational hysteresis losses in silicon iron single crystals with different orientations clarified that the greater part of rotational loss is explained by changes in the domain structure. During these changes, the energy is dissipated as a result of annihilation of the domain walls. The results obtained by these authors [104], [105] show that the rotational loss in the {111} plane is highest because the {111} surface does not contain magnetic easy axis and, as a result, the domains are very fine. Rotational loss in {110} plane is smaller because there exists only one easy axis. In {100} plane there are two easy axes and the rotational loss is the smallest.

In polycrystalline materials, the process of domain wall creation and annihilation is more complicated because an additional magnetostatic energy appears at the grain boundaries, but this process is also influenced by crystallite orientation.

The rotational losses in the four non-oriented silicon steel samples were calculated using equation (2.40) and the experimental values of power losses measured in longitudinal and transverse directions of the steel sheets are shown in Table 3.4.

Volume fractions of material where the crystallites are oriented with the **h** = <hkl> crystallographic direction parallel to the sample normal direction (ND) are calculated using the orientation distribution function f(g):

$$\frac{\Delta V(\boldsymbol{h} \parallel ND)}{V} = \frac{1}{8\pi^2} \oint_{\boldsymbol{h} \parallel ND} f(g)\, dg \qquad (8.51)$$

Using this formula, the volume fractions of crystallites having the {100}, {110}, and {111} planes in the sheet plane,

Fig.8.4. Rotational loss as a function of volume fraction with <111> || ND

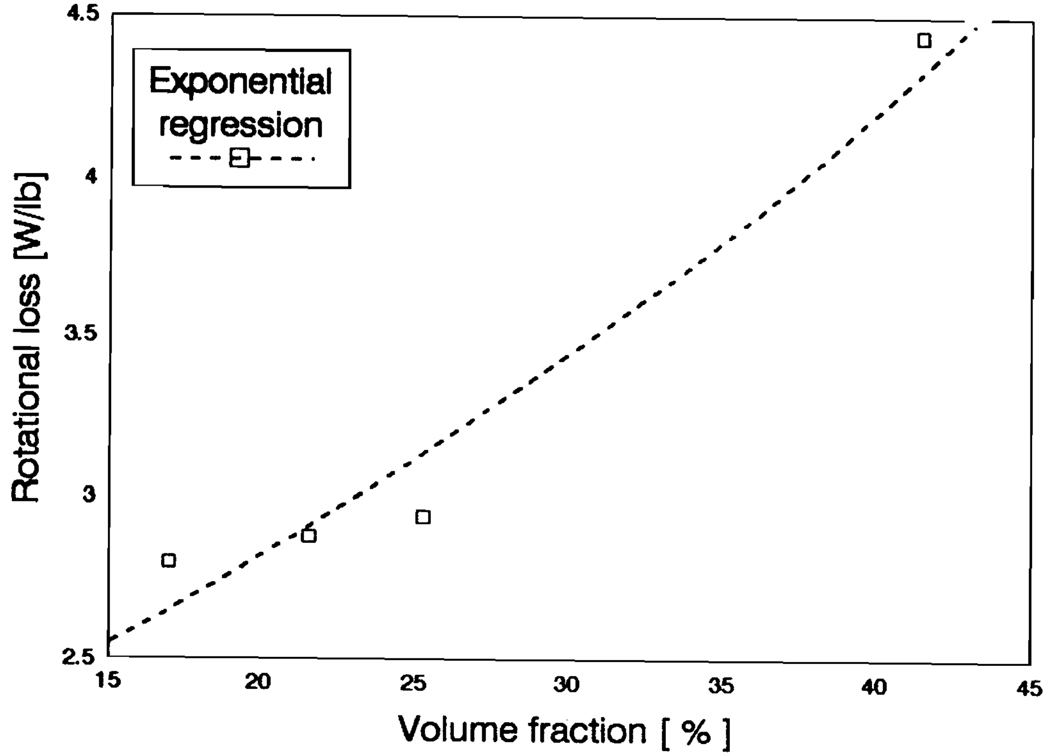

respectively, have been calculated. The results are presented in Table 8.1.

Table 8.1. Volume fractions of grains having crystallographic directions <hkl> parallel to the normal direction (ND).

Sample	<100> ∥ ND	<110> ∥ ND	<111> ∥ ND
0 %	16.5 %	2.4 %	41.5 %
2 %	17.0 %	7.8 %	21.6 %
6 %	13.3 %	6.6 %	25.3 %
12 %	18.2 %	4.4 %	17.0 %

Comparing this calculated data to the experimental rotational loss values, one sees that there exists a strong correlation between the rotational loss and the volume fraction of crystallites with the direction **h** = <111> parallel to the sample normal direction. This correlation is presented in Figure 8.4.

For other crystallite orientations, it is difficult to find a correlation with rotational loss because, on the one hand, the volume fraction of crystallites having **h** = <110> parallel to the normal direction is small and, on the other hand, the rotational loss produced in the crystallites having {100} plane in the plane of the sheet is very small.

8.5. COMPARISON BETWEEN DIFFERENT PROPOSED MODELS

The influence of texture on the anisotropy of the magnetic properties of rimmed steel and non-oriented silicon iron was investigated by Hutchinson and Swift [36], and by Morris and Flowers [26]. The present work extends this study and describes the correlation of ODF data with core loss in grain oriented silicon steels. The magnetic anisotropy energy parameter F_4(RD) is defined by equation (2.51), and calculated using the C_l^{mn} coefficients presented in Table 4.3. The regression analysis presented in this paragraph makes use of the experimental values of power losses listed in Table 3.2. Figure 8.5 shows the regression of the fourth order texture parameter F_4(RD) as a function of power loss measured at 1.5 T and 1.7 T (60 Hz). From this graph we see that texture is indeed one parameter influencing power loss. In grain oriented materials, however, the core loss is poorly described by a common least-squares line, compared to the data presented by Morris and Flowers [26] for non-oriented materials.

It is interesting to note that we observed no significant difference in the quality of the regressions based on the 1.5 T power losses and those based on the 1.7 T power losses. Due to the fact that higher induction reaches a further point on the hysteresis curve, we should have expected a better correlation for the 1.7 T power loss data, than that obtained for 1.5 T; this is however, not the case.

In the case of non-oriented materials, no correlation between the power loss and the texture function F_4(RD) was found . This result confirms that the power losses in non-oriented materials is entirely due to texture-independent factors, such as grain size differences.

Modelling the magnetization process in a wide single crystal slab slightly misoriented from the ideal (110)[001] orientation, Imamura et al. [54] derived a formula for the domain wall spacing from the minimization of the total magnetization energy. The analytical expression for domain wall spacing derived by Imamura is given in equation (8.39).

The domain wall spacing is related to power loss through the model developed by Pry and Bean. This model predicts only the eddy current loss, but in grain oriented materials at the magnetizing frequency of 60 Hz the eddy current loss represents the main contribution to the total power losses. The regression of the domain wall spacing (or $1/\langle\sin\gamma\rangle$, see equation 6.25) as a function of power loss measured at 1.5 T and 1.7 T, is shown in Figure 8.6. It is evident that the texture parameter $\langle\sin\gamma\rangle$ poorly correlates to power loss. While these relationships point toward the correlation between texture and power loss, we must mention that

Fig.8.5. Power loss in grain oriented samples (9 mil)

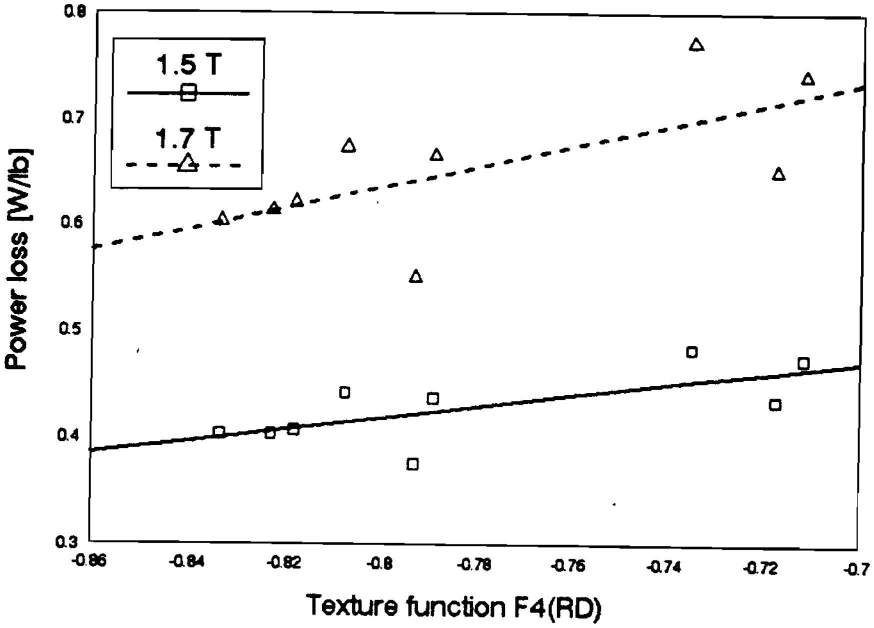

Fig.8.6. Power loss in grain oriented samples (9 mil)

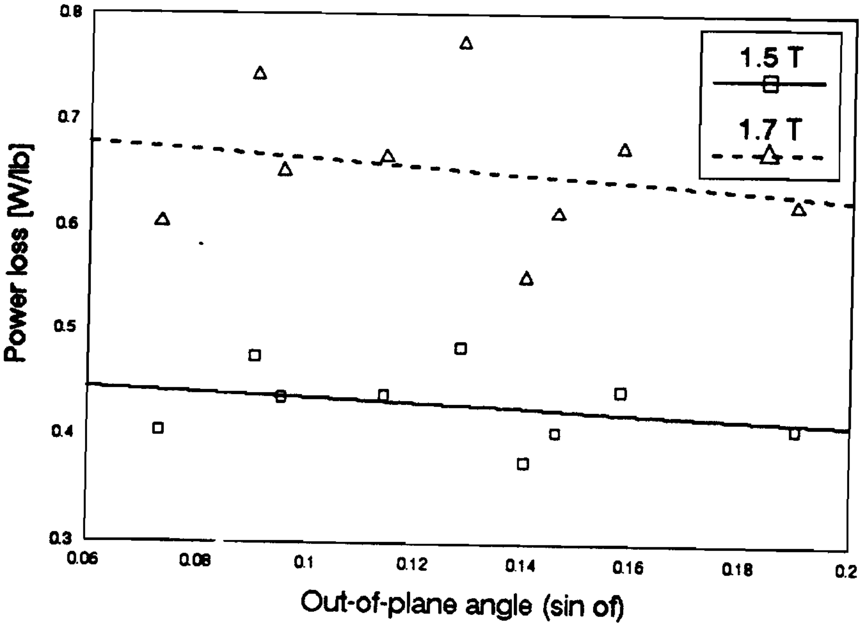

Fig.8.7.a. MBN power vs. core loss in grain oriented samples (9 and 7 mil)

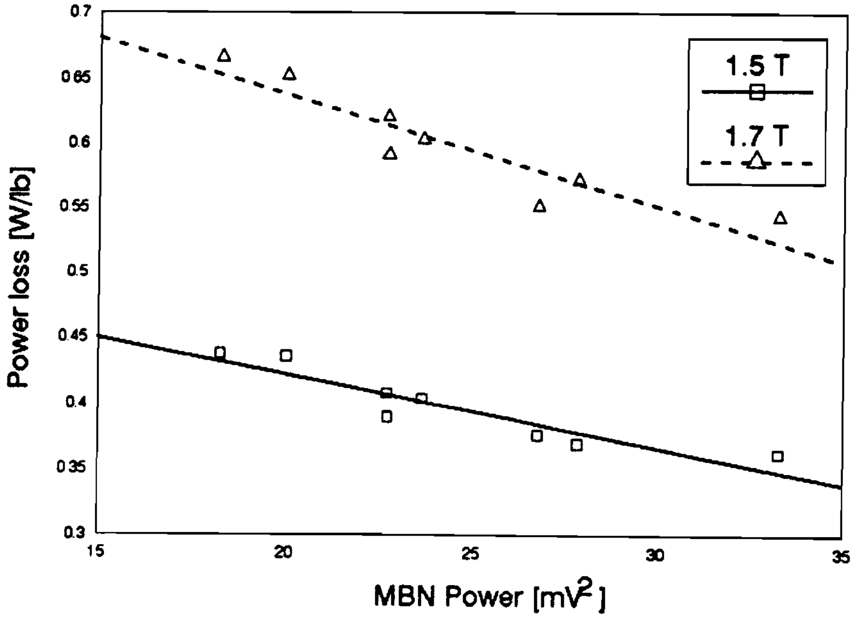

Fig.8.7.b. Regression of MBN power as a function of core loss and grain size

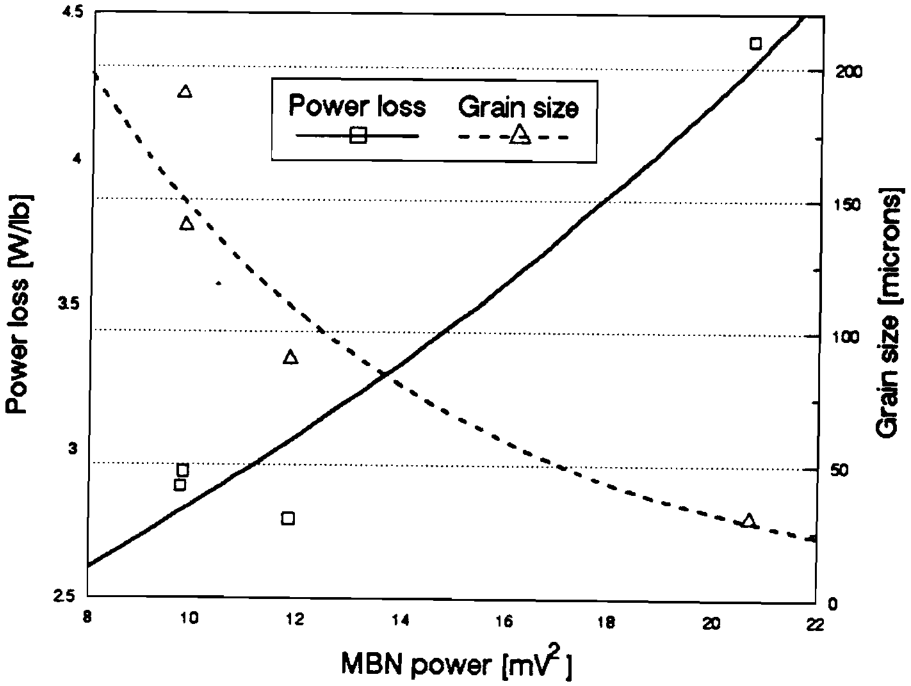

these correlations are weak, ranging in terms of the correlation coefficient R^2 to somewhere between 0.1 and 0.5. There is no way to correlate the power loss with domain wall spacing in non-oriented materials.

The model proposed in this work relates power loss to the number of Barkhausen jumps characterizing the irreversible magnetization process. The parameter controlling this process is the characteristic field V_0. Even if we are not able to calculate the value of this parameter using the information related to the material structure, it can be directly evaluated from the magnetic Barkhausen noise (MBN) measurements. The regression of MBN power as a function of power losses is shown in Figure 8.7 (a and b) for grain oriented and non-oriented materials respectively.

These graphs clearly indicate a correlation between the power loss and the measured Barkhausen spectra. The power loss depends on the number of walls released from the pinning centres at each infinitesimal increase of the magnetic field. In grain oriented materials, there is an inverse proportionality between the power loss and the density of pinning centres per unit critical field, demonstrating that the power loss improvement is obtained by increasing the number of moving walls at each stroke of displacement, or equivalently, by decreasing the loss due to eddy currents surrounding the moving wall.

In non-oriented materials, the power loss is proportional to the pinning point density per unit critical field, which may indicate that a correlation exists between the total power losses and grain size. The relationship between the power loss and the pinning point density per unit critical field demonstrates that the power loss in non-oriented materials is primarily caused by the hysteresis loss.

As our contribution to the understanding of the magnetization process, the characteristic field $V_0 = 1/f_0$ was defined as the critical field per unit pinning centre, and it is interpreted as the minimum field necessary to obtain at least one moving wall when the magnetic field is increased from H to $(H+\Delta H)$. It was proven that the characteristic field V_0 is the fundamental parameter controlling the power loss of ferromagnetic materials.

SUMMARY AND CONCLUSIONS

This work focussed on the correlation between the microstructure and magnetic properties of grain oriented and non-oriented electrical steels. The aim was to predict their magnetic behaviour, especially the permeability and power losses. Various models and methods for predicting the magnetic properties from structural characteristics of materials were proposed and tested. This led to the development of reliable methods of monitoring the quality of these materials, enabling a rapid and non-destructive characterization. Such methods are of considerable importance to the manufacturers of electrical steels.

From a theoretical perspective, the results increase our understanding of the correlation between the microstructure and magnetic properties of ferromagnetic materials.

Various topics were investigated in this thesis:

I. Experimental work was carried out on grain oriented and non-oriented commercial electrical steels. This included texture analysis, macromagnetic testing, domain observation, magnetic anisotropy energy, and Barkhausen noise measurements. In this way, the materials structure and magnetic properties were characterized. The experimental data enabled us to establish structural and textural differences between the various types of electrical steels, and to correlate them with differences in magnetic properties.

II. Theoretical models of interpreting the magnetic permeability and power losses were reviewed. Experimental data were compared with the theoretical predictions. This suggested new directions of research, and new approaches were used to find a better description of various mechanisms of the magnetization process.

In particular, the Bertotti's model correctly describes the power losses in ferromagnetic materials, but the equations were derived from dimensional and qualitative considerations. In this work, it was demonstrated that the minimum entropy production principle can be used to describe the loss mechanism.

The anisotropy of the magnetic properties was described by Morris and Flowers using an equation which was chosen to maintain consistency with the conventional treatment of magnetic anisotropy energy. In this work, we gave a theoretical justification for using the fourth order texture parameter F_4, as a general function which describes, to the first approximation, the anisotropy of permeability and power losses in textured materials.

III. To interpret the experimental magnetic data in textured materials, new models were developed. The saturation approach law was experimentally tested on materials with a sharp texture, and was explained using a model based on the magnetic anisotropy energy. The Barkhausen noise measurements were also interpreted using a new model based on the random variation of domain wall energy with its position in the sample.

IV. For a better understanding of the relationship between the magnetic properties and the material structure, new techniques of investigation were developed to analyze the magnetization process in ferromagnetic materials. The most promising method for further research in ferromagnetism is the neutron diffraction technique used for magnetic texture determination.

The new techniques based on Barkhausen noise measurements and on the determination of torque produced by the magnetization rotation offer the possibility for a rapid and non-destructive evaluation of material quality.

From the work presented in this thesis, the following conclusions can be drawn:

1. Study of the magnetic torque of the materials under investigation at the magnetic field strong enough to saturate the sample, confirms the existing relationship between the crystallographic texture and magnetic anisotropy energy.

As a simple method of evaluating the magnetic anisotropy in electrical steels, the torque magnetometry is suitable for non-oriented materials, where the number of grains in investigated specimen is high, and offers a reliable statistics of measurements.

2. The rotation of magnetic moments toward the increasing magnetic field is fully controlled by the magnetic anisotropy energy. This process was analytically described as a function of texture parameters and experimentally tested. Agreement between the experimental data and the predicted values was strong, demonstrating that the crystallographic texture controls the magnetization process from the knee of the magnetization curve to saturation.

These theoretical findings were used to build an instrument evaluating the texture quality, and which can be implemented for on-line texture inspection.

3. The quantitative correlation between the magnetization rotation process and the material texture is realized through the coefficient C^2, which characterizes the approach to saturation. It was shown that this coefficient is not constant, but depends on the distribution of grain orientation and on the direction of magnetization. It was demonstrated, using the proposed theoretical approach, that the process of magnetization rotation toward the

external field provides useful information about the angular spread of grain orientation.

4. Using the powder pattern technique, the domain wall spacing in individual grains of four grain oriented samples was measured. The correlation between the grain size and domain wall spacing is poor, leading to the conclusion that, in these materials, the misorientation of the crystallite from the ideal (110)[001] orientation is the factor dictating the dimension of the magnetic domain. This factor prevails when compared with the magnetostatic energy due to free magnetic poles existing at the grain boundaries.

The average domain wall spacing could not be correlated with power losses of the investigated samples. This means that the domain wall spacing does not entirely control the domain wall dynamics in investigated materials.

5. It was proposed that the minimum entropy production principle controls the global features of the magnetization dynamics. According to the model developed in this work, the number of active domain walls increases with the magnetizing frequency and the value of peak magnetization. The analytical formula which was derived represents a generalization of the Pry and Bean model, and it correctly describes the magnetization process. This formula was also used to explain the experimental data published by Imamura, Haller and Kramer, and Bertotti.

The minimum entropy production principle controls both the reversible and irreversible magnetization processes. When applied to the irreversible process, it determines the number of Barkhausen jumps which reverse the flux at a certain moment, such that the energy dissipated by the eddy current surrounding the moving wall is minimum. This is equivalent to the presence in the magnetic body of a fictitious field which determines the ability of the applied field to increase the number of moving domain walls. It was found that the value of this field is determined by the critical field (retarding force) per pinning centre.

6. A non-destructive method was developed and tested to study the effects of texture and microstructure on the magnetic Barkhausen noise (MBN), and also on the total power losses. The method relates the MBN power to the core loss through a model based on domain walls displacement after they are released from pinning centres. The fundamental parameter in this model is the characteristic field V_0, governing the progressive homogenization of the magnetization process. V_0 controls the irregularities in the wall motion which tend to disappear as the magnetizing frequency increases. The main result of this study is that the loss behaviour in the frequency range of practical interest (60 Hz) is basically governed by V_0 only, while the static domain wall spacing does not play any significant role.

7. A new mechanism of power loss in ferromagnetic materials was proposed. When the magnetization direction does not coincide with the easy direction, the magnetic anisotropy energy determines the appearance of a perpendicular component of magnetization, which is equivalent to a loss because it dissipates part of the energy supplied by the external field. We called this energy loss the reactive energy, and we demonstrated that this energy is anisotropic, and depends on the value of peak magnetization.

8. A unique method to investigate the magnetic texture in ferromagnetic materials was developed using non-polarized neutron diffraction. It offers the possibility of determining the evolution of the orientation distribution of the magnetic moments at different stages of the magnetization process.

This method was experimentally verified on determining the orientation distribution of magnetic moments in a magnetized sample of non-oriented silicon steel. It was observed that the magnetization process in electrical steels is related to the <100> easy directions. This method offers the possibility of investigating the internal magnetic structure of the sample.

9. It was demonstrated that, in texture measurements using polarized neutron diffraction, one can easily separate the magnetic part from the total scattering. However, the magnetic texture determination cannot be properly performed when the distribution of magnetic moment orientations has orthorhombic symmetry.

10. The magnetization process in grain oriented materials can be studied using the neutron depolarization effect. This new method was developed as a result of the important advantage it offered in directly measuring the sample magnetization in static conditions. As far as we know, there is no other method which makes this kind of measurement possible.

11. Study of the correlation between the rotational loss and texture of non-oriented silicon steels led to the conclusion that the crystallite orientation determines the value of losses due to the creation and annihilation of domain walls. Very high values of rotational losses were obtained in single crystals where the magnetization occurred in the {111} plane. This observation could be generalized to the case of polycrystalline materials with different textures. Therefore, in evaluating the rotational loss in a textured steel specimen, valuable information is contained in the γ fibre of the crystallite orientation distribution space.

12. To measure texture in coarse grained material, the neutron diffraction technique was used. To correct the experimental data, we studied the phenomenon of the neutron extinction in a textured material. To our knowledge, this is the first attempt to investigate the effect of the extinction phenomenon on texture measurements. The perfection of the grain structure and the grain shape anisotropy causes the extinction anisotropy. When the texture is measured, the intensities of the diffracted beam in symmetrical equivalent directions are not the same. As a result, errors are introduced in the ODF calculation. A correction method was proposed which eliminates the effects of the anisotropy of extinction.

It was demonstrated that the sample absorbtion coefficient increases when the crystallographic perfection of the grains is destroyed. This so-called "secondary extinction" is related to the multiple scattering, and it is associated with mosaic blocks with the same orientation but situated in different grains. All these blocks have roughly the same dimension and their shape is isotropic. No intensity correction is necessary when measuring texture.

STATEMENT OF ORIGINALITY AND CONTRIBUTION TO KNOWLEDGE

The original contributions of this work to the area of magnetization process in textured ferromagnetic materials could be classified as following:

A. Development of new methods to analyze the influence of texture and structure on magnetic properties of electrical steels:

1. Using polarized and non-polarized neutron diffraction, the magnetic texture of ferromagnetic materials was determined for the first time. To obtain such information, two problems were solved:

- separation of magnetic scattering from the total diffracted intensity, and
- calculation of the function which describes the orientation distribution of magnetic moments.

2. The polarized neutron diffraction was used, for the first time, to separate the magnetic signal. It was demonstrated that this method is not applicable for magnetic texture calculation in the case where the orientation distribution of magnetic moments has orthorhombic symmetry.

3. A method based on the depolarization of the neutron beam

passing through a ferromagnetic specimen was developed to analyze the anisotropy of the magnetization process in static conditions. The measurements and analysis were performed at both constant magnetization and constant field applied along different directions of the metal sheet.

4. A non-destructive method for Barkhausen noise determination was developed in this work. It was proposed that the measurements of magnetic Barkhausen noise can be used to reveal the existence of the characteristic field controlling the homogenization of the magnetic flux.

5. The relationship between texture and magnetization process from the knee of the magnetization curve to saturation was proposed and tested using the magnetic torque instrument, which has been designed and built as a part of this research.

B. Development of new models linking the magnetic properties to texture and microstructure:

1. The model of magnetization based on the minimum entropy production principle was proposed. This model was used to calculate the domain wall spacing and power losses.

2. A new mechanism of power loss in ferromagnetic materials was proposed. Reactive energy, due to the inherent presence of the perpendicular component of magnetization, is anisotropic and it depends on the value of peak magnetization. For the first time it was shown that the loss generated by the new mechanism can be described using a texture function.

3. To interpret the magnetic Barkhausen noise (MBN) data, a new model was developed to describe the irreversible magnetization process. The proposed model links the MBN power to core loss by means of the characteristic field.

4. For the first time, the upper and lower bounds of the permeability in a magnetic multiphase material were described using the texture function (ODF). It was shown that the anisotropy of permeability can be expressed using a texture function which corresponds, to the first approximation, to the fourth order texture parameter.

5. An analytical expression was derived for the coefficient C^2, characterizing the magnetization rotation process. Then, a formula for the approach to saturation law was obtained as a function of texture coefficients.

C. Development of new methods to monitor the quality of electrical steels:

1. The approach to saturation law has offered us the theoretical background for obtaining information about the quality of material texture. A method to evaluate texture was devised and tested using a modified torquemeter. The variations in texture quality were easily detected. This method can be implemented on-line and may be of practical importance to the grain oriented steels industry.

2. It was demonstrated that the quality of the electrical steel can be tested using the magnetic Barkhausen noise (MBN) instrument. Since the correlation between the MBN power and core loss is very good, this method can be used for rapid and non-destructive evaluation of electrical steel quality (power losses). The method applies to both grain oriented and non-oriented electrical steels.

REFERENCES:

[1] H.J.Bunge, "*Texture Analysis in Materials Science*", Butterworths Publ., London (1982)

[2] J. Pospiech, Proc.ICOTOM-8, Santa Fe, pp.93 (1988)

[3] P. Weiss, J. de Phys. 6, pp.661 (1907)

[4] W.Heisenberg, Z.Physik. 49, pp.619 (1928)

[5] H. Barkhausen, Phys.Z. 20, pp.401 (1919)

[6] J.W.Shilling and G.L.Houze, IEEE Trans.Magn. vol.MAG-10, pp.195 (1974)

[7] F.Bloch, Zeit fur Phys. 61, pp.206 (1930)

[8] H.R.Wenk, "*Preferred orientation in deformed metals and rocks*", Orlando: Academic Press (1985)

[9] S.Chikazumi, "*Physics of magnetism*", John Wiley & Sons Inc., New York (1964)

[10] K.H.Stewart, "*Ferromagnetic domains*",Cambridge: Cambridge University Press (1964)

[11] J.Kranz and B.Passon, J.Angew. Phys. 13, pp.122 (1961)

[12] W.Paxton and T.Nilan, J.Appl.Phys. 26, pp.994 (1955)

[13] Y.Shur and Y.Dragoshansky, Phys.Met.Met. 22, pp.57 (1968)

[14] J.J.Backer, J.Appl.Phys. 34, pp.1327 (1963)

[15] J.A.Szpunar and B.Szpunar, IEEE Trans.Magn. vol. MAG-21, pp.2613 (1985)

[16] J.A. Szpunar, Atomic Energy Review 142, pp.199 (1976)

[17] B.Alessandro, C.Beatrice, G.Bertotti and A.Montorsi, J.Appl.Phys. 68, pp.2901 (1990)

[18] M.Celasco, M. Masoero, P. Mazzetti and A. Stephanescu, IEEE Trans. Magn. vol. MAG-20, pp. 1837 (1984)

[19] J.A.Szpunar, A.Oles, B.Buras, I.Sosnovska, E.Pietras, Nucleonika 13, pp.1111 (1968)

[20] U.Zink, H.G.Brokmeier and H.J.Bunge, Proc. 10-th ICOTOM, pp. 251, Clausthal Germany (1993)

[21] K.Henning, E.Wieser, M.Betzl and K.Feldmann, Proc. 6-th ICOTOM, vol.2, pp.967, Tokyo Japan (1981)

[22] H.J.Bunge, Textures and Microstructures, vol.11, pp.75 (1989)

[23] M.F.Littmann, J.Appl.Phys. 38, pp.1104 (1967).

[24] J.W.Shilling and G.L.Houze Jr., IEEE Trans.Magn. vol MAG-10, pp. 195 (1974)

[25] D.J.Craik and D.A.McIntyre, IEEE Trans.Magn. vol MAG-5, pp.378 (1969)

[26] P.R.Morris and J.W.Flowers, Texture of Crystalline Solids, vol.4, pp.129 (1981)

[27] R.M.Bozorth, "*Ferromagnetism*", D. Van Nostrand Co., Inc., New York (1951)

[28] R.H.Pry and C.P.Bean, J.Appl.Phys. 29, pp.532 (1958)

[29] G.Bertotti, J.Appl.Phys. 54, pp.5293 (1983)

[30] J.E.L.Bishop, IEEE Trans.Magn. vol.MAG-20, pp.1527 (1984)

[31] M.Enokizono, T.Suzuki, J.Sievert and J.Xu, IEEE Trans.Magn. vol.MAG-26, pp.2562 (1990)

[32] B.D.Cullity, "*Introduction to Magnetic Materials*", Reading, Massachusets: Addison-Wesley (1972)

[33] K.Narita and T.Yamaguchi, IEEE Trans.Magn. vol.MAG-11, pp.1661 (1975)

[34] F.Brailsford, J.IEE vol.84, pp.399 (1939)

[35] W.B.Hutchinson and J.G.Swift, Texture vol.1, pp.117 (1972)

[36] R.L.Sanford and I.L.Cooter, "*Basic magnetic quantities and the measurement of the magnetic properties of materials*", National Bureau of Standards Monograph 47 (1962)

[37] P.Coulomb, "*Les textures dans les metaux de reseau cubique*", Dunod, Paris (1972)

[38] F.A.Underwood, "*Textures in metal sheets*", MacDonald London (1961)

[39] M.Humbert, in "*Experimental Techniques of Texture Analysis*", edited by H.J.Bunge, DGM Verlag, Oberursel (1986)

[40] C.G. Darwin, Philos. Mag. 43, pp.800 (1922)

[41] W.H.Zachariasen, "*Theory of X-ray diffraction in crystals*", John Wiley & Sons Inc., New York (1945)

[42] W.H.Zachariasen, Acta Cryst. A 23, pp.558 (1967)

[43] W.H.Zachariasen, Acta Cryst. A 24, pp.421 (1968)

[44] M.J.Cooper and K.D.Rouse, Acta Cryst. A 27, pp.622 (1970)

[45] P.J.Becker and P.Coppens, Acta Cryst. A 30, pp.129 (1974)

[46] A.A.Aldenkamp, C.P.Marks and H.Zijlstra, Rev.Sci.Inst. 31, pp.544 (1960)

[47] R.R.Birss and C.H.Shepherd, J.Phys. E 11, pp.935 (1978)

[48] I.H.Phillips and R.G.Shephard, J.Phys. D, vol.3, pp.721 (1970)

[49] B.D.Cullity, "*Introduction to Magnetic Materials*", Reading, Mass., Addison-Wesley (1972)

[50] J.G.Benford, IEEE Trans.Magn. vol.MAG-10, pp.1053 (1974)

[51] S.Chikazumi, "*Physics of Magnetism*", § 13.3, pp.274, John Wiley & Sons Inc., New York (1964)

[53] M.Celasco and P.Mazzetti, IEEE Trans. Magn., vol. MAG-5, pp.372 (1969)

[54] M.Imamura, Y.Sasaki and H.Nishimura, IEEE Trans.Magn. vol.MAG-19, pp.20 (1983)

[55] S.R.Hoon and J.Lowe, IEEE Trans. Mag. MAG-25, pp.1813 (1990)

[56] R.M.Bozorth and H.J.Williams, Phys.Rev. 59, pp.827 (1941)

[57] L.P.Tarasov, Phys.Rev. 56, pp.1224 (1939)

[58] E.R.Callen and H.B.Callen, J.Phys.Chem.Solids 16, pp.310 (1960)

[59] J.H.Phillips and R.G.Shepherd, J.Phys. D3, pp.721 (1970)

[60] F.Ono, J.Phys.Soc.Japan 50, pp.2564 (1981)

[61] J.E.L.Bishop, J.Phys. D: Appl.Phys., vol.9, pp.1367 (1976)

[62] C.Kittel, Rev.Mod.Phys. 21, pp.702 (1966)

[63] C.Heiden and L.Storm, Z.Angew.Phys. 21, pp.349 (1966)

[64] S.Saynajakangas, IEEE Trans.Magn., vol. MAG-10, pp.44 (1974)

[65] P.Mazzetti and G.Montalenti, Proceedings of the ICM Conference, Nottingham, pp.701 (1964)

[66] G.Bertotti, F.Fiorillo and M.P.Sassi, J.Magn.Magn.Mat. 23, pp.136 (1981)

[67] B.Alessandro, C.Beatrice, G.Bertotti and A.Montorsi, J.Appl.Phys. 64, pp.5355 (1988)

[68] B.Alessandro et al., J.Appl.Phys. 68, pp.2908 (1990)

[69] G.Bertotti and F.Fiorillo, IEEE Trans.Magn., vol.MAG-20, pp.1475 (1984)

[70] G.Bertotti, F.Fiorillo and A.M.Rietto, IEEE Trans.Magn., vol.MAG-20, pp.1481 (1984)

[71] G.E.Bacon,"*Neutron Diffraction*", Clarendon Press, Oxford (1975)

[72] B.R.Frieden, J.Opt.Soc.Am. 62, pp.511 (1972)

[73] B.R.Frieden and D.C.Wells, J.Opt.Soc.Am. 68, pp.93 (1978)

[74] J.Skilling and R.K.Bryan, Mon. Not. R. astr. Soc. 211, pp.111 (1984)

[75] E.Laue, J.Skilling, J.Staunton, S.Sibisi and R.G.Brereton, J.Mag.Res. 62, pp.437 (1985)

[76] P.J.Hore, J.Mag.Res. 62, pp.561 (1985)

[77] E.T.Jaynes, in "*The Maximum Entropy Formalism*", R.D.Levine and M. Tribus ed., MIT Press, Cambridge Mass. and London (1978)

[78] B.R.Frieden, in "*Deconvolution: with Applications in Spectroscopy*", P.A.Jansson ed., Academic Press (1984)

[79] W.H.Press, B.P.Flannery, S.A.Tenkolsky and W.T.Vetterling, "*Numerical Recipes*", Cambridge Univ. Press, Cambridge (1986)

[80] H.T.Halpern and M.H.Johnson, Phys.Rev. 55, pp.898 (1939)

[81] O.Halpern and T.Holstein, Phys.Rev. 59, pp.960 (1941)

[82] M.Th.Rekveldt, Z.Physik 259, pp.391 (1973)

[83] L.A.Akselrod, G.P.Gordeev, J.M.Lazebnick and V.I.Lebedev, Nuclear Instruments and Methods vol.164, pp.521 (1979)

[84] S.V.Maleyev and V.A.Ruban, Sov.Sol.Stat.Phys. 18, pp.1331 (1976)

[85] M.F.Littmann, J.Appl.Phys. 38, pp.1104 (1967)

[86] J.W.Shilling and G.L.Houze, Jr., IEEE Trans.Magn., vol.MAG-10, pp. 195 (1974)

[87] D.J.Craik and D.A.McIntyre, IEEE Trans.Magn., vol.MAG-5, pp.378 (1969)

[88] W.F.Brown,Jr., J.Chem.Phys. 23, pp.1514 (1955)

[89] Z.Hashin and S.Shtrikman, J.Appl.Phys. 33, pp.3125 (1962)

[90] W.Woodside and J.H.Messner, J.Appl.Phys. 32, pp.1688 (1961)

[91] C.J.F.Bottcher, "*Theory of Electric Polarization*", Elsevier Publishing Co., Houston, Texas (1952), pp.415-420

[92] W.M.Swift, W.R.Reynolds and J.W.Shilling, AIP Conf. Proc. #10, pp.976 (1972)

[93] J.W.Shilling, IEEE Trans.Magn. vol.MAG-17, pp.351 (1973)

[94] Y.Sakaki, IEEE Trans.Magn. vol.MAG-17, pp.1478 (1981)

[95] J.E.L.Bishop, IEEE Trans.Magn. vol.MAG-20, pp.1527 (1984)

[96] P.Mazzetti, IEEE Trans.Magn. vol.MAG-14, pp.758 (1978)

[97] G.Bertotti, J.Appl.Phys. 55, pp.4339 (1984)

[98] G.Bertotti, J.Appl.Phys. 55, pp.4348 (1984)

[99] G.Bertotti, J.Appl.Phys. 57, pp.2110 (1985)

[100] G.Bertotti, J.Appl.Phys. 57, pp.2118 (1985)

[101] T.R.Haller and J.J.Kramer, J.Appl.Phys. 41, pp.1036 (1970)

[102] C.Kooy and V.Enz, Philips Res. Rep., vol.15, pp.7 (1960)

[103] G.Bertotti, J. de Physique, vol. 46-C6, pp.389 (1985)

[104] K.Narita and T.Yamaguchi, IEEE Trans.Magn., vol. MAG-11, pp.1661 (1975)

[105] K.Narita and T.Yamaguchi, IEEE Trans.Magn., vol. MAG-10, pp.165 (1974)

[106] S. Saynajakangas and M. Otala, IEEE Trans.Magn., vol. MAG-9, pp.641 (1973)